Title
Open-Hardware Electronic Embedded Systems for Biological Cell Culturing

Author
Pansodtee, Pattawong

Publication Date
2021

UNIVERSITY OF CALIFORNIA
SANTA CRUZ

OPEN-HARDWARE ELECTRONIC EMBEDDED SYSTEMS FOR BIOLOGICAL CELL CULTURING

A dissertation submitted in partial satisfaction of the
requirements for the degree of

DOCTOR OF PHILOSOPHY

in

COMPUTER ENGINEERING

by

Pattawong Pansodtee

December 2021

The Dissertation of Pattawong Pansodtee
is approved:

Dr. Mircea Teodorescu, Chair

Dr. Marco Rolandi

Dr. David Haussler

Peter Biehl
Vice Provost and Dean of Graduate Studies

Table of Contents

List of Figures

List of Tables

Abstract

Open-hardware Electronic Embedded Systems for Biological Cell Culturing

Pattawong Pansodtee

In-vitro cell culturing is one of the most exciting tools scientists use to study cellular and molecular biology. Its applications range from normal physiology and biochemistry of cells, mutagenesis, carcinogenesis, drug screening and development, and manufacturing of biological compounds (e.g., vaccines). Studies of cell culture morphology often involved equipment such as a cell culture hood, incubator, microscope, centrifuge, etc. These pieces of equipment are often expensive and inaccessible. In addition, some equipment simply does not exist at all (e.g., equipment that can electronically change ion concentration in cell culture). Therefore, novel and more accessible equipment is needed.

This work explores various aspects of *in-vitro* related equipment and identifies the following equipment that needs to be revised. As biosensors get smaller and cheaper, a data acquisition system also needs to be more portable and accessible. A low-cost in-incubator imaging system that allows a long-term and high-throughput study of cell cultures is needed to study the long-term effect of various factors in cell cultures. An array of ion pumps require a more versatile and low-cost multi-channel potentiostat. The work addressed the needs mentioned above.

Specifically, in this thesis I discussed the sensing side, including Glucose sensor, Ions sensors, and high-throughput imaging system. I designed data acquisition systems for a glucose sensor and ion sensors, and electronic circuits for high-throughput imaging system. Additionally, an ion actuation and equipment that operate an array of ion pump (i.e., multi-channel potentiostat) is investigated. I proposed a novel, low-cost, multi-channel potentiostat tailored toward an array of ion pumps and general electrochemical applications. The multi-channel potentiostat was iterated and tested with several ion pump designs. Ion pumps and the multi-channel potentiostat are tested with fluorescent dyes and later genetically modified stem cells. Next, I introduce machine learning, closed-loop control for control V_{mem} of stem cells. Finally, to provide a glimpse of one possible future expansion of my work, I present a preliminary result from a work in-progress, *in-vivo* device.

Acknowledgments

First, I would like to offer my sincerest thanks and praise to my supervisor, Mircea Teodorescu who gave me a myriad of opportunities, including the chance to explore various research topics and other excellent opportunities that I would not be able to find elsewhere. Not only did he challenge me to expand my academic knowledge but he also taught me countless invaluable life lessons along the way.

I would like to give the utmost praise to Marco Rolandi and Marcella Gomez, whom I worked closely with and taught me how to communicate my ideas and collaborate in a large group setting.

Thanks to David Haussler and Sofie Salama, who sparked my interest in the intricate and mysterious world of biology.

I am deeply indebted to Arash Alex Mazhari for being my first friend in the states and helping me navigate an environment that was new and foreign to me at the time. Also, to Mazhari's family who were kind and generous enough to adopt me into their family and share countless holidays together.

I am genuinely grateful to have had a chance to work and share many memories with John Selberg, a highly talented individual, who always has creative ways to solve problems.

I would like to express my gratitude and appreciation to Erik and Victoria, the best labmates and housemates I could ever ask for.

Thanks should also go to Sergio Cordero for all his help and company during the past few years.

Special thanks to Maryam Tebyani, a wonderful friend who is always helping me fix my writing and being a great colleague in academic work.

From the bottom of my heart, I would like to thank all past and present members of the DANSER Lab for all their courage and support. Ash Robbins,

Anca Popescu, Gordon Keller, Aviv Elor, Mike Powell, Samira Zare, Jinghui (Sury) Geng, Alex Spaeth, Sebastián Torres Montoya, Pierre Baudin, and Steve Lessard.

I also had great pleasure of working with such exceptional undergraduates, including Thomas Thomsen, James Trombadore, Calvin Chopra, and Mel Ho.

This work could not happen without the amazing collaboration of Rolandi's and Gomez's groups, whom I had collaborated with over the past few years. Harika Dechiraju, Manping Jia, Mohammad Jafari, Xenofon Strakosas, Chunxiao Wu, Giovanny Marquez, and Carrie Bradley.

Thanks to the Braingeneers group, especially Gary Mantalas, Kateryna Voitiuk, Yohei M Rosen, Ryan Hoffman, Mohammed A. Mostajo-Radji.

Many thanks to my friends who inspired me to believe in myself and encouraged me to keep moving forward. Thanat Tothong, Sunisa Somssookh, Linda Cai, Sophia Wendt, Nima Bazofti, Supanong Sookmongkolgul, James Yasuhara, Yin Chaosantia, Kamolmas Ruengthong, Onaroon Budchanyaphot, and Piladelak Yindeesap.

Finally, to my family for their unconditional support and guidance. Sarawudh Pansodtee who inspired me to become an engineer and pursue higher education. Patcharaporn Pansodtee who taught me how to be kind and strive to be better. Sopana Pansodtee who taught me how to appreciate the little things in life. As well as my uncle and aunt, John and Sarrah Thomas who showed me great hospitality, especially during my very first months in the US.

Publications directly linked to the topic of this dissertation

Ion pump integration

Pansodtee, P., Selberg, J., Jia, M., Jafari, M., Dechiraju, H., Thomsen, T., Gomez, M., Rolandi, M. and Teodorescu, M. (2021). The multi-channel potentiostat: Development and evaluation of a scalable mini-potentiostat array for investigating electrochemical reaction mechanisms. PLoS ONE, 16(9): e0257167

Selberg, J., Jafari, M., Mathews, J., Jia, M., **Pansodtee, P.**, Dechiraju, H., Wu, C., Cordero, S., Flora, A., Yonas, N. and Jannetty, S., 2020. Machine Learning-Driven Bioelectronics for Closed-Loop Control of Cells. Advanced Intelligent Systems, 2(12), p.2000140.

Jafari, M., Marquez, G., Selberg, J., Jia, M., Dechiraju, H., **Pansodtee, P.**, Teodorescu, M., Rolandi, M. and Gomez, M., 2020. Feedback control of bioelectronic devices using machine learning. IEEE Control Systems Letters, 5(4), pp.1133-1138.

Jia, M., Dechiruji, H., Selberg, J., **Pansodtee, P**., Mathews, J., Wu, C., Levin, M., Teodorescu, M. and Rolandi, M., 2020. Bioelectronic control of chloride ions and concentration with Ag/AgCl contacts. APL Materials, 8(9), p.091106.

Bio sensing

Wu, C., Selberg, J., Nguyen, B., **Pansodtee, P.**, Jia, M., Dechiraju, H., Teodorescu, M. and Rolandi, M., 2020. A Microfluidic Ion Sensor Array. Small, 16(6), p.1906436.

Strakosas, X., Selberg, J., **Pansodtee, P**., Yonas, N., Manapongpun, P., Teodorescu, M. and Rolandi, M., 2019. A non-enzymatic glucose sensor enabled by bioelectronic pH control. Scientific reports, 9(1), pp.1-7.

Imaging system

Baudin, P.V., Ly, V.T., **Pansodtee, P**., Jung, E.A., Currie, R., Hoffman, R., Willsey, H.R., Pollen, A.A., Nowakowski, T.J., Haussler, D. and Mostajo-Radji, M.A., 2021. Low cost cloud based remote microscopy for biological sciences. Internet of Things, p.100454.

Ly, V.T., Baudin, P.V., **Pansodtee, P**., Jung, E.A., Voitiuk, K., Rosen, Y., Willsey, H.R., Mantalas, G.L., Seiler, S.T., Selberg, J.A. and Cordero, S.A., 2021. Development of a Low-Cost System for Simultaneous Longitudinal Biological Imaging. Communications Biology.

Additional publications

Lessard, S., **Pansodtee, P**., Robbins, A., Baltaxe-Admony, L.B., Trombadore, J.M., Teodorescu, M., Agogino, A. and Kurniawan, S., 2017, July. Crux: A compliant robotic upper-extremity exosuit for lightweight, portable, multi-joint muscular augmentation. In 2017 International Conference on Rehabilitation Robotics (ICORR) (pp. 1633-1638). IEEE.

Lessard, S., **Pansodtee, P.**, Robbins, A., Trombadore, J.M., Kurniawan, S. and Teodorescu, M., 2018. A soft exosuit for flexible upper-extremity rehabilitation. IEEE Transactions on Neural Systems and Rehabilitation Engineering, 26(8), pp.1604-1617.

Devlin, T., Dickerhoff, R., Durney, K., Forrest, A., **Pansodtee, P.**, Adabi, A. and Teodorescu, M., 2018. Elbowquad: Thrust vectoring quadcopter. In 2018 AIAA Information Systems-AIAA Infotech@ Aerospace (p. 0893).

Chapter 1

Introduction

1.1 Motivation

Cell culturing is a process where cells are grown in strictly controlled environments. The first cell culture originates from Yale University laboratory in 1907, where Ross Harrison maintained frog nerves in a salt solution for several days. Since then, cell cultures have become a new tool for scientists to study organism development. Nowadays, cell cultures are used for a variety of studies such as organ/tissue development, pathogenesis of viruses, genetic expression, and drug development to cure diseases.

However, the cell culturing technique is only one part of the equation; it provides a platform to grow tissue in a controlled environment. Later information such as images, electrical activity, and DNA sequence can be extracted from cell culture using various equipment. These pieces of equipment are not only expensive and inaccessible but also often not suitable for certain experiments. For instance, a longitudinal imaging study of a cell culture requires a bright-field microscope which can cost five thousand to ten thousand dollars and requires a human operator. This limits how often an image can be taken, which is usually a few times a day.

Another example is a study of a relationship between ionic concentration and cell culture. The traditional approach lacks spatial and temporal resolution (cell cultures are placed in an incubator and media is changed every several days). Recently, a bioelectronic device, the organic electrophoretic ion pump (OEIP), was invented, enabling a high spatial and temporal resolution modulation of ionic concentration. Nevertheless, operating an array of OEIP is still a challenging problem because it requires another piece of equipment called a potentiostat in order to operate. An array of OEIPs would require more than one potentiostat. A traditional potentiostat is a bulky and expensive bench-top equipment that makes running multiple potentiostats simultaneously become infeasible from economic and spatial standpoints.

In addition, the high spatial and temporal resolution characteristics of OEIP enables the possibility of real-time feedback control in cell cultures with an OEIP device. In feedback control, an ionic sensor that senses an ionic concentration in a solution is also needed. Similar to an OEIP, ionic sensors often require a potentiostat to operate and perform a measurement. An array of ionic sensors also requires multiple potentiostats; thus, a smaller and cheaper data acquisition system is necessary.

For the reasons mentioned above, better tools are needed to enable and accelerate new scientific discoveries in cell culture studies. The overarching goal of this dissertation is to design and develop better, more accessible (low-cost and open-source) tools/equipment for studying cell culture.

1.2 Applications

The author believes that the works in this dissertation can be applied in the following areas.

- Longitudinal study of cell culture - the proposed low-cost system minimizes human intervention and maximizes data points acquired from cell culture. Typically, imaging a cell culture requires a biologist to put a cell culture plate under a microscope. Due to how labor-intensive the task is, it is infeasible to perform more than a few times a day. The proposed system can perform imaging as many as 144 data points per day or every ten minutes.

- Measuring various ion concentrations in cell culture - the proposed low-cost data acquisition system can be connected to a bioelectronic ion sensor and used to measure various ion concentrations. This work enables cheaper and more portable ion sensor equipment.

- Studying relationship and performing feedback control between ion concentrations and cell culture responses - for example, the proposed low-cost, multi-channel potentiostat was used to control the organic electrophoretic ion pump developed by Rolandi group to stimulate cell cultures with different ions electronically and monitor results via fluorescence imaging. This leads to a more in-depth understanding of cell culture and ion concentration dynamics and demonstrates the very first application of bioelectronic closed-loop control in cell systems.

1.3 Contributions of this Work

This work takes a holistic approach to the design and analysis of open hardware and open source embedded systems for cell culture study, which results in various contributions to the field as listed below.

- Designed data acquisition systems tailored to bioelectronic sensors and devices.
- Proposed a new ultra-low current measurement technique for multi-channel potentiostat and developed a low-cost, modular, multi-channel potentiostat.
- Explored the use of feedback control in bioelectronic devices and cell cultures using the multi-channel potentiostat.
- Contributed to the development of electronic circuits for the low-cost, high-throughput cell culture imaging systems.

Chapter 2

Literature Review

The first step to developing better and more accessible tools for studying cell culture systems is understanding the scope and relevant information in regards to the biology, electrical engineering, and computer engineering fields. The purpose of this literature survey is to briefly highlight cell culturing techniques and different tools used to study cell cultures. In this review, the author explores current state-of-the-art cell culturing techniques, both two-dimensional and three-dimensional. Later, pieces of equipment used to study cell cultures are investigated (e.g., imaging system, biosensor, and ion pumps). Finally, the author examines equipment and techniques used to operate imaging systems, biosensors, and ion pumps.

2.1 Cell culturing

In the past, studying a living organism could only be done via experimenting with the living organism in its natural habitat. Recently, scientific communities have developed several procedures to study a living organism without requiring the original living organism. One of the techniques is cell culturing, a process where cells of a living organism grow in a strictly controlled environment, typically simulating how they grow in the living organism (i.e., temperature, humidity, and nutrients). Cell culturing allows scientists to study living organisms on a micro molecular level like never before.

The cell culturing techniques itself can be categorized into two different forms:

- Two-dimensional
- Three-dimensional

In the past century, two-dimensional cell culturing technique had been an essential part of many studies ranging from drug screening to developmental biology [Haycock, 2011] [Zhang et al., 1991]. However, all of the two-dimensional cultures do not represent structural, functional, and proper conditions for organization and cell signaling networks observed *in-vivo* [Wang et al., 1998]. As a result, the three-dimensional cell culturing technique has gained popularity in the last decade.

2.1.1 Two-dimensional Cell Culturing Techniques

[Ringer, 1883] developed the first cell culture media used for maintaining the beat of an animal heart outside the original body. It is compromised of a salt solution that contains chlorides of sodium, potassium, calcium, and magnesium. He observed the absence of heart contractions when calcium-free cell culture media are used. This experiment also gives insight into the role of calcium in the contraction of the heart.

The first artificial tissue culture was performed by [Harrison, 1910]. He took a different piece of tissue from the frog and put it inside the drop of a frog's clotted lymph. Just by chance, neuroblast tissues were observed to remain alive and continued growing. Later, he identified the outgrowth as a nerve fiber/cell.

Cell cultures have been extensively adopted to grow almost everything except human embryonic stem cells (hESCs) for the last century. This was only until [Bongso et al., 1994] proposed the technique to isolate proliferating hESC from human embryos. This derived hESC is a culture inside an incubator showing properties of proliferating *in-vitro* without differentiation.

Although two-dimensional cell culture had been widely adopted in every aspect of biology, from a study of micro-molecular to drug discovery, it still does not accurately represent tissue that grows *in-vivo*. Thus, a more sophisticated cell culturing technique is needed.

2.1.2 Three-dimensional Cell Culturing Techniques

The goal of the three-dimensional technique is to narrow down the gap between cellular monolayers (two-dimensional cell culture) and an original living organism. In the past decade, publications related to three-dimensional cell culturing techniques have grown exponentially, shown in Figure 2.1.

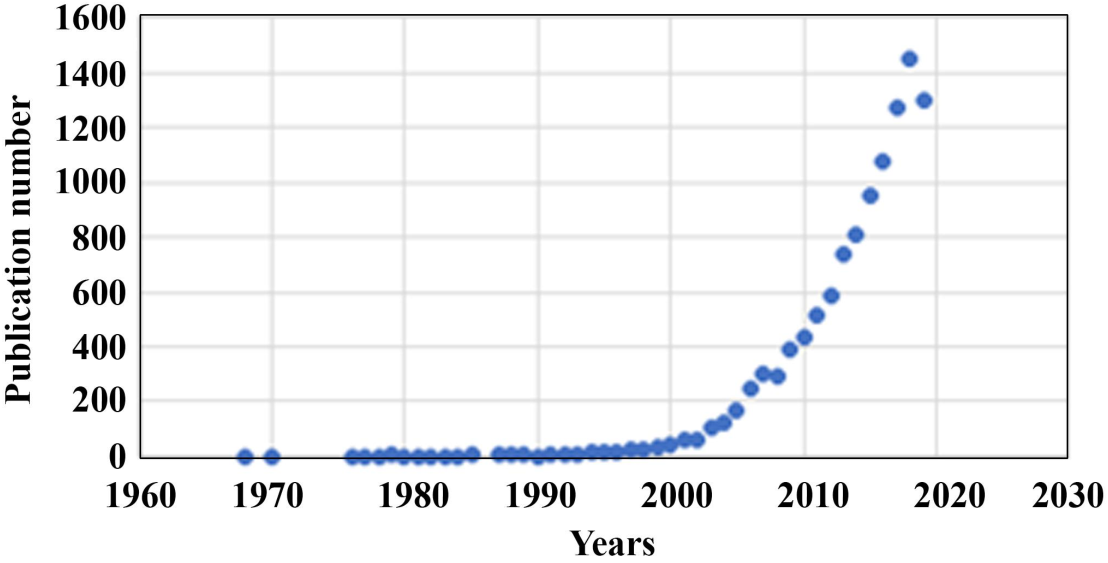

Figure 2.1: Three-dimensional cell culturing technique related publications [Jensen and Teng, 2020].

The three-dimensional techniques can be categorized into the following main categories.

- *Scaffold-based techniques*: hydrogel-based support, polymeric hard material-based support, hydrophilic glass fiber, and organoids
- *Scaffold-free techniques*: hanging drop microplates, magnetic levitation, and spheroid microplates

Scaffold-based techniques

Scaffold-based techniques utilize various gel-like materials (e.g., hydrogel) to mimic an extracellular matrix (ECM) and form a three-dimensional structure instead of monolayers. Hydrogel has a beneficial property where it highly resembles natural ECM while allowing soluble and growth factors to pass through [Langhans, 2018]. There are various hydrogels that are applicable for three-dimensional cell culturing (e.g., Natural hydrogel: fibrinogen, hyaluronic acid, collagen, Matrigel, gelatin, chitosan, and alginate, Synthetic hydrogel: polyethylene glycol (PEG), polylactic acid (PLA), or poly(vinyl acetate) (PVA)) [Dhandayuthapani et al., 2011]. Polymeric hard scaffolds are an alternative to hydrogel, since they provide an excellent ECM-like structure.

One of the groundbreaking use cases of the three-dimensional cell culturing technique was culturing a Cerebral Organoid. [Lancaster et al., 2013] developed a protocol for culturing Cerebral Organoids from human pluripotent stem cells (hPSCs) using Matrigel. The results prove that cultured Cerebral Organoids have a developmental and structural resemblance to an actual human brain. Later on, several research groups proposed multiple protocols to grow diverse kinds of three-dimensional cultures (e.g., [Eiraku et al., 2008] three-dimensional cerebral cortex tissue, [Sato et al., 2009] Gut Organoid cell culture in Matrigel from intestinal stem cells, [Spence et al., 2011] Gut organoid cell culture from hPSC, [Nakano et al., 2012] Retinal organoids from hPSC).

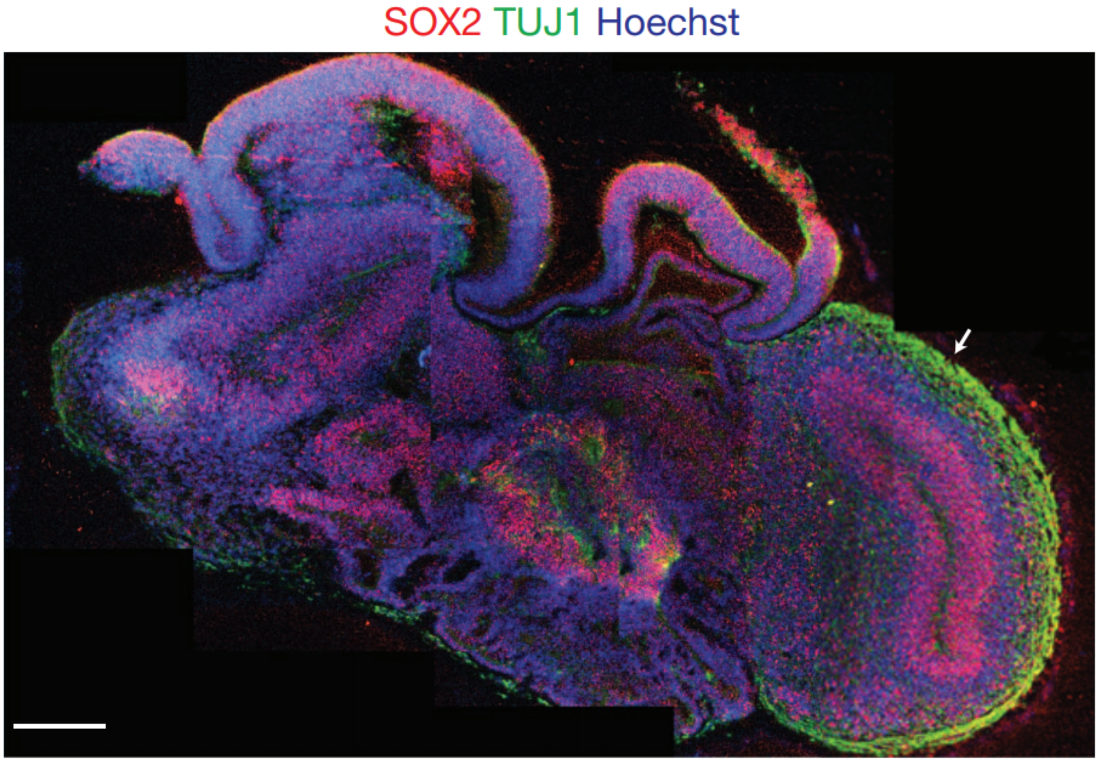

Figure 2.2: Immunohistochemistry of Organoids shows neuron markers, SOX2 in red and TUJI in green. as well as extensive cell death in the core area. [Lancaster et al., 2013]

Scaffold-free techniques

The scaffold-free techniques use the concept of suspending a droplet of cell culture via magnetic levitation or surface tension or a special coated cell-culture plate. Once a cell culture is suspended, it will self-aggregate due to the effect of gravity. [Haisler et al., 2013] proposed the technique to suspend a cell culture via magnetic levitation by injecting magnetic nanoparticles into the cell culture. Later, [Türker et al., 2018] also used a similar technique to study cell viability in the presence of paramagnetic gadolinium agents. [Boyer et al., 2018] used 3D printing to make a 3D printed insert for a 96-well plate which allows a cell culture droplet to be suspended. [Napolitano et al., 2007] designed a PDMS micromold, which was later used to cast agarose hydrogels, creating a 24-well cell culture plate.

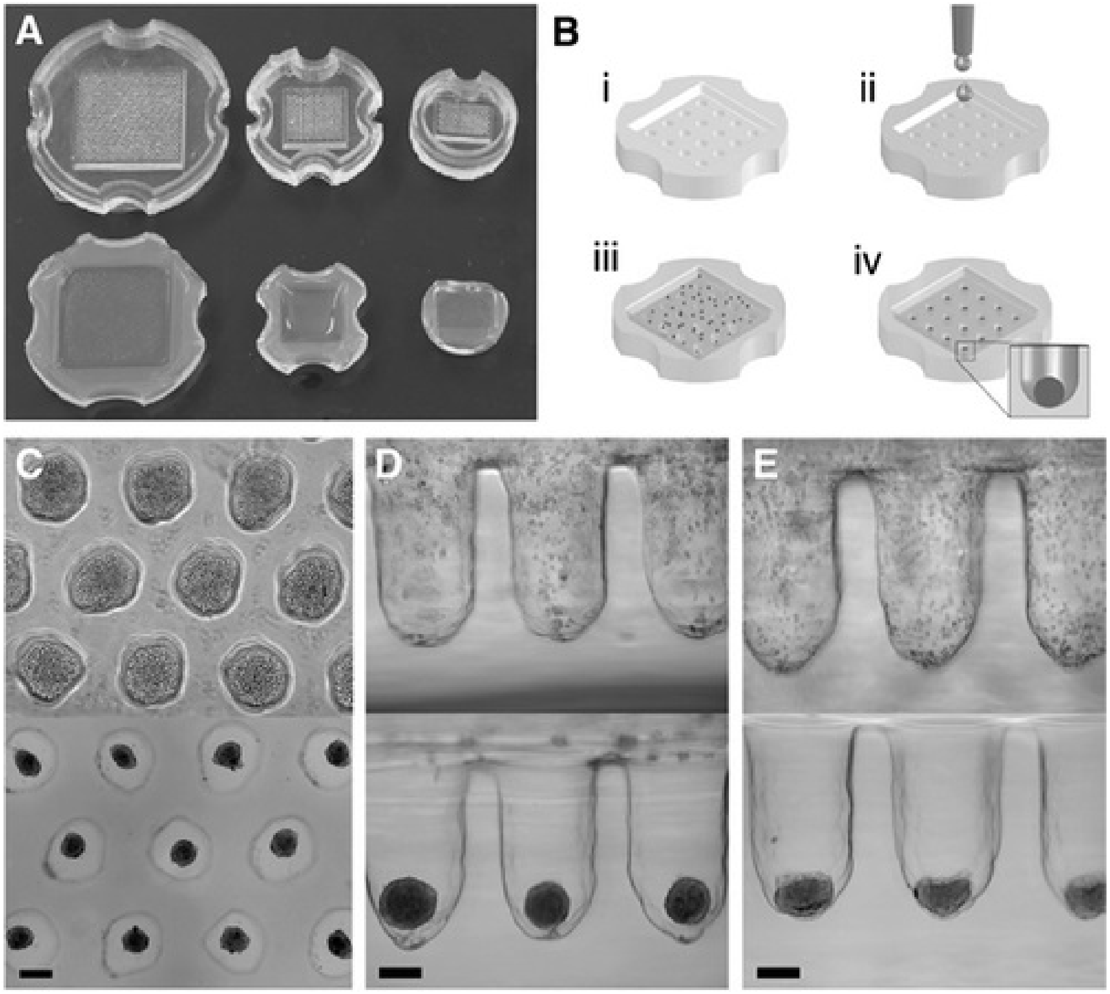

Figure 2.3: A) PDMS micromolds B)The self-assembly protocol C)Normal human fibroblasts (NHF) D) NHF and E) rate hepatoma cells in micromolded cell culture plate [Napolitano et al., 2007]

2.1.3 Ion Concentration Effect on Organism Growth

Cell membranes contain various types of ion channels (e.g., Na^+, K^+, H^+, Cl^- and Ca^{2+}) as small anatomical structures. These ion channels interact with an ionic concentration outside the cell membrane (e.g., cell culture media), and result in closed or opened ion channels. Ionic concentrations affect several aspects of an organism such as resting membrane potential (V_{mem}), neuron action potential, cardiac muscle contraction, and cell growth. This section will explore how ion concentrations affect the cell.

Na^+ and K^+ ion channels are primarily responsible for osmotic balance across the animal cell membrane and resting membrane potential [Alberts et al., 2002]. Thus, changing ionic concentration in a cell culture environment will change a cell's resting potential or polarization stage.

When amputating a planarian and applying a gradient of tissue polarization, [Durant et al., 2017] was able to force it to grow two heads instead of resulting in a head and tail. The tissue polarization is altered using an octanol solution (8-OH). He found that if both parts above the amputated plane are depolarized, the planarian will grow two heads. This discovery confirmed that cell fate and morphology could be altered by the way cells depolarize or hyperpolarize (change in resting potential). [Levin et al., 2017] represents the chart Fig 2.4 where different tissue types have slightly different resting membrane potential. Thus, it implies that cell fate could be manipulated by altering a membrane potential. At the same time, a membrane potential can be changed by environmental ion concentrations.

It remains unclear on how to quantify the ion concentrations needed to change cell fate. However, [Lodish H, 2000] summarizes differences in concentration of different ions in Mammalian cell and Squid Axon (Table 2.1).

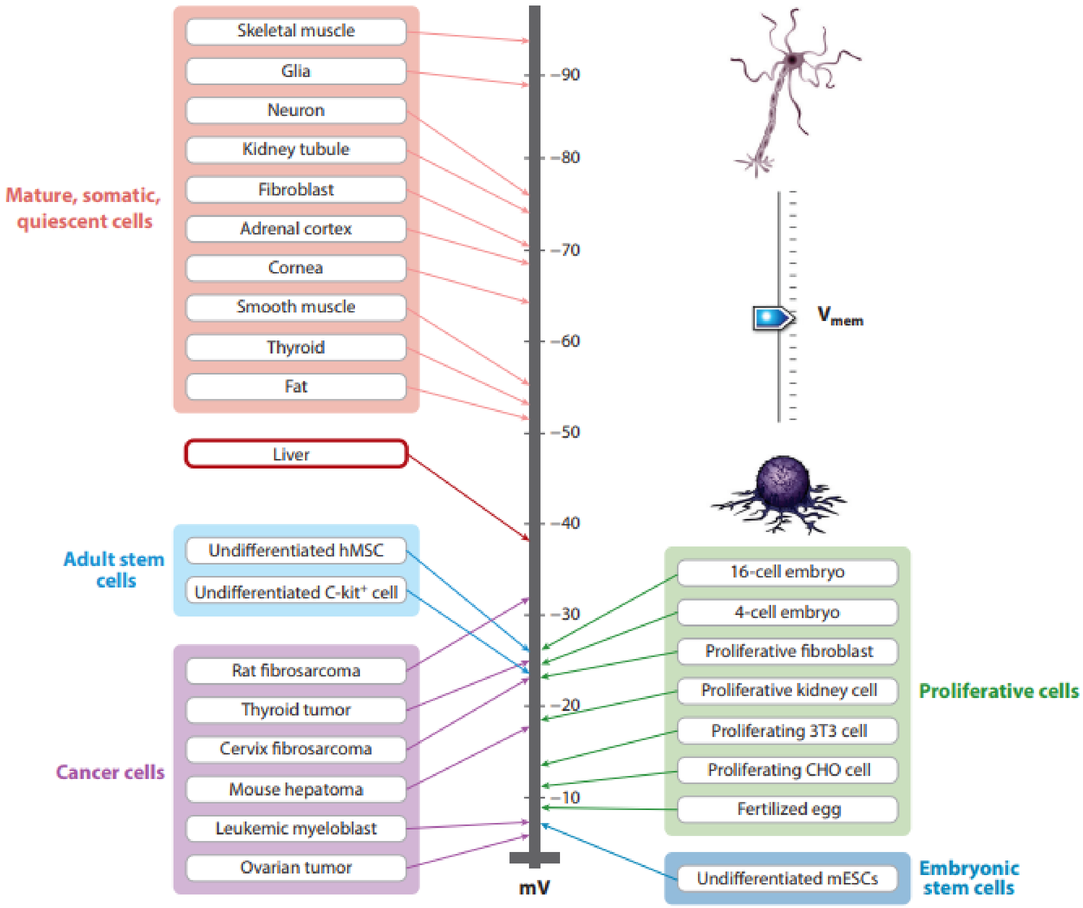

Figure 2.4: Resting potential of different cell types [Levin et al., 2017]

	Ion	Cell (mM)	Blood (mM)
Squid Axon	K^+	400	20
	Na^+	50	440
	Cl^-	40 - 150	560
	Ca^{2+}	0.0003	10
Mammalian Cell	K^+	139	4
	Na^+	12	145
	Cl^-	4	116
	HCO^{3-}	12	29
	Mg^{2+}	0.8	1.5

Table 2.1: Ions concentration of different ions in Mammalian cell and Squid Axon [Lodish H, 2000]

2.2 Cell Culture Imaging

One way of studying cell cultures is through imaging. Capturing images of a cell culture can give insight into the its physical states, especially the cell culture's morphology (i.e., shape and appearance). Currently, the process of taking an image of cell cultures is complicated and slow. It consists of biologists or lab technicians transporting cell cultures from an incubator and placing them under a microscope. The imaging usually takes place every couple of days due to labor limitations, and also to minimize the impact of transportation. Every time a cell culture is imaged, it is taken out of its ideal conditions, which is inside an incubator. Moreover, the process of transportation introduces unavoidable uncertainty to the cell culture. This section will cover various types of imaging techniques and explore the possibility of an in-incubator imaging solution.

2.2.1 Benchtop Imaging

[Kalderon, 1983] suggests that the first compound microscope that was comprised of two lenses in a sliding tube was invented in 1590. A decade later, the famous Galilei et al. invented the very same device called the tubum opticum, or today known as the telescope [Kriss and Kriss, 1998]. [Kalderon, 1983] constructed a microscope with coarse and fine adjustment using a ball and socket joint. With the same microscope, he discovered the cell. [Marvin, 1961] patented this concept of confocal imaging. This patent consists of two main principles; use of point illumination, and pinhole to block unfocused background signal from hitting the optical sensor.

[Prasher et al., 1992, Renz, 2013] developed a procedure to clone Green Fluorescent Protein (GFP) for the first time, and this marked the realization of fluorescence microscopy. A confocal microscope can be turned into fluorescence

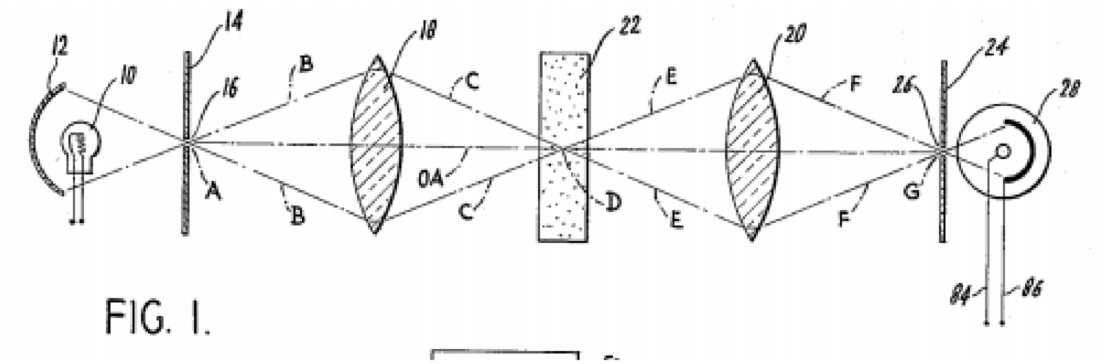

FIG. 1.

Figure 2.5: Principle of Confocal microscope in Minsky's patent [Marvin, 1961]

microscopy by use of point illumination with excitation wavelength, and instead of a pinhole, a dichroic mirror that only allows emission wavelength to pass.

[Williams and Carter, 1996] proposed the idea of a Transmission Electron Microscope which uses electrons to image the specimen all at once. Transmission electron microscope provides a tremendous improvement in resolution due to electrons having a shorter wavelength than visible light. However, specimens rely on a thin layer around 100 nm thick in order for electrons to pass through.

[McMullan, 1995] proposed the first scanning electron microscope (SEM). Unlike a Transmission electron microscope that uses electron beams to illuminate through a specimen, this form of microscope uses a beam of an electron that reflects to the detector to scan one area at a time and form an image. SEM can be used to image a living cell but additional treatment is required.

[Zernike, 1942] invented the Phase Contrast Microscope which uses the technique of constructing images based on a phase shift of light that passes through a specimen. This technique can be used to reveal the invisible part of an organism and image living cells.

[Freund et al., 1988] [Wu and Ozcan, 2018] proposed the concept of Digital holographic microscopy or lens-less microscope (2.6). Instead of recording the direct projected image of an object, it records light wavelength information that reconstructs a digital image using an algorithm.

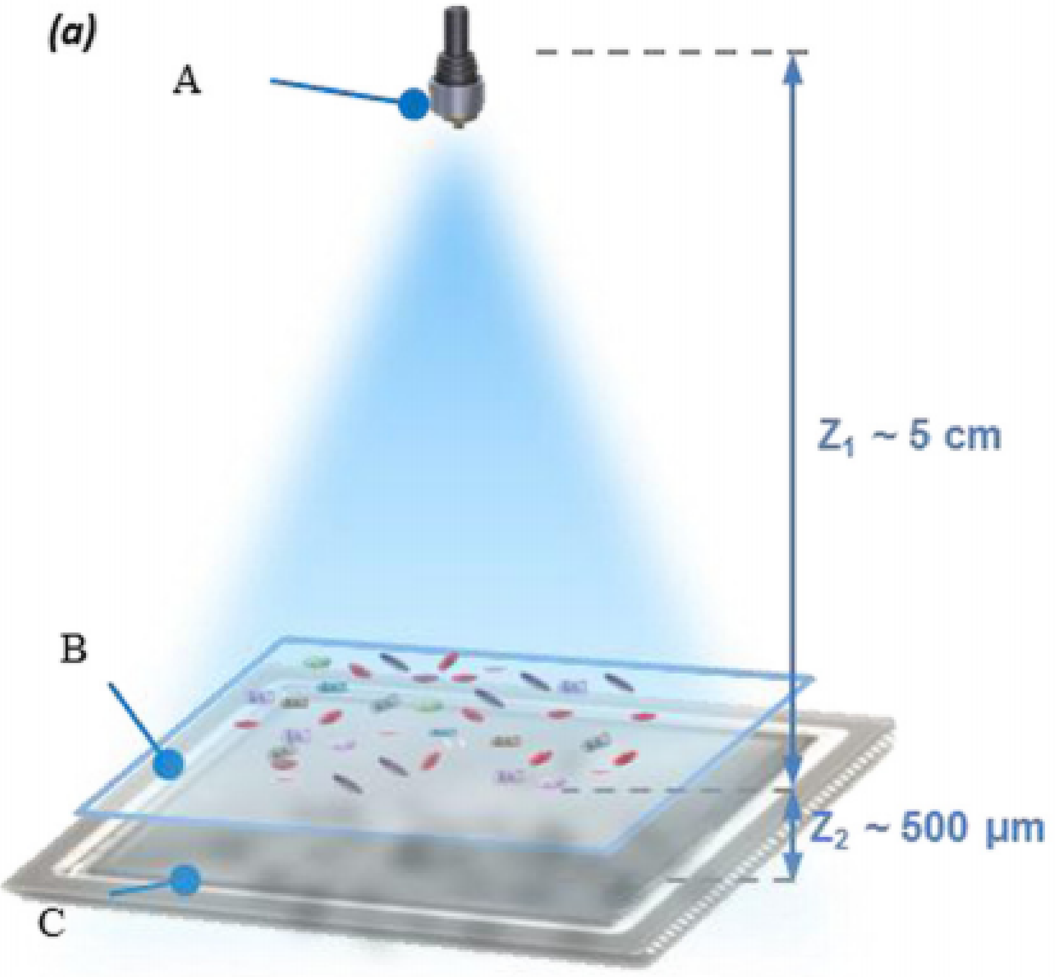

Figure 2.6: Schematic of lens-less microscopy a) coherent light source b) sample to be imaged c) image sensor [Freund et al., 1988]

2.2.2 In-incubator Imaging

In-incubator imaging is another engineering challenge. This is mostly due to extreme conditions inside of an incubator:

- Temperature: 37 C (98 F)
- CO2: 5%

- Humidity: 95%

As a result, there are a limited number of in-incubator imaging systems available.

[Kim et al., 2012] proposed a mini-microscope for conventional cell culture containers (e.g., petri dishes and multi-well plates). The system consists of a CMOS imaging module, a white LED illumination source, and a small plastic lens.

[Kesavan et al., 2014] designed an in-incubator, high-throughput, lens-less microscope using a digital holographic microscopy principle. The proposed microscope proves to be bio-compatible and able to continue monitoring cell cultures inside a standard incubator.

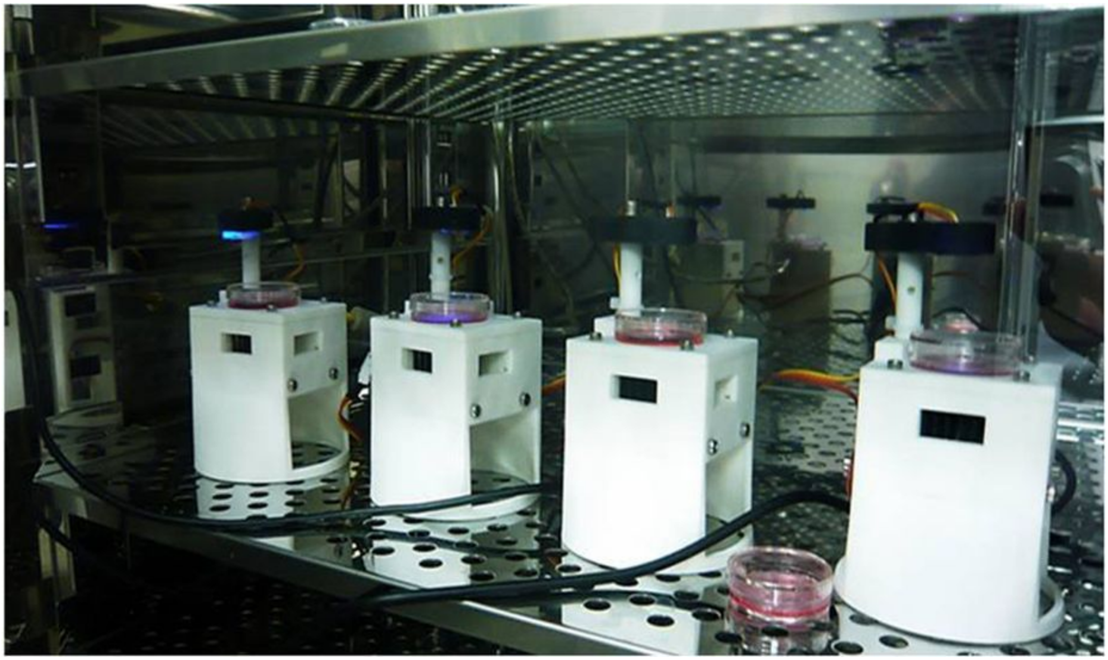

Figure 2.7: High-throughput lens-less microscope inside standard incubator [Kesavan et al., 2014]

[Zhang et al., 2015] presented a low-cost, fluorescent in-incubator microscope built from a component from an off-the-shelf webcam. However, this system is designed for proprietary bioreactors and is not compatible with conventional cell culture containers.

The designs proposed by [Kim et al., 2012], [Kesavan et al., 2014] , and [Zhang et al., 2015] suffer from lack of height adjustable mechanics and thus, are unable to adjust the focal plane. To overcome the focal plane issue, [Wang et al., 2017] suggested an in-incubator, wireless imaging system that also includes an adjustable Z-stage. The design allows adjusting a focal plane by manually adjusting Z-stage height.

[Diederich et al., 2020] proposed a modular microscopy toolbox that can customized according to application needs. Later, it demonstrated the ability to monitor monocyte to macrophage cell differentiation for seven days (i.e., 2 um resolution).

[Merces et al., 2021] proposed a high-throughput in-incubator microscope that features moving X, Y, and Z stages. Not only does this design mitigate the focal plane problem, but it also enables multi-well monitoring without human intervention.

[Aidukas et al., 2019] developed a miniature wide-field computational microscope based on off-the-shelve hardware 2.8. This drastically reduces the cost of a sub-micron resolution microscope.

According to in-incubator designs mentioned above, there is still a lack of a truly high-throughput, in-incubator imaging system with an adjustable focal plane.

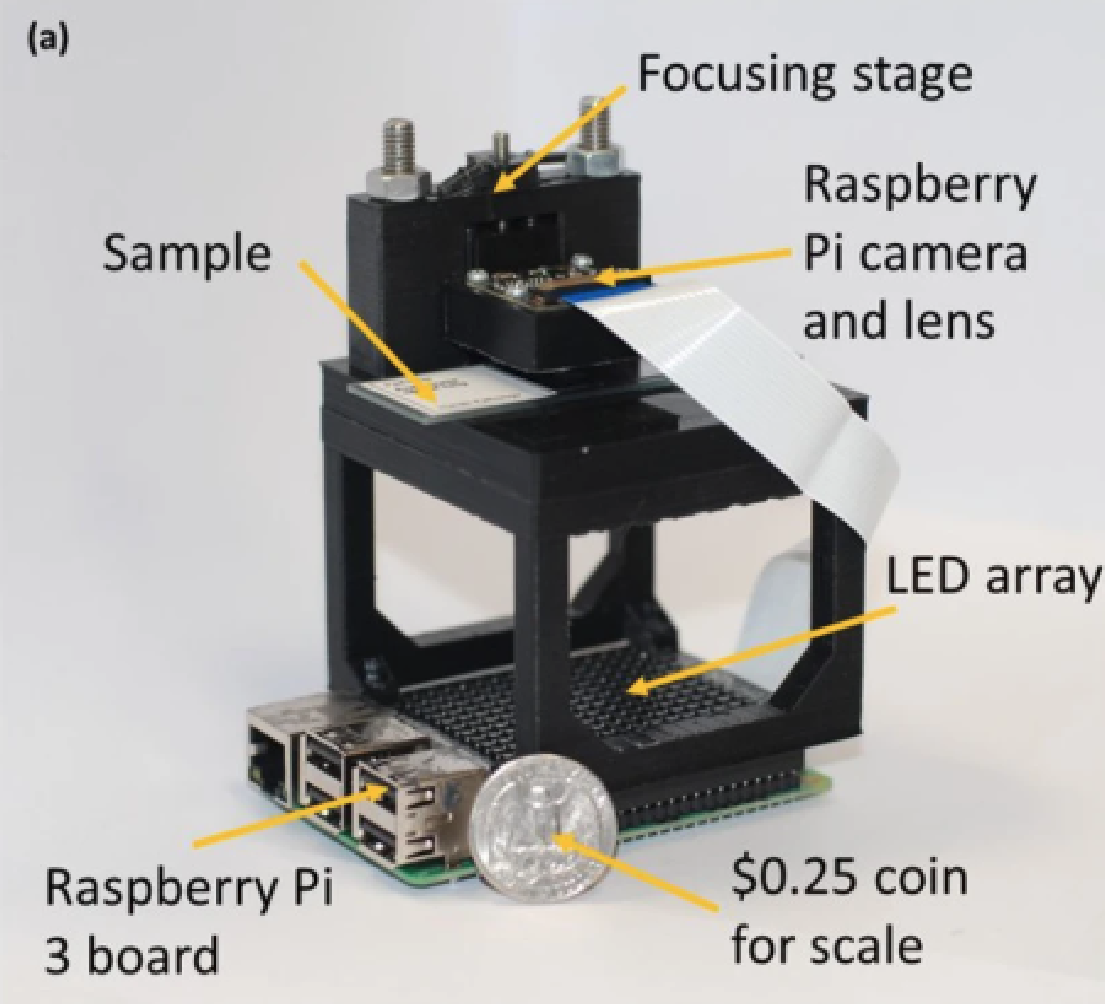

Figure 2.8: Open-source, low-cost sub-micron microscope [Aidukas et al., 2019]

2.3 Biosensing

Biosensing is a fast-emerging field with over ten thousand publications in the past ten years [Turner, 2013]. However, the definition of the biosensor is still fluid and constantly changing. In this work, the author uses the following definition: ”Biosensors are analytical devices incorporating a biological sensing element” [Turner, 2013]. Some examples of biosensors are glucose and ion sensors which are described below.

2.3.1 Glucose Sensing

[Clark Jr and Lyons, 1962] proposed the first glucose sensor, which incorporates immobilized enzymes with his invention, an oxygen detector. Several decades later, the majority of glucose sensors still use the idea of using immobilised enzymes combined with electrochemical reaction (e.g., [Gao et al., 2016], [Yao et al., 2012], [Kim et al., 2018b]). One advantage of modern glucose sensors such as Continuous Glucose Monitoring (CGM) is that they utilize less invasive sources of glucose samples such as tears and sweat. However, the majority of CGMs still rely on enzyme reactions which limits the life-span of the sensors [Van Enter and Von Hauff, 2018], [Block et al., 2008].

A non-enzymatic glucose sensor has proven to be possible and offer a longer life-span [Toghill and Compton, 2010], [Lang et al., 2013]. On the other hand, non-enzymatic glucose sensors tend to require the pH of a measured solution to be above 11 pH, which is not in the range of typical human sweat and tears (pH 4-7) [Corrie et al., 2015].

2.3.2 Ion Sensing

Ionic concentration is an essential biomarker for sensing due to the ubiquitous role of ions in cellular and organism-wide signaling, metabolism, and regulation. Electrochemical ion sensors that can measure ion concentration have taken many forms with high sensitivity, and selectivity [Moreno et al., 2006] [Chapp et al., 2018]. These sensors typically record the electrode potential caused by the accumulation of the charged ion of interest that is filtered by an ion-selective membrane (ISM) [Bakker et al., 1997], [Parrilla et al., 2019].

[Weltin et al., 2014] developed a thin-film iridium oxide electrode H^+ sensor that is embedded within a multi-sensor (e.g., Oxygen) cell culture monitoring platform. This cell culture monitoring platform enables multiparametric microphysiometry monitoring for human cancer cells.

[Wu et al., 2020] proposed ion-selective micro-electrode array that is able to simultaneously monitor H^+, K^+, Na^+, and Cl^-. The work also highlights ionic concentration differences of fresh cell cultures media and consumed ones.

2.4 Ion delivery

The system capable of injecting/removing various kind of ions is crucial for studying how ion concentrations affect cell culture growth. It has been shown that the most successful methods of delivering ions are listed below.

1. Microfluidic
2. Electrochemical
3. Electrophoretic

This proceeding section describes the benefits and drawbacks of each method chosen for this project.

2.4.1 Microfluidic Ion Delivery

Micro-fluidics have been the most established technique of delivering molecules and ions for several decades [Convery and Gadegaard, 2019]. Using micro-fluidics to deliver ions is achieved by pumping a solution that contains free-floating ions of interest to the target.

[Blake et al., 2007] developed three-layer micro-fluidics to control micro environments for brain slices based on polydimethylsiloxane (PDMS) substrate. The device has a flexible holder for brain slices with two distinct solutions to flow through and two suction electrodes for recording spontaneous respiratory motor signal. This tool demonstrates the ability to flow two different solutions by flowing Na^+-free solution on one side of a mouse brain slice. The result has shown that half the brain where the Na^+-free solution flowed through did not exhibit rhythmic respiratory motor bursts shown in figure 2.9.

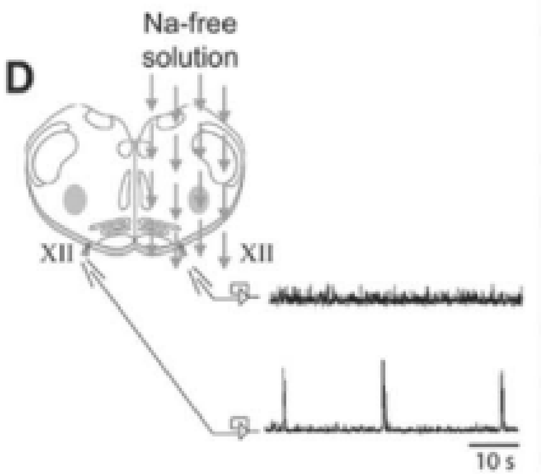

Figure 2.9: Right part of the brain slice shows lack of rhythmic respiratory motor bursts due to lack of Na^+ in solution [Blake et al., 2007]

[Nguyen et al., 2013] reviewed the design, fabrication, and characterization of drug delivery systems based on a Lab-on-a-chip technology and found that various system behave differently based on differing scales due to the fundamentals of scaling (i.e., for mass transfer and basic fabrication techniques).The paper concludes that drug delivery on Lab-on-chip/microfluidics is suitable on a cellular level where the concentration gradient generator is the main application.

Despite having high control over delivery volume, microfluidics have a problem of changing solution volume. Microfluidics, when operating, changes its volume of target solution, and thus is not suitable for delivering ions for *in-vitro* or *in-vivo* applications.

2.4.2 Electrochemical Ion Delivering

Certain ions or molecules can be injected or removed using chemical reactions. [Deng et al., 2016] developed an H^+ bio-transducer device which is able to monitor and control its H^+ ion concentration. The bio-transducer design is based on the reaction of an $PdHx$ electrode that applies an electric field, resulting in an absorption or release of H^+ causing a change in pH. Later, [Deng et al., 2016] combines H^+ bio-transducers with bi-stable pH modulation form an "enzymatic flip-flop" circuit based on glucose dehydrogenase and alcohol dehydrogenase reaction. The device was deployed on firefly luciferase bioluminescence, which changes intensity based on H^+ (pH) concentration. [Strakosas et al., 2019a] developed a non-enzymatic glucose sensor that uses the same reaction of $PdHx$ to change sweat and tear pH levels before glucose measurement.

[Zhang et al., 2018] expanded the idea of [Deng et al., 2016], and proposed an H^+ biotransducer based on electrochemical reactions on a conductive polymer, sulfonated polyaniline instead of $PdHx$ reaction. The H^+ bio-transducer is calibrated with the pH indicator solution, bromothymol blue dye. As a result, the pH indicator shows an effective pH range of $6.5 - 7.5$. The use of an H^+ bio-transducer modulated the rate of mitochondrial ATP synthesis on neuron cells which is represented by figure 2.10.

The electrochemical process can remove/inject a large number of ions, however, the type of ion which can be manipulated is limited to the type of electrode (e.g., Palladium/Polyaniline electrodes can only bind to H^+). Moreover, the amount of ions is limited to the capacity of the electrode.

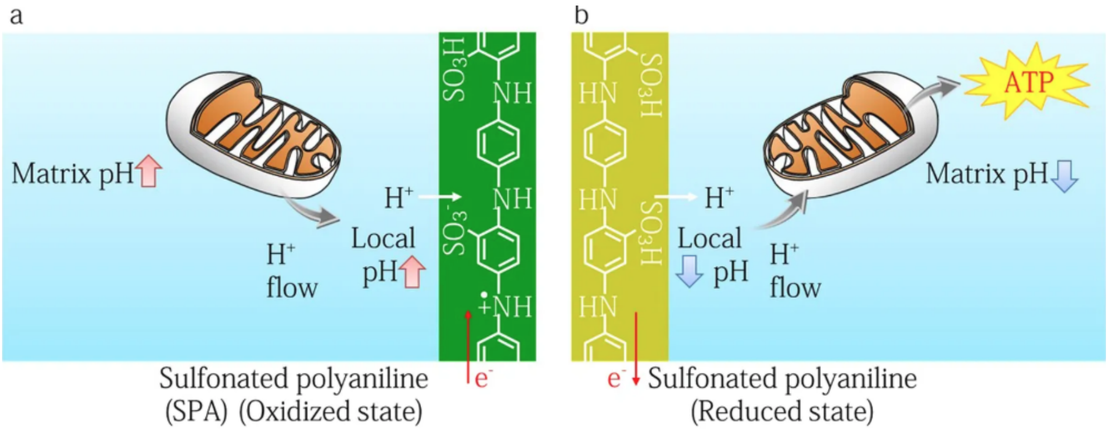

Figure 2.10: [Zhang et al., 2018] bio-transducer modulates mitochondrial ATP synthesis on neuron cells a) Increase of pH b) Decrease of pH

2.4.3 Electrophoretic Ion Delivery

[Carle et al., 1986] developed a method to separate DNA molecules through electrophoretic principles. By periodically changing electric field potentials between 0.01 to 10 Hz, [Carle et al., 1986] successfully separates DNA molecules with sizes ranging from 15 to 700 Kilo-base pairs. Electrophoretics was strictly used for DNA, RNA, and protein analysis applications until [Isaksson et al., 2007] came up with the novel idea that used electrophoretic principle to create an ion pump that delivers Ca^{2+} ions. The ion pump's Ion-selective membrane (IEM) is made of poly(3,4-ethylene dioxythiophene) doped with poly(styrene sulphonate) (PEDOT:PSS). Its design moves the Ca^{2+} ion to a single-cell target with 50 um wide channel. The device operates by applying voltages between 0-10V which pushes ions from the reservoir to the target or the other way around. [Simon et al., 2009] extended the model of [Isaksson et al., 2007] and published another version of the ion pump that operates between 0-10V. It was designed for moving neurotransmitter molecules such as Glutamate (Glu), Aspartate (Asp) and Gamma-Aminobutyric Acid (GABA) instead of Ca^{2+} to the Cochlea.

[Williamson et al., 2015] developed a subsequent ion pump that delivers GABA to control an epileptiform activity. The ion pumps made from PEDOT:PSS and PSSA-co-MA as cation exchange membrane (CEM), operating between 0-20V.[Williamson et al., 2015] tests ion pumps in the hippocampus area of a mouse's brain slice. The result has shown success in suppressing epileptiform activity after ion pumps turns on.

[Jonsson et al., 2016] introduced another GABA ion pump based on the [Williamson et al., 2015] design, but embedded with sensing electrodes in a single unit called a "bio-electronic neural pixel". The goal is to perform GABA delivery and sensing at the same location. This ion pump was also tested on a hippocampus area on a mouse's brain slice. The result has shown success in suppressing epileptiform activity after the ion pumps turns on. The ion pumps operate between 0-10V, shown in figure 2.11

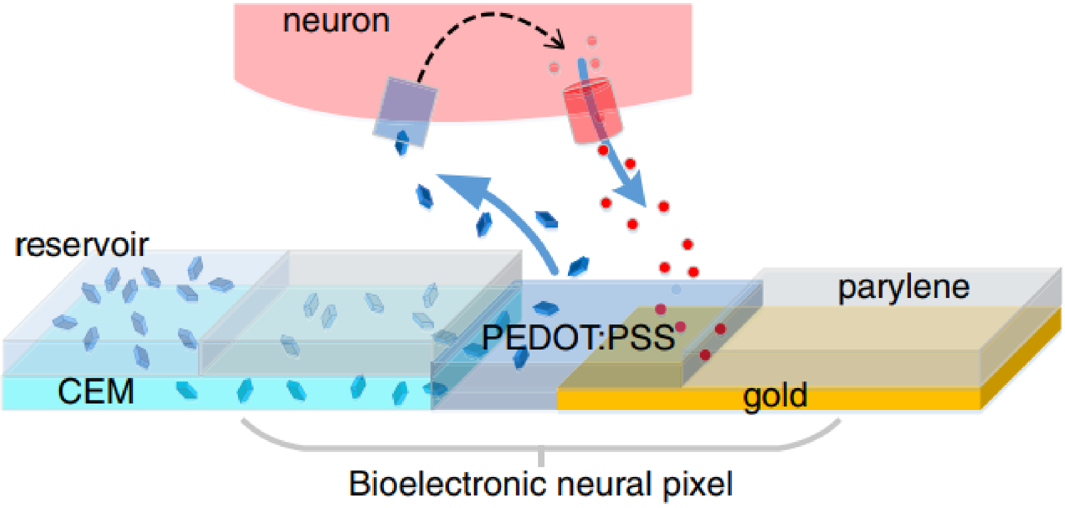

Figure 2.11: Architecture of bio-electronic neural pixel (GABA ion pumps) [Jonsson et al., 2016]

[Cherian et al., 2019] proposed a novel way to fabricate ion pumps with screen printing. The ion pump is capable of delivering Na^+, K^+, Cl^-, H^+ and biologically-relevant molecules such as Ach^+ and SA^-. This pump had to operate in a lower voltage range compared to other ion pumps, between 0-1.4 V.

[Poxson et al., 2019] [Poxson et al., 2017] demonstrate that delivering big ion molecules is difficult with ion pumps. The ion pump is based on a new class of PE: hyperbranched polyglycerols (dPGs) forming dendrolytes (DLs). The result demonstrates the ability to move K^+, Na^+, Li^+ and $acetylcholine^+$ ions.

All ion pumps mentioned above are operated in the range of 0 - 20V, with a single ion pump per device and relying on controllers/test equipment that are either the Keithley 2602 [1] or the Keithley 2400 Source Meter.

[Selberg et al.,] developed a device that is comprised of an array of 5x4 ion pumps. The design combines two micro-fluidic channels for refilling the reservoir and cell culture media. PVA:PSS is used as an ion bridge and SU-8 is used to form micro-fluidic channels.

[Arbring Sjöström et al., 2018] suggests the following advantages of ion pumps:

- Operate without affecting the volume of the target solution
- Good spatial resolution
- Easy to monitor and good control over the delivery quantity

It is worth noting that an ion pump has a few disadvantages where the molecules are required to be positively or negatively charged, and it is very challenging to manipulate larger molecules. Despite having a few drawbacks, an ion pump is still the best candidate for delivering ions to a cell culture.

2.5 Electroanalysis

In the last few decades, the use of miniaturized electrochemical devices has grown rapidly and found diverse applications in scientific and consumer prod-

---

[1] https://www.tek.com/source-measure-units/2602a

ucts (e.g., batteries [Nitta et al., 2015], Glucose sensors [Strakosas et al., 2019a] [Zhao et al., 2020], and Breathalyzers [Bihar et al., 2016]). Unfortunately, the process of developing specialized electrochemical devices is often time-consuming and expensive [Abdulbari and Basheer, 2017].

Electroanalysis is a collection of techniques used to study and operate electrochemical devices, which is one of the most essential steps of electrochemical device development [Bard et al., 2001]. To perform electroanalysis, it often involves the following measurement equipment:

- Galvanometer: maintain a constant current flow
- Potentiostat: maintain a constant voltage
- Electrochemical Impedance Spectroscopy (EIM): apply low amplitude sinusoidal signal over a range of frequencies.

In this work, the author will focus on potentiostat due to its versatility and practicality.

2.5.1 Potentiostat

A potentiostat is an instrument that controls the voltage between two or more electrodes. It is an essential piece of measurement equipment used to investigate electrochemical reaction mechanisms using electroanalytical methods [Gopinath and Russell, 2005]. The main role of the potentiostat is to control the electrochemical reaction using either two electrodes (a working electrode and a counter electrode) or three electrodes (a working electrode, a counter electrode, and a reference electrode). The accuracy and precision of the applied or measured voltages and currents depends on the quality of the electronic hardware, which for commercially available potentiostats, often correlate with the price and portability of each unit. Consequently, one of the challenges faced by the research community is how to test and operate electrochemical devices with less expensive and more portable equipment without compromising the quality of the experiment [Adams et al., 2019]. Due to the high cost and limited access to quality components, access to quality potentiostats is usually limited, especially in developing countries [Rowe et al., 2011]. As a result, a potentiostat is a significant bottleneck in the process of developing and testing electrochemical devices [Cruz et al., 2014].

Portability is a major obstacle in testing small, wearable devices. For instance, large and expensive bench-top potentiostats are not feasible options for operating wearable glucose sensors. Not only is portability a big issue but also the cost of a potentiostat. Commercial potentiostat costs range from a few thousand to tens of thousands of dollars [BV, 2020, Metrohm Autolab, 2020, NuVant Systems, 2020].

As electrochemical devices become more sophisticated and diverse, the number of electrodes and their operating range increases. For instance, the emerging trend of sensor arrays such as [Gao et al., 2016], [Zhao et al., 2020], and [Xu et al., 2019] sweat sensor arrays have more than five electrodes. [Selberg et al.,] and [Jia et al., 2020a] proposed bioelectronic actuators that have as many as 24 electrodes and require an actuation range of 0-3 V. Since these novel electrochemical devices have many more electrodes, traditional three-electrode potentiostats are no longer a practical option.

From the problems mentioned above, scientific communities have been proposing many potentiostat designs to address the problems.

2.5.2 Traditional Potentiostat

A traditional potentiostat is a potentiostat that consists of three electrodes (i.e., Working-electrode, counter-electrode, and reference-electrode). All the designs mentioned below are traditional potentiostats that do not support more than a three electrode setup.

[Turner et al., 1987], [Kakerow et al., 1995], [Stanacevic et al., 2007], [Ayers et al., 2007], and [Martin et al., 2009] proposed low-level VLSI (CMOS single Chip design) single-channel potentiostats. Although they are more affordable and smaller, they are difficult to replicate. Therefore, there are other approaches that utilize commercial off-the-shelf components. For instance, [Meloni, 2016], [Li et al., 2018], proposed open-source single-channel potentiostats, [Jenkins et al., 2019] and [Ainla et al., 2018] proposed open-source wireless systems, and [Glasscott et al., 2019] designed a Labview-controlled device for low-current applications. [Rowe et al., 2011] proposed a high-level circuit board design of a portable and less expensive potentiostat (less than $200) that supports various electroanalysis methods (e.g., cyclic, square wave, linear sweep, and stripping voltammetry) over the voltage range of -0.99 to +0.99V. [Friedman et al., 2012], [Dryden and Wheeler, 2015], [Cruz et al., 2014], [Hoilett et al., 2020], and [Adams et al., 2019] proposed similar devices with smaller form-factor. [Dobbelaere et al., 2017] potentiostat design can reach up to 8V where most of the affordable solutions output a range less than 1 V.

2.5.3 Multi-channel Potentiostat

A multi-channel is a novel concept that has emerged in the last decade. Therefore, there are a limited number of multi-channel potentiostat designs. As a result, most multi-channel equipment is still primarily commercial multi-channel potentiostat such as [NuVant Systems, 2020], [Metrohm Autolab, 2020], [Ametek, 2021], and [Gamry Instruments, 2021].

The multi-channel potentiostat concept has two primary purposes: operating multiple devices simultaneously (multi-device potentiostat) and operating more sophisticated devices (i.e., devices with more than three electrodes) (multi-electrode potentiostat) shown in Figure 2.12.

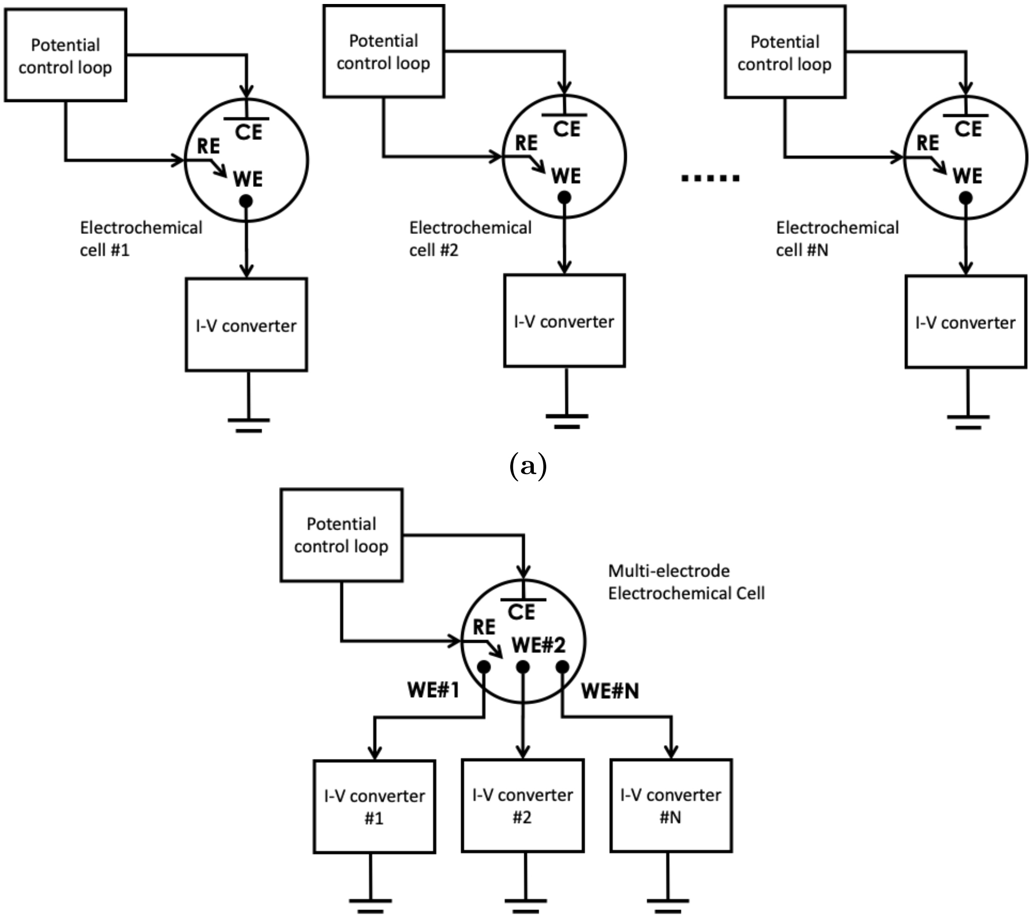

(a)

(b)

Figure 2.12: a) Multi-device potentiostat b)Multi-electrode potentiostat

Multi-device Potentiostat

The multi-device approach utilizes multiple copies of three-electrode potentiostat circuitry. One of the earliest ideas of the multi-device potentiostat is proposed by [Li et al., 2004]. The potentiostat consists of 6042 E DAQ card and discrete components, supporting up to 4 devices simultaneously that can be controlled and displays results via LabView. Similar to [Li et al., 2004] design, [Tapsak et al., 2007] proposed a 16 device potentiostat which features PCI-6024E DAQ card and discrete components. [Abdullah et al., 2020] takes a different approach where they build a six device potentiostat from all discrete components, including DAC and ADC but still interface and display results through LabView interface.

Multi-electrode/Shared Electrode Potentiostat

Instead of having multiple three-electrode potentiostat hardware, the multi-working-electrode exploits the concept of sharing counter-electrode and/or reference-electrode. Thus, this approach employed one DAC/potentiostat circuit and multiple current measurement circuits through multiplexing and multiple dedicated current measurement units.

[Cumyn et al., 2003] proposed a multi-working-electrode that is built from interconnected independent pieces of off-the-shelf lab equipment (i.e., Keithley 213 voltage source, Keithley 2750 multimeter, and Keithley 7708 multiplexer). [Hu et al., 2016] design deploys both five copies of dedicated current measurement hardware and multiplexing technique. As a result, the potentiostat is capable of operating up to 80 channels simultaneously.

[Molderez et al., 2020] presents a 128 channels potentiostat that employs capacitor-based channel circuitry, multiple copies of current measurement units, and multiplexing technique results in much lower cost per channel.

Table A.1 shows a comparison between the proposed system, research-grade potentiostats, and commercial-grade potentiostats.

2.6 Closed-Loop Control

A closed-loop control system or feedback control system is a control system that has feedback loops in addition to a typical open-loop system as a forward path. The feedback loop is a way for a system to achieve and maintain desired output automatically.

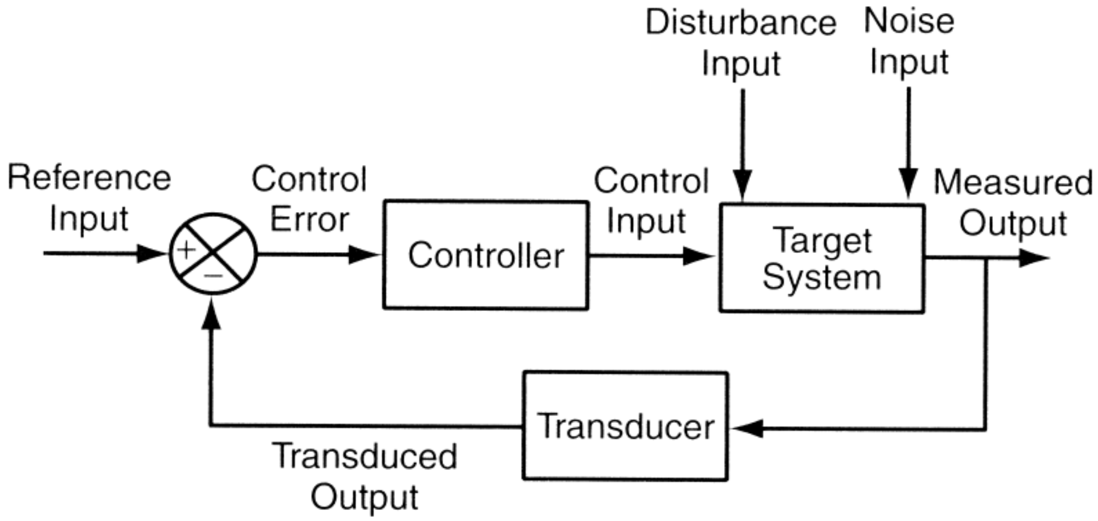

Figure 2.13: Block diagram of a feedback control system. The desired value of the system's output is set as reference input. The system maintains the desired value by changing its control input according to differences between the reference input and measured output. [Hellerstein et al., 2004]

One of the most common feedback control algorithms is the PID controller proposed by [Bennett, 1993]. The reason why the PID controller is so popular is mainly due to its efficiency and simplicity [Pessen, 1994]. However, in a more complex feedback control system (e.g., cell culture closed-loop control), the PID controller no longer provides a good result, and other control algorithms are needed [Cheon et al., 2015].

Chapter 3

Sensing

3.1 Introduction

This chapter explores the possibility of cell culture monitoring applications using biosensors and low-cost, high-throughput imaging devices. First, I described work on a non-enzymatic glucose sensor [Strakosas et al., 2019a] where I designed and prototype the portable wireless-enable data acquisition system.

Second, I detailed the data acquisition system for microfluidic ion sensor array [Wu et al., 2020]. The microfluidic ion sensor array can be uses to monitoring K^+, Na^+, and Cl^- simultaneously. Typically a biosensor can be operated using a bench-top potentiostat. However, these biosensors have unique electrodes configurations which are not practical to operate with a off-the-shelf potentiostat. Therefore, custom data acquisition systems are designed for the biosensors. The data acquisition systems not only cheaper than bench-top potentiostat but also more portable which can be uses to turn a biosensor into a wearable device.

Finally, this section overviews the design and prototyping of the electronic circuit boards for the low-cost, high-throughput imaging system. The low-cost imaging system is designed with the idea of open-source and easy to replicate in mind (i.e., all the components can be purchase off-the-shelve or easy to reproduce). The works including several printed circuit board designs and architecture the interlock system that allows 24 Raspberry Pi Zero W and OVA564, image sensors to tightly pack in 24-well plate form-factor.

3.2 Biosensor

3.2.1 Non-enzymatic Glucose Sensor

Author contribution: This project collaborates with Xenofon Strakosas, John Selberg, and Nebyu Yonas from Rolandi's lab and Pattawut Manapongpun and me from Teodorescu's lab. Xenofon Strakosas and John Selberg are responsible for the design and fabrication of the non-enzymatic glucose sensor. Nebyu Yonas assisted in the fabrication process. Pattawut Manapongpun and I designed and prototyped an electronic circuit of a data acquisition. Xenofon Strakosas, John Selberg, and I also performed the majority of experiments and measurements.

Publication: Strakosas, X., Selberg, J., Pansodtee, P., Yonas, N., Manapongpun, P., Teodorescu, M. and Rolandi, M., 2019. A non-enzymatic glucose sensor enabled by bioelectronic pH control. Scientific reports, 9(1), pp.1-7.

Introduction

According to the CDC [1], in 2017, more than one hundred million U.S. adults have diabetes or a prediabetic condition. Continuous monitoring of glucose from sweat and tears can provide a significant improvement to the quality-of-life for these individuals. Currently available sweat and tears glucose-sensing devices

---

[1] https://www.cdc.gov/diabetes/pdfs/data/statistics/national-diabetes-statistics-report.pdf

suffer from short life-spans, typically lasting 1-2 weeks. Newly developed non-enzymatic glucose sensors offer longer life-spans compared to their enzymatic counter parts.

This section will describe work on the non-enzymatic glucose sensor, which was developed by [Strakosas et al., 2019a]. The sensor applies the principle of cobalt metal-oxide reactions, which are then used to measure glucose concentration. Compared to an enzymatic sensor, a non-enzymatic glucose sensor has a much longer lifespan and can last for several months instead of several weeks. However, a major drawback of glucose metal-oxide sensors are that they are only compliant with high pH levels (>10). Thus, in addition to the cobalt metal-oxide sensor, palladium electrodes are introduced as pH actuators. The device consists of two electrode pairs, a palladium electrode for changing pH and a cobalt electrode for glucose measurement. When applying voltage (V_{ph}), a palladium electrode can be used to absorb H^+ and thus change the pH from 7 to 11. The sensor measures glucose by first applying voltage to a cobalt electrode (V_g) and then measuring the resulting flow of current.

To miniaturize the non-enzymatic glucose sensor into a portable device, small-scale computing was utilized. Specifically, a controlling circuit board needed to be designed to regulate the following requirements:

- The ability to supply two isolated adjustable voltages, in a range of $\pm 1.4V$.
- The ability to measure current from a range of voltages, adjusted with respect to uA.
- The ability to wirelessly communicate with other devices, such as a smartphone or laptop.

The first two generations of DAQ are platforms for experimenting with various power supply designs. A wireless-enabled microcontroller was added in the third and forth generations. The resulting design (4th generation) consists of a Wi-fi enabled microcontroller (ESP8266), V_g power supply, V_{ph} power supply, and the ability to measure current. V_g features an adjustable positive power supply (MCP601 and potentiometer) with a current measurement feature shunt-resistor, instrumentation amplifier (INA122U) for amplified voltage across a shunt resistor. This feature is also used for analog-to-digital conversion in 16-bits (ADS1115). The instrumentation amplifier gain is set to 100 times the gain resistor result for the current-to-voltage conversion ratio of 1 μA to 100 mV. When combined with 16-bit analog-to-digital, the results in current measurement scale from 0 - 33 μA, at a resolution of 1.25 nA. The V_{ph} power supply consists of one adjustable-positive (MCP601), one fixed-positive power supply (S-13R1A14), and a multiplexer powered by a second battery. It communicates with ESP8266 via an opto-isolator. The multiplexer (TS5A22362) creates a virtual positive and negative power supply by altering between an adjustable positive power supply, a fixed positive power supply, and ground.

A high-level system diagram is shown in Figure 3.3. An electrical schematic is provided in Figure A.1 and A.2

The results collected using the custom-made data acquisition system 3.5a show comparable results with the significantly more expensive and non-portable LabVIEW PXI system 3.5b. To obtain the results, a non-enzymatic glucose sensor enabled by bio-electronic pH control and iteration of glucose data acquisition system (4th generation) was tested under various glucose concentrations.

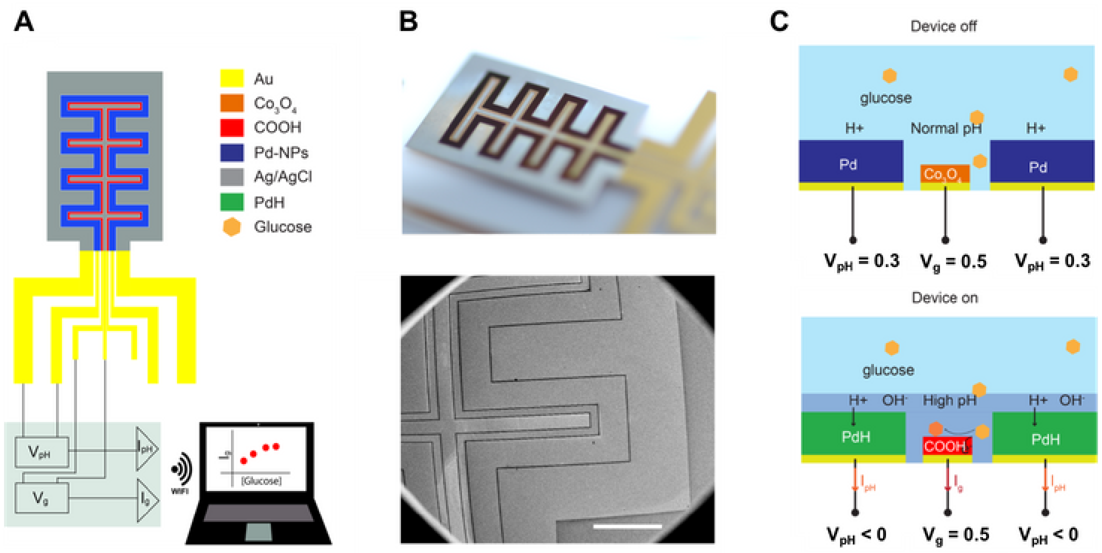

Figure 3.1: a) A schematic of the non-enzymatic glucose biosensor b) Modified contacts, with an optical image (top) and an SEM image (bottom) c) The operating principle for glucose sensing

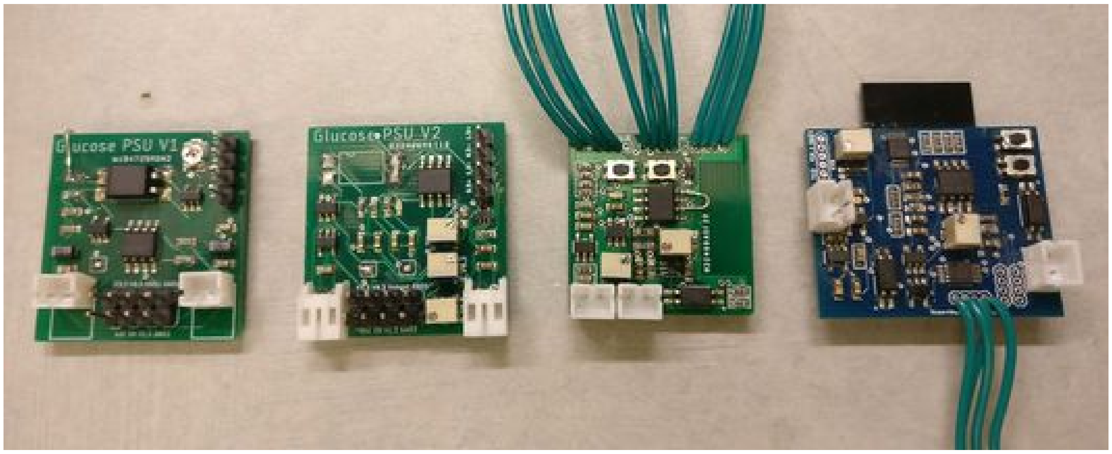

Figure 3.2: Prototype of portable data acquisition system for glucose sensing (Left to right, generation 1 to genration 4)

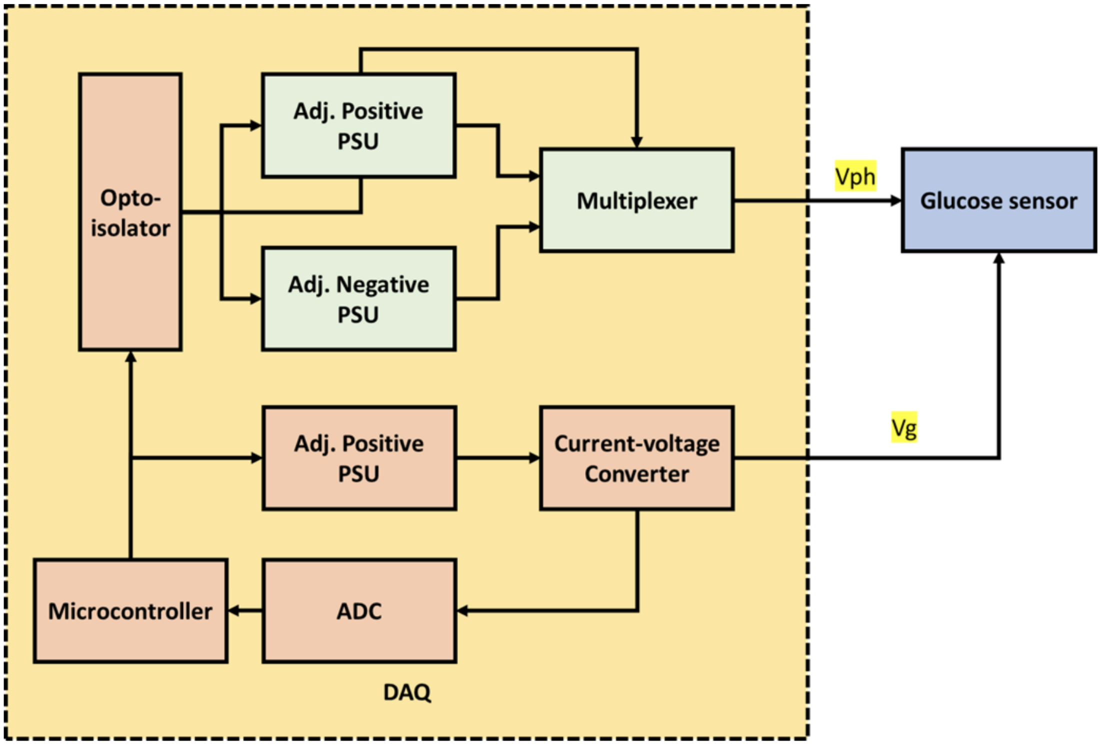

Figure 3.3: High-level system block diagram of glucose sensor's data acquisition system generation 4

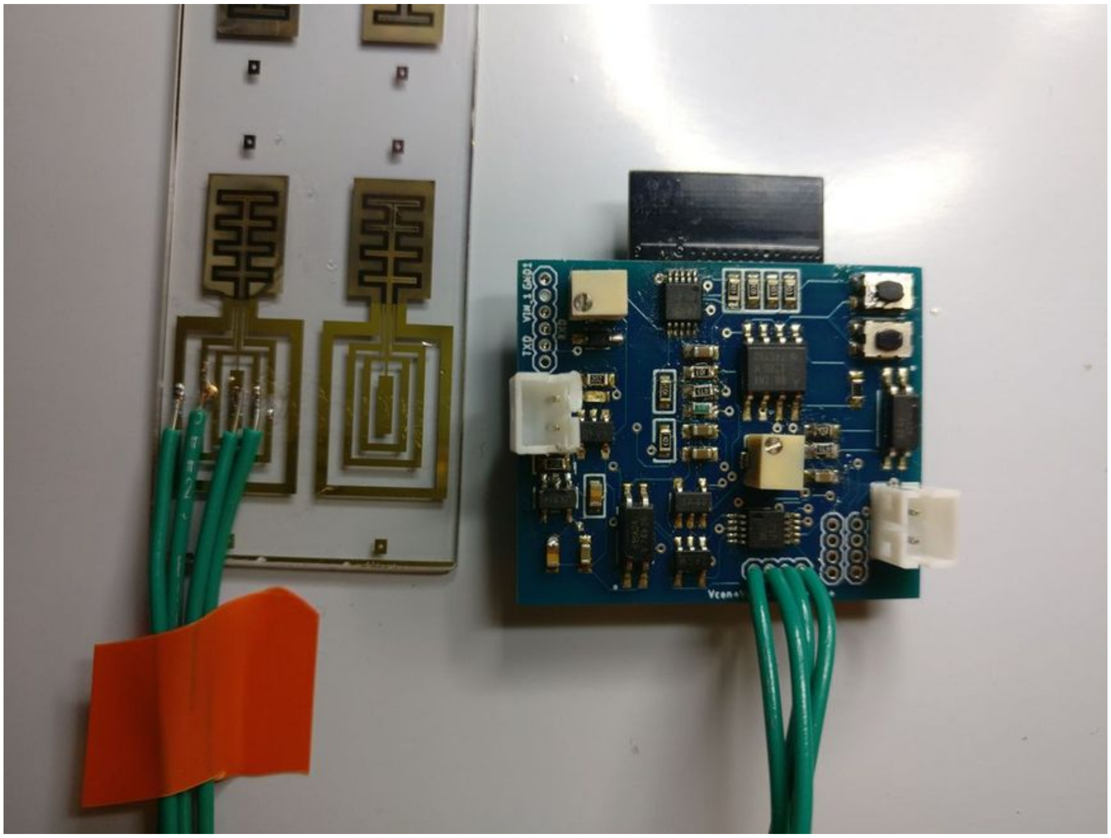

Figure 3.4: Final Prototype of Wifi-enable potentiostat for glucose sensor

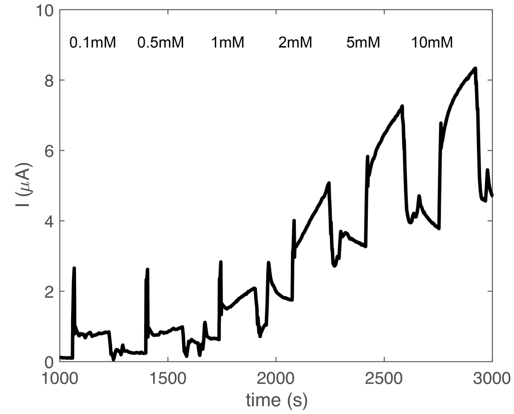

(a) Current reading at different glucose concentration on portable glucose data acquisition system version 4. Size of a current indicate glucose concentration. Higher a current, higher a glucose concentration.

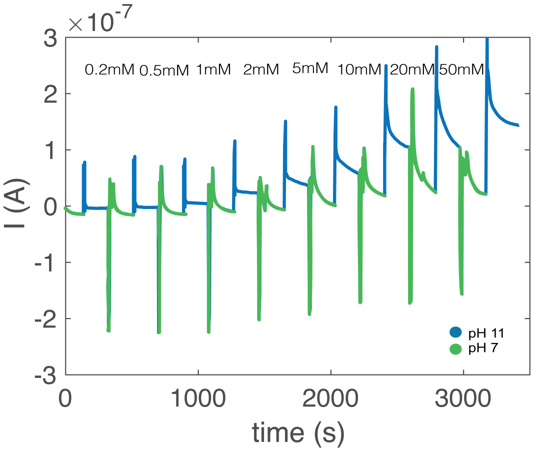

(b) Current measurement at different glucose concentration on LabVIEW PXI system. The plot shown that glucose sensing sensitivity increase as the pH increase.

3.2.2 Ion Sensor

Author contribution: This project is in collaboration with Chunxiao Wu, John Selberg, Brian Nguyen, Manping Jia, and Harika Dechiraju from Rolandi's lab. Chunxiao Wu, John Selberg, Brian Nguyen are responsible for the design and fabrication of the microfluidic ion sensor array. Manping Jia and Harika Dechiraju also assisted in the fabrication process. I designed and prototyped the electronic circuit board, interface board and fixture. Chunxiao Wu, John Selberg, and I performed the majority of experiments and measurements.

Publication: Wu, C., Selberg, J., Nguyen, B., Pansodtee, P., Jia, M., Dechiraju, H., Teodorescu, M. and Rolandi, M., 2020. A Microfluidic Ion Sensor Array. Small, 16(6), p.1906436.

Introduction

This section will describe work on an ion-selective micro-electrode array which was developed by [Wu et al., 2020]. The ion-selective micro-electrode array utilizes ion-selective membranes and microfluidics pattern technique to sense [K+], [Na+], and [Cl-] ions.

The data acquisition (DAQ) design is based on the output range of the ion-selective array sensor which produces potential range from -250 to + 250 mV. The custom-designed preamplifier circuit board consists of Op-amp buffers and Op-amp bias. An Op-amp buffer, as the name suggests, works as a buffer, matching the impedance between the sensor array and ADC. In this design, a Texas Instruments LMC6042 was picked due to its ultra-low input current properties. Undesirable loss of signal transfer will occur if the system is designed without a proper consideration of buffer, especially in a high-impedance sensor like the ion-selective array sensor. The Op-amp bias uses a Texas Instruments OPA4209 to offset the output from an Op-amp buffer circuit before feeding into an external 16-bit ADC module. This circuit is needed because the 16-bit ADC's input range is 0 - 3.3V, or only positive range, but the sensor output can range from -250 to + 250 mV. The output of bias circuit can be calculated as the following: $Vo = Vin + 1.65$. Subsequently, the DAQ input range is ±1.65V and has a resolution of 0.125 mV.

I also designed and prototyped an interface board which contains 6 x 3 spring-loaded pins (Mill-Max Mfg. Corp., 825-22-006-10-001101) and 5 pins pin-header shown in Figure 3.6a and 3.6b. Instead of using five probe stations per experiment, the interface board enables a faster and more reliable interface without sacrificing signal quality. A testing apparatus is designed to accelerate the testing process even further. The testing apparatus consists of the interface board, custom-designed acrylic adapter plate, and Z-stage showed in Figure 3.7. It reduces experiment setup time from 20 minutes down to 5 minutes per experiment.

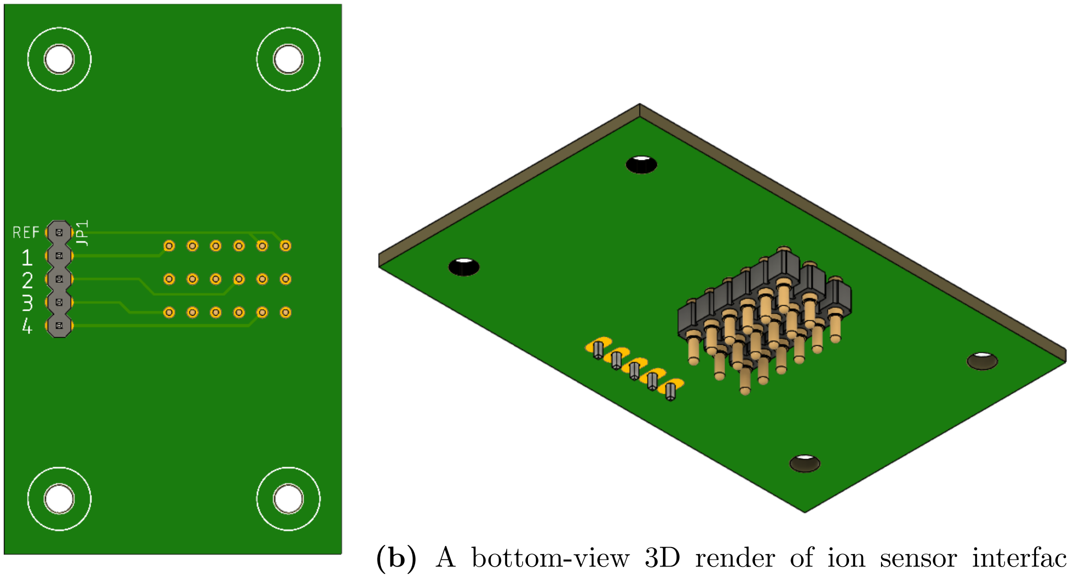

(a) A top-view 3D render of ion sensor interface board

(b) A bottom-view 3D render of ion sensor interface board

Figure 3.6: Ion sensor array interface board. The interface board interfaces with the gold contact pads of the ion sensor and connects to the pin header for the data acquisition system.

The ion-selective micro-electrode array and DAQ demonstrate the ability to measure [K+], [Na+], and [Cl-] ion concentration shown in Figure 3.9

In addition, the author also uses the ion-selective micro-electrode array to measure and compare a fresh cell culture media with a consumed cell culture media. The result in Figure 3.10 shows a reduction of all ion concentrations after the cell culture media is consumed.

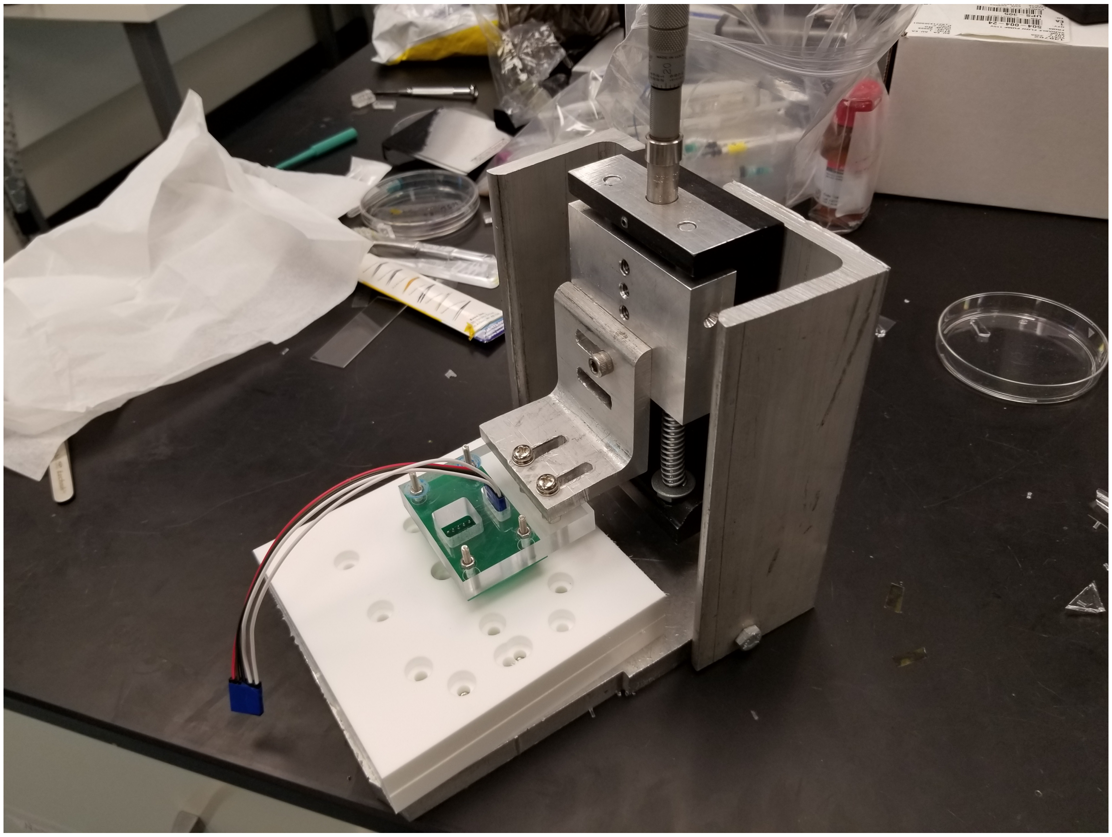

Figure 3.7: Ion sensor testing apparatus consisting of an interface board, a custom-designed acrylic adapter plate and a Z-stage used to adjust the height

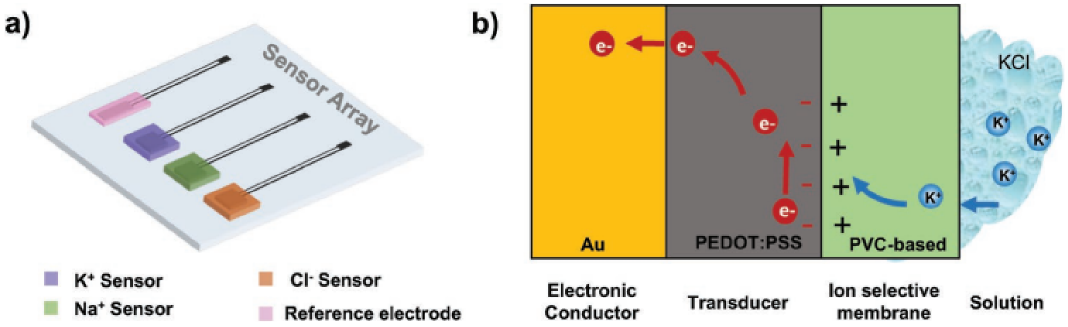

Figure 3.8: a) A schematic view of ion sensor array platform. b) The working principle of the device [Wu et al., 2020]

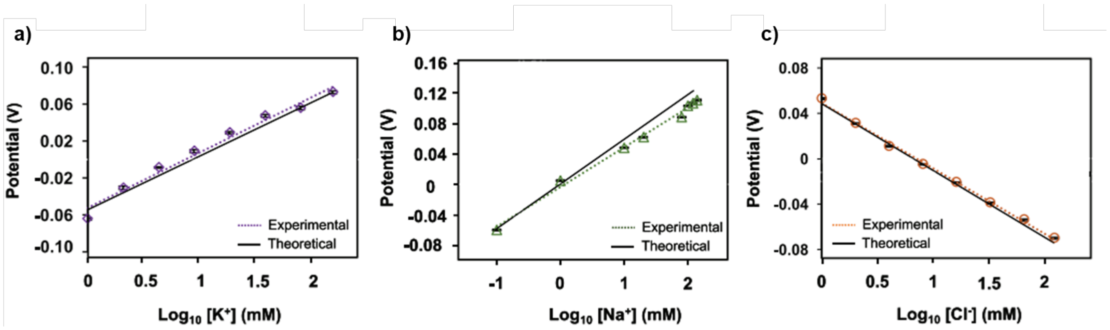

Figure 3.9: Ion sensor results. The ion sensor demonstrates the ability to measure K^+, Na^+, and Cl^- concentrations simultaneously [Wu et al., 2020]

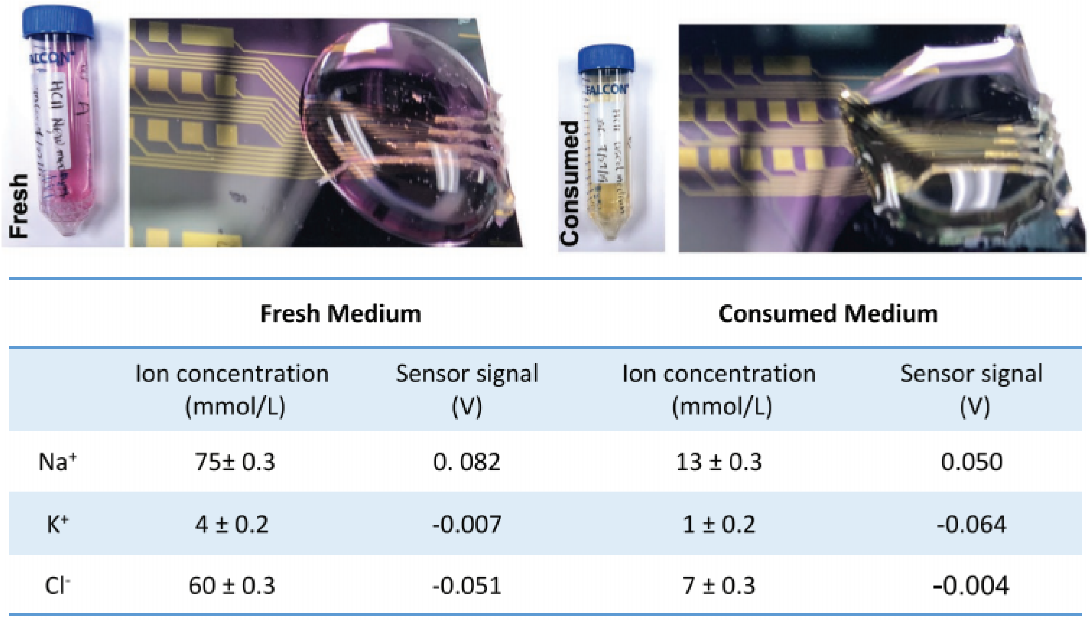

	Fresh Medium		Consumed Medium	
	Ion concentration (mmol/L)	Sensor signal (V)	Ion concentration (mmol/L)	Sensor signal (V)
Na^+	75± 0.3	0. 082	13 ± 0.3	0.050
K^+	4 ± 0.2	-0.007	1 ± 0.2	-0.064
Cl^-	60 ± 0.3	-0.051	7 ± 0.3	-0.004

Figure 3.10: Ion sensor measurement from a fresh and consumed cell culture media. As expected, the consumed cell culture media shows significantly less K^+, Na^+, and Cl^- ions [Wu et al., 2020].

3.3 Low-cost, High-thoughput Cell Culture Imaging System

Author contribution: This project is in collaboration with UCSC Braingeneer's group, which includes Victoria Ly, Pierre Baudin, Erik Jung, Kateryna Voitiuk, Yohei Rosen, Garry Mantalas, Ryan Hoffman, Spencer Seiler, John Selberg, Sergio Cordero, Robert Currie, David Haussler, Sofie Salama, Mircea Teodorescu, and also the UCSF Braingeneer's group, which includes Helen Willsey, Alex Pollen, Tomasz Nowakowski, and Mohammed Mostajo-Radji.

Victoria Ly, Erik Jung, Kateryna Voitiuk, Yohei Rosen and myself are responsible for the hardware design and prototyping of the low-cost in-incubator imaging system. Pierre Baudin, Robert Currie, Erik Jung, and myself designed the software for the system. Spencer Seiler, John Selberg, and Sergio Cordero designed a microfluidic add-on for the long-term feeding experiment. Garry Mantalas, Ryan Hoffman, Spencer Seiler and Helen Willsey managed the handling of various cell culture and live experiments.

Publications: Baudin, P.V., Ly, V.T., Pansodtee, P., Jung, E.A., Currie, R., Hoffman, R., Willsey, H.R., Pollen, A.A., Nowakowski, T.J., Haussler, D. and Mostajo-Radji, M.A., 2021. Low cost cloud based remote microscopy for biological sciences. Internet of Things, p.100454.

Ly, V.T., Baudin, P.V., Pansodtee, P., Jung, E.A., Voitiuk, K., Rosen, Y., Willsey, H.R., Mantalas, G.L., Seiler, S.T., Selberg, J.A. and Cordero, S.A., 2021. Development of a Low-Cost System for Simultaneous Longitudinal Biological Imaging. Communications Biology.

3.3.1 Introduction

Simultaneous longitudinal imaging across multiple conditions and replications has been crucial for scientific studies aiming to understand biological processes and disease. Nevertheless, imaging systems capable of accomplishing these tasks are economically unattainable for most academic and teaching laboratories around the world. Here we propose the ”Picroscope”, the first open-source, low-cost system for simultaneous longitudinal biological imaging made primarily using off-the-shelf and 3D-printed materials. The system is compatible with 24-well cell culture plates and can capture 3D z-stack images of cell culture.

This work is focused on the electronic part of the Picroscope design. More information about the mechanical and software can be found in [Ly et al., 2021] and [Baudin et al., 2021]

The system consists of 24 sets of Raspberry Pi Zero W and OV564 image sensors powered by custom-designed power distribution boards, one Raspberry Pi 4 (Pi hub), two stepper motors, and a stepper motor driver board shown in Figure 3.12. They are currently two options for illumination: over-the-plate, and below-the-plate. The whole system is powered and controlled by the custom-designed relay board, which switches on/off various components such as illumination boards, power distribution boards, and a motor driver.

The Pi hub is responsible for controlling the whole stack of hardware, ranging from controlling the relay board, overseeing the image capture process of 24 Raspberry Pi Zero W and cloud uploading. Once each image is uploaded to the Amazon S3 storage, users can view it via a web interface.

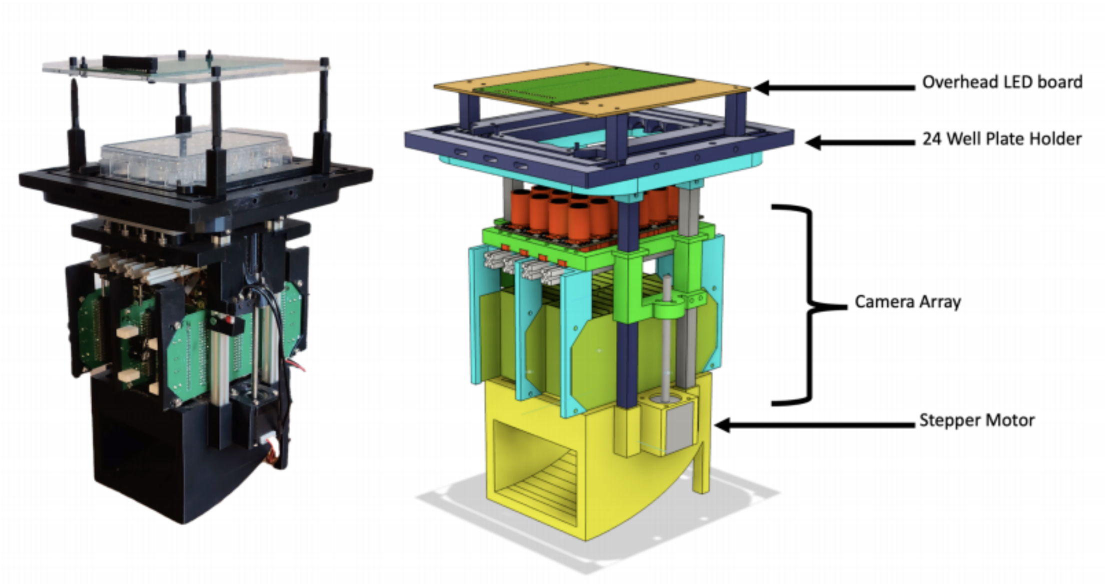

Figure 3.11: The Picroscope, low-cost, high-throughput in-incubator imaging system. Left) the actual system. Right) the 3D render of the system.

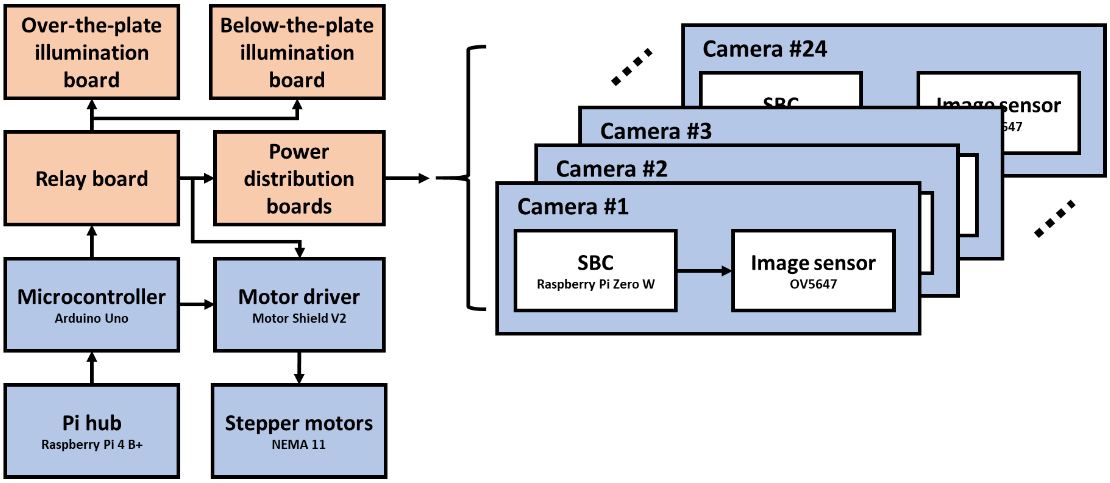

Figure 3.12: The Picroscope electronic block diagram. Blue blocks denote off-the-shelf components and orange blocks denote custom-designed circuit board.

3.3.2 System Design

Power distribution board

One major challenge of designing high-throughput imaging in a limited space is figuring out how to tightly pack image sensors and data acquisition units. Instead of using a custom-designed FPGA or custom-designed circuit board as an imaging system, we opted for using 24 off-the-shelf Raspberry Pi Zero W and OV564 image sensors. This is due to our goal of keeping the design open-source and easy to reproduce. However, this approach also creates the following challenges.

- How to tightly pack image sensors and data acquisition units.
- How to power tightly packed image sensors and data acquisition units.

The author designed the interlock system that allows tightly packing of 24 Raspberry Pi Zero W in a limited space as shown in Figure 3.13. There are two ways to power a Raspberry Pi Zero W: through GPIO pins and a USB port. In this design, we chose to power it through GPIO pins because GPIO pins also provided structural support and held the Raspberry Pi Zero W in place without additional support. Thus, the author designs the single power distribution circuit board that allows three distinct configurations, as demonstrated in Figure 3.14. The 65 x 160 mm circuit board includes ceramic decoupling capacitors for each Raspberry Pi, filtering electrolytic capacitors for the power rail, Mini-Fit Jr headers, and a Zener diode. The board is designed to hold 6 or 12 Raspberry Pi Zero W, depending on the configuration. Mini-Fit Jr connectors (Molex, 39301022) are used to supply 5V power throughout the whole system. A Zener diode is added to ensure that the power distribution board's input voltage does not exceed 5.1 V. The middle power distribution board holds and powers 12 Raspberry Pi Zero W, while the left and right power distribution boards hold and power 6 Raspberry Pi Zero.

Relay board

The relay board is another crucial component in the system. Its objective is to control power delivery to the power distribution boards, motor driver board, illumination boards, and to monitor the system state (e.g., temperature, humidity,

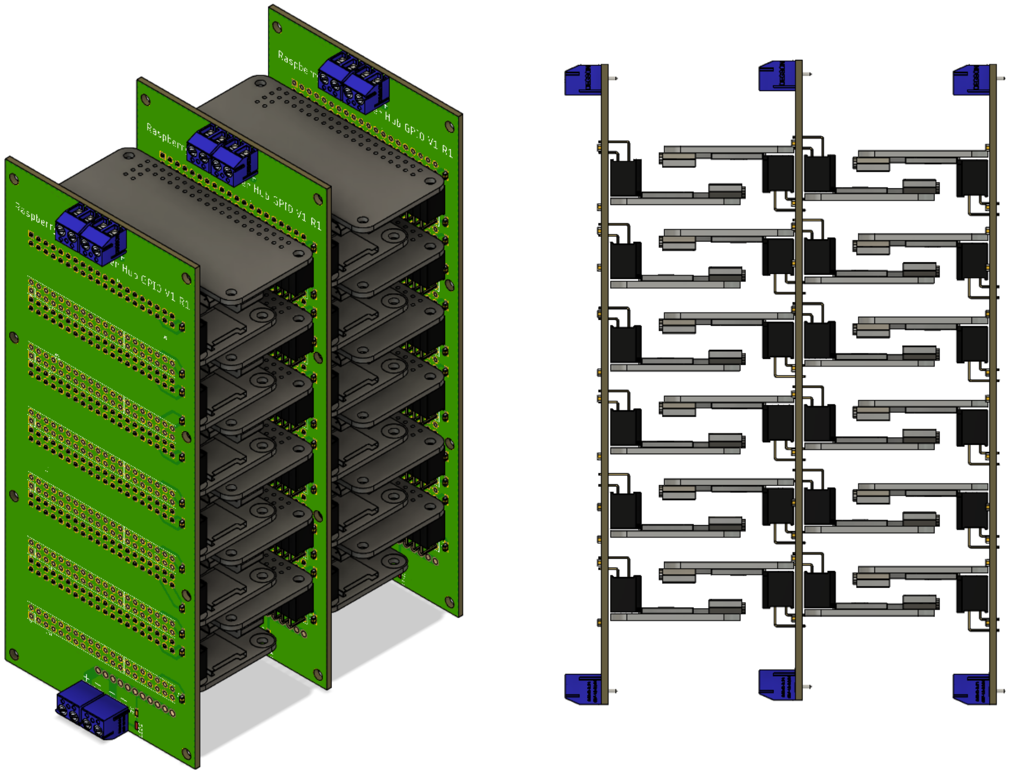

(a) A 3D render of Power distribution board interlock system

(b) A 3D render of power distribution and Raspberry Pis zero W side-way

Figure 3.13: The proposed interlock system mounted on three power distribution boards

and limit switches). The power supply consists of three DC/DC converters (ABB, PVX012A0X3) designed for a wide range of input voltage (i.e., 3 - 14.4 V). It also delivers a constant 5 V to the rest of the system. One DC/DC converter is reserved for illumination boards and motor drivers, while the other two are reserved for 12 Raspberry Pi Zero W each. The goal of the separated power supply design is to address voltage-drop issues when operating stepper motors. The board also features six Single Pole Single Throw (SPST) relays. Two relays are dedicated for controlling the power distribution boards and one relay is responsible for controlling 12 Raspberry Pi Zero W. The output of the two relays is connected

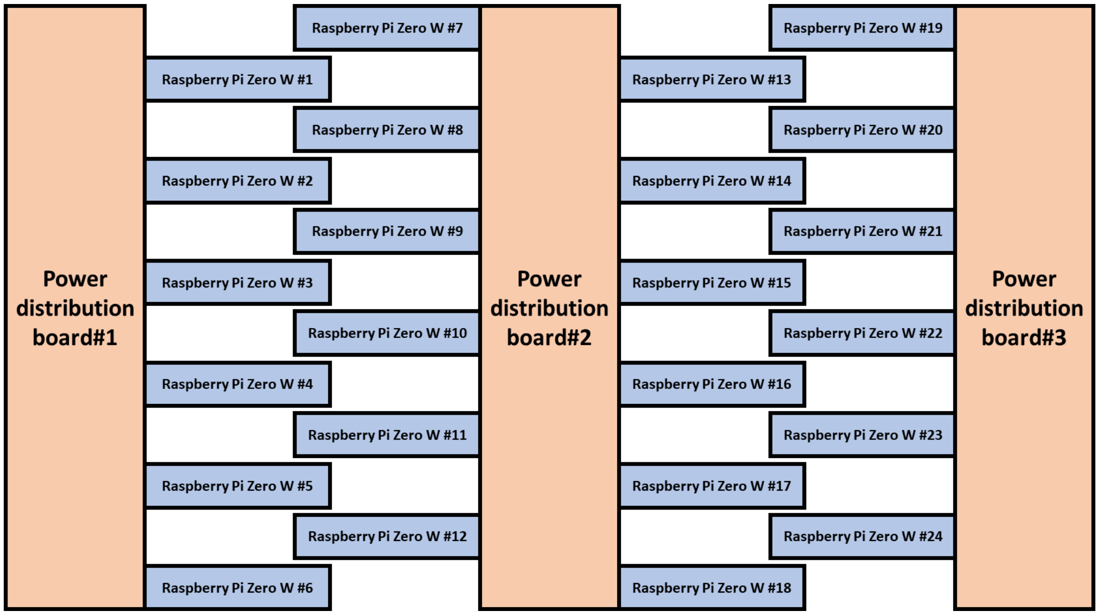

Figure 3.14: The arrangement of 24 Raspberry Pi Zero W on three power distribution boards

to three Mini-Fit Jr headers, and each connector connects to a power distribution board. The rest of the relays are reserved for the motor driver board and other illumination boards, and their outputs are connected to individual Mini-Fit Jr headers.

One essential function of the relay board is to read the status of limit switches. The limit switches are used for imaging unit height calibration. The relay board contains a passive debouching circuit which allows for smoother detection. In addition, the relay board can also measure ambient temperature and humidity via Adadfruit, DHT22. This proves to be one of the most critical features of the imaging system due to its ability to shut down all the Raspberry Pi, the motor driver, and illumination boards if the system's temperature rises above a set limit. Figure 3.15 shows the relay board internal connections including power rail and digital control signals.

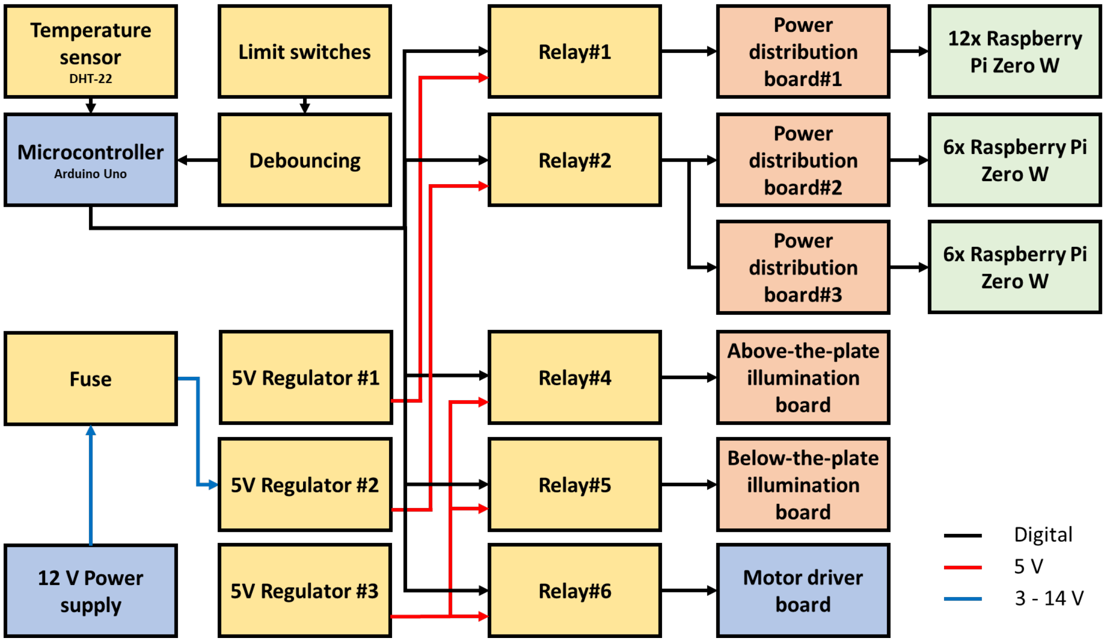

Figure 3.15: Block diagram of the relay board including power and signal wiring. The relay board is mounted on an Arduino Uno microcontroller and consists of three DC/DC converters, five relays, temperature/humidity sensor, limit switch connectors and power connectors.

Over-the-plate Illumination Board

The over-the-plate illumination, as the name suggests, provides white light illumination from above. A light shines directly on top of the 24-well cell culture plate. In this setup, the light passes through a specimen and then goes to the imaging sensor, similar to typical Upright Microscopes. The board consists of 24 3-Watt Chanzon 10DGL-DZ-3W-WH white LEDs, one DC/DC converter (ABB, PVX012A0X3), one trimmer resistor, and two Mini-Fit Jr headers. The trimmer can be used to adjust the output voltage of the DC/DC converter and subsequently change the brightness of the 24 LEDs. The DC/DC converter's output can be calculated using the following formula.

$$V_o = \frac{12K}{R_{trim}} + 0.6$$

R_{trim} consists of a 5 K trimmer resistor and a 4 K fixed value resistor. As a result, DC/DC converter's output is between 1.9 - 3.6 V.

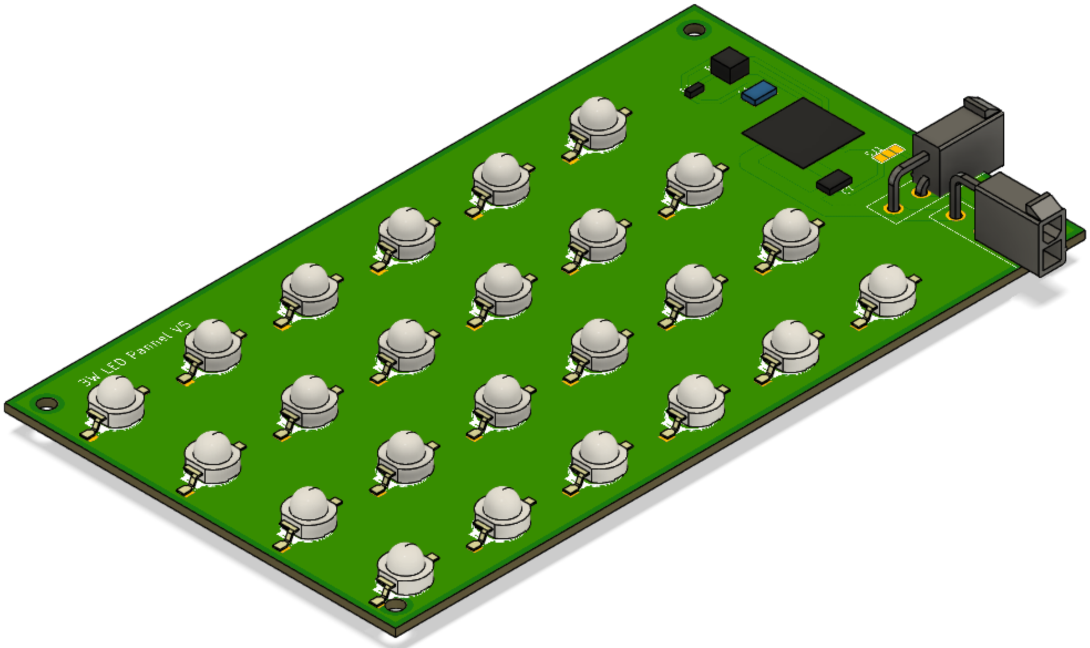

Figure 3.16: A 3D render of Over-the-plate illumination board which consists of 24 3-watt white light LEDs, adjustable power regulator and connector.

Below-the-plate Illumination Board

In addition to the over-the-plate illumination board, we also proposed an below-the-plate illumination board. The below-the-plate illumination shines a light from underneath hits the specimen and reflects back to the imaging sensor. This provides a similar result to a Confocal and Fluorescence microscope. The board consists of 232, 0603 Surface-mount (SMD) LEDs and two Mini-Fit Jr connectors. The 0603 LED package is picked up due to its wide selection of off-the-shelve LEDs, compact size, and hand soldering feasibility. MEIHUA, MHT192WDT-C2 (VF 2.8 and IF 25 mA), and 100 Ω are used in the current design.

$$Resistor = \frac{5 - 2.8}{0.025} = 88\Omega$$

However, a different LED (e.g., blue LED) can be swapped in for potential future applications, such as Fluorescence imaging.

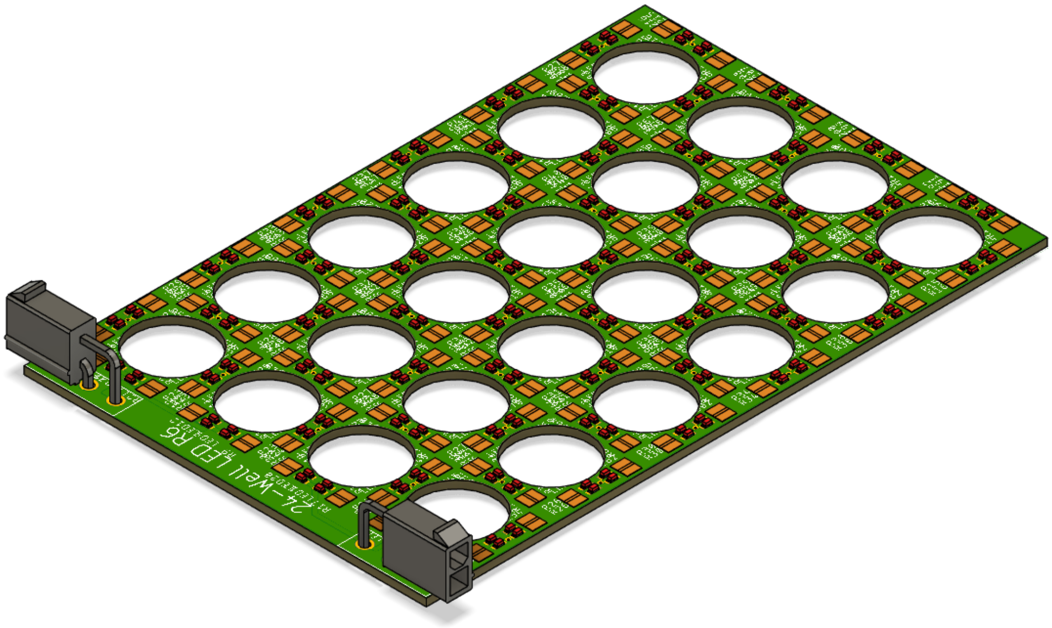

Figure 3.17: A 3D render of Below-the-plate illumination board consists of 232 white, 0603 SMD LEDs.

3.3.3 Result

The Low-cost, high-throughput cell culture imaging system or ”Picroscope” was deployed in several experiments. The first experiment is a Zebrafish where the experiment was conducted for 28 hours from Gastrulation to Organogenesis phase shown in Figure 3.18, 3.19, and 3.20. Fertilized zebrafish eggs were purchased from Carolina Biological Supply Company (Catalog # 155591) and maintained in media containing 15 mM sodium chloride (Sigma-Aldrich, S9888), 0.5 mM potassium chloride (Sigma-Aldrich, P3911), 1 mM calcium chloride dihydrate (Sigma-Aldrich, 223506), 1 mM magnesium sulfate heptahydrate (Sigma-Aldrich, 1058822500), 150 µM potassium phosphate monobasic (Sigma-Aldrich, P5655), 50 µM sodium phosphate dibasic heptahydrate (Sigma-Aldrich, S9390), 0.7 mM sodium bicarbonate (Sigma-Aldrich, S5761) and 0.1% methylene blue (Sigma-Aldrich, M9140).

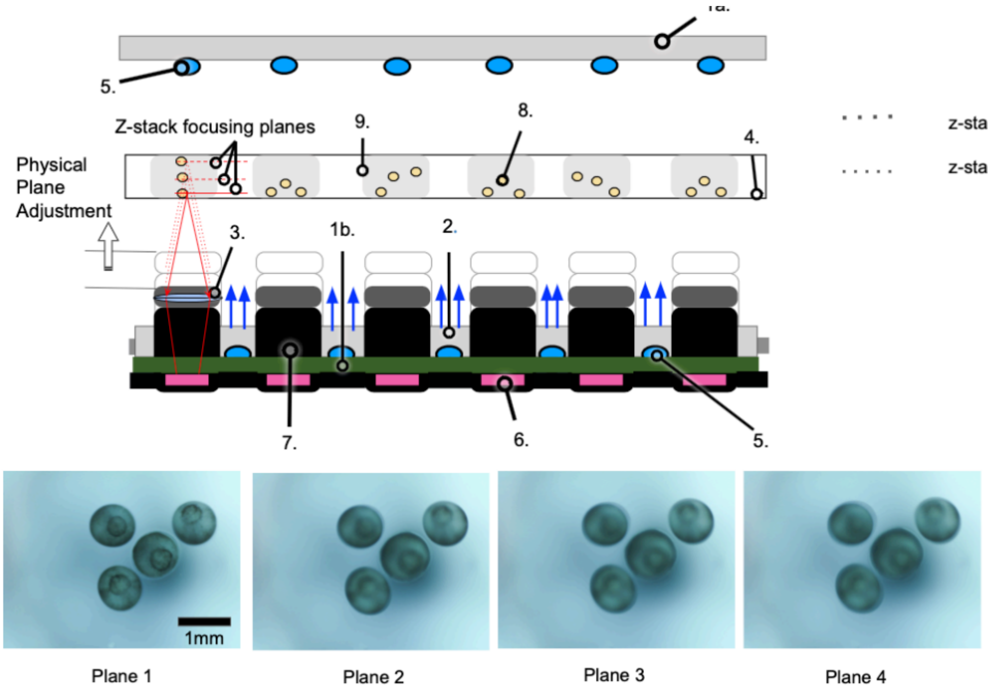

Figure 3.18: Schematic representation of the z-stack function 1.a = Over-the-plate illumination board, 1.b = Under-the-plate illumination board, 2 = Acrylic Light Diffuser, 3 = Lenses, 4 = Cell Culture Plate, 5 = LEDs, 6 = Raspberry Spy Cameras, 7 = 3D Printed Camera Bodies, 8 = Biological Sample (e.g., Frog Embryos), 9 = Individual Culture Well. The photos at the bottom were taken at four planes 0.3 mm apart. The blastopore is only in focus in Plane 1 [Ly et al., 2021]

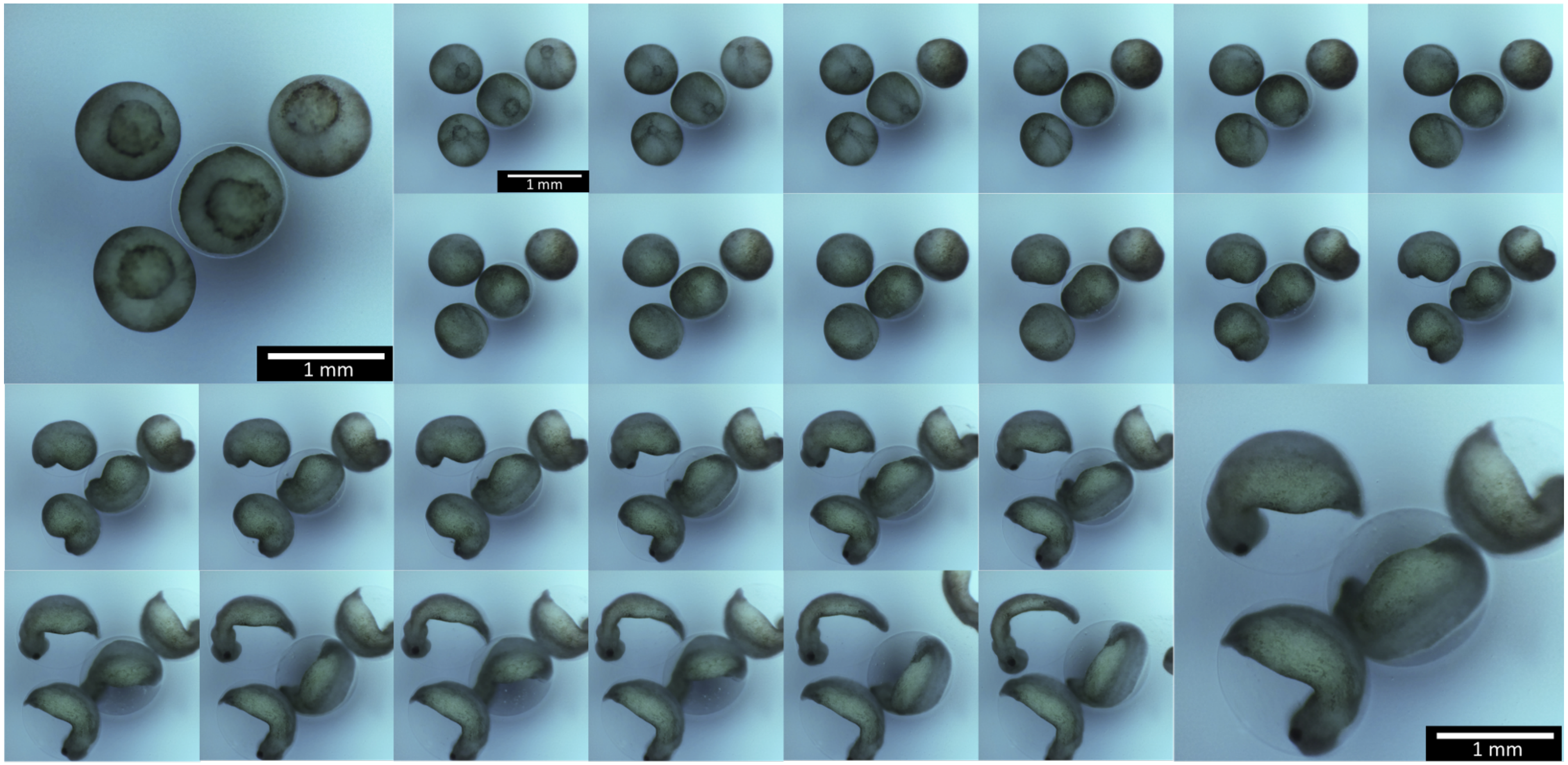

Figure 3.19: Longitudinal imaging of Xenopus tropicalis development. Images of a representative well in which 4 frog embryos developed over a 28 hour period. Images were taken hourly. White Balance adjusted for visibility [Ly et al., 2021].

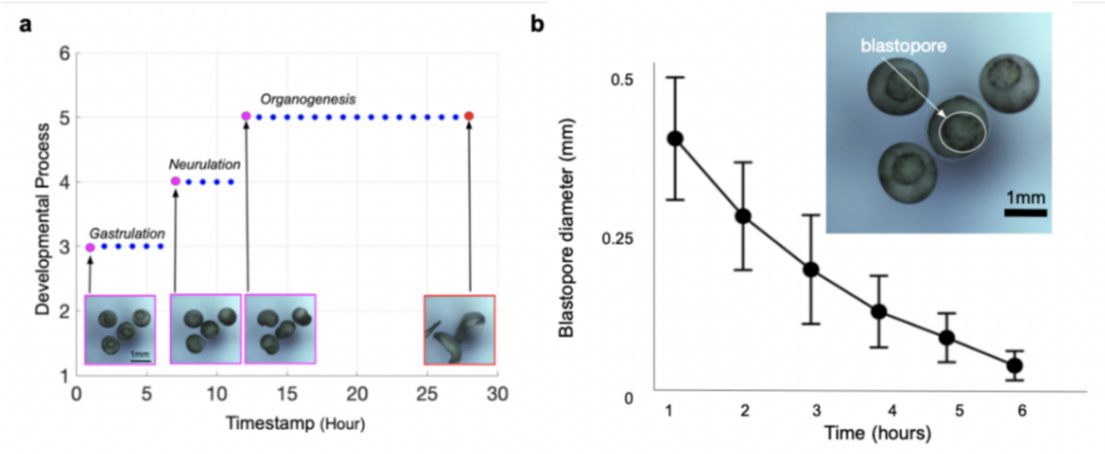

Figure 3.20: Longitudinal imaging allows the tracking of individual developmental processes: a) The images shown in figure 5 were taken hourly over a 28 hour period and encompass 3 developmental stages: Gastrulation, neurulation and organogenesis. Y-Axis represents the stages of frog embryonic development: 1 = Fertilization , 2 = Cleavage, 3 = Gastrulation, 4 = Neurulation, 5 = Organogenesis, 6 = Metamorphosis. X-Axis represents the timepoint at which it occurs. Each dot in the plot represents a timepoint in which the images were taken. Magenta = the beginning of each developmental process. Red = the end of the experiment at 28 hours. Blue = intermediate timepoints. b) Diameter of the blastopore is reduced over time from gastrulation to neurulation. Top right panel shows an example of an individual blastopore. A total of 27 embryos were considered for the analysis [Ly et al., 2021].

The second experiment features Human embryonic stem cells and cortical organoids shown in Figure 3.21. All hESC experiments used the H9 cell line (WiCell)75. hESCs were grown on vitronectin (Thermo Fisher Scientific, A14700) coated plates and cultured using StemFlex Medium (Thermo Fisher Scientific, A3349401). Passages were performed incubating the cells in 0.5mM EDTA (Thermo Fisher Scientific, 15575020), in DPBS for 5 minutes.) To generate cortical organoids, we first dissociated hESCs into single cells and re-aggregated them in Aggrewell 800 24-well plates (STEMcell Technologies) at a density of 3,000,000 cells per well with 2mL of Aggrewell Medium (STEMcell Technologies) supplemented with Rho Kinase Inhibitor (Y-27632, 10 µM, Tocris, 1254) (Day 0). The following day

(Day 1), we supplemented the aggregates with WNT inhibitor (IWR1-ϵ, 3 µM, Cayman Chemical, 13659, Days 1-10) and TGF-βinhibitor (SB431542, Tocris, 1614, 5 µM, days 0-10). On Day 2, aggregates were transferred by pipetting out of the Aggrewell plate with wide bore P1000 pipette tips onto a 37 µm filter and then transferred to ultra low adhesion 6-well plates. Media was changed on Days 4, 8 and 10, by replacing 2mL of conditioned media with fresh media. On Day 11, the medium was changed to Neuronal Differentiation Medium containing Eagle Medium: Nutrient Mixture F-12 with GlutaMAX supplement (DMEM/F12, Thermo Fisher Scientific, 10565018), 1X N-2 Supplement (Thermo Fisher Scientific, 17502048), 1X Chemically Defined Lipid Concentrate (Thermo Fisher Scientific, 11905031) and 100 U/mL Penicillin/Streptomycin supplemented with 0.1% recombinant human Fetal Growth Factor b (Alamone F-170) and 0.1% recombinant human Epidermal Growth Factor (R&D systems 236-EG). On Day 12, the organoids were transferred in 90 µL media to a custom glass-PDMS microfluidic chip for imaging/feeding containing 50 µL Matrigel hESC Qualif Matrix (BD 354277) bringing the total volume in the well to 120 µL. Partially embedding the organoid in Matrigel in this way led to 2D outgrowths on the surface of the Matrigel. Feeding occurred automatically every hour replacing 30 µL Neuronal Differentiation Medium.

In addition, both illumination modes (i.e., above-the-plate, below-the-plate) are tested on both cortical Organoid and frog egg. An organoid is translucent and best imaged using below-the-plate illumination, while a frog egg is opaque and best imaged using above-the-plate illumination. Figure 3.22 shown images of cortical Organoid and frog eggs in both illumination modes.

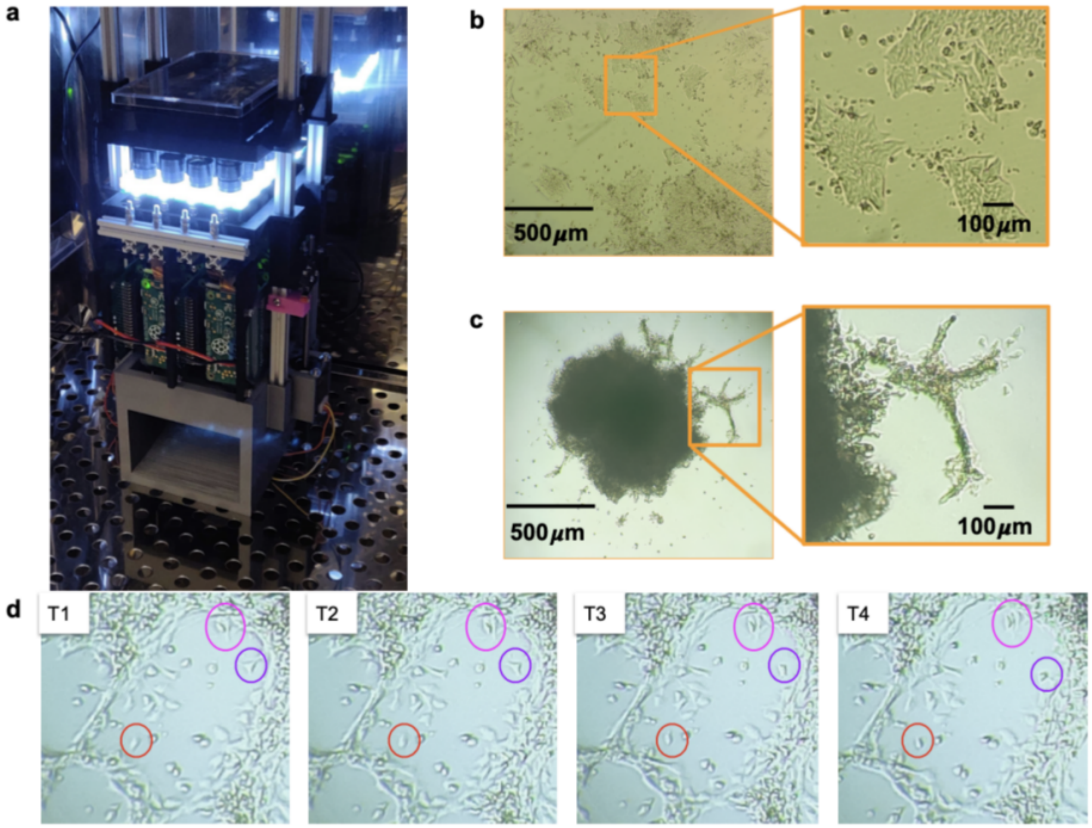

Figure 3.21: In-incubator imaging of mammalian cell and cortical organoid models. a) The Picroscope inside a standard tissue culture incubator. b) Imaging of human embryonic stem cells as a model of 2D-monolayer cell cultures. c) Longitudinal imaging of human cortical organoids embedded in Matrigel. Zoomed images show the outgrowth of neuronal processes originating in the organoids. d) Manual Longitudinal tracking of migration of individual cells in embedded cortical organoids over 40 minutes. Images were taken every 10 minutes [Ly et al., 2021].

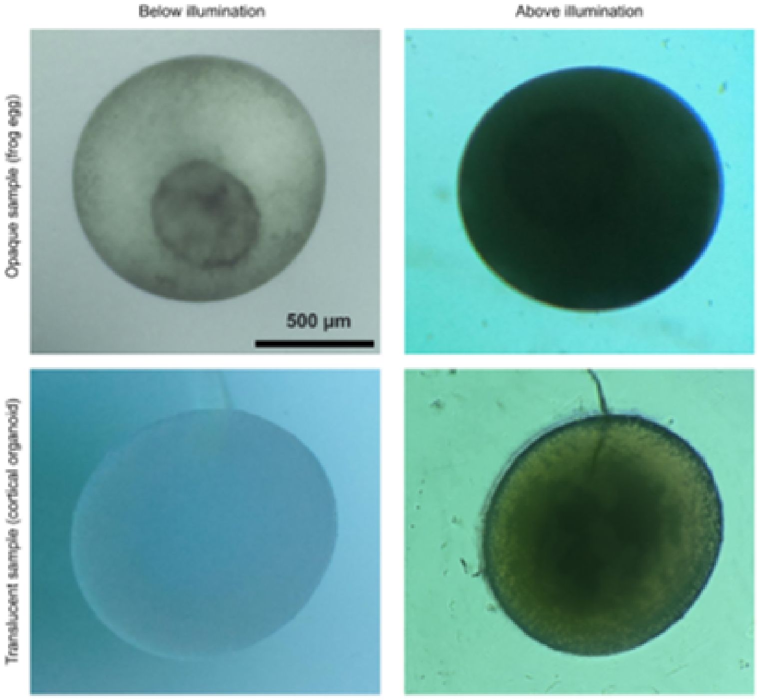

Figure 3.22: Comparison of illumination modes in different sample types. Comparison between above-the-plate and below-the-plate illumination for imaging opaque samples (frog egg) and translucent samples (cortical Organoid) [Ly et al., 2021].

3.4 Conclusion

This chapter presents several systems used for monitoring and sensing cell culture systems. First, I present a custom-design portable and wireless data acquisition system for a non-enzymatic glucose sensor developed by Rolandi's lab. Due to the unconventional electrodes setup of the sensor, two potentiostats are required to operate the sensor. The standalone custom-designed data acquisition demonstrated the capability of measuring glucose concentration range from 0.1 mM to 50 mM. Results from the data acquisition are comparable with more expensive benchtop potentiostat.

Second, I present a custom-design data acquisition unit, an interface board, and a testing jig for ion-selective micro-electrode array also developed by Rolandi's lab. The data acquisition translates weak potential signals from an array of ion sensors to a more suitable signal for a standard analog-to-digital converter. The interface board and test testing jib is helping speed up an experiment setup time from 20 minutes to 5 minutes. The system shows that the result from the DAQ matches with theoretical calculation and later shows an expected ion concentration when comparing a fresh cell culture medium to a consumed one.

Finally, I designed all circuit boards and a few mechanical fixtures for a low-cost, high-throughput, in-incubator imaging system. I invented the interlock system that allows tightly packed 24 Raspberry Pi Zero W and OV5647 image sensors into 24-well spacing. The custom-design circuit boards, including three power distribution boards, relay boards, and two illumination boards, were designed for this purpose. The imaging system performs longitudinal studies of various biological samples (e.g., Human embryonic stem cells, cortical organoids, frog embryos, and Zebrafish eggs) in both in-incubator and outside an incubator.

Chapter 4

Actuation

Publications: Pansodtee, P., Selberg, J., Jia, M., Jafari, M., Dechiraju, H., Thomsen, T., Gomez, M., Rolandi, M. and Teodorescu, M. (2021). The multi-channel potentiostat: Development and evaluation of a scalable mini-potentiostat array for investigating electrochemical reaction mechanisms. PLoS ONE, 16(9): e0257167

Selberg, J., Jafari, M., Mathews, J., Jia, M., Pansodtee, P., Dechiraju, H., Wu, C., Cordero, S., Flora, A., Yonas, N. and Jannetty, S., 2020. Machine Learning-Driven Bioelectronics for Closed-Loop Control of Cells. Advanced Intelligent Systems, 2(12), p.2000140.

Jia, M., Dechiruji, H., Selberg, J., Pansodtee, P., Mathews, J., Wu, C., Levin, M., Teodorescu, M. and Rolandi, M., 2020. Bioelectronic control of chloride ions and concentration with Ag/AgCl contacts. APL Materials, 8(9), p.091106.

Jafari, M., Marquez, G., Selberg, J., Jia, M., Dechiraju, H., Pansodtee, P., Teodorescu, M., Rolandi, M. and Gomez, M., 2020. Feedback control of bioelectronic devices using machine learning. IEEE Control Systems Letters, 5(4), pp.1133-1138.

Author contribution: This project collaborates with John Selberg, Manping

Jia, Harika Dechiraju from Rolandi's lab, Mohammad Jafari from Gomez's group, and Thomas Thomsen from Teodorescu's lab.

John Selberg, Manping Jia, and Harika Dechiraju are responsible for designing and conducting electrochemical experiments. Thomas Thomsen and I designed and prototyped an electronic circuit consisting of multi-channel potentiostat and software development. Mohammad Jafari tested and provided feedback on API and closed-loop control experiment. John Selberg, and I also performed the majority of experiments and measurements.

4.1 Introduction

To develop a multi-channel potentiostat for an array of ion pumps, it is necessary to start the design process from a single-channel (traditional) potentiostat and later adapt the design into modular and non-modular multi-channel potentiostats.

One distinct feature of [Selberg et al.,] ion pumps is the electrodes configuration. Unlike a typical 3-electrode electrochemical device which consists of a working electrode (WE), a counter electrode (CE), and a reference electrode (RE), the ion pump features multiple working electrodes and one counter electrode. Thus, the author intentionally disregards a reference electrode in all proposed designs.

First, the author explores the basic construction of single-channel/traditional potentiostat for a two-electrode electrochemical cell that only has a WE and a CE, and tailors the design toward actuating the ion pumps. Later, the single-channel potentiostat was redesign into multi-channel modular and non-modular versions. The modular version supports up to 64 channels suitable for an enormous array of ion pumps (e.g., 4-ions ion pump has 49 electrodes). However, most of the applications only require a number of channels in the range of ten channels. Thus, for

16 channels, a non-modular potentiostat is designed for a general application that does not need more than 16 electrodes. The non-modular design also features a slightly simplified circuit and more adequate power supplies to minimize assembly difficulty, footprint and cost.

4.2 Single-Channel Potentiostat

4.2.1 Introduction

To develop a multi-channel potentiostat, it is crucial to start with a single-channel/potentiostat design. The single-channel design is the foundation that is eventually converted into multi-channel potentiostat.

A potentiostat consists of two stages, output and input. An output stage is where a potentiostat actuates an electrochemical device with a wide range of voltage. In contrast, an input stage is designed to measure a current that been supply to an electrochemical device. The range and resolution needed for output and input stages of a potentiostat are vastly diverse and largely depend on a type and application of an electrochemical device. The majority of commercial potentiostats tend to support a wide range of output and input; however, the author opted for a more narrow range tailor toward the [Selberg et al.,] to reducing cost and device footprint.

4.2.2 Output Stage

The required voltage range and resolution of the ion pump is $\pm 2V$ and 10 mV per step. Therefore, the author designed the adjustable voltage source to be ±4V and a resolution of 2 mV.

Adjustable Voltage Source

The voltage source is comprised of two main components, the Digital-to-Analog converter (DAC); turns digital signal into an analog signal, and a shift and scale operational amplifier; shifts and scales the output from $0 - 3.3V$ to $\pm 4V$.

Microchip MCP4728, 12-Bit, Quad Digital-to-Analog Converter with EEPROM Memory is chosen due to its number of channels, 12-bit resolution, support of high-speed I2C (3.4 Mbps) and scalability (8 I2C address available). MCP4728 gives an output range of 0 - 3.3 V so an additional circuit is needed to shift and scale the output range to $\pm 4V$. Shift and scale circuity consists of OPA209, a Precision operational amplifier, and MCP601, a general-purpose operational amplifier for reference. Combining these two Op-amps scales and shifts the 0 to +3.3 V signal to a $\pm 4V$ output with the resolution of 1.95 mV. The shifted and scaled output can be calculated as

$$V_o = 2.42 * V_{in} - 4 \tag{4.1}$$

The circuit is simulated in TI-TINA SPICE simulator where the input signal is given by a function generator and generates a sine wave with 3.3 V_{p-p} at 1 kHz with 1.65 V DC offset.

4.2.3 Input Stage

The ion pump consumed current in the range of $\pm 0 - 1\mu A$ and required a resolution higher than 1 nA. There are two state-of-the-art current measurement techniques for different ranges: transimpedance amplifier and shunt resistor techniques. A transimpedance amplifier technique is suitable for current in the range of fA to nA, and a shunt resistor technique is suitable for current in the range of

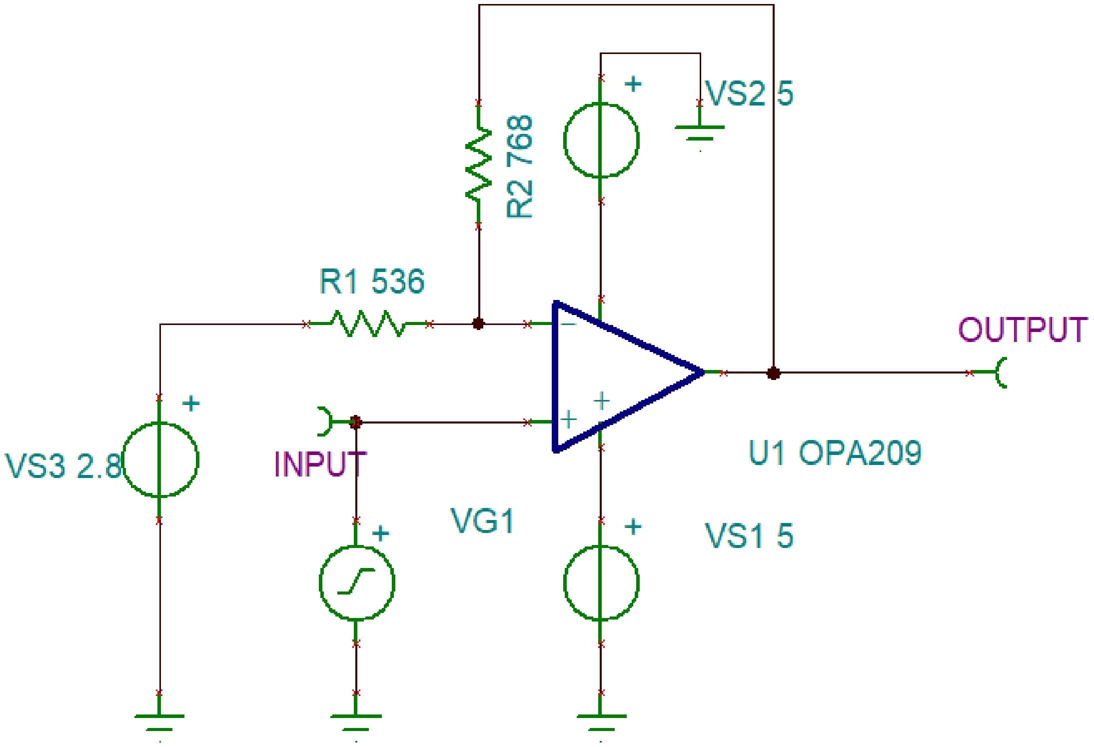

Figure 4.1: Schematic of shift and scale circuit. The circuit consists of Op-amp, 536 and 768 Ω resistors and 2.8 V bias reference.

μA to A. However, the current range and resolution of the ion pump is in between both techniques nA to μA. Thus, the author explored both techniques and settled on a shunt resistor technique. However, it is important to note that the shunt resistor approach has low accuracy, and therefore, many precautions were added to minimize this inherent measurement error.

Current Measurement: Transimpedance Amplifier

A property of an ideal operational amplifiers is that the difference between the positive and negative terminal is zero. By connecting the negative terminal to the output of the current source, and the positive terminal to ground, it provides

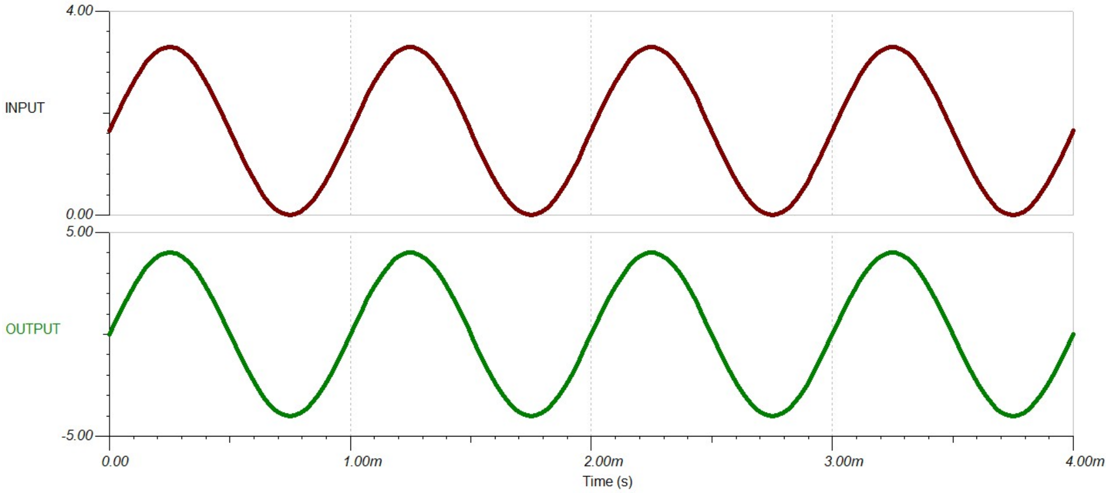

Figure 4.2: Plot of input and output of shift and scale circuit. The input range from 0 - 3.3 V and the output result in -4 - 4 V.

a near-zero burden-voltage. The output of the Op-amp is the measured current multiple by the value of feedback resistors.

$$-I_{in} = \frac{V_{out}}{R_f} \tag{4.2}$$

$$V_{out} = -I_{in} * R_f \tag{4.3}$$

$$V_{out} = -I_{in} * 10^6 \tag{4.4}$$

LMP7721, 3 Femtoampere Input Bias Current Precision Amplifier, is chosen due to ultra-low bias current which provides superior precision. A feedback resistor value of 1 Megaohm is used for a current-to-voltage conversion ratio of 1 nA to -1 mV.

The circuit is simulated with an input signal of a sine wave 4 V_{p-p} at 1 KHz from a function generator. The load of the circuit is simulated at 10 MegaOhm. Due to the nature of the bidirectional signal, the output range of an LMP7721 is in both positive and negative regions. However, the analog-to-digital converter can only handle a voltage range from 0 to 3.3 V. Thus, an additional circuit is required to offset LMP7721 output signal back to only the positive side.

OPA4209, a quad Precision operational amplifier, is used to provide an offset to the output of LMP7721 and convert $\pm V_{out}$ to $\pm Vout + 1.65$.

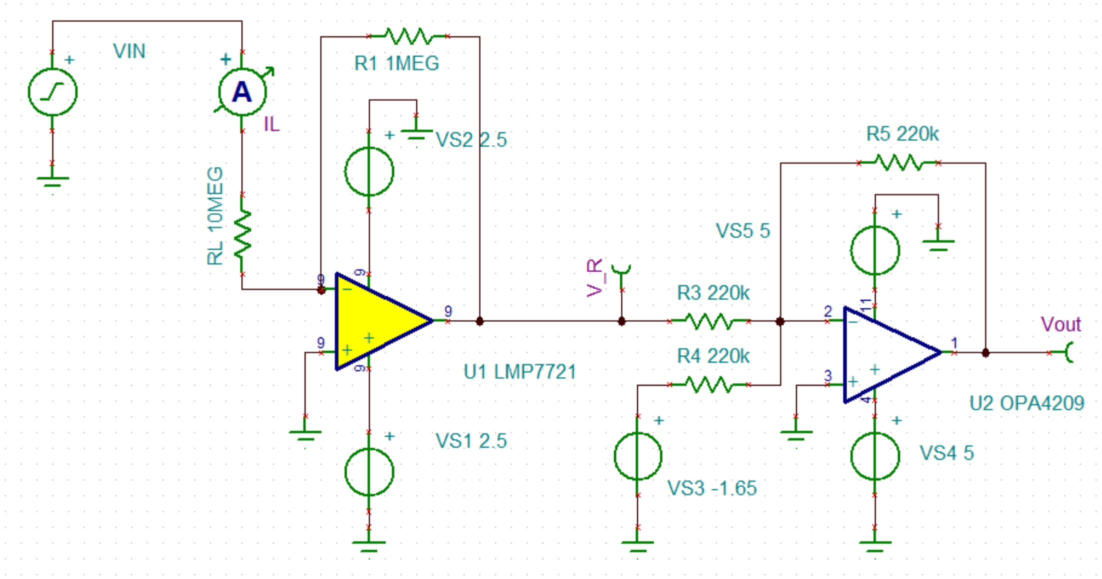

Figure 4.3: Schematic of transimpedance amplifier (Current to voltage conversion) and level-shifting circuits.

Current Measurement: Shunt Resistor

Although the Transimpedance amplifier technique provides accurate current measurement in the fA range, to scale up a number of channels requires many more components compared to a shunt resistor. In addition, the Transimpedance amplifier technique is not compatible with a high-side current sensing setup which is crucial for a multi-channel potentiostat.

The measurement of current is employed with the shunt resistor technique, where the voltage is measured across a known resistor value. Thus, the current

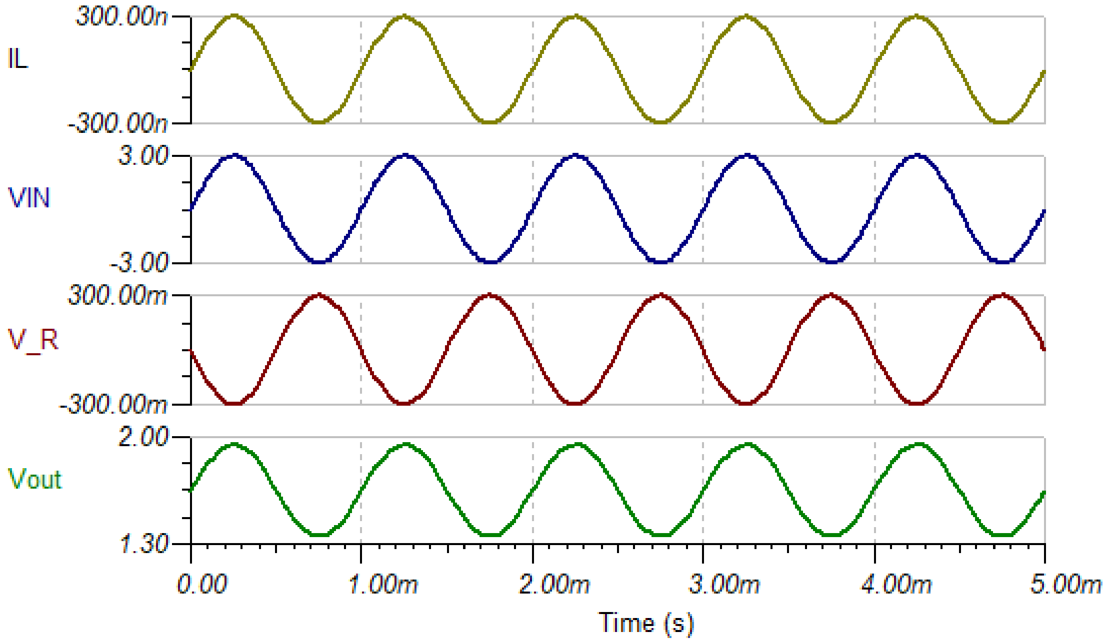

Figure 4.4: The simulation result of Transimpedance amplifier current to voltage conversion with output offset. The input current (IL) is range -300 to 300 nA, the output of transimpedance amplifier (V_R) is -300 to 300 mV. Later, V_R is shifted by +1.65V and result in V_{out} of 1.35 to 1.95 V.

value can be calculated based on measured voltage and known resistor.

$$I = \frac{V}{R} \tag{4.5}$$

As a rule of thumb, the value of the shunt resistors should be less than 0.1% of the load resistance. Load resistance (R_L) can be estimated based on voltage range and current.

$$R = \frac{V}{I} \tag{4.6}$$

For example, at 1V and 1200 nA current, R_L? is approximated to be

$$R_L = \frac{1}{1200nA} = 883.33Kohm \tag{4.7}$$

Therefore, the Shunt resistor should be less than 88.3 Kohm. To minimize error even further, a 10 Kohm resistor with 0.1% tolerance is chosen. However, due to the very minimal value of the shunt resistor, the voltage drops across the shunt resistor are also very small. On the high-side, $V_{Shunt} = 10kohm*1200nA = 12mV$, and on the low-side, $V_{Shunt} = 10kohm * 10nA = 0.1mV$ To accurately measure small voltages across a shunt resistor, the signal needs to be amplified.

INA121, an ultra-low bias current instrumental amplifier with a gain of -100, is used to maximize accuracy in measuring current in the nA range. After amplified, the high-side result is 1.2V and the low-side is 0.1 V, which is within the range of ADC.

The circuit is simulated under the input signal of a function generation with a sine wave, 4 V_{p-p} at 1 KHz. The load of the circuit is simulated at 10 MegaOhms. Similar to the Transimpedance amplifier design, the output of INA121 provides output in both positive and negative voltages. The same circuit design of OPA4209 is used to offset the output from INA121.

Current Measurement: First-order RC Low Pass Filter

To eliminate high-frequency noises from the digital bus and environment, a first-order RC low pass filter is added. The cut-off frequency of a first-order RC low pass filter can be calculated from the following equations.

$$fc = \frac{1}{2\pi RC} \tag{4.8}$$

$$fc = \frac{1}{(2)(\pi)(220K)(10n)} = 72.34Hz \tag{4.9}$$

The author picked the cut-off frequency to be 72.34 Hz from combination of 220 K resistor and 10 nF capacitor.

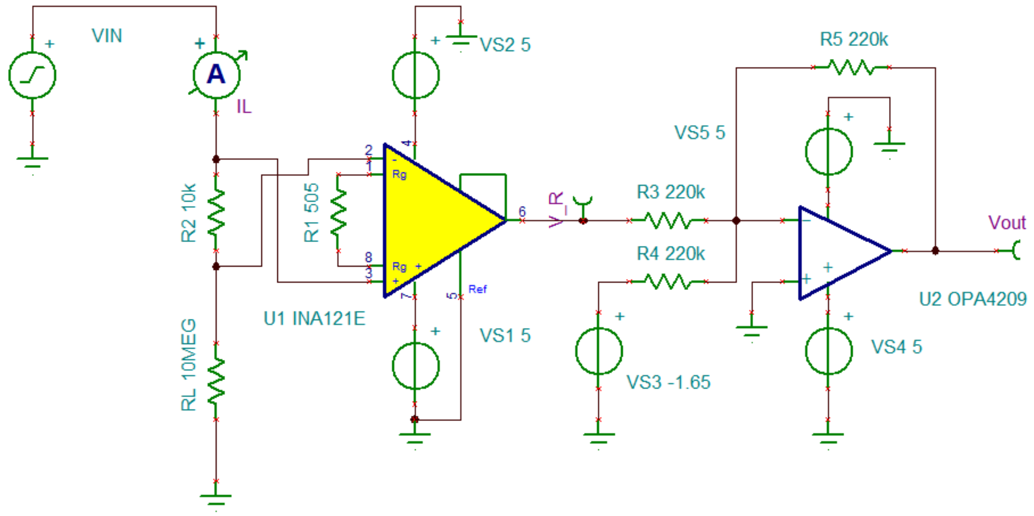

Figure 4.5: Schematic of shunt resistor, current to voltage conversion with output offset circuit. The level-shifting circuit is same as transimpedance amplifier technique.

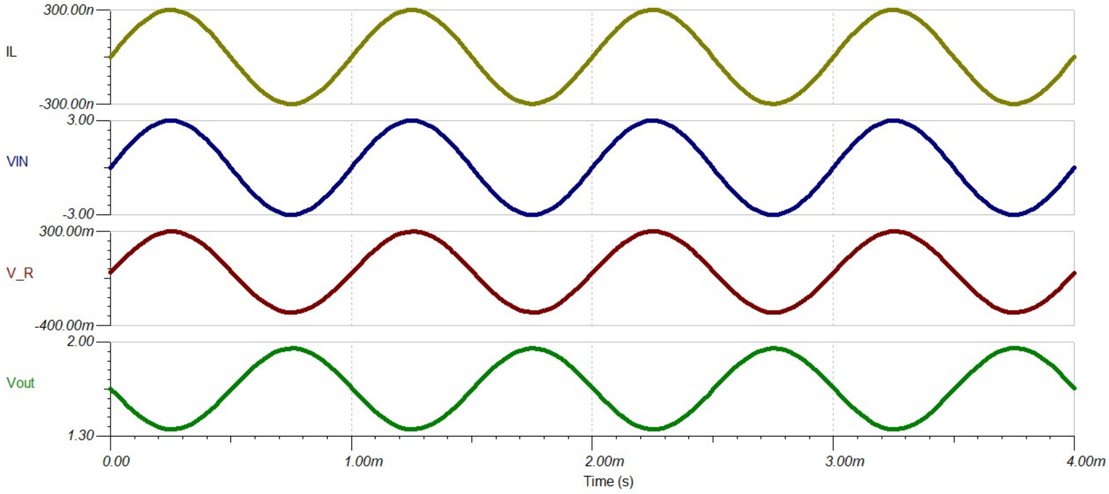

Figure 4.6: The simulation result of shunt resistor current to voltage conversion with output offset. The input current (IL) is range -300 to 300 nA, the output of instrumentation amplifier (V_R) is -300 to 300 mV. Later, V_R is shifted by +1.65V and result in V_{out} of 1.35 to 1.95 V.

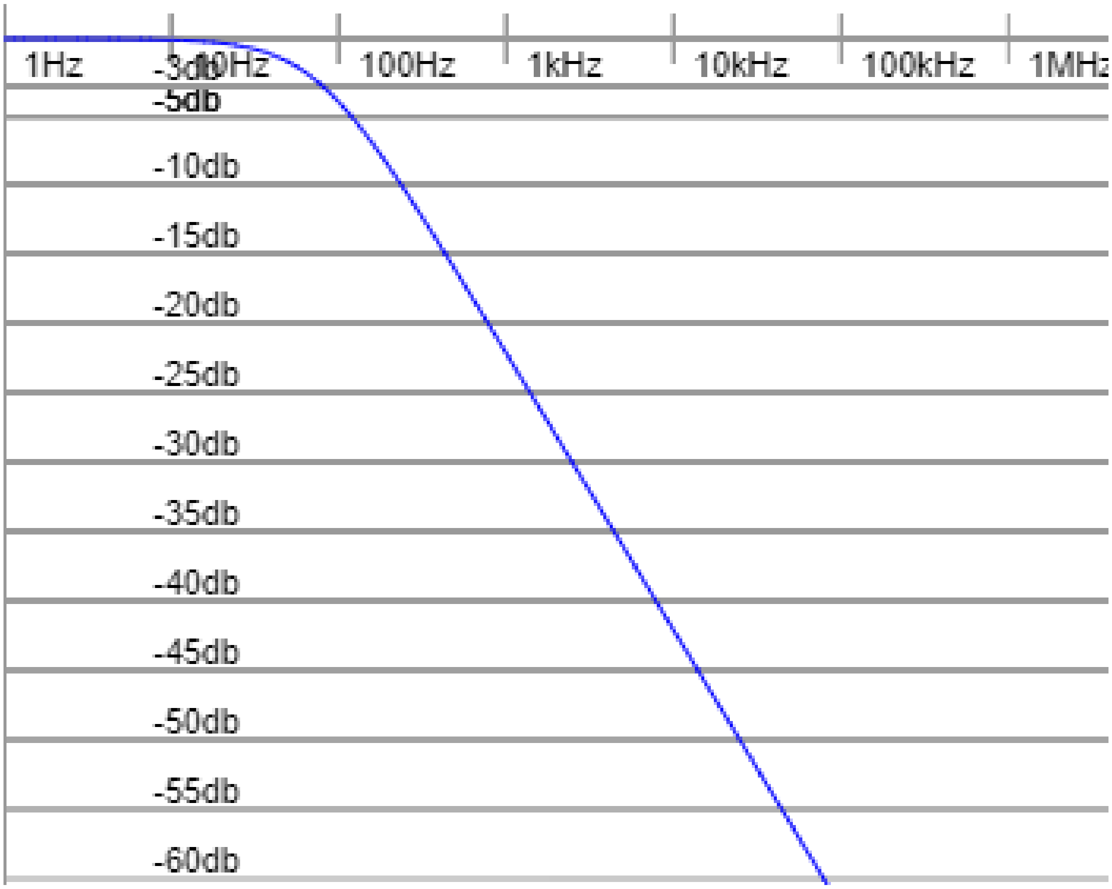

Figure 4.7: Bode plot of first-order RC filter with R = 220K and C = 10 nF

4.3 Modular potentiostat

4.3.1 Introduction

There are several challenging problems associated with turning a single-channel potentiostat design into a multi-channel potentiostat. A couple of them include the current source and unintentional actuation problems.

Current Sources Problem

The problem comes from a typical single-channel potentiostat design where there is one current measurement node (current sink) and multiple current sources.

For instance, a current measurement unit measured 500 nA shown in Figure 4.8. Scenario 1, 500 nA is a summation of 200 nA from I_1, 200 nA from I_2 and 100 nA from I_3. This means, WE1, WE2 and WE3 are working, but WE3 does not work as well as the other electrodes. Scenario 2, 500 nA is a 500 nA from I_1 and the rest produce zero current. In this scenario, WE1 is the only electrode that is working. In both scenarios, I_T is measured 500 nA but WE1, WE2 and WE3 are completely different.

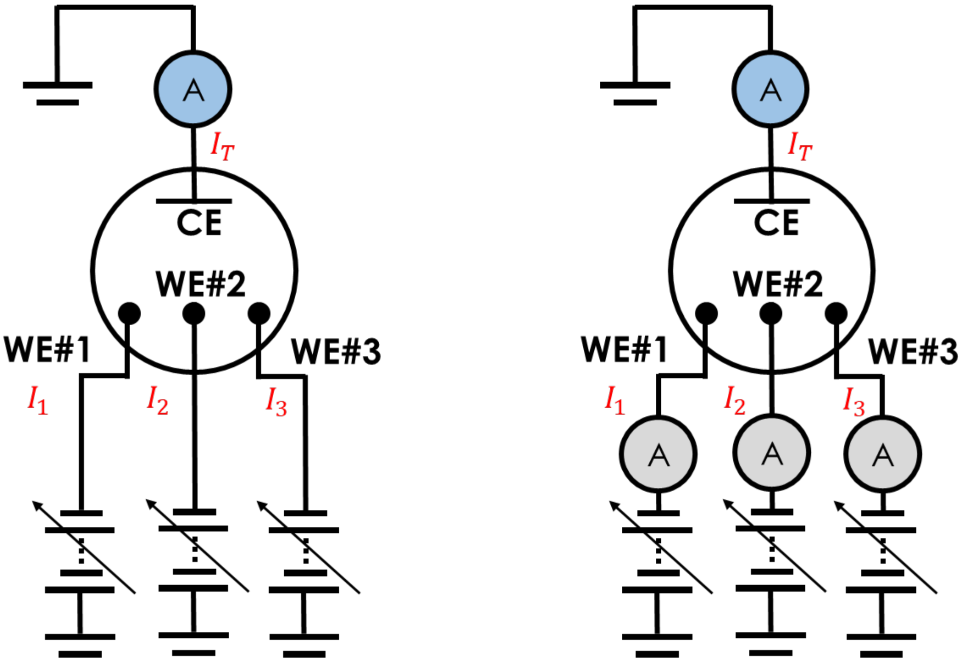

Single current measurement Multiple current measurement

Figure 4.8: Left) potentiostat with a single current measurement unit. Right) potentiostat with multiple current measurement units.

In order to get a full picture of how a multi-electrode electrochemical works, a multi-channel potentiostat needs an individual current measurement unit in every single channel.

Unintentional Actuation Problem

A traditional potentiostat output can be set between a certain range of voltage (e.g., $\pm 4V$). However, in the multi-electrode setup sets an electrode output to 0 V or ground can yield unexpected consequence. For instance, in this 4-electrode setup, if a user intends to actuate only WE3 and CE, the user will unintentionally actuate WE1 and WE2. This is due to inability to disconnect WE1 and WE2, there will be current flow through WE1 and WE2 shown in Figure 4.9.

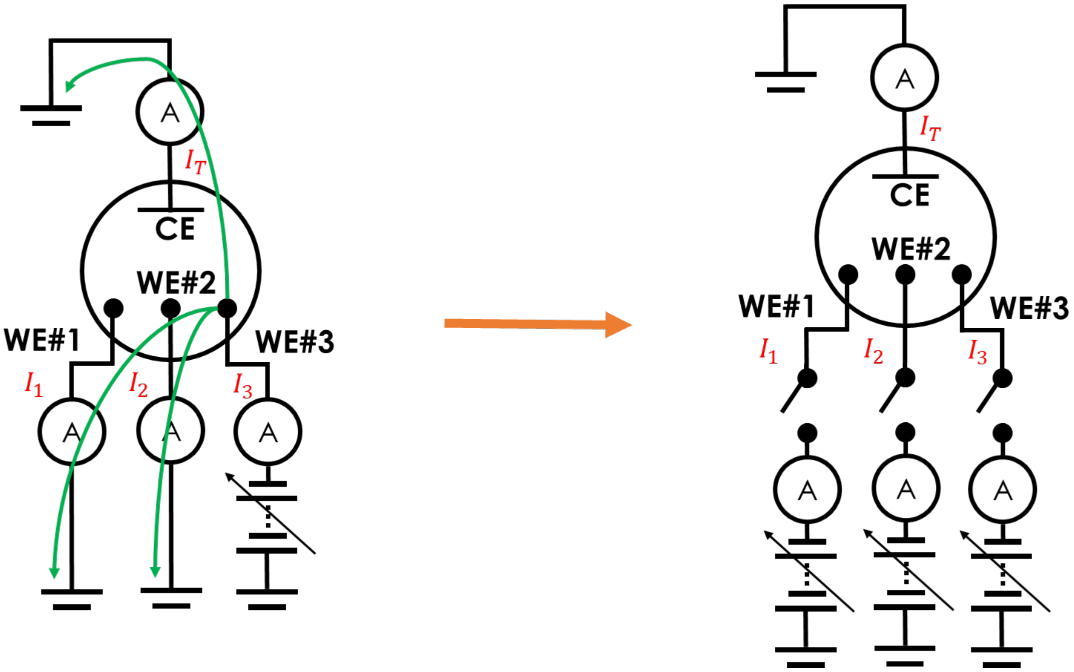

Figure 4.9: Left) A multi-channel potentiostat without an individual switches. Right) the proposed design with switches in every channel

To prevent this problem, an individual switch must be added to every single channel of a multi-channel potentiostat.

4.3.2 System Design

The target application of this multi-channel potentiostat is the Ion pump [Selberg et al.,] which features 26 electrodes with a set of requirements:

- Able to supply voltage range from $\pm 2V$
- Able to measure current in nA range
- Able to interface with external software (e.g., Matlab, Python, etc.)
- Scalable up to at least 26 channels
- Each channel is able to change stage to high-impedance/not connected stage

The modular multi-channel potentiostat consists of two components, one Base unit and up-to eight Stackable boards shown in Figure 4.10.

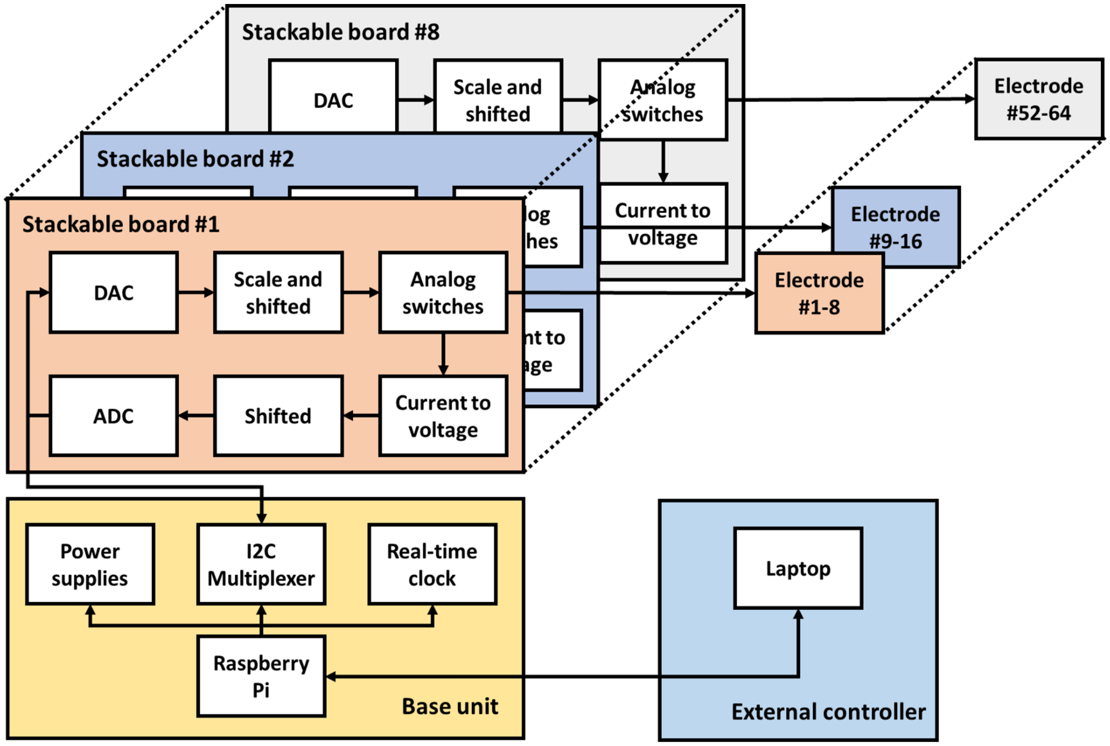

Figure 4.10: The modular multi-channel potentiostat block diagram. The diagram shows up to 8 stackable boards can be add to the system, expand number of channel to 64.

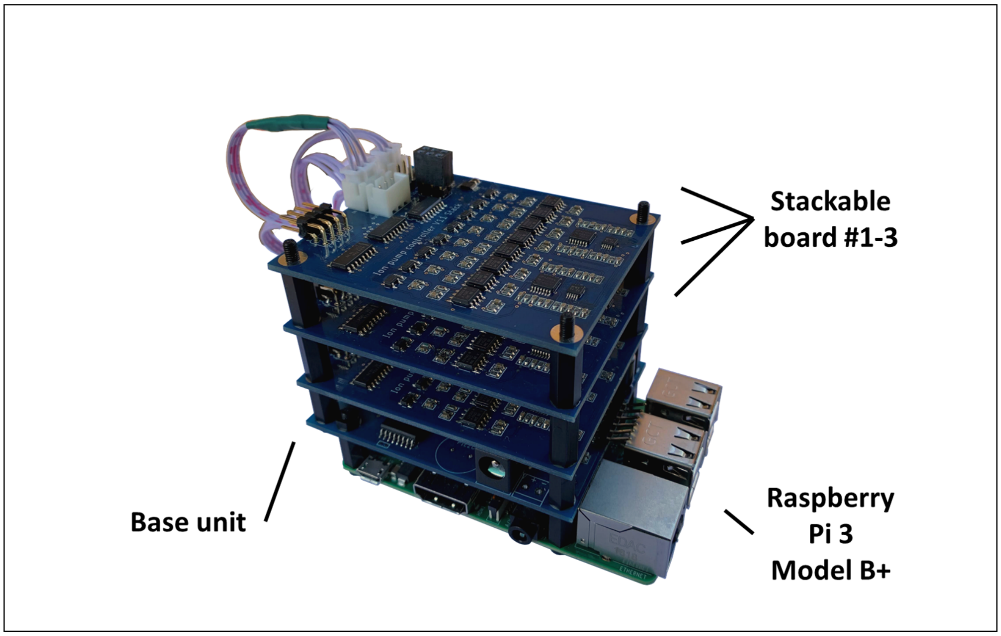

(a) The assembled system

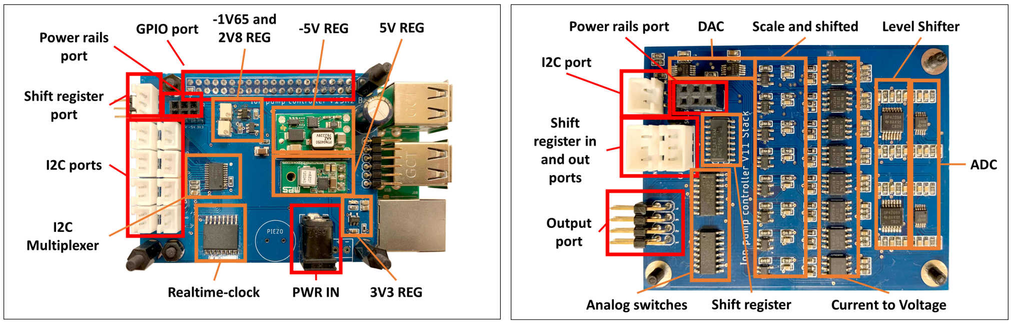

(b) Base unit

(c) Stackable board]

Figure 4.11: (A) A 24 channels assembled unite with three stackable boards (B) The base unit attached to the Raspberry Pi 3 B+ (C) Stackable board. For (B) and (C), the main electronic Integrated circuit (IC) are highlighted in Orange and connection ports are highlighted in Red.

Base Unit

The base unit contains the voltage regulators interfacing with the stackable boards. It consists of a single-board computer (SBC) and a custom Hardware Attached on Top (HAT) printed circuit board (PCB) that provides an interface between the SBC and the stackable boards, as well as supplying the necessary power. The SBC is a low-cost Raspberry Pi 3 Model B+ computer that has Wi-Fi, Ethernet, 40-GPIO connectivity, and runs Raspbian OS version 10 (Buster) and Python 3.5. The multi-channel potentiostat has two operation modes, Standalone (that operate the multi-channel potentiostat independently) and Application Program Interface (API) mode (the multi-channel potentiostat is externally controlled). The HAT is designed in the form-factor of a Raspberry Pi and can accommodate up to eight stackable boards. The HAT contains +5, -5, +3.3, +2.8, and -1.65 V voltage regulators, TCA9548A, I2C multiplexer, DS3231 real-time clock, and a backup battery. It can interface with a Raspberry Pi via GPIO pin headers, one I2C communication bus, and one shift register bus.

Stackable Boards

Each stackable board contains eight analog potentiostats with adjustable voltage sources, built-in ammeters, analog switches, and digital communication buses to the base unit. This is essentially taken from the design of single-channel potentiostat mentioned earlier in chapter 4.2. Each board is powered by a six-pin stacking header and interfaces with a Base unit via one of a 4-pin I2C cables. A Shift register is either chained with a custom-designed HAT, or with another stackable board's port. The most basic configuration consists of one base unit and one stackable board, but the system has a maximum of eight stackable boards for each single base unit. As a result, the multi-channel potentiostat support ranges from a minimum of 8 channels to a maximum of 64 channels.

One feature that distinguishes the multi-channel potentiostat from other potentiostat designs to date is the ability to disconnect (open-circuit) individual output channels. The analog switches are added to connect or disconnect individual electrodes, altering electrode configurations automatically. Maxim Integrated MAX326 is a quad CMOS Analog switch, Single Pole Single Throw (SPST), and Ultra-Low-Leakage. It allows the multi-channel potentiostat to connect or disconnect to the electrode independently. The analog switches have 10 pA maximum leak current and 2 pC typical charge injection. In a low current application, leak current from a switch could unintentionally actuate the electrochemical device making these ultra-low leak characteristics crucial.

The input stage of the multi-channel potentiostat measures the current from an adjustable voltage source that consists of an ammeter and Analog-to-Digital Converter (ADC). Unlike traditional potentiostat designs that use a transimpedance amplifier for current measurements, our multi-channel potentiostat has a shunt resistor. This approach might lower the accuracy but it allows simultaneous recording of multiple voltage sources. For instance, the multi-channel potentiostat with eight channels can operate four independent, two-electrode systems simultaneously, where four standard potentiostats would be required for the same setup. Additionally, the benefits of the multi-channel potentiostat are unlike traditional potentiostats because it can interface with electrochemical cells with three or more electrodes.

4.3.3 API

In many applications [Selberg et al., 2020a], instead of applying a predefined voltage (wave) in an open-loop fashion, the system needs to interact with the environment in real-time closed-loop form through feedback. Thus, an API is needed to provide remote control ability to the multi-channel potentiostat.

On the multi-channel potentiostat side (server-side), it a Python script contains low-lever drivers used for control the multi-channel potentiostat, data logging system and UDP server. The UDP server is listening for command for an external laptop shown in Figure 4.12.

UDP is picked due to simplicity and accessibility. Any programming languages can be interface with the multi-channel potentiostat by sending and receiving UDP message.

To simplified this process, the author created an API library in Python and MATLAB wrapper which uses the Python API. These Python and MATLAB API wrappers allow 3rd party developers to interface with a multi-channel potentiostat in less than ten minutes.

This functionality of a multi-channel potentiostat will be discuss in further detail in section 5.

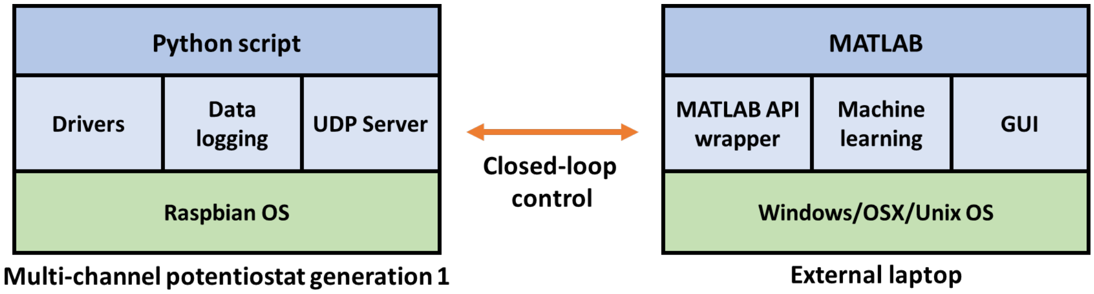

Figure 4.12: Networking architecture of modular multi-channel potentiostat. The potentiostat running a Raspbian OS and Python script with an UDP server. The external laptop run in MATLAB with a API (MATLAB API wrapper)

4.3.4 Cyclic Voltammetry Validation

The multi-channel potentiostat's performance during sensitive cyclic voltammetry (CV) experiments is validated against a commercial system (Autolab PGSTAT128N). For both systems, we run linear sweep voltammetry tests between -0.9V and 0.5V. Figure 4.13a shows the schematic representation of the experimental setup. The multi-channel potentiostat used a palladium nanoparticle coated gold (Au/PdNP) working electrode (250 μm x 250 μm) and an Ag/AgCl pellet counter electrode (2 mm dia. x 2 mm thick) in 50 mM NaCl solution (pH 7). The palladium nanoparticle coating is chosen due to palladium's ability to reversibly form palladium hydride by absorbing hydrogen (H) when negatively biased in the presence of water [Grdeń et al., 2008]. The experiment was conducted using three different scan speeds, 10, 50, and 100 mV/second. The 100mV scan rate shows the expected peaks for surface oxide formation (positive peak near 0.15 V), surface oxide reduction (negative peak near -0.2 V), hydrogen adsorption and absorption forming palladium hydride (peak near -0.65 V), and H desorption (positive peak near -0.75) shown in Figure 4.13d. The CV sweeps with this system are consistent with the PGSTAT128N over a range from 10 mV/s to 100 mV/s shown in Figure 4.13b - 4.13d. The positive peak indicating H desorption is shifted when using the multi-channel potentiostat system by 50 mV.

This is explained by the combination of environmental noise and error from the multi-channel potentiostat's output stages. The environment noise can be minimized by better shielding of the potentiostat which includes cables and an electrochemical cell. The output stage of the multi-channel potentiostat can be improved with changing a 12-bit DAC to a DAC with higher resolution, such as 16-bit, and adding an additional calibration step.

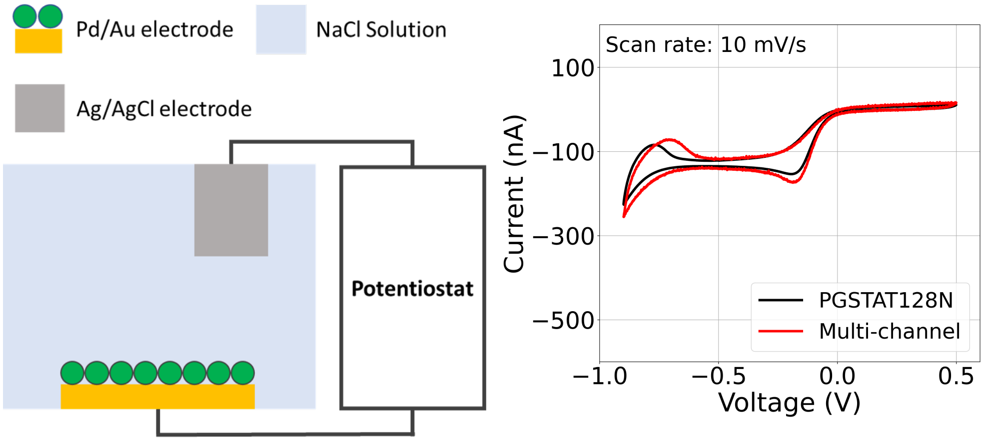

(a) NaCl Experiment setup

(b) CV 10 mV/s

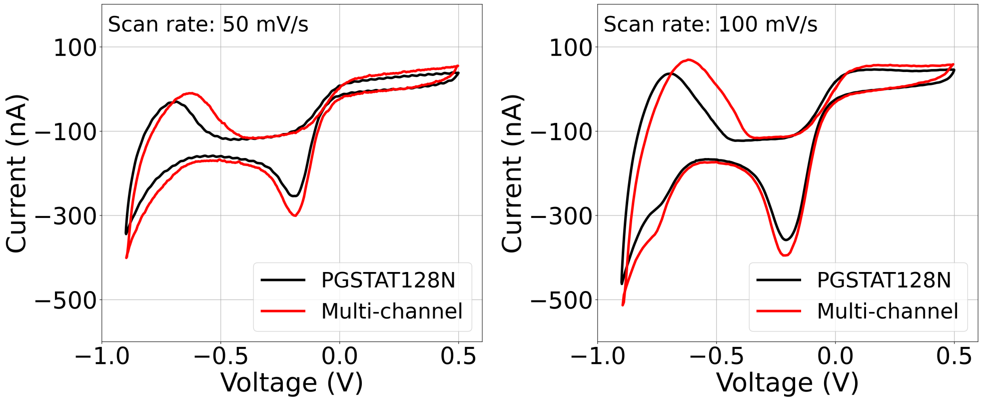

(c) CV 50 mV/s

(d) CV 100 mV/s

Figure 4.13: (A) Experimental CV setup with Pd functionalized Au electrode vs AgCl pellet electrode in NaCl solution. (B-D) CV of Pd NP/Au vs AgCl with various scan rates recorded with a commercial potentiostat and the multi-channel potentiostat device. (B) 10 mV/s scan rate (C) 50 mV/s scan rate (D) 100 mV/s scan rate.

4.3.5 Ion Pump Amperometry

Amperometry is a technique used to study redox reactions by providing a DC voltage between two electrodes and measuring the generated current. Ion pumps are bioelectronic devices that can manipulate physiological processes *in-vitro* and *in-vivo* delivering ions and small molecules directly to living matters [Selberg et al.,] [Jia et al., 2020a]. The devices operate by applying a DC voltage to the electrodes position in a reservoir and a target electrolyte, where ions are driven from the reservoir to the target through an ionic conducting material. Figure 4.14a shows the experimental setup where the ion pump has 1 electrode in the reservoir and 9 individual electrodes in the target. The multi-channel potentiostat controls the ion pump and records the current with a 15Hz sampling rate. In contrast, the KEYENCE, BZ-X710 fluorescent microscope images the experiment using a 0.5 Hz recording rate through a GFP filter. The multi-channel potentiostat is connected to nine working electrodes and one counter electrode of the ion pump. It is programmed to generate a square wave with amplitude +1.4 and -1.4 V and a period of 30 seconds where it cycles from the first to the ninth electrode. While one electrode is active, the rest of the electrodes are on open-circuit mode. Here we measure the proton concentration (pH) using fluorescence microscopy simultaneously while the voltage is swept. The target well is filled with pH sensitive fluorescent dye(SNARF®-1). In this process, each proton that moves from the reservoir to a certain electrode in the target results in an electron collected in the corresponding circuit channel. Figure 6B shows the fluorescence intensity sampled from each electrode, which increases with fewer protons in the solution. By applying a negative voltage, the ion pump moves protons from the target to the reservoir resulting in higher fluorescence intensity and vice versa. The current profiles synchronizing with the changes of fluorescence intensity in

Figure 4.14C indicates that the multi-channel potentiostat can run amperometry experiments and provide reliable current data. This experiment does not use electrodes 4 and 6 of the ion pump. Overall, the amperometry results show good agreement with the actuation voltage and the fluorescent results.

4.4 Non-modular potentiostat

4.4.1 Introduction

The major downside of the modular multi-channel potentiostat is the problematical assembly process and tall footprint. The modular potentiostat requires a set of stand-offs, and two inter-board cables route between each stackable board. These prove to be a challenging part of the assembly process. In addition, most applications require less than 16 channels making the modular design not as helpful as intended. Therefore, the author designed the non-modular 16-channel multi-channel potentiostat. The non-modular multi-channel potentiostat is packed with similar electrical specifications but also includes several minor improvements.

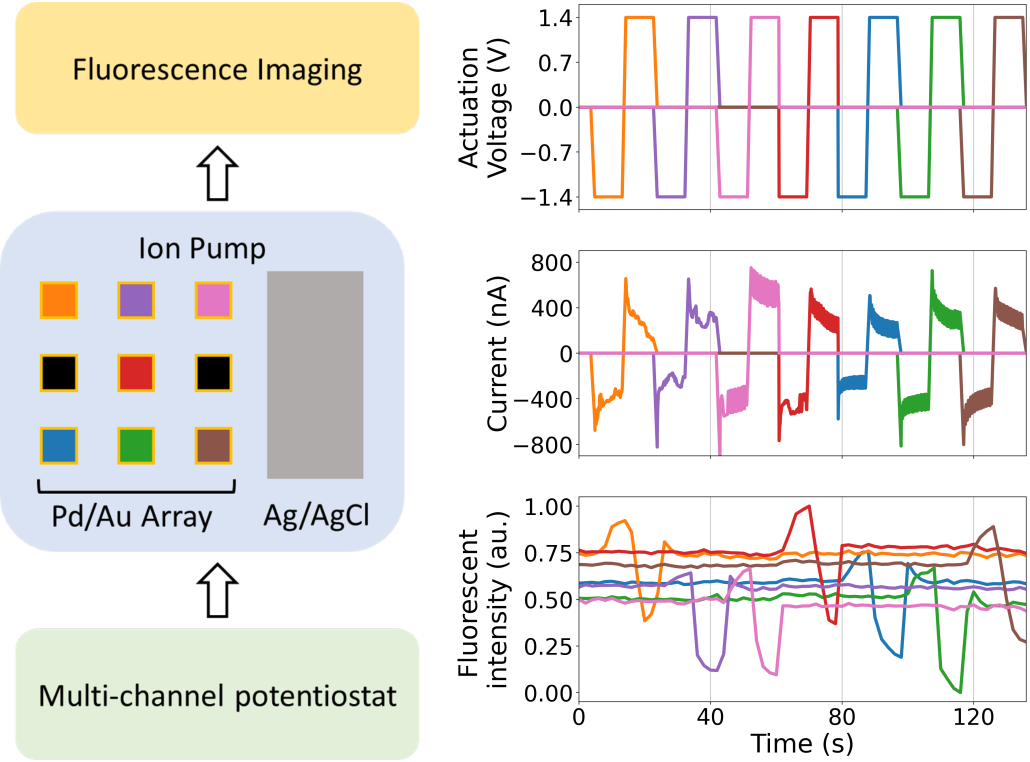

(a) Spatial map of the Ion pump **(b)** Fluorescent and Amperometry results

Figure 4.14: (A) Physical configuration of electrode placement of the ion pump. KEYENCE, BZ-X710 fluorescence microscope is used to image proton concentration (pH) every 2 seconds. Various colors represent different working electrodes and the black color indicates unused electrodes. (B) Actuation voltage and Amperometry results of in-house Ion pump and normalized fluorescent intensity correspond directly to Cl^- ion concentration. The output shows that Cl^- ion concentration changes according to the amperometry results from the ion pump.

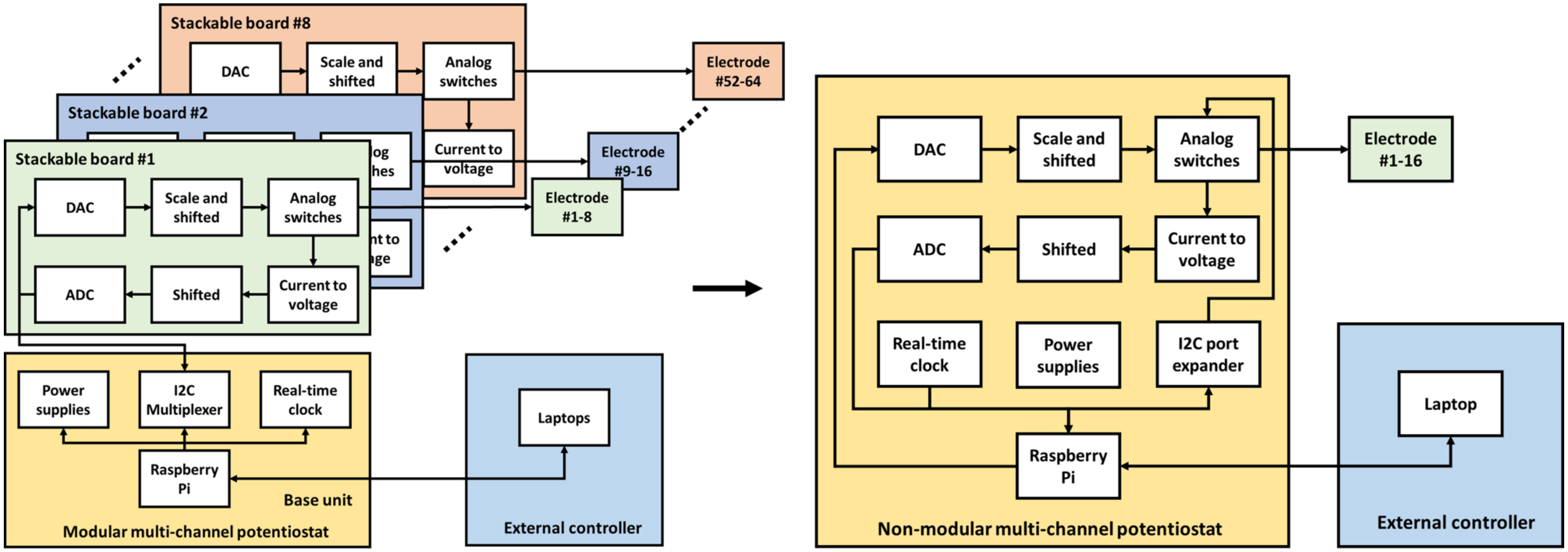

Figure 4.15: High-level comparison between modular and non-modular multi-channel potentiostat. The non-modular version encapsulated every components within the same circuit board.

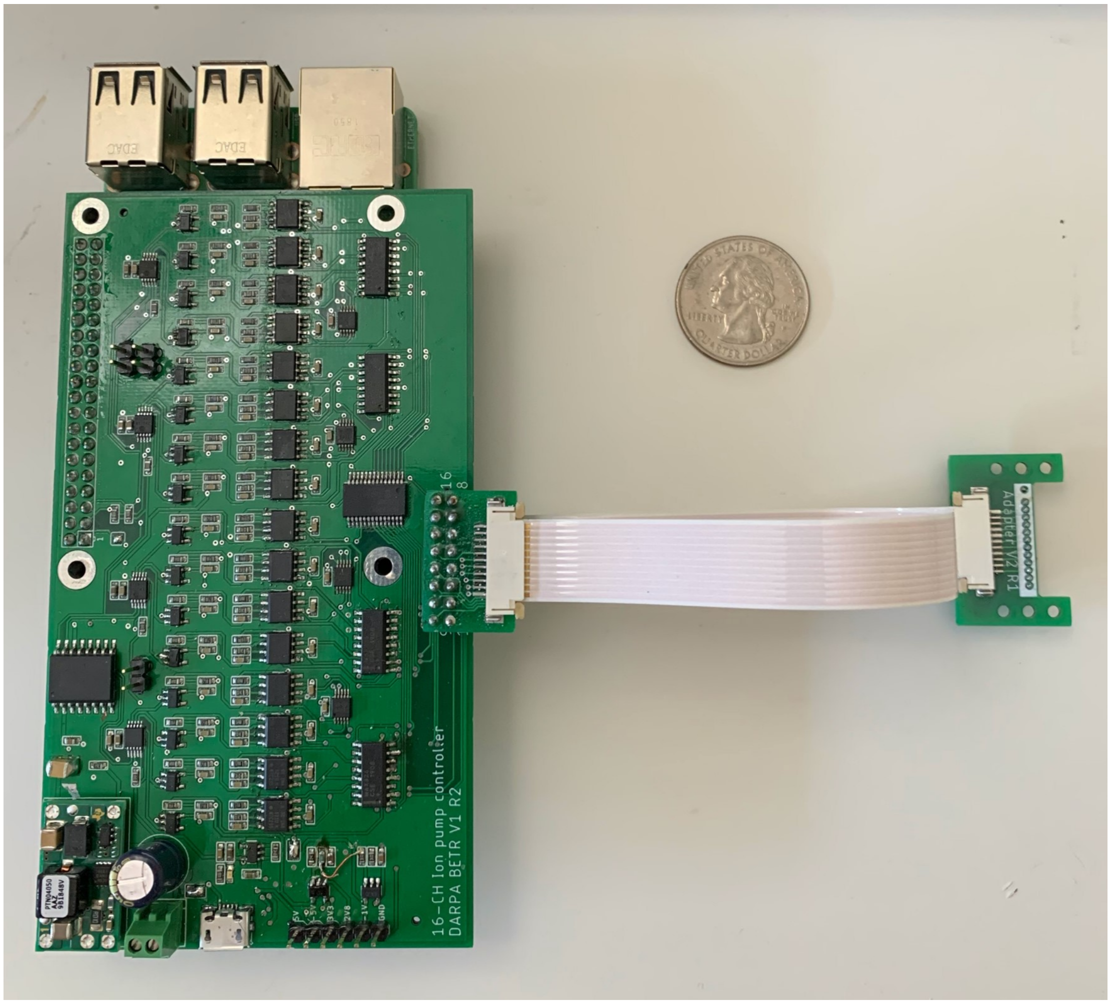

Figure 4.16: The non-modular multi-channel potentiostat with an custom adapter and interface board for the Vertical ion pump.

Potentiostat	Number of channel	Modular	Inter-board cable	GPIOs	PCB assembly	Dimension (mm)
Modular	8-64	Yes	Yes	Shift register	Stack	72.5 x 57 x 40 - 72.5 x 57 x 140
Non-Modular	16	No	No	I2C ports expander	Single piece	120 x 68 x 25

Table 4.1: Comparison between Modular and Non-modular potentiostat

4.4.2 System design

In this design, the author addresses the difficulty of the assembly process by designing the whole system in a single-piece circuit board by limiting the number of channels, simplifying the current measurement circuit and change the shift-register to an I2C port expander. This approach eliminates a need for an extra inter-board cable and thus reduces the height of the potentiostat to 25 mm instead of up to 140 mm.

Analog switches

The modular design employed a shift-register technique to expand a Raspberry Pi GPIO to control the analog switches. In this design, four shift-register were replaced with a single Microchip, MCP23017, 16 ports I2C GPIO expander shown in Figure 4.17. At the same time, eliminating the need for an extra shift-register bus by shared the I2C bus with ADC and DAC.

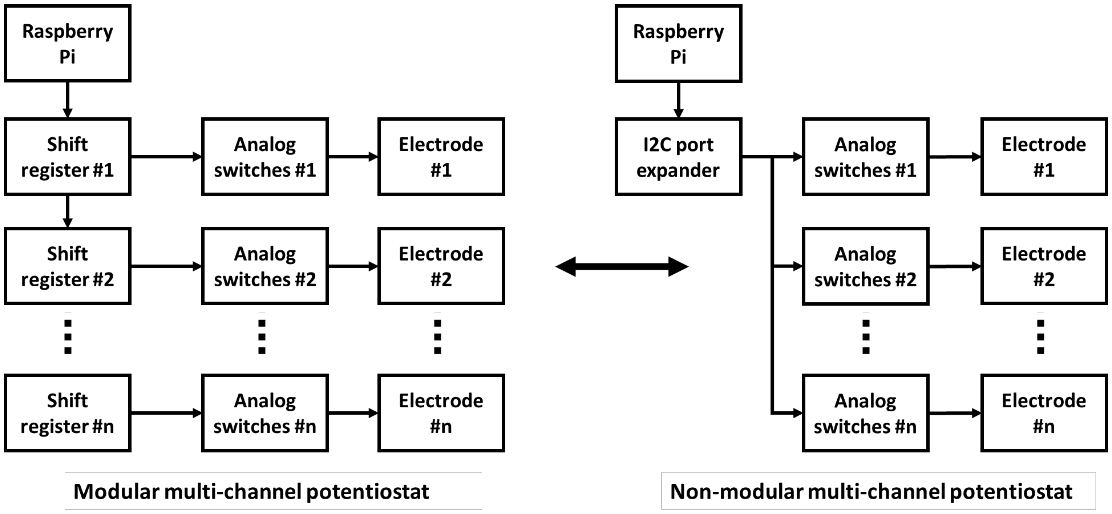

Figure 4.17: Comparison of modular and non-modular multi-channel potentiostat analog switches design. The modular potentiostat utilize shift register as a way to expand GPIOs however the non-modular one uses I2C port expander IC instead.

Current measurement

The modular design used an extra Op-amp to perform shift-scale current measurement output from $\pm 1.65V$ to $0 - 3.3V$. This new design utilizes the reference functionality of an INA112, Instrumentation amplifier to shift output from $\pm 1.65V$ to $0 - 3.3V$ shown in Figure 4.18. This approach eliminates a need for an extra shift-scale Op-amp and first-order filter. However, the lack of a first-order filter does not pose any significance in the potentiostat performance.

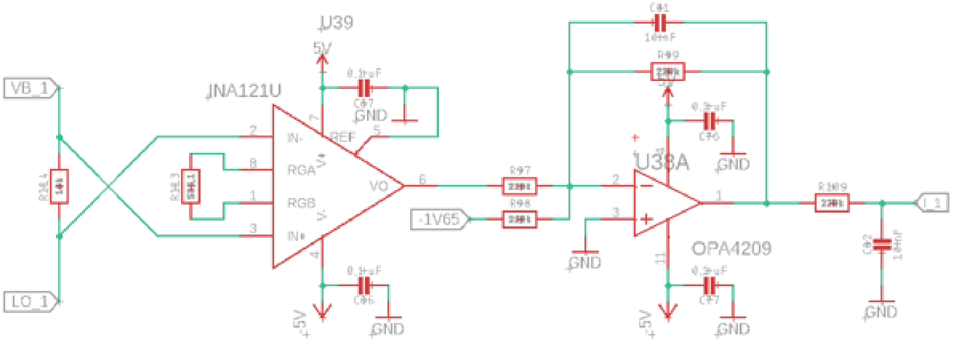

(a) Modular multi-channel potentiostat

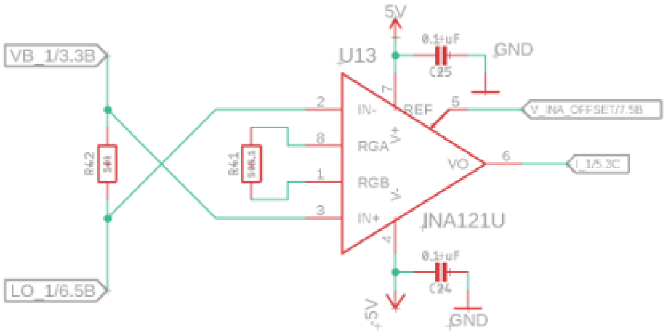

(b) Non-modular multi-channel potentiostat

Figure 4.18: Comparison of modular and non-modular multi-channel potentiostat current measurement circuit. The non-modular potentiostat opted for a simpler design by using the instrumentation amplifier internal reference to level-shifted a output signal. This design choice eliminate need for an extra Op-amp.

4.4.3 API and Graphic interface

Similar to the modular multi-channel potentiostat, the non-modular multi-channel potentiostat also features an API that allows external remote control of the device. However, a minor change in protocol from a UDP to a TCP connection demonstrates to be more reliable and suitable for real-time experiement. The networking architecture of the non-modular potentiostat is shown in Figure 4.19. One disadvantage of the previous potentiostat design is that a user needs to control the potentiostat via command-line. This can be difficult for a non-technical user such as a biologist. Thus, the author had developed a graphic interface software shown in Figure 4.20 that allows a user without a technical background to able to control the non-modular potentiostat.

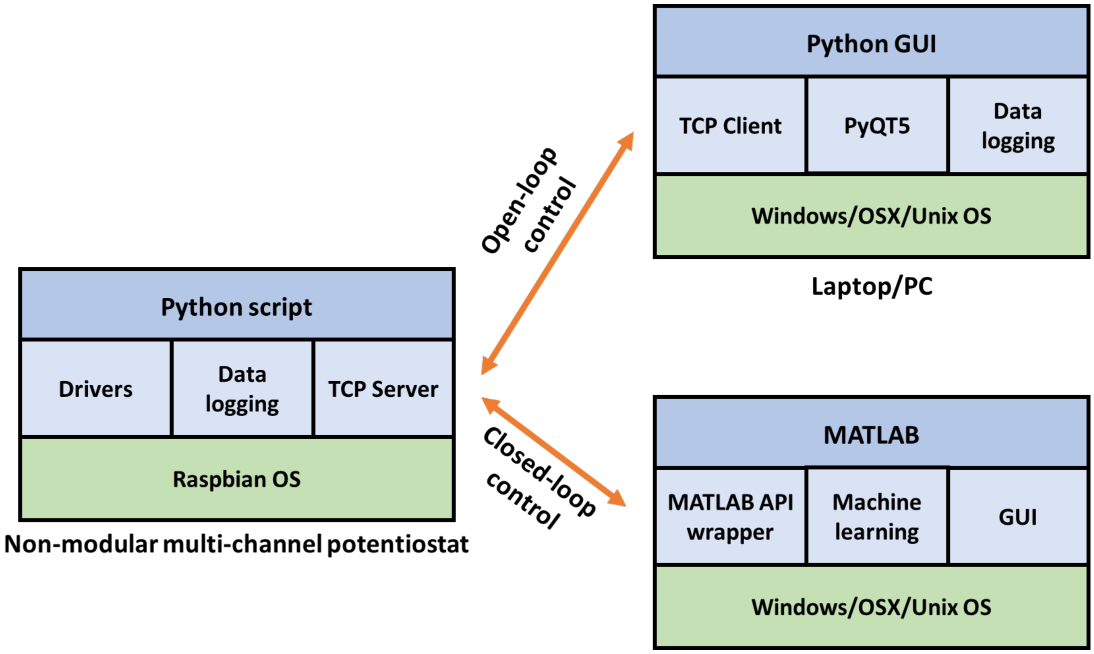

Figure 4.19: Networking architecture of non-modular multi-channel potentiostat. The non-modular potentiostat switch to TCP connection over UDP to improve reliability. The Python GUI also developed for a more user-friendly control interface.

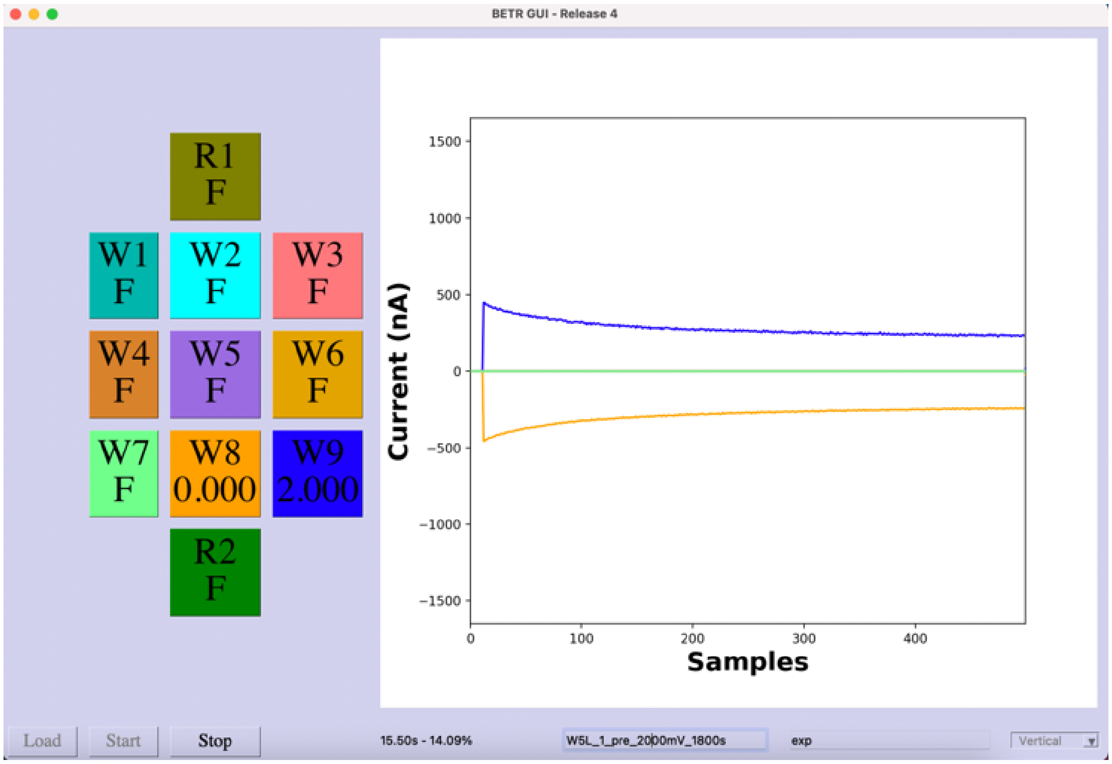

15.50s - 14.09%

W5L_1_pre_2000mV_1800s

exp

Figure 4.20: Graphic interface (GUI) software for the non-modular multi-channel potentiostat. The software allows user to run a predefined protocols, plot real-time current measurement and directly store a current result on a user computer.

4.5 Conclusion

This chapter encompasses novel potentiostat designs, consideration, and evaluation start from scratch. First, the author explores a basic design of potentiostat, a single-channel potentiostat. The single-channel potentiostat design consists of one output and one input stage. The output stage is designed to accommodate a wide range of output ± 4V to support both aqueous and non-aqueous solutions. In the input stage design, the work explores both advantages and disadvantages of different current measurement techniques primary for 1 nA to 1 μA range (e.g., Shunt resistor and Transimpedance amplifier)

Second, the author takes the single-channel potentiostat input and output stage designs and incorporates them into a modular, multi-channel potentiostat. However, the process is not straightforward to make multiple copies of a single-channel design. The current sources and unintentional actuation problems arise. These unique problems only happen to a multi-channel potentiostat and a black-box multi-electrode electrochemical cell (e.g., an array of ion pumps). As a result, the author concluded that the multi-channel potentiostat design needs to have a current measurement unit in every channel to mitigate the current sources problem and ultra-low leak switch in every channel to mitigate the unintended actuation issue.

Later, the author designed the modular system by separating the design into a base unit and a stackable board where the base unit contains supplement circuity such as the power supplies, real-time-clock, and the stackable board consisting of eight-channel potentiostat circuity. This modular design allows the system to be scalable from 8 to 64 channels. The author also designed another version of the multi-channel potentiostat, a non-modular version, that tailors to general applications that need less than 16 channels and drastically reduces the assembly process difficultly. Both modular and non-modular multi-channel potentiostat were evaluated against a benchtop potentiostat and showed a comparable result.

Finally, the author developed the software for both modular and non-modular multi-channel potentiostats. The software had two operation modes, standalone and external control. A standalone mode is a regular software like other commercial potentiostats, but externally control mode offers a more complex and resource intense control algorithm to be ran on an external machine and send commands to a multi-channel potentiostat. This characteristic is another unique feature of the design, which is crucial to a more sophisticated setup shown in the next chapter.

Chapter 5

System integration

5.1 Introduction

The multi-channel potentiostats were used in experiments with ion pumps in both *in-vitro* and *in-vivo* experiments. In *in-vitro* experiments, the multi-channel potentiostats are demonstrated in open-loop mode (standalone) and eventually a machine learning, closed-loop control. In *in-vivo* experiments, the multi-channel potentiostats are also used to actuate *in-vivo* ion pump in open-loop mode. Various ion pumps experiment setups and different variants of ion pumps are also described in 5.2

Author contribution: This project is in collaboration with John Selberg, Manping Jia, Harika Dechiraju, Chunxiao Wu, Nebyu Yonas, and Sergio Cordero from Rolandi's lab, Mohammad Jafari and Giovanny Marquez from Gomez's group, Juanita Mathews, Alexander Flora, Sophia Jannetty, Miranda Diberardinis from Levin's group, and Maryam Tebyani, Gordon Keller, Prabhat Baniya, Thomas Thomsen from Teodorescu's lab.

John Selberg, Manping Jia, Harika Dechiraju, and Chunxiao Wu are responsible for designing ion pumps and microfluidic systems. John Selberg, Manping

Jia, Harika Dechiraju, Chunxiao Wu, Nebyu Yonas, and Sergio Cordero also manufacture and tested ion pumps. Thomas Thomsen and I designed and prototyped the multi-channel potentiostat, and also developed the software and planned the system integration for *in-vivo* and *in-vitro* experiment. Maryam Tebyani, Gordon Keller, Prabhat Baniya and I developed the software and planned the system integration for the *in-vitro* experiment. Juanita Mathews, Alexander Flora, Sophia Jannetty, and Miranda Diberardinis prepared and cultured various hiPSCs cell lines, and handled the cell cultures. John Selberg, Manping Jia, Harika Dechiraju, Chunxiao Wu, Juanita Mathews, Alexander Flora, Sophia Jannetty, Miranda Diberardinis, and I also performed the majority of *in-vitro* experiments and measurements. Mohammad Jafari and Giovanny Marquez architecture and implement closed-loop control algorithm in *in-vitro* experiments both with cell cultures and fluorescent dyes. Maryam Tebyani, Gordon Keller, Prabhat Baniya, Manping Jia and I also performed most of the *in-vivo* experiments.

Publications:

- Pansodtee, P., Selberg, J., Jia, M., Jafari, M., Dechiraju, H., Thomsen, T., Gomez, M., Rolandi, M. and Teodorescu, M. (2021). The multi-channel potentiostat: Development and evaluation of a scalable mini-potentiostat array for investigating electrochemical reaction mechanisms. PLoS ONE, 16(9): e0257167

- Selberg, J., Jafari, M., Mathews, J., Jia, M., Pansodtee, P., Dechiraju, H., Wu, C., Cordero, S., Flora, A., Yonas, N. and Jannetty, S., 2020. Machine Learning-Driven Bioelectronics for Closed-Loop Control of Cells. Advanced Intelligent Systems, 2(12), p.2000140.

- Jia, M., Dechiruji, H., Selberg, J., Pansodtee, P., Mathews, J., Wu, C., Levin, M., Teodorescu, M. and Rolandi, M., 2020. Bioelectronic control of chloride ions and concentration with Ag/AgCl contacts. APL Materials, 8(9), p.091106.

- Jafari, M., Marquez, G., Selberg, J., Jia, M., Dechiraju, H., Pansodtee, P., Teodorescu, M., Rolandi, M. and Gomez, M., 2020. Feedback control of bioelectronic devices using machine learning. IEEE Control Systems Letters, 5(4), pp.1133-1138.

5.2 System Architecture

The multi-channel potentiostat is designed to have two operation modes: open-loop (standalone) and closed-loop (remotely control). Figure 5.1 shows an experimental setup where the multi-channel potentiostat connects to an ion pump array. The system alters the ion concentration in either a dye solution or a cell culture media. Later, the change in fluorescence can be captured via a fluorescence microscope. In open-loop experiments, the multi-channel potentiostat actuates the ion pump with a predefined sequence or protocol. However, in closed-loop control, a machine learning algorithm takes a fluorescence image, calculates how much the ion pump should be actuated to reach a set goal, and then sends those values to the multi-channel potentiostat.

In this chapter, four variations of the ion pumps are used in the experiments: horizontal ion pumps (1st and 2nd generation single-ion and multi-ion) and vertical ion pumps.

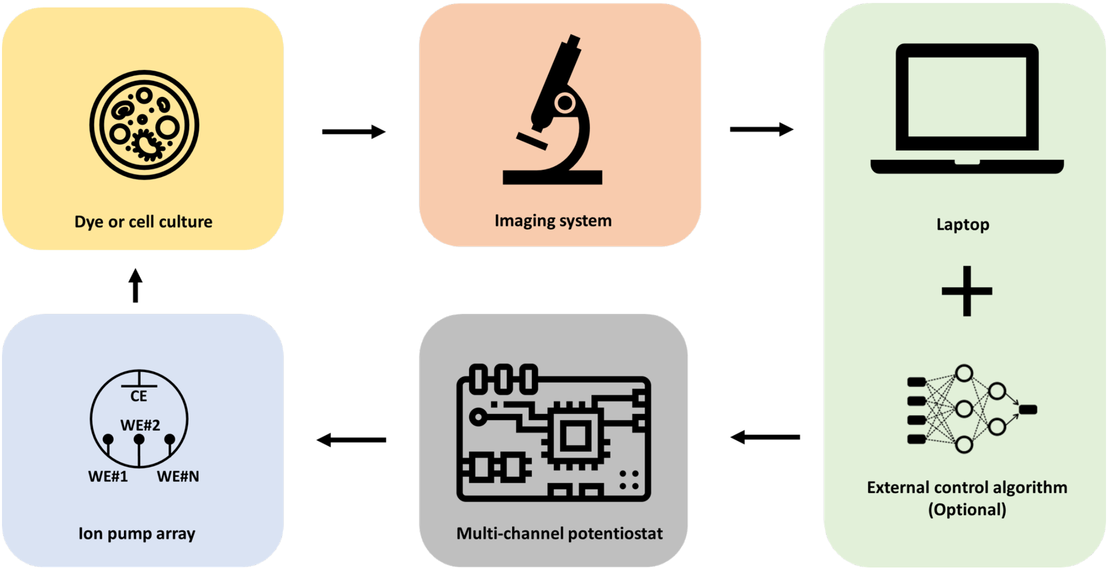

Figure 5.1: High-level system block diagram of experiment setup. An external control algorithm is optional and only required for closed-loop control experiments

5.2.1 Horizontal Ion Pump

Single-Ion - First Generation

The first generation of horizontal ion pumps consists of an array of 20 ion pumps and 20 working electrodes, and two counter electrodes with integrated microfluidic channels packed on a transparent substrate size 60 x 22.5 mm shown in Figure 5.3a. Each ion pump (pixel) is a 100 μm x 100 μm working electrode aligned in a 5x4 grid with a 250 twenty pitch. Figure 5.2 shows a cross sectional layer of a Single-ion, horizontal ion pump. By applying a voltage between a working electrode and auxiliary electrode (counter-electrode), an ion pump would transport ions between reservoir and target solution. Depending on the ion-selective membrane material, an ion-specific pump such as a H^+, K^+, Na^+, or Cl^- ion pump can be produced.

Without a custom adapter, the ion pumps and the multi-channel potentiostat cannot directly interface with each other. This is due to mismatched interface;

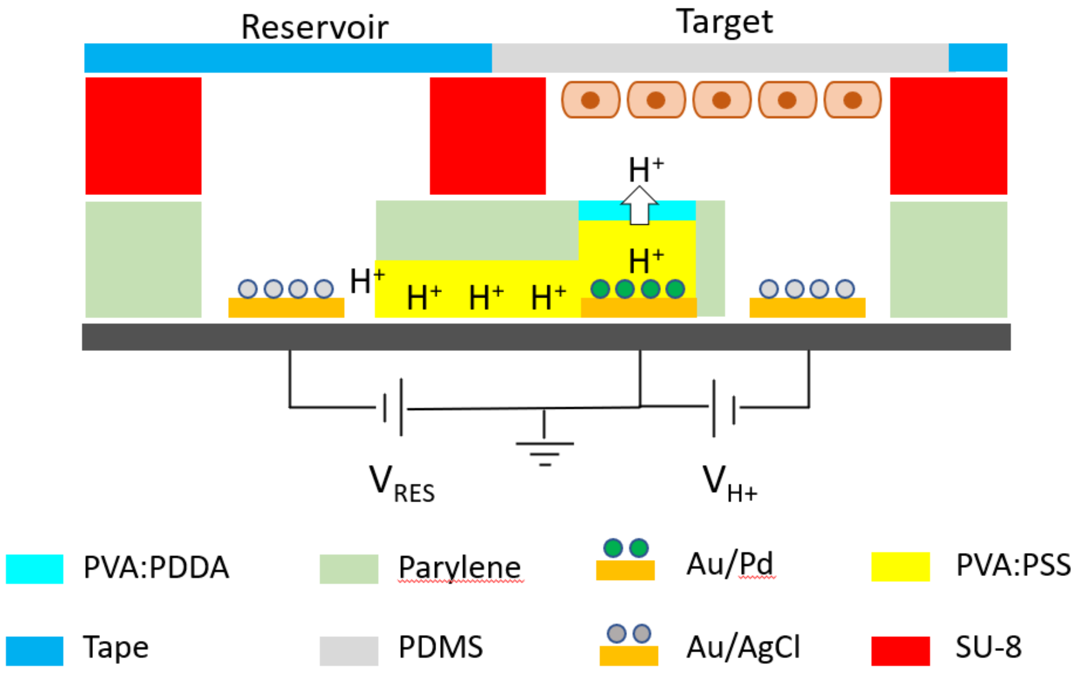

Figure 5.2: Cross section of Single-ion, horizontal ion pump.

the ion pump has gold contact pads while the multi-channel potentiostat has a pin header.

We designed an interface board consisting of 22 spring-loaded pins and a 22-pin pin header. The spring-loaded pin (Mill-Max Manufacturing Corp, 825-22-010-10-001101) has gold-coated contact, a stroke length of 2.28 mm, and a maximum force of 60 grams, allowing for tight contact with an ion pump's gold contact pad without putting too much pressure on an ion pump. Since ion pumps are very fragile, this particular spring-loaded pin was picked due to its low maximum force. The PCB arranges the spring-loaded pins in a 5 x 4 grid with 2.54 mm pitch for 20 working electrodes and two more for the reference electrodes. It also features six mounting holes for clamping with an acrylic holder shown in Figure 5.4b.

We also designed an acrylic holder that holds an ion pump and an interface board together and is mounted on two microscope systems (i.e., EVOS, FL Auto

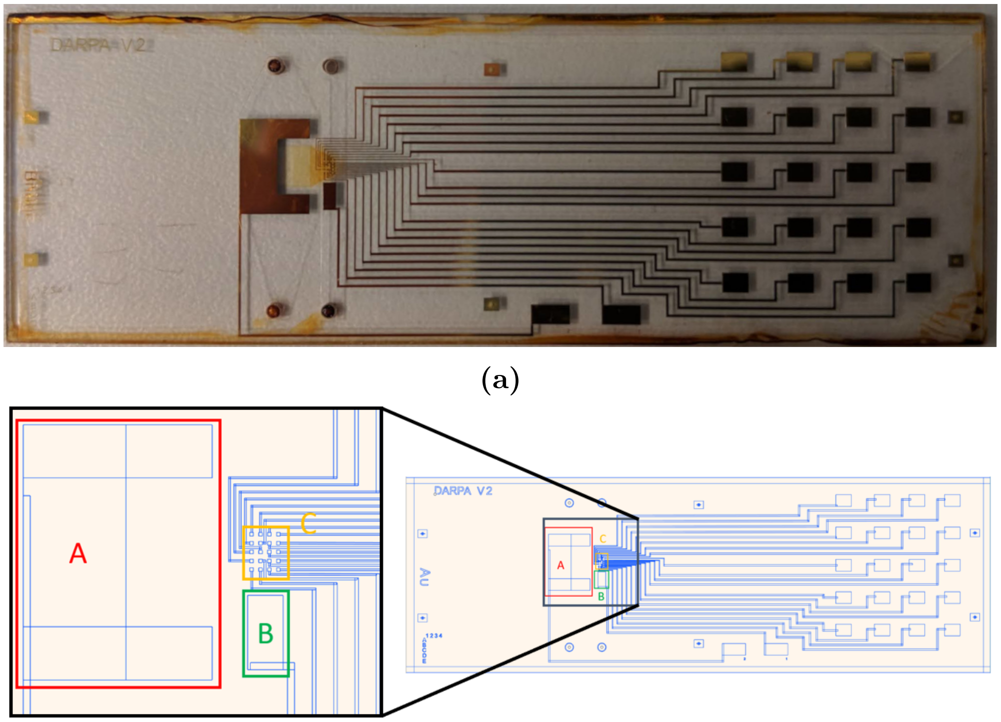

(a)

(b)

Figure 5.3: a) H^+ Ion pump. The 22 gold contact pads are 1.5 x 1.5 mm squares with 2.54 mm spacing b) Drawing of H^+ Ion pump gold layer. Left shows an array of 5 x 4 ion pumps/working electrodes, A and B are counter electrodes.

2, and KEYENCE, BZ-X710). A 1/8' acrylic piece features a viewing window and holes for microfluidics, and can be manufactured using a laser cutter machine or CNC machine shown in Figure 5.4c.

Single-Ion - Second Generation

The second-generation single-ion ion pump shares the same operation principle as the first generation. In addition, the second generation also features one auxiliary counter electrode and four auxiliary reference electrodes shown in Figure 5.5. In total, the second generation single-ion ion pump has 27 electrodes and 27 contact pads. Not only does the number of contact pads change but also the

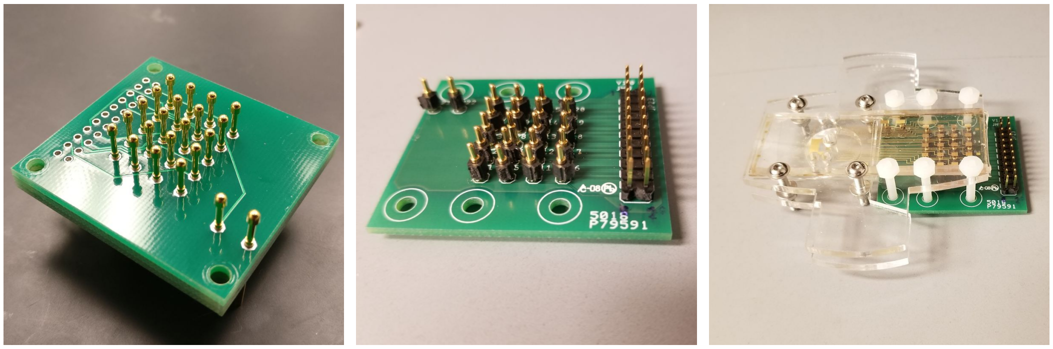
(a) (b) (c)

Figure 5.4: Spring-loaded pin interface board for 1st generation single-ion ion pump a) First generation of Spring-loaded pins interface board b) Low profile spring-loaded pins interface board c) Low profile spring-loaded pins interface board with EVOS FL AUTO 2 acrylic clamp.

layout of it. Therefore, a new version of the interface board needs to be designed.

The second-generation interface board consists of 27 spring-loaded pins (Mill-Max Manufacturing Corp, 825-22-010-10-001101) and a 28-pin pin header. The board connects to 20 working electrodes, two main counter electrodes, four auxiliary reference electrodes, one auxiliary counter electrode, and six mounting holes shown in Figure 5.6a. Similar to the previous design, two versions of the acrylic holder are made for the EVOS FL Auto 2 (Figure 5.6c) and KEYENCE, BZ-X710 microscopes (Figure 5.6b).

Multi-Ion Ion Pump

A multi-ion ion pump shares the same principle as a Single-ion ion pump. However, instead of having one ion on a single device, a multi-ion ion pump, as the name suggests, can individually transport H^+, K^+, Na^+, and Cl^- simultaneously.

The four independent reservoirs connect to one target electrolyte on a single platform, which is controlled in 4-dimensions. Here, we used H^+, K^+, Na^+ as the cation representatives, and Cl^- as anion representatives to be delivered with

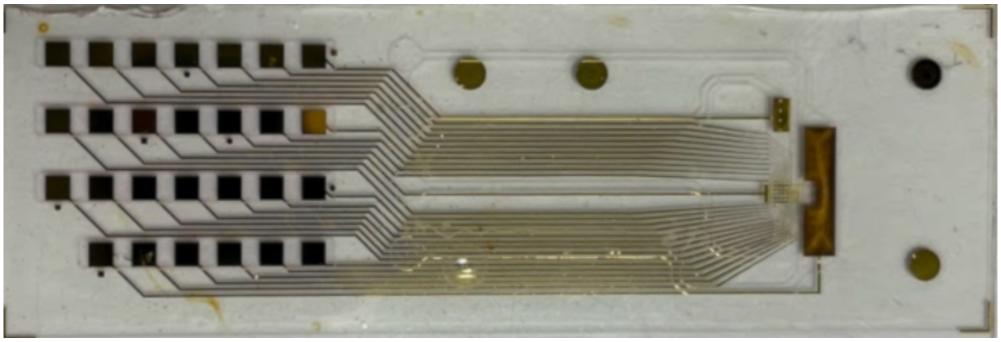

(a)

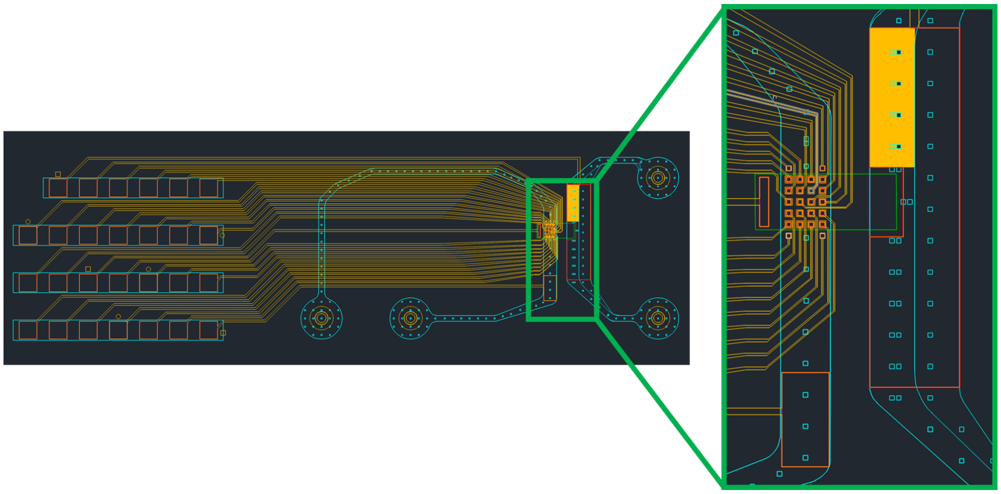

(b)

Figure 5.5: a) Second-generation H^+ Ion pump. The 27 gold contact pads are 1.5 x 1.5 mm squares with 2.54 mm spacing b) Drawing of Second-generation H^+ Ion pump gold layer. Right shows array of 5 x 4 ion pumps.

the multiple-ion pump. Like the conventional ion pump, each reservoir electrolyte provides different ion sources, and all of them share one target electrolyte, which are separated by SU8. An auxiliary electrode located in a target electrolyte is used to regulate ion distribution within that target electrolyte. The reference electrodes in the reservoir and auxiliary electrode are AgCl nanoparticles (NPs) deposited by electrochemical plating, which are good for electron to ion conversion. The working electrodes in a target electrolyte are 6 x 6 microelectrode arrays (MEAs) customized for different ions: the 36 MEAs were composed of 9 matrices, and each

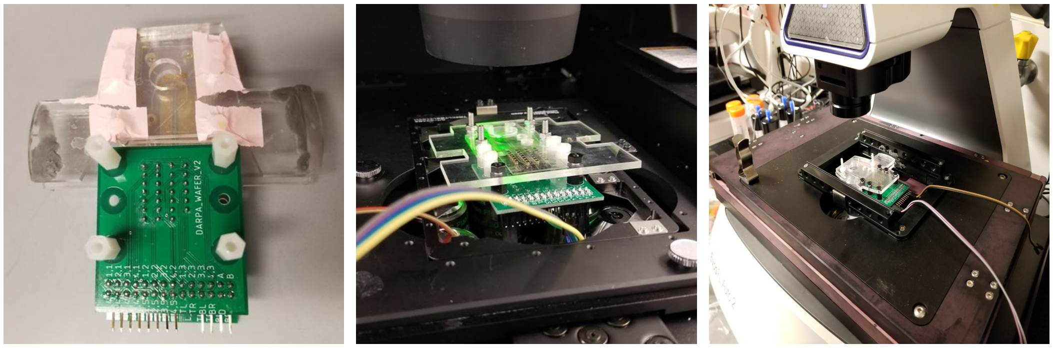

(a) (b) (c)

Figure 5.6: Spring-loaded pins interface board for second generation single-ion ion pump a) Spring-loaded pins interface board with acrylic clamp b) Low profile spring-loaded pins interface board with acrylic holder for KEYENCE, BZ-X710 c) Low profile spring-loaded pins interface board with EVOS FL AUTO 2 acrylic clamp.

matrix has 4 MEAs that are each connected to the H^+ pump, Na^+ pump, K^+ pump, and Cl^- pump, respectively (i.e., 50 x 50 μm and 150 μm pitch) shown in Figure 5.8. The MEAs of the H^+ pump are coated with Pd NPs, which are selective to H^+ by forming PdHx, and AgCl NPs are coated on MEAs connected to Cl^- pump because of its selectivity to Cl^-. Platinum nanoparticles (Pt NPs) are used in K^+ and Na^+ pump to increase the surface area of the MEAs as well as the capacitance. Each source reservoir is connected to the corresponding MEAs by AEM or CEM. Here, negatively charged Poly vinyl Alcohol: Polystyrene sulfonate (PVA:PSS) was used to transfer H^+, K^+, and Na^+, and positively charged PVA:Chitosan was used in Cl^- pump. The chessboard-like ion bridge is patterned by spin-coating in two layers separated by parylene to avoid interference.

In total, the multi-ion ion pump has 36 working electrodes, four counter electrodes, four auxiliary electrodes, and one reference electrode. Figure 5.8 shows 45 gold contact pads which are 1.5 x 1.5 mm squares with 2.54 mm spacing and 3 x 3 grid of group of ion pumps.

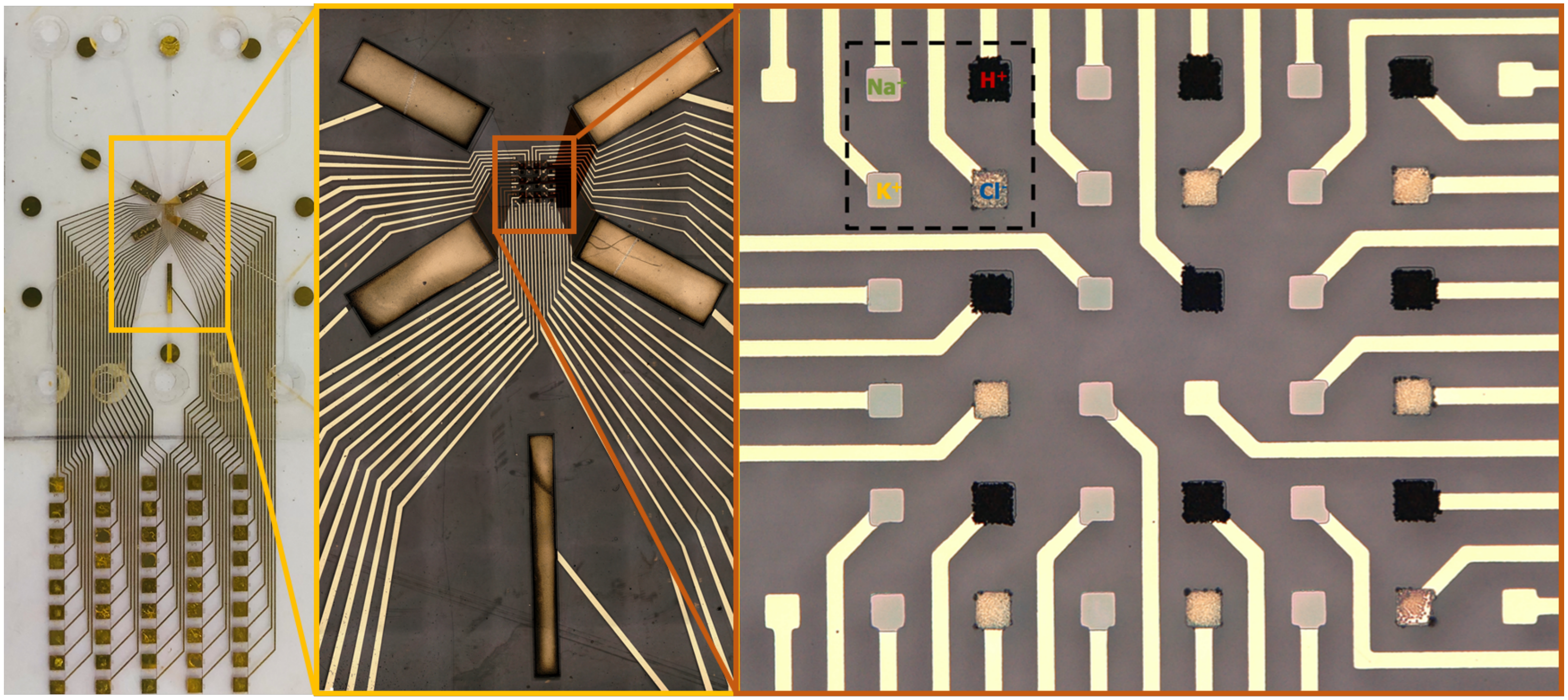

Figure 5.7: left) Photo of the multiple-ion pump. middle) Optical microscope image of the multiple-ion pump. right) Microelectrodes layout of the multiple-ion pump.

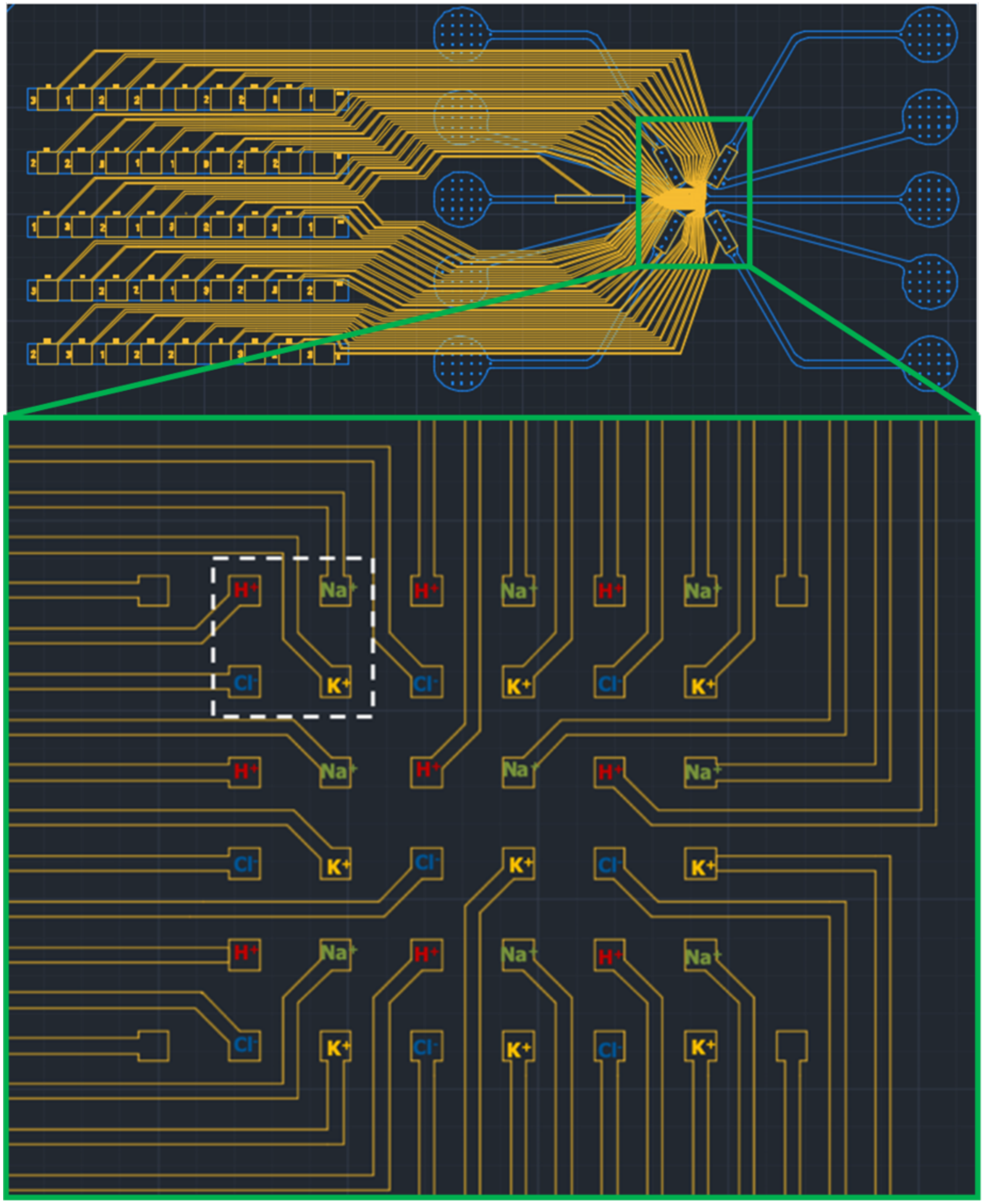

Figure 5.8: Multi-ion ion pump. The 45 gold contact pads are 1.5 x 1.5 mm squares with 2.54 mm spacing.

Unlike single-ion ion pumps, the multi-ion ion pump features a different number of contact pads and layouts. Therefore, we designed a new interface board with a Flexible Printed Circuit (FPC) connector. The interface board consists of an FPC connector (Molex, 505110-5091) and five rolls of nine spring-loaded pins (Mill-Max Manufacturing Corp, 825-22-010-10-001101). This approach drastically reduces the footprint of the interface board. We also designed a custom acrylic holder for a multi-ion ion pump and the interface board shown in Figure 5.9.

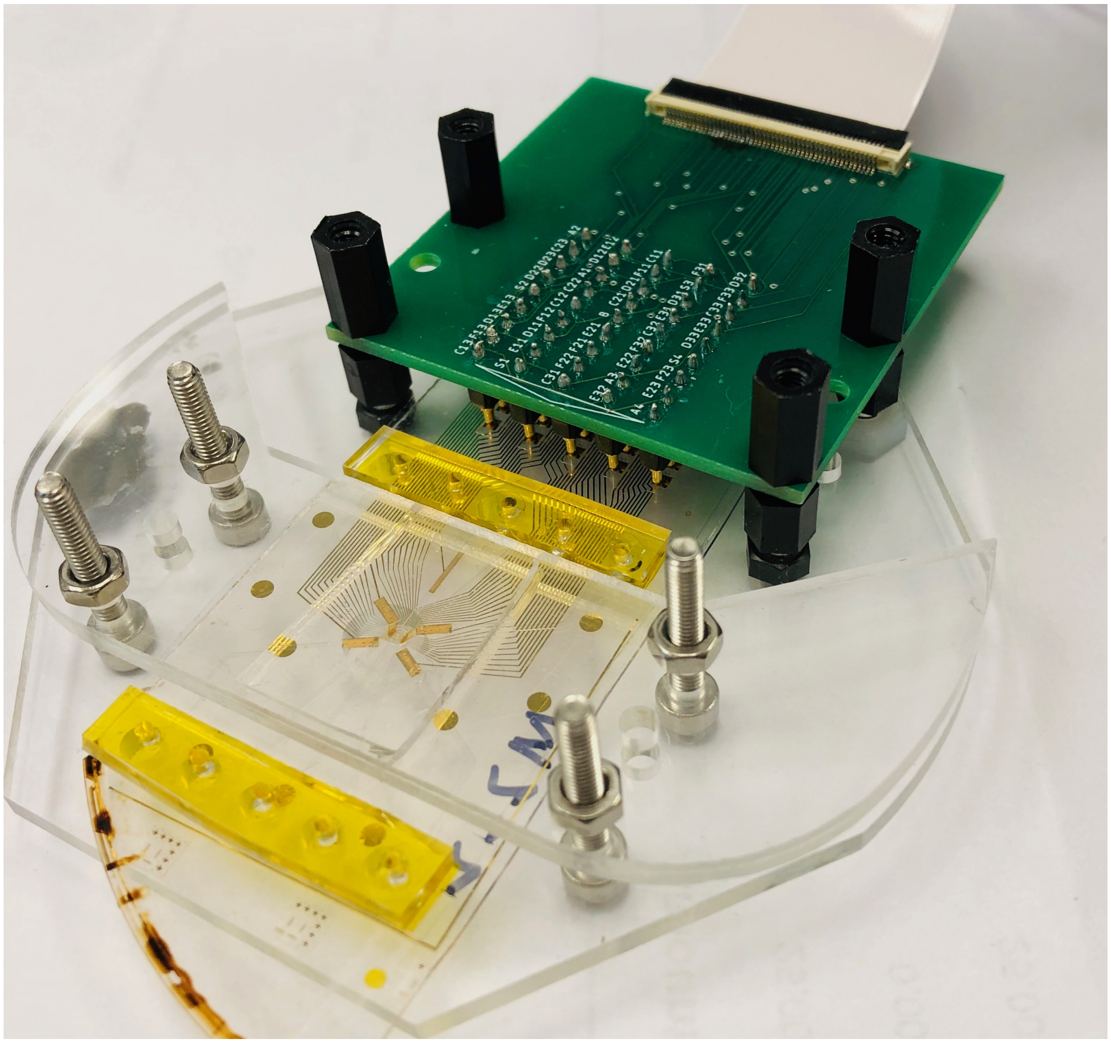

Figure 5.9: Multi-ion ion pump on custom acrylic holder and custom interface board. The multi-ion ion pump connects to a modular multi-channel potentiostat via an interface board and FPC cable.

5.2.2 Vertical Ion Pump

The vertical ion pump consists of a layer of gold used to pattern the electrodes and traces, followed by an insulation layer and 2 layers of SU-8 which creates closed micro fluidic channels. These channels are filled with ion-conducting hydrogels which act as the ion-exchange layer as opposed to the previous polymer based design. This change enables the delivery of ions larger than protons and also neurotransmitters and other small biomolecules. The hydrogel based pumps have lower resistance to ions and hence improves performance over the previous design. Applying a voltage across the hydrogel transports the desired ions from the reservoir to the target regions of the ion pump.

We learned from the previous generation of ion pumps that assembling an ion pump with an interface board using nuts and screws are inefficient and prone to an user error. In this version, we designed a magnetic interlock system that automatically aligns the vertical ion pump device and also allowed the interface board to be magnetically clipped into the acrylic holder shown in Figure 5.13 and 5.14.

The 1 mm pitch of a vertical ion pump is another challenge in redesigning the interface board. Currently, there is no available off-the-shelve, low-profile spring-loaded/ compression contact that has a 1 mm pitch, so spring finger connectors were chosen instead (TE Connectivity AMP Connectors, 2336713-2). However, using individual spring finger connectors instead of a row of the spring-loaded connectors makes circuit board assembly more challenging but still manageable.

The interface board consists of 11 spring finger connectors, one FPC connector, and six mounting holes for magnets. The spring finger connector is plated with 0.25 μm gold particles and has a stroke range of 0.8 to 1.15 mm. The new stroke range is significantly smaller than the previous spring-loaded pin; as a result, we

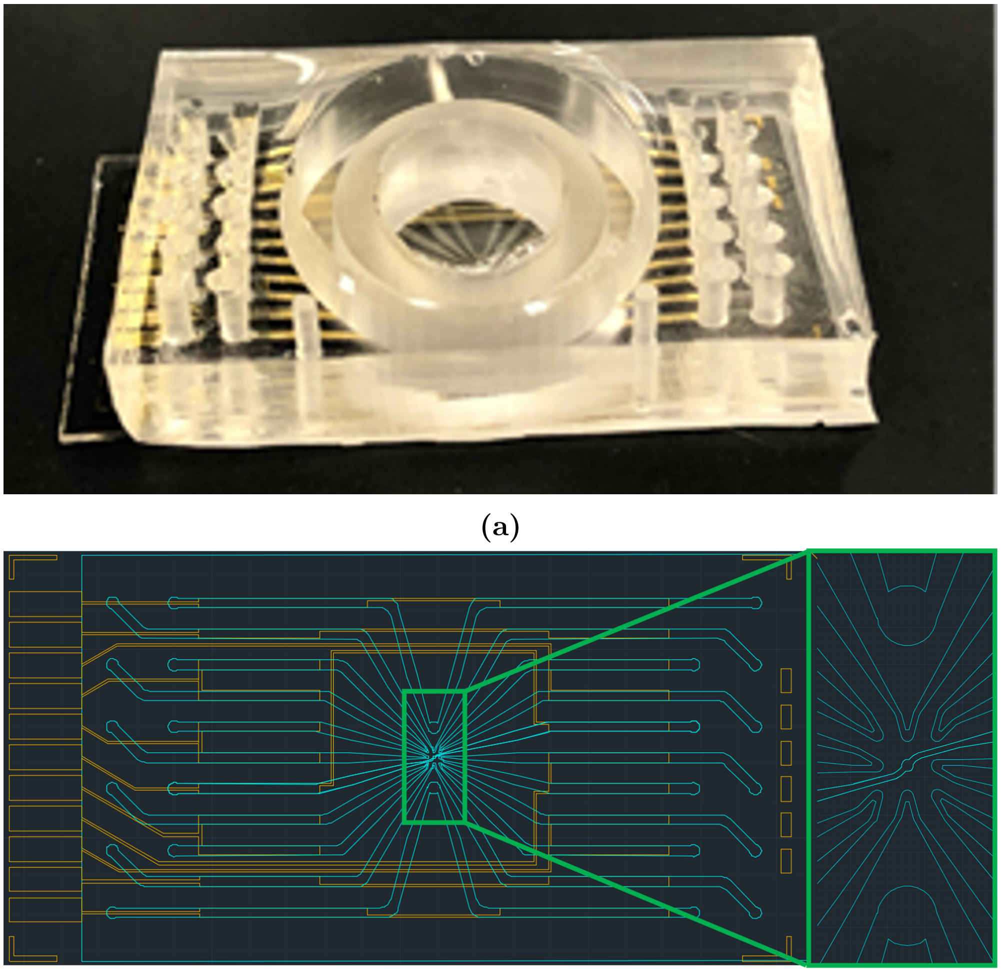

(a)

(b)

Figure 5.10: a) Vertical ion pump b) Layout of Vertical ion pump, yellow: Gold traces, blue: SU-8 micro-channel.

are able to reduce the height of the whole system by a few mm.

Like previous ion pump designs, the acrylic holder features four device alignment magnets and six interface board magnets for both the EVOS FL Auto 2 and KEYENCE, BZ-X710 microscopes.

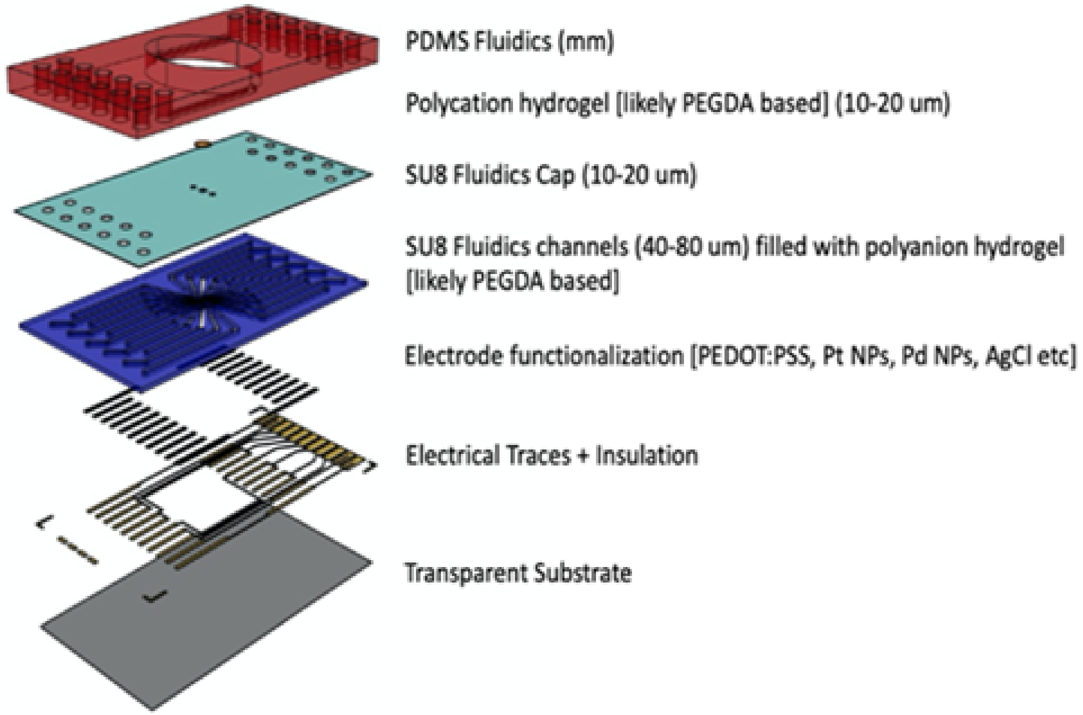

Figure 5.11: Schematic of the vertical ion pump. The vertical ion pump is fabricated on a transparent substrate and goes through a multi-step photolithography and is later bonded to a PDMS fluidics layer.

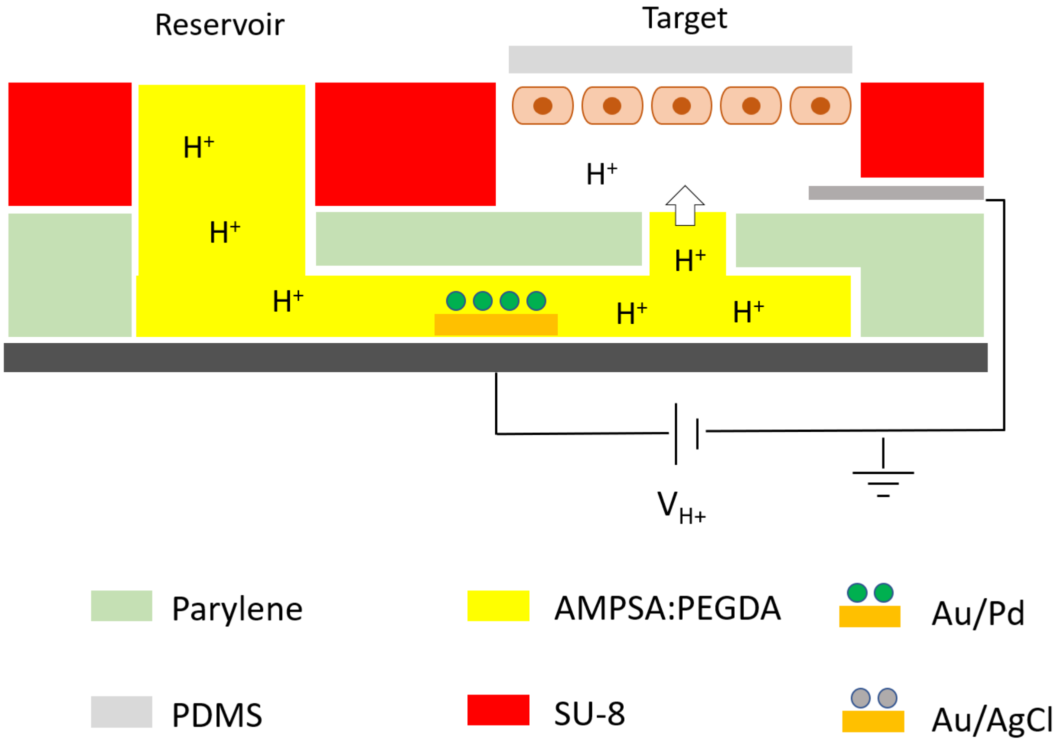

Figure 5.12: Cross section of a Vertical ion pump shown that this design utilizes a SU-8 channel to isolate a reservoir and a target solution.

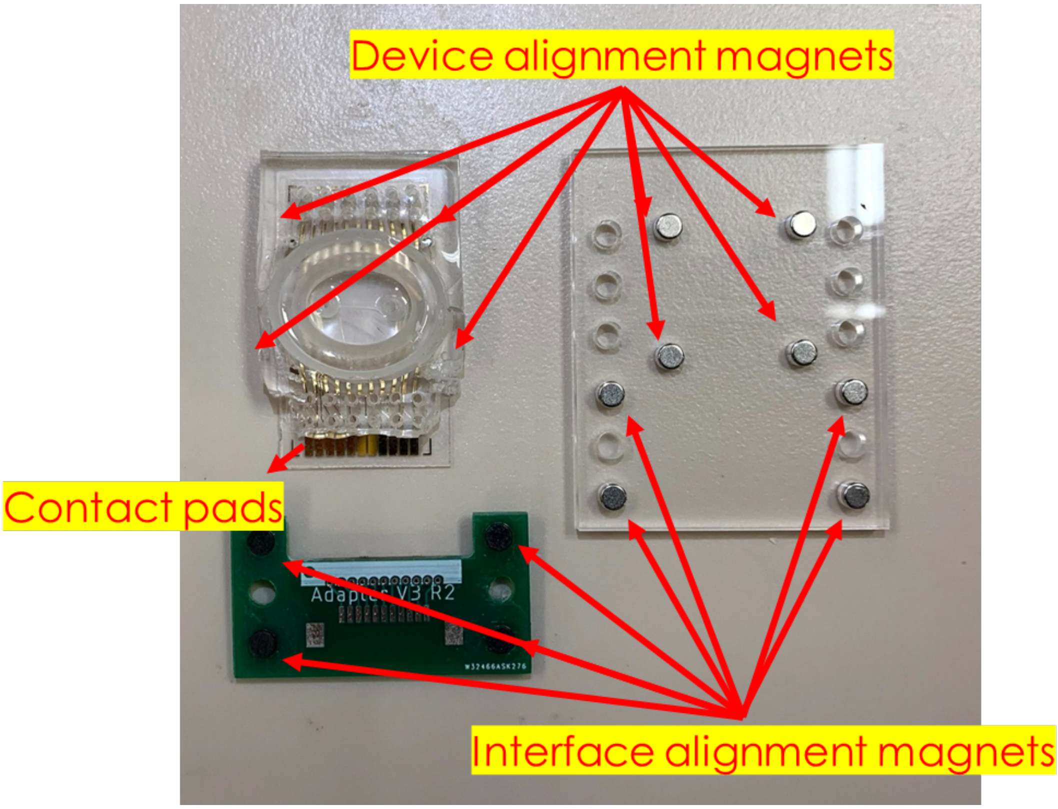

Figure 5.13: Magnetic interlock overview. Top left) vertical ion pump has four alignment magnets embedded in a PDMS layer that mates with four alignment magnets on an acrylic holder. The acrylic holder also features another four alignment magnets for interfacing with an interface board.

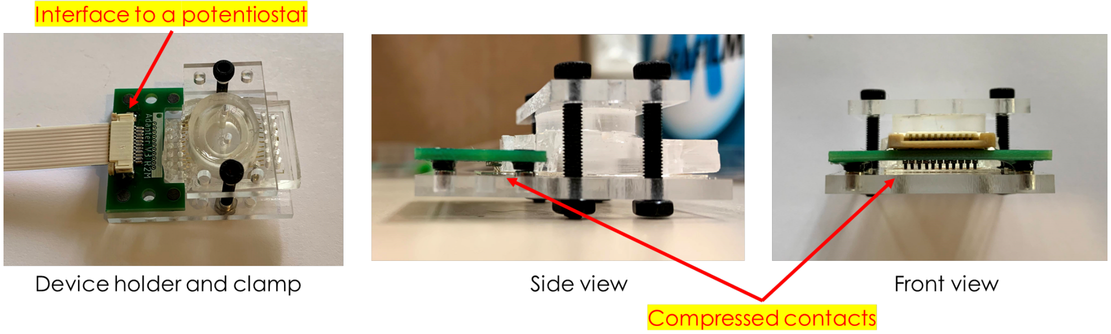

Device holder and clamp

Side view

Front view

Figure 5.14: Acrylic holder overview. Left) A vertical ion pump clamped to an acrylic holder and PDMS cap with two screws and an FPC cable connect to a non-modular multi-channel potentiostat. Middle and Right) compressed contact on an interface board pressed against a vertical ion pump.

Figure 5.15: The non-modular multi-channel potentiostat connects to a vertical ion pump clamped on an acrylic holder mounted on the KEYENCE, BZ-X710 microscope.

5.3 In-vitro

5.3.1 Open-Loop Control with Ion Pumps

Introduction

This section demonstrates how the multi-channel potentiostat operates with a few variations of ion pumps ranging from H^+, K^+, and Cl^-. The H^+ ion pump is tested with color-metric dye, fluorescent dye, and genetically modified stem cells in both open-loop and closed-loop settings. In addition, K^+, and Cl^- ion pumps were also tested with a fluorescent dye in open-loop mode.

Color-metric pH Dye

[Selberg et al., 2020b] had developed a H^+ ion pump which is able to inject or remove H^+ ion from a solution. In this experiment, the H^+ ion pump was used with the multi-channel potentiostat to change a H^+ ion concentration, or pH, on a pH Color-metric dye U-110, Universal pH Indicator Solution. A schematic of the H^+ pump is shown in 5.16 where electrode A and B are reference electrodes and C is an array of working electrodes.

The 1st generation H^+ ion pump is clamped on a low-profile interface board. The multi-channel potentiostat's output channel 1 and 2 are connected to V_A, V_B and the rest of the channels are connected to V_C of H^+ ion pump. Procedure shown in Table 5.1 is used in this experiment. Figure 5.17 shows time-lapse images of changes in pH during different cycles.

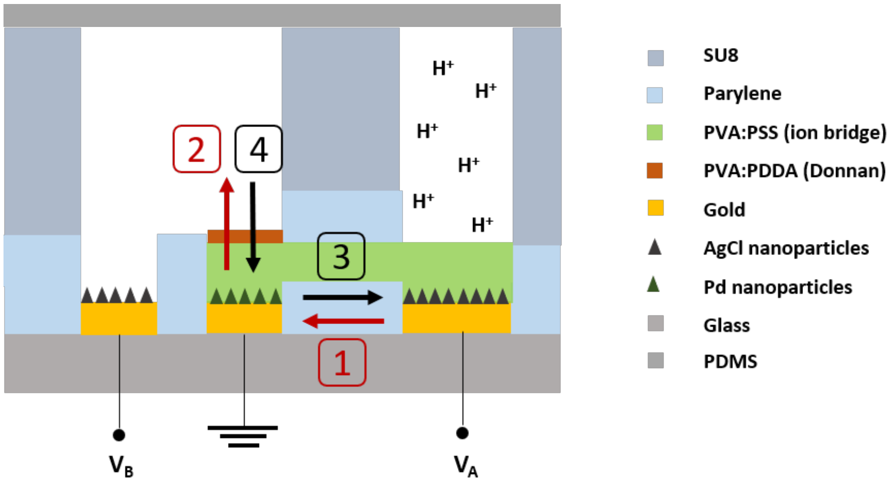

Figure 5.16: Simplified schematic of 1st generation of horizontal H^+ ion pump

Stages	V_A	V_B	V_C	Duration	Acid/Base	Description
1	1	0	0	5	Acid	pump H^+ from reservoir to Pd NPs
2	0	-1	0	10	Acid	release H^+ from Pd NPs to target well
3	-2	0	0	5	Base	Pd NPs absorb H^+
4	0	1.5	0	30	Base	pump H^+ back to reservoir

Table 5.1: Standard procedure for testing the H^+ ion pump by applying different voltages to electrodes A, B and C.

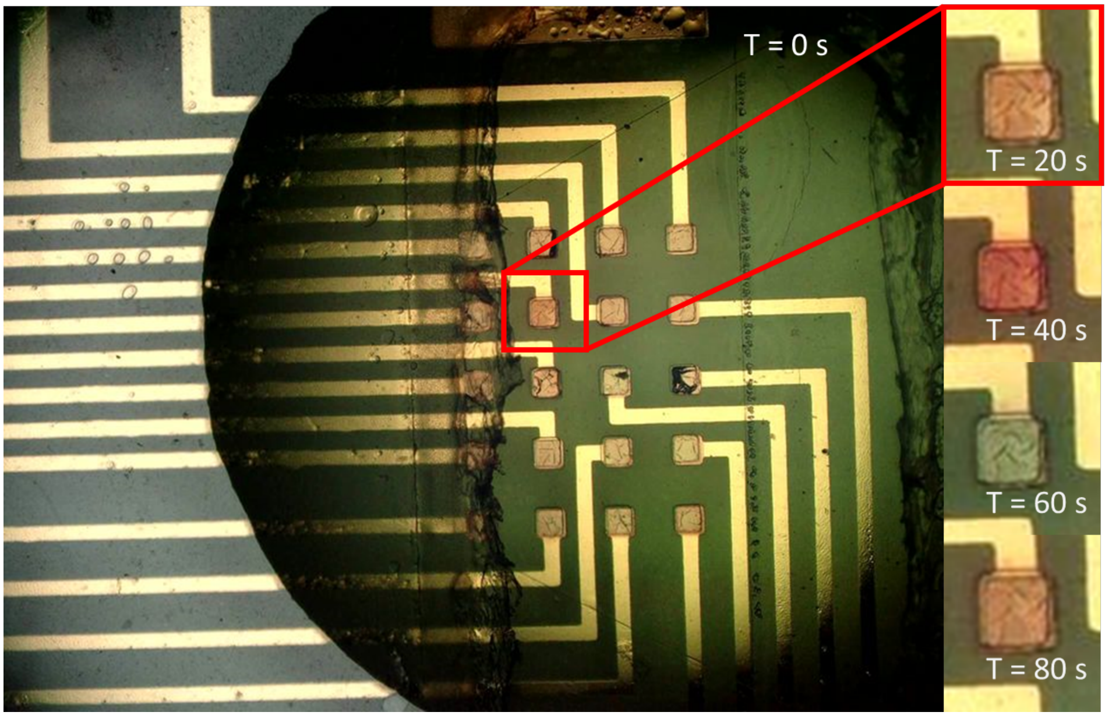

Figure 5.17: Demonstration of changing pH cycle on pH sensitive dye on H^+ pump. Red color indicates acidic and blue indicates more basic.

Fluorescent dye

In addition to the H^+ ion pump, [Selberg et al., 2020b] and [Jia et al., 2020b] also developed K^+ and Cl^- ion pumps. Due to limitations of color-metric dyes, various Fluorescent dyes are used to evaluate the performance of various ion pumps shown in table 5.2.

Ion type	Dye	Filter
H^+	5-(and-6)-Carboxy SNARF-1^{TM}	GFP and TX Red
K^+	ION Potassium Green-4 TMA+	YFP
Cl^-	N-(6-methoxyquinolyl)-acetoethylester (MQAE)	DAPI

Table 5.2: Ion type and their corresponding Fluorescent dyes and microscope filters cubes.

Fluorescence Image Result Normalization

Due to the nature of fluorescence cell/dye decay and background noise, post-processing is required to ensure accurate results. In this circumstance, the author is using the two step process shown in 5.18. Fluorescence intensity values were normalized with respect to the maximum recorded value.

$$Normalized\, value = \frac{F_i}{F_{max}}$$

Then the normalized background plot was subtracted from the normalized measurement plot.

$$Ffinal_i = Fdata_i - Fbackground_i$$

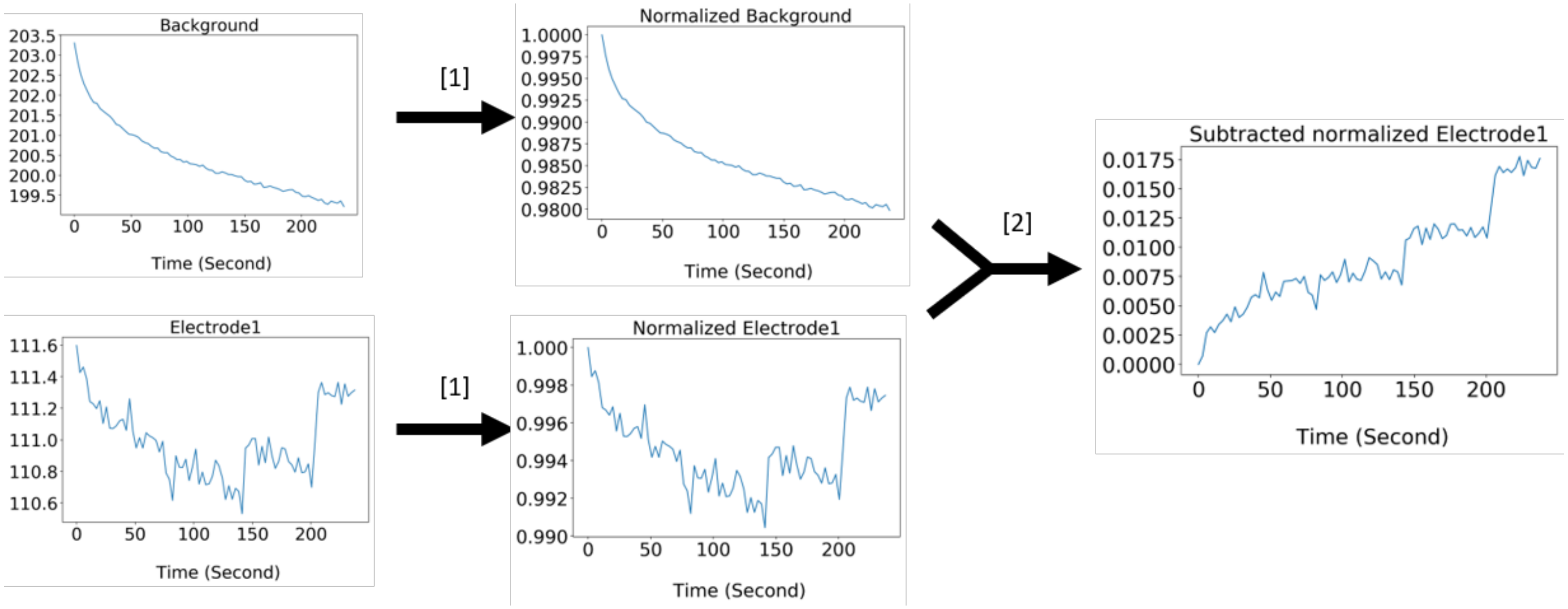

Figure 5.18: Data Normalization workflow. First step [1], both background and data point of interest are normalized and later a normalized data point is subtracted from the normalized background [2].

H^+ Ion Pump

Fluorescent dye, $5-(and-6)-CarboxySNARF-1^{TM}$ was used to evaluate performance of the H^+ ion pump. $5-(and-6)-CarboxySNARF-1^{TM}$ have two excitation and emission profiles, one fitted with GFP filter and another one fitted with TX Red filter. In the GFP channel, fluorescence intensity increases when the concentration of H^+ decreases (solution become more basic). In contrast, TX Red channel fluorescence intensity increases when the concentration of H^+ increases (solution becomes more acidic). The experiment is conducted under the EVOS AUTO FL2 Fluorescence microscope at Tufts University.

The experiment was conducted with the modular multi-channel potentiostat with the standard procedure shown in table 5.1. The four pixels on the second column are actuated at the same time. The EVOS microscope performed a time-lapse recording on GFP and TX Red filters every second for five minutes. Image sequences are saved in raw .TIF format and are later analyzed by plotting the intensity over time (Stack - Plot Z-axis) using ImageJ software. The result shows both good performance in pH change of H^+ and excellent control over spatial and temporal resolution.

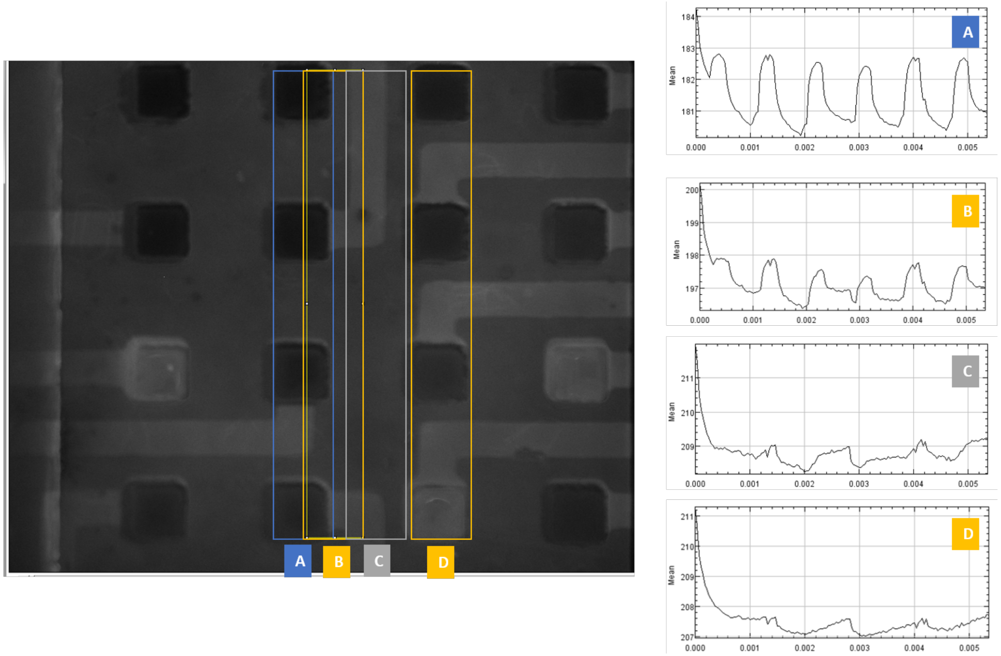

Figure 5.19: H^+ Intensity change over time on electrodes and proximity. The response gradually decreases as the distance from electrode increases.

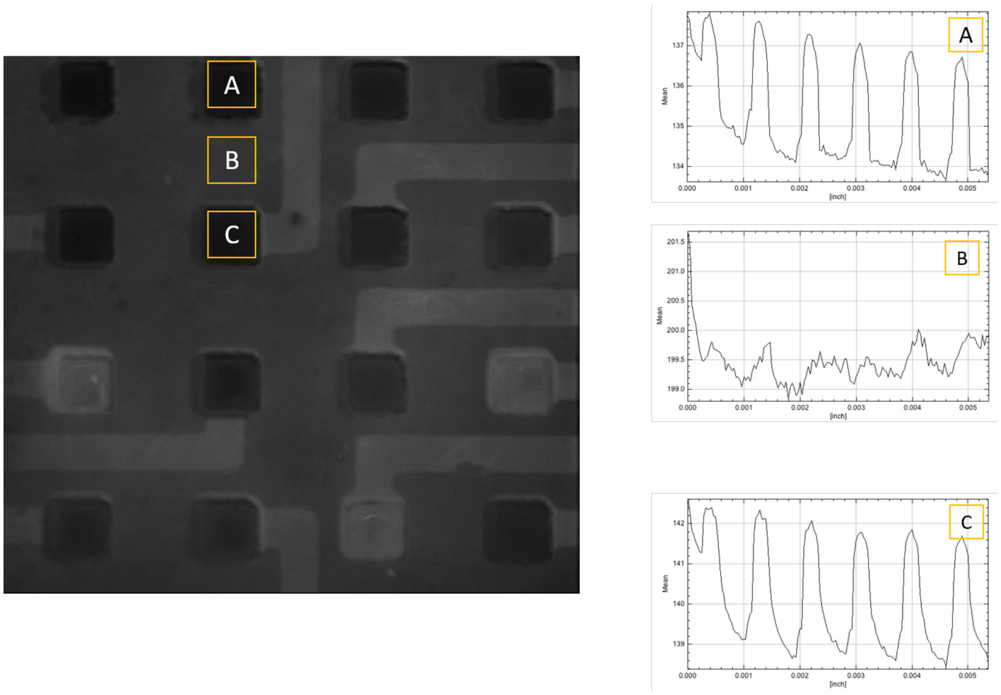

Figure 5.20: H^+ Intensity changes over time on two adjacent electrodes and the area in-between shows high spatial resolution.

K^+ Ion Pump

K^+ Fluorescent dye, $ION\ Potassium\ Green - 4\ TMA+\ \ Salt$ was used to evaluate performance of the K^+ ion pump. Fluorescent intensity increases with an increase in K^+ ion concentration.

A schematic of the K^+ pump is shown in 5.21. Similar to the H^+ ion pump experiments, the experiments were conducted with the modular multi-channel potentiostat with the procedure shown in table 5.3. Only one pixel on the second column (area A on 5.22) is connected and actuated in this experiment. The EVOS microscope performed a time-lapse recording on YFP filters every second for four minutes. Image sequences are saved in raw .TIF format and are later analyzed by plotting intensity over time (Stack - Plot Z-axis) using ImageJ software. The results shows both good performance in changing $K+$ concentration and also excellent control over spatial resolution.

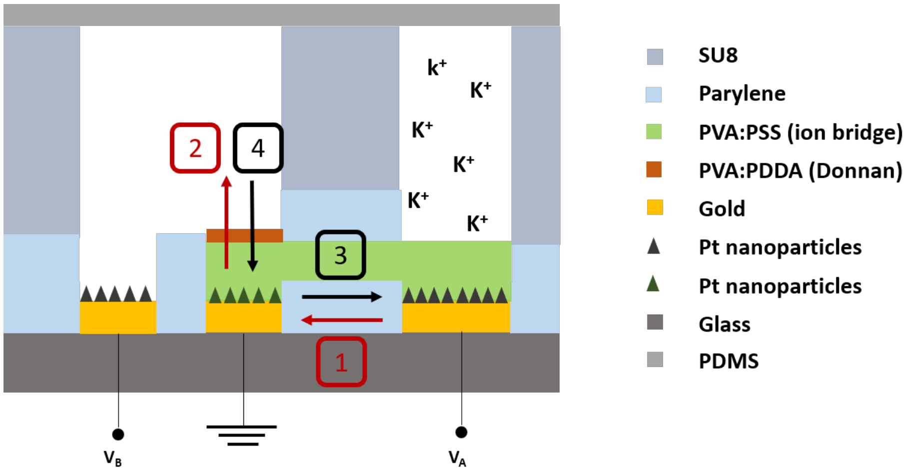

Figure 5.21: Simplified schematic of 1st generation of horizontal K^+ ion pump.

Stages	V_A	V_B	V_C	Duration	Description
1	1	0	0	5	pump K^+ from the reservoir to Pt NPs
2	0	-1	0	10	release K^+ from Pt NPs to target well
3	-2	0	0	5	pump K^+ back to the reservoir
4	0	1.5	0	30	Pt NPs absorb K^+

Table 5.3: Standard procedure for test K^+ ion pump by applying different voltages at electrodes A, B and C.

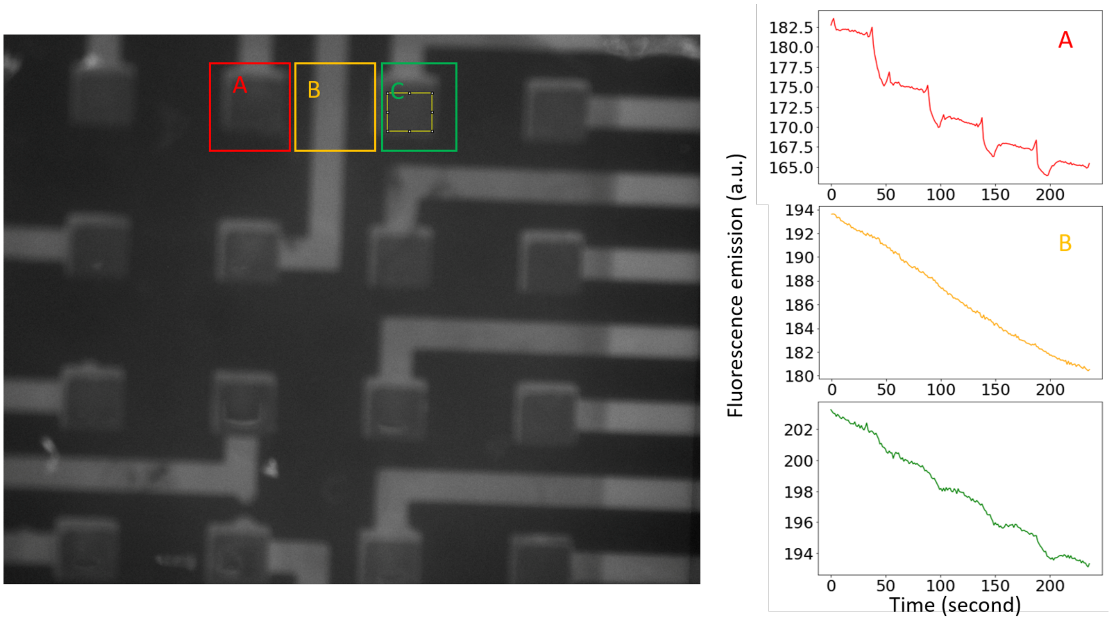

Figure 5.22: K^+ ion pump where only pixel A is actuated. Area A (red) is where the pixel is actuated. B and C (yellow and green) show no significant change. This proves that the ion pump has high spatial resolution.

Cl^- Ion Pump

Cl^- Fluorescent dye, N-(6-methoxyquinolyl)-acetoethyl ester (MQAE) is used to report Cl^- concentration in solutions. Fluorescence intensity increases with a decrease in Cl^- ion concentration.

The schematic of Cl^- pump is shown in 5.23. The experiment uses the same setup as the H^+ ion pump where the four pixels on the second column (area A on 5.24) are connected to the modular multi-channel potentiostat and actuated at the same time. The standard procedure shown in table 5.4 is used.

The EVOS microscope performed a time-lapse recording on DAPI filters every second for five minutes. Image sequences are saved in raw .TIF format and are later analyzed by plotting intensity over time(Stack - Plot Z-axis) using ImageJ software. The results shows both good performance in changing Cl^- concentration and also excellent control over spatial resolution.

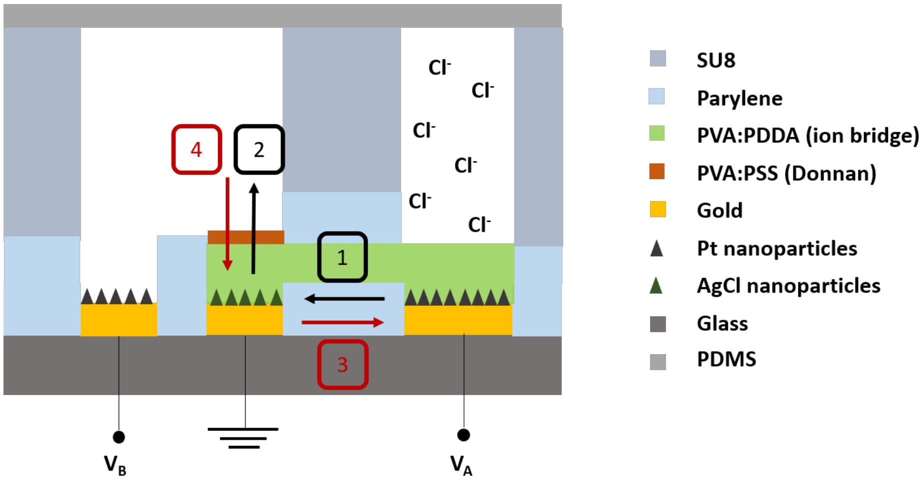

Figure 5.23: Simplified schematic of 1st generation of horizontal Cl^- ion pump.

Stages	V_A	V_B	V_C	Duration	Description
1	1	0	0	5	pump Cl- from reservoir to AgCl NPs
2	0	-1	0	10	release Cl- to target well
3	-2	0	0	5	pump Cl- back to the reservoir
4	0	1.5	0	30	AgCl NPs absorb Cl- from target well

Table 5.4: Standard procedure for test Cl^- ion pump by applying different voltage at electrode A, B and C.

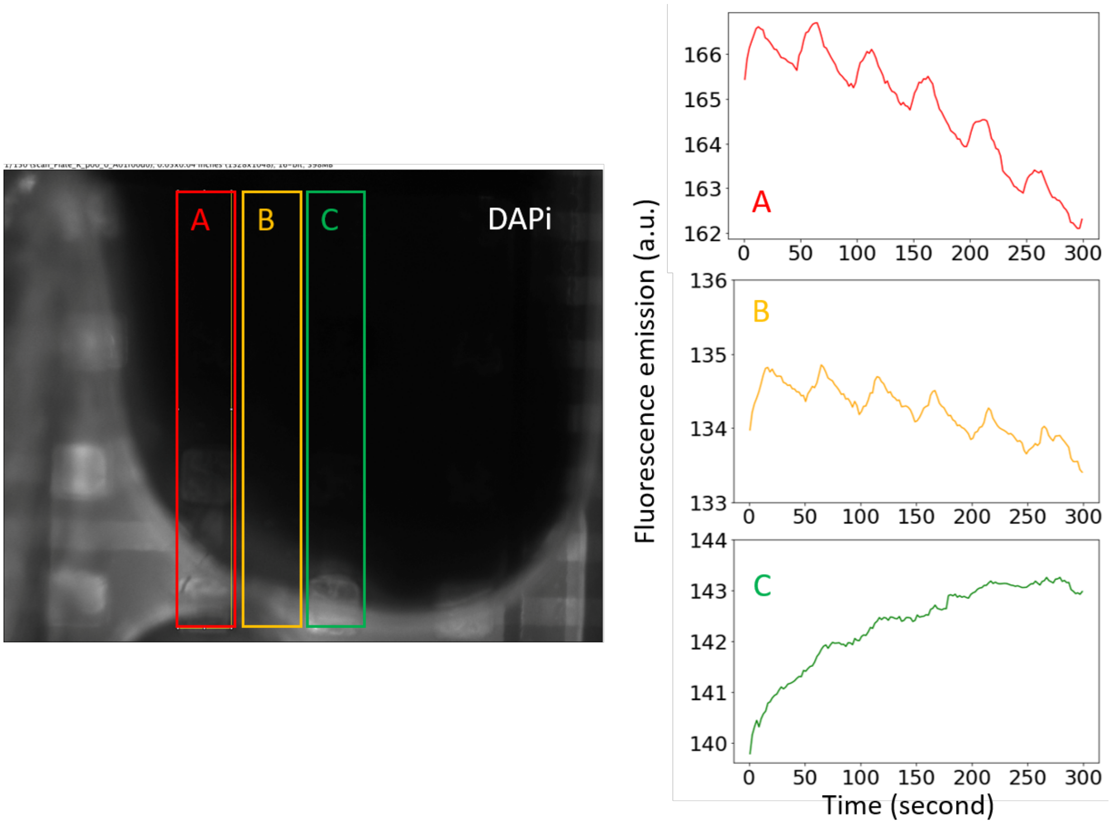

Figure 5.24: Cl^- ion pump. Only four pixels on second column (A) were activated. B (yellow) shows a smaller magnitude change compared to activated area (A). C (green) shows no significant change. Again, this shows that the ion pump has high-spatial resolution.

Genetically Modified Stem Cells

In the previous section, the author conducted experiments with the H^+ ion pump using both color-metric and Fluorescent dyes. This section is dedicated to cell culture experiments where H^+ ion pump is used to manipulate H^+ concentration in genetically modified stem cell cultures, hIPSC Arclight stem cell cultures and cpYFP stem cell cultures.

H^+ Ion Pump with ArcLight Stem Cell

hIPSC Arclight stem cells are genetically modified stem cells with the voltage reporter in the form of green fluorescence. The modular multi-channel potentiostat is used to operate an H^+ ion pump using step 2 and 4 from the standard procedure table 5.1. Four pixels on the third column and the second pixel from the top of the second column (electrodes with yellow circles on 5.25) are connected and actuated at the same time. EVOS microscope performed a time-lapse recording on GFP filters every second for five minutes. Image sequences are saved in raw .TIF format and are later analyzed by plotting intensity over time(Stack - Plot Z-axis) using ImageJ software.

The results show both good performance in changing the hIPSC Arclight stem cells fluorescence intensity (V_{mem}) and also excellent control over spatial resolution.

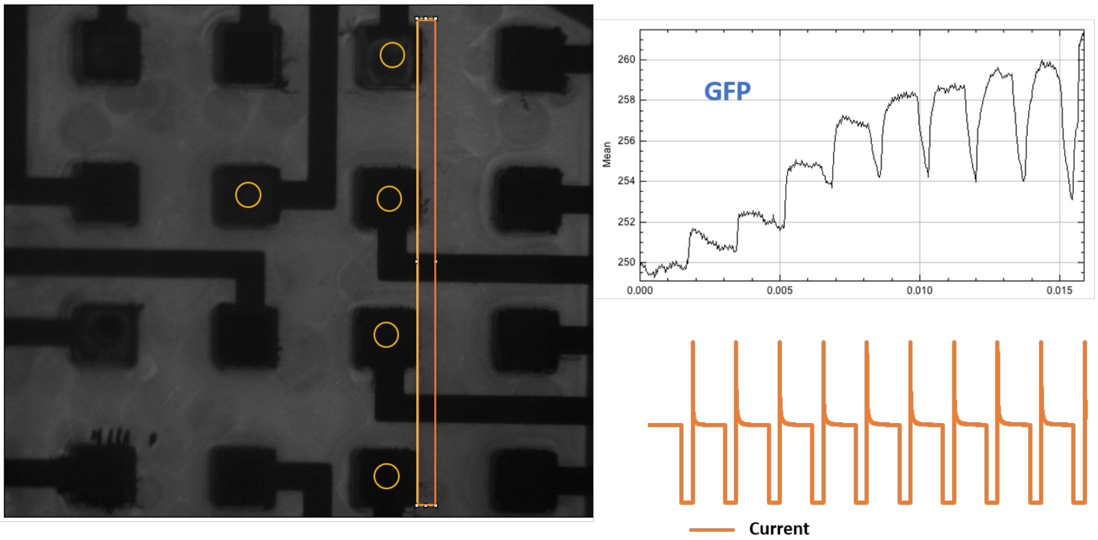

Figure 5.25: hIPSC Arclight stem cells over H^+ pump (electrodes in-focus). Yellow circle shows activated electrodes. Top right) GFP fluorescence intensity change over time. Bottom right) shows current measured from modular multi-channel potentiostat.

H^+ Ion Pump with cpYFP Cells

In addition to the Arclight stem cell, stem cells with V_{mem} reporter in the form of YFP is used to verify the performance of the H^+ ion pump. The H^+ ion pump operates using only step 2 and 4 from table 5.1. The recording is performed on the EVOS FL Auto 2 microscope every two seconds for four minutes.

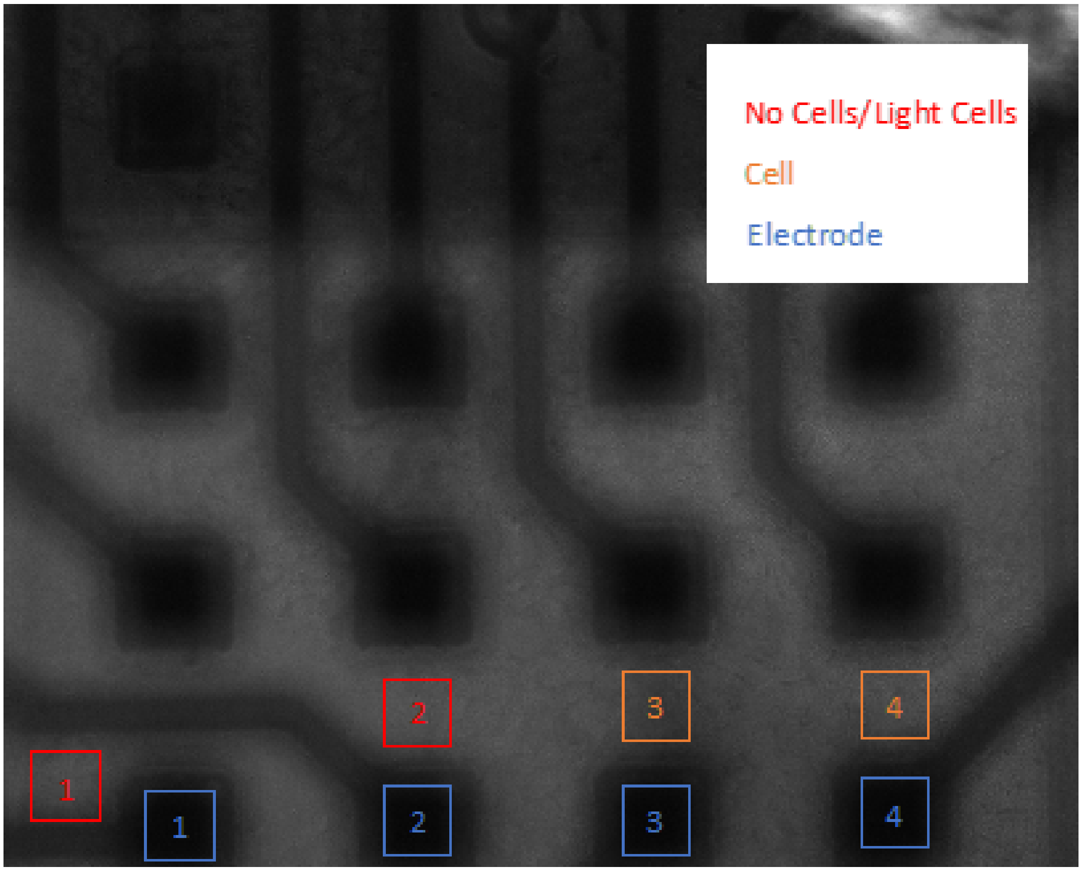

Figure 5.26: Mapping of eight regions, four on activated electrodes, two regions with dense cell and two regions without cells.

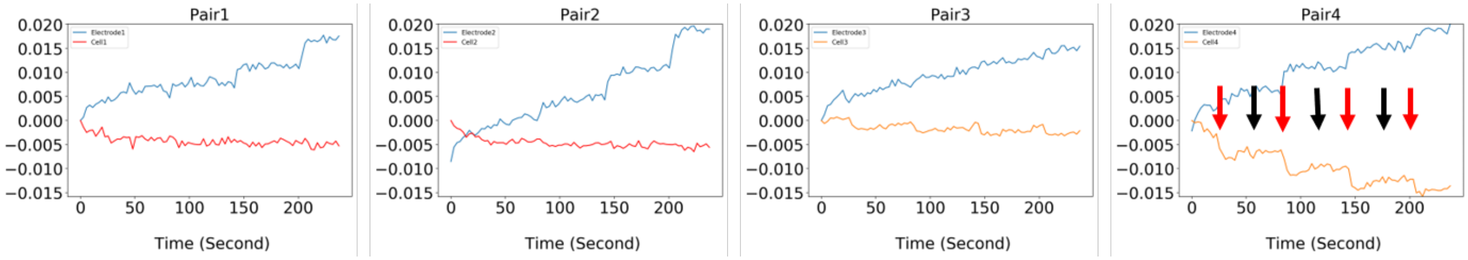

(a) Plot of eight regions, four on activated electrodes, two high-density and two low-density regions under GFP filter.

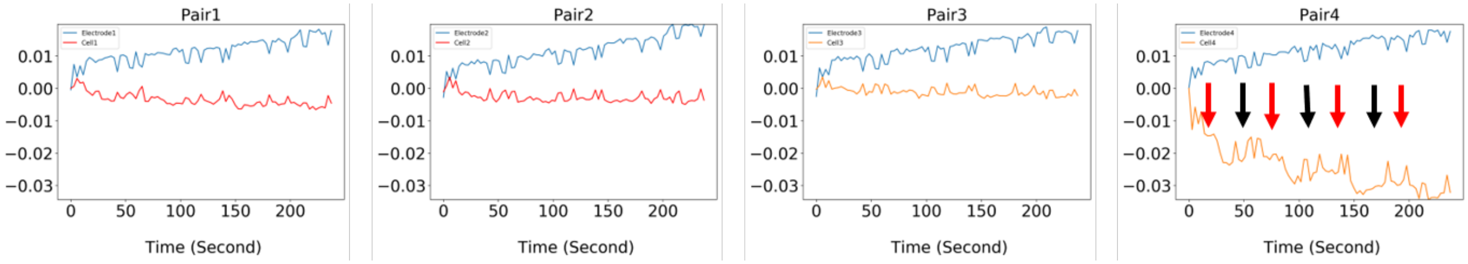

(b) Plot of eight regions, four on activated electrodes, two high-density and two low-density regions under YFP filter.

Figure 5.27

The result shows cells responding in the high cell density areas on both the GFP and YFP filter.

5.3.2 Closed-loop Control with Ion Pumps

Introduction

We explored the use of machine learning control algorithms to perform a closed-loop control on various ion pumps in both Fluorescent dye and genetically modified cell cultures.

H^+, K^+, Na^+, and Cl^- were tested with Fluorescent dyes. H^+ was also tested with ArcLight stem cell cultures.

Machine Learning Algorithms

Due to non-linear nature of ion pumps and cell culture responses, a traditional control algorithm (i.e., PID) would be not be a suitable for this task. Thus, a more complex machine learning algorithm is deployed in this situation instead. [Jafari et al., 2020] had developed an adapting machine learning control algorithm designed for an ion pump shown in Figure 5.28.

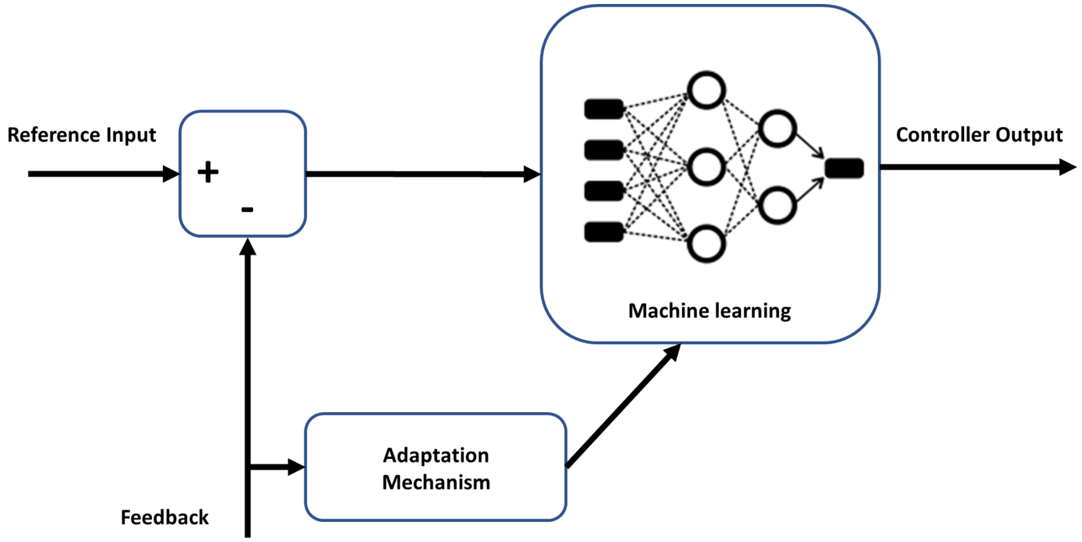

Figure 5.28: Architecture of the implemented online machine learning based feedback controller designed for the H^+ ion pump.

Fluorescent Dye

Single-ion Pump System

One goal of the multi-channel potentiostat is to enable an integration with an external controller, allowing an experiment with a more sophisticated control algorithm (e.g., machine learning). Similar to the open-loop control experiments, the system had been tested with different variants of ion pumps and fluorescent dyes. In this experiment a H^+, K^+, Na^+, and Cl^- ion pump were used with their corresponding dyes shown in Table 5.5.

Ion type	Dye	Filter
H^+	5-(and-6)-Carboxy SNARF-1^{TM}	GFP and TX Red
Na^+	CoroNa Green	DAPI
K^+	ION Potassium Green-4 TMA+	YFP
Cl^-	N-(6-methoxyquinolyl)-acetoethylester (MQAE)	DAPI

Table 5.5: Ion types and their corresponding fluorescent dyes and microscope filters cubes.

The setup consists of KEYENCE, BZ-X710 recording images into the shared folder. It is connected to the laptop that runs a machine learning controller via Ethernet cable; the same laptop also connects to the multi-channel potentiostat via Wi-Fi as shown in Figure 5.1.

Machine learning (ML) based controller consists of a ML-based control algorithm which is running on a PC. It reads images from the shared folder using MATLAB scripts, and computes the mean value of the active part of the micro electrodes arrays. This value then is used as the system's feedback input to update the ML-based control output. The interfacing device consists of a modular multi-channel potentiostat which applies the commands received from the ML-based controller to the ion pumps.

In all figures, blue is the reference signal and red is the system output (i.e., fluorescence intensity). The middle column shows the output of the controller applied to the ion pumps (i.e., V_B) and the right column shows the tracking error of the system. The tracking performance of all pumps seems promising. We do note differences in performance with the different ions. This can be due to the size of the molecule, resulting in different transients.

The feedback control algorithm was tested on Na^+ pump. In Figure 5.30, left plot shows the fluorescence intensity change of Na^+ indicator, CoroNa Green, with GFP filter of the selected area controlled by ML-based controller. The blue line is the reference signal and the red line is the system output (i.e., fluorescence intensity). The middle plot shows the output of the controller applied to the Na^+ ion pump and the right plot shows the tracking error of the system. The tracking performance of Na^+ ion pump shows a promising response to the controller commands.

Figure 5.31 shows the results for the spatial-temporal control of H^+. The top left plot shows the fluorescence intensity change of pH indicator, SNARF-1,

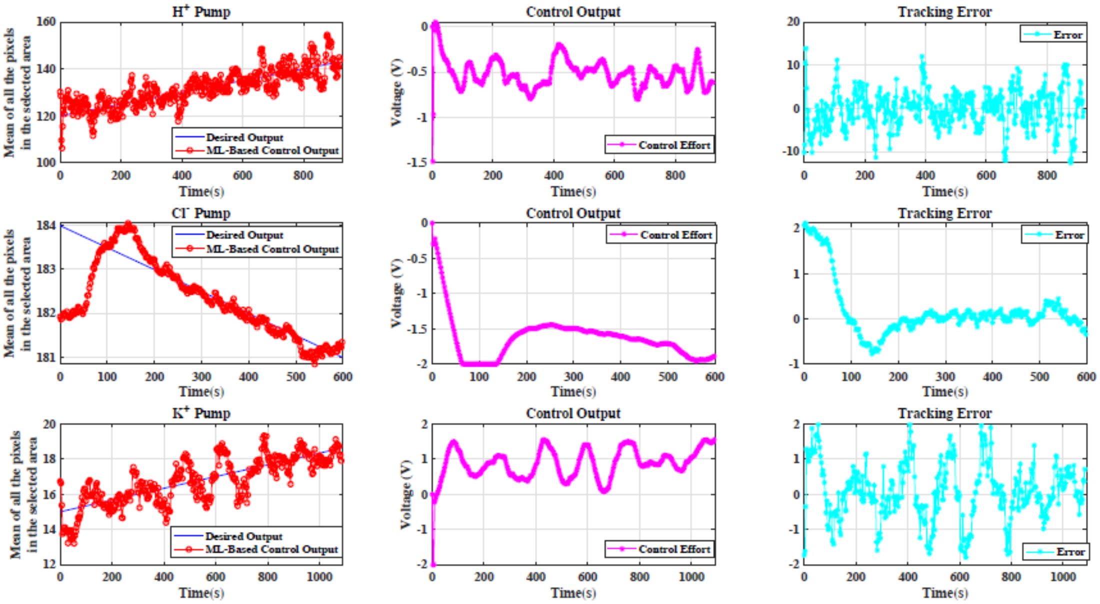

Figure 5.29: Left shows the fluorescence intensity change of fluorescent dyes of different ion pumps controlled by ML-based controller (reference signal shown in blue and system's output, fluorescence intensity, shown in red).Middle shows the output of the controller applied to the ion pumps (i.e., V_B) and right shows the tracking error of the system.

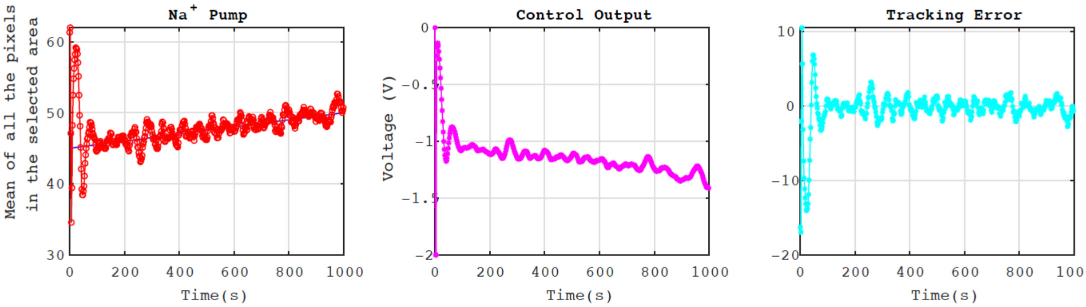

Figure 5.30: Na^+ pump with CoroNa Green indicator (100mM NaCl in the reservoir; 50uM CoroNa Green in the target.)

with Texas Red filter of Channel #1 controlled by ML-based controller and the bottom left plot shows the fluorescence intensity change of pH indicator, SNARF-1, with Texas Red filter of Channel #2 controlled by ML-based controller. The blue line in the left column is the reference signal and red line is the system output (i.e., fluorescence intensity). The middle column shows the output of the controller applied to the respective ion pumps and the right shows the tracking error of the system. The tracking performance for both rows of the ion pump show a response to the controller commands. However, further improvements will be made in order to improve the tracking performance. There is evidence of undesired coupling between actuation in one row and response of the other. Other improvement approaches include modifications to the device design and variations on voltages not assigned by the controller.

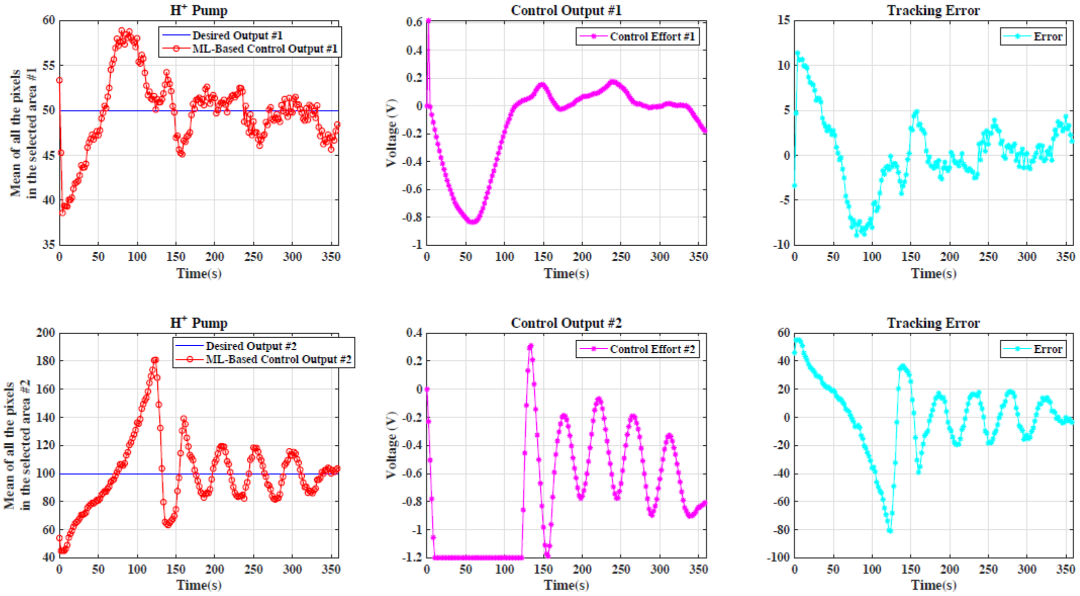

Figure 5.31: The top left plot shows the fluorescence intensity change of pH indicator, SNARF-1, with Texas Red filter of Channel #1 controlled by ML-based controller and the bottom left plot shows the fluorescence intensity change of pH indicator, SNARF-1, with Texas Red filter of Channel #2 controlled by ML-based controller. The blue line in the left column is the reference signal and red line is the system output (i.e., fluorescence intensity). The middle column shows the output of the controller applied to the respective ion pumps and the right shows the tracking error of the system.

In Figure 5.32, left plots show the fluorescence intensity change of H^+ with pH indicator, SNARF-1, with Texas Red filter for the selected areas controlled by

ML-based controller in columns 3 and 5. The blue lines are reference signals and red lines are system outputs (i.e., fluorescence intensity). The middle plots show the outputs of the controllers applied to the ion pumps and the right plots show the tracking error of the system.

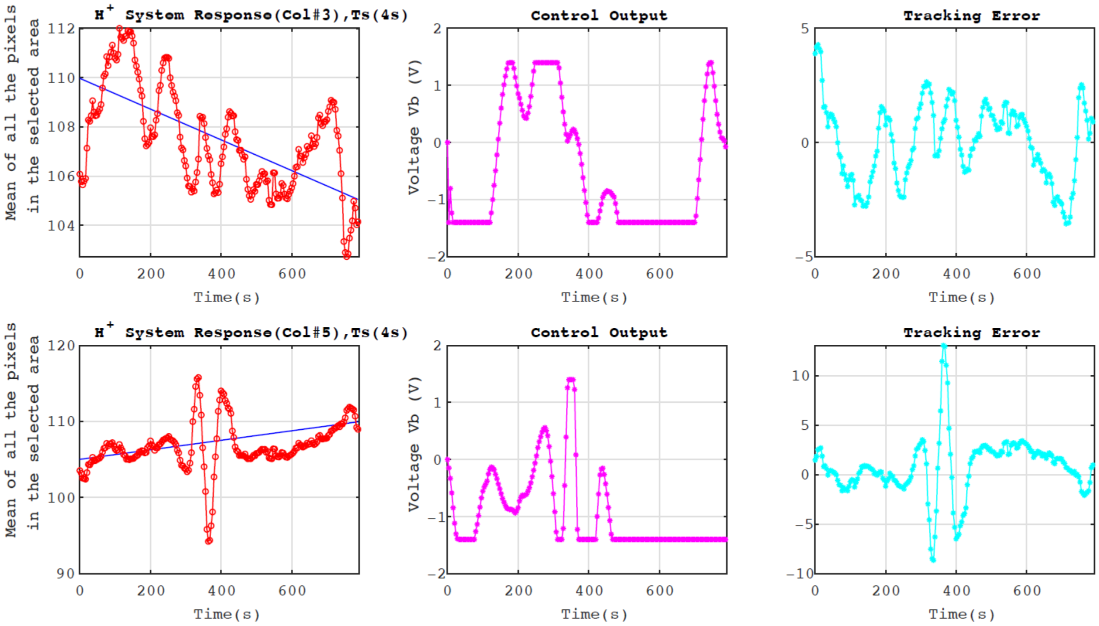

Figure 5.32: Spatially in-homogeneous delivery of H^+ (Water (H2O) in the reservoir; 50uM water with dye in the target.

Multiple-ion Pump System

In addition to individual H^+, K^+, Na^+, and Cl^- ion pumps, we also demonstrate usage of modular multi-channel potentiostat with multiple-ion pump system. Figure 5.7 shows the optical image of the fully fabricated multiple ion pump. The platform is an integration of 4 single ion pumps, H^+, K^+, Na^+, and Cl^- . Each ion pump has a reservoir electrolyte providing ion source, and all of them share one target electrolyte, which are controlled in 4-dimensions. Additionally, an auxiliary electrode located in the target electrolyte is used to manipulate the ion distribution within target electrolyte. The reference electrodes in the source reservoirs and auxiliary electrode are AgCl NPs deposited by electrochemical plating. The reservoirs and target chamber are defined by SU8 insulation layer and the whole channels are covered by microfluidic tapes. Here, 0.1 M HCl, NaCl, KCl and KCl are used as ion sources in the reservoirs of H+ pump, Na+ pump, K+ pump, and Cl- pump, respectively, and the corresponding fluorescent dyes are dissolved in 0.1 M Tris buffer. 5.7 d) shows the microelectrodes array (MEAs) distribution in target electrolyte: the 6 x 6 MEAs was composed of 9 matrixes, and each matrix has 4 MEAs, corresponding to a H+ pump, a Na+ pump, a K+ pump, and a Cl- pump, respectively. The MEAs of H+ pump are coated by Pd NPs, which are selective to H+, and AgCl NPs are used for Cl- pump because of its selectivity to Cl-. Pt NPs are used for K+ and Na+ pump.

In Figure 5.33, the top-left plot shows the fluorescence intensity change of pH indicator, SNARF-1, with Texas Red filter controlled by ML-based controller. Middle-left plot shows the fluorescence intensity change of Na^+ indicator, CoroNa Green, with GFP filter of the selected area controlled by ML-based controller. Bottom-left plot shows the fluorescence intensity change of DAPi images of Cl^- pump with MQAE indicator controlled by ML-based controller. In all plots, the blue line is the reference signal and the red line is the system output (i.e., fluorescence intensity). In addition, the middle-column plots show the output of the controller applied to a multiple-ion pump and the right-column plots show the tracking error of the system. The tracking performance of the multiple-ion pump shows a promising response to the controller commands.

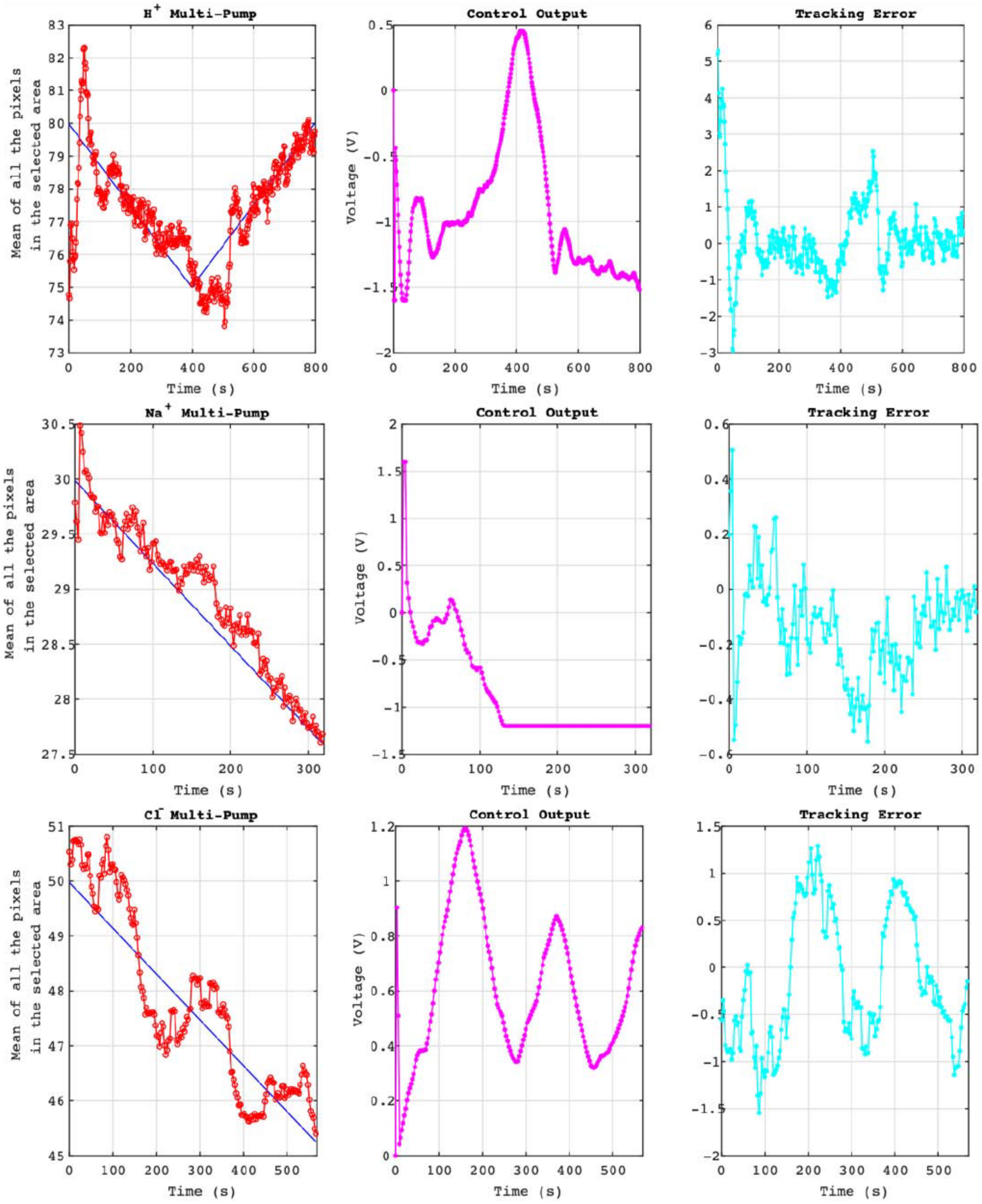

Figure 5.33: Performance of the ML-based controller design for the multiple-ion pump system.

Genetically Modified Stem Cells

This experiment shared a similar setup to the previous closed-loop control with fluorescent dyes but with a hIPSC Arclight stem cell culture instead of fluorescent dye.

The setup consists of EVOS FL Auto 2 recording images into the shared folder. It is connected to the laptop that runs a machine learning controller via Ethernet cable; the same laptop also connects to the multi-channel potentiostat via Wi-Fi as shown in Figure 5.1.

[Jafari et al., 2020] demonstrates a machine learning control algorithm for control of H^+ concentration in a cell culture. Experiments were conducted on Arclight iPSC cell line with H^+ ion pump and [Pansodtee et al., 2019] multi-channel potentiostat.

We successfully ran the ML-based control on hIPSC Arclight stem cells using both H+ and K+ ion pumps. In Figure 5.34, left plot shows the fluorescence intensity change of hIPSC Arclight stem cells membrane potential with GFP filter of the selected area controlled by the ML-based controller. The blue line in the left plot is the reference signal and red line is the system output (i.e., fluorescence intensity). The middle plot shows the output of the controller applied to the H+ ion pump and the right plot shows the tracking error of the system. The tracking performance of V_{mem} control with H+ pump shows a promising response to the controller commands.

In Figure 5.35, left plot shows the fluorescence intensity change of hIPSC Arclight stem cells membrane potential with GFP filter of the selected area controlled by the ML-based controller. The blue line in the left plot is the reference signal

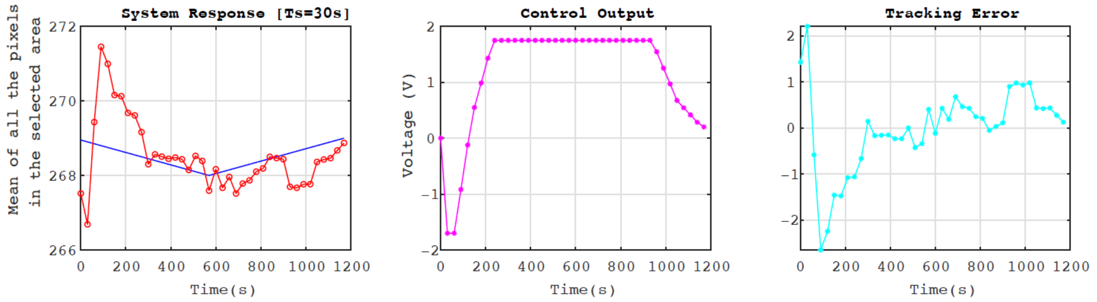

Figure 5.34: V_{mem} control with H^{+} ion pump, sampling every 30 seconds

and red line is the system output (i.e., fluorescence intensity). The middle plot shows the output of the controller applied to the K+ ion pump and the right plot shows the tracking error of the system. The tracking performance of V_{mem} control with K+ pump shows a promising response to the controller commands.

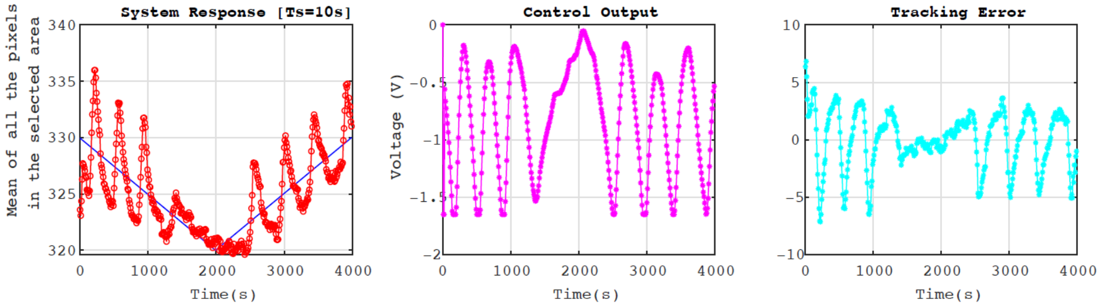

Figure 5.35: V_{mem} control with K^{+} ion pump, sampling every 10 seconds.

We successfully ran the spatial control on hIPSC Arclight stem cells using both H+ and K+ with this remote scheme. In Figure 5.36, left plot shows the fluorescence intensity change of hIPSC Arclight stem cells membrane potential at the selected areas controlled by ML-based controller. The blue line is reference signal and red line is the system output (i.e., fluorescence intensity). The middle plot shows the output of the controller applied to the H+ ion pumps and the right plot shows the tracking error of the system. Each controller only applies the voltage VB to its associated row. Whenever the voltage is applied to a specific row, the other rows are floated. The sampling time (Ts) is divided equally for each active row to be controlled.

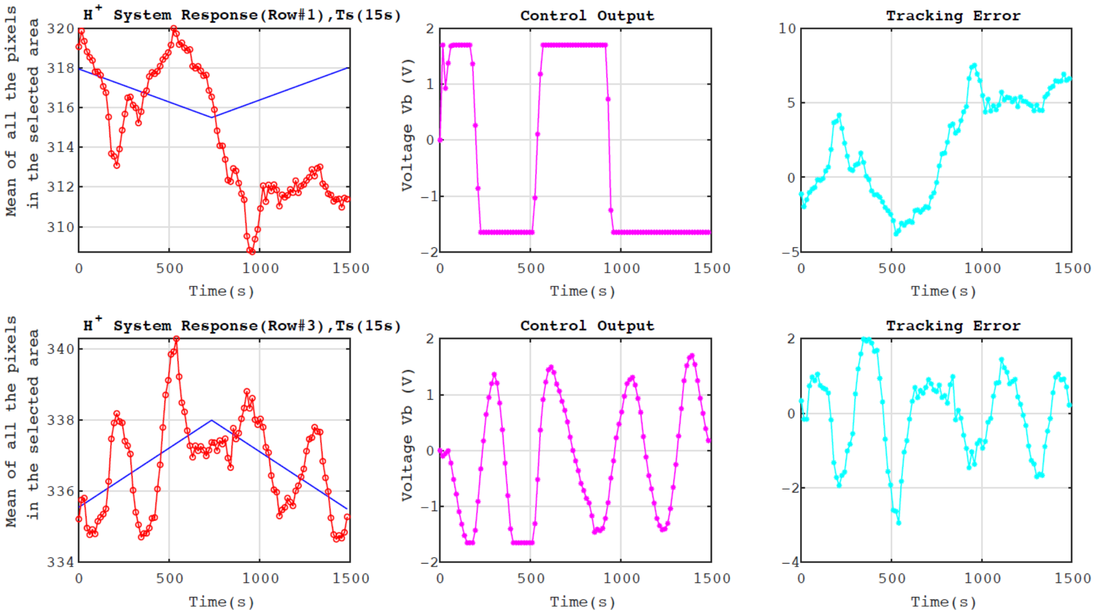

Figure 5.36: Spatial V_{mem} control with H^+ ion pump, sampling time every 15 seconds.

In Figure 5.37, left plot shows the fluorescence intensity change of hIPSC Arclight stem cells membrane potential at the selected areas controlled by ML-based controller. The blue line is reference signal and red line is the system output (i.e., fluorescence intensity). The middle plot shows the output of the controller applied to the K+ ion pumps and the right plot shows the tracking error of the system. Each controller only applies the voltage VB to its associated row. Whenever the voltage is applied to a specific row, the other rows are floated. The sampling time (Ts) is divided equally for each active row to be controlled.

Note that there are occasions when cells stop responding for unknown reasons. Some possible explanations include the inability of cells to continuously respond under consistent excitation, possible contamination, and/or stressful conditions from reduced flow in the microfluidics device. In addition, the sampling time is

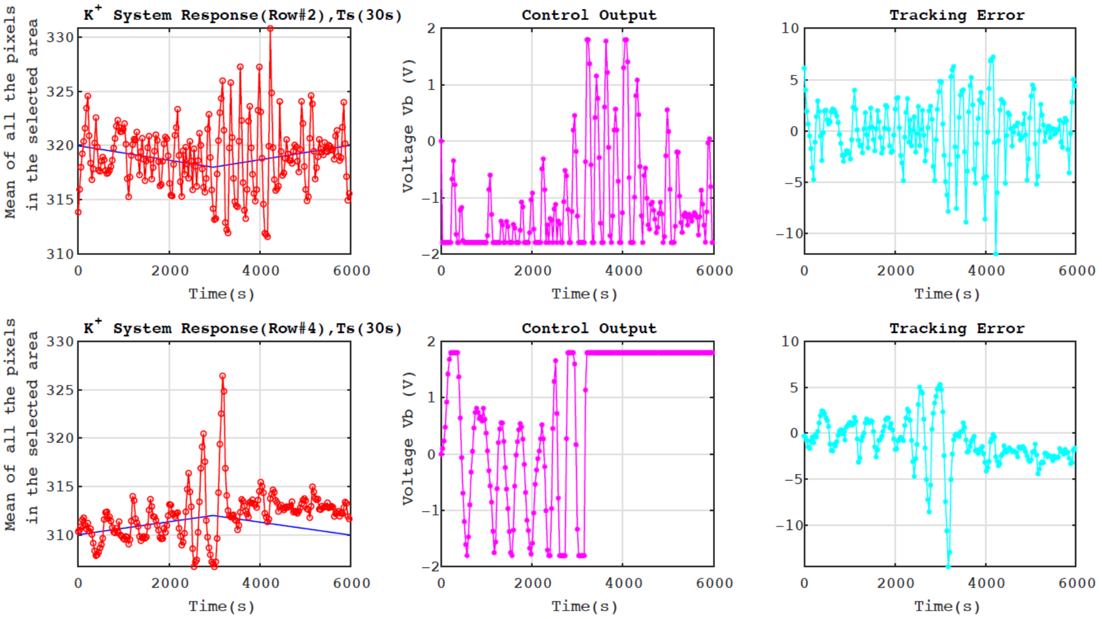

Figure 5.37: Spatial V_{mem} control with K^+ ion pump, sampling time every 30 seconds.

high and could be imparting phototoxicity or bleaching. Moreover, we observed some oscillations, which could be due to the run being too short or steady-state could not be achieved (e.g. dynamics are too slow to keep up with the reference signal). To improve the above mentioned issues, we tried longer runs in order to demonstrate convergence of algorithm and to better assess performance (e.g., damping the oscillations). Furthermore, to achieve long-term runs, we proposed a new method in which we alternate between stimulating cells and letting them rest.

Figure 5.38 shows the proposed scheme described above and tested as an improvement to the current method of continuously stimulating the cells. The idea is to reach the target in a finite time ("Achieving the Target Time" scheme) by combining the floating and stimulating steps. We stimulated the cells during the "Stimulation Time" and gave them some time to rest during the "Floating Time". In other words, instead of stimulating cells continuously, this idea is to stimulate and rest cells on alternating turns. During the stimulation time, we direct the cells towards the temporal target; during the floating time, we do nothing in order to give cells time to rest.

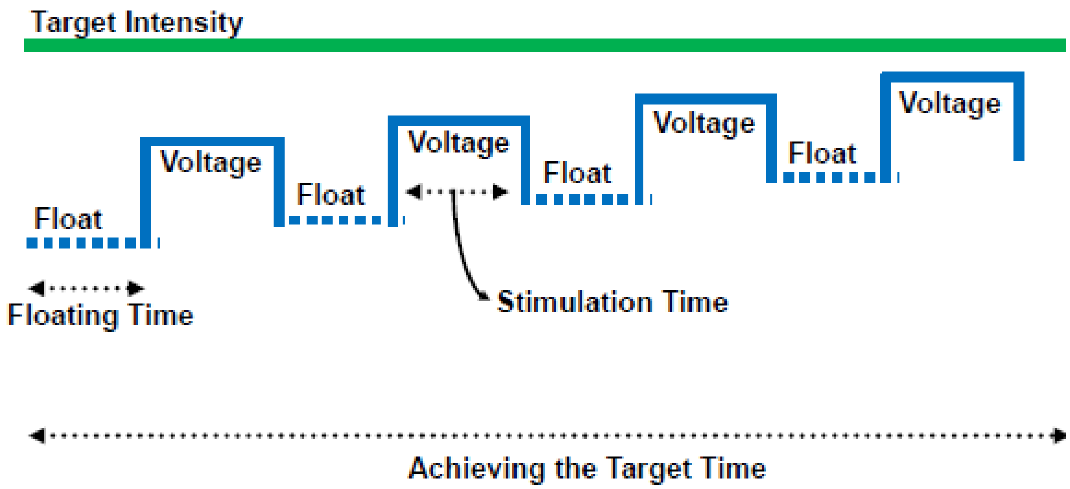

Figure 5.38: Proposed scheme for achieving long term V_{mem} control ("Floating + Stimulation" approach).

To achieve long term V_{mem} control with the "Floating + Stimulation" approach (see Figure 5.39), we tried several schemes. We observed that the following scheme (30 mins floating + 30min stimulation and relative increase by +2 fluorescence intensity unit) is promising and the fluorescence intensity of cells increased by about 8 units in total over the course of the experiment (10 mV change). In Figure 5.39, the top plot shows the fluorescence intensity change of cell membrane potential at the selected areas controlled by ML-based controller for over 13 hours. The blue line is the reference signal, the green line is the mean value of the fluorescence intensity during the floating time and red line is the system output (i.e., fluorescence intensity). The bottom plot shows the output of the controller applied to the H+ ion pump (no control during the floating time).

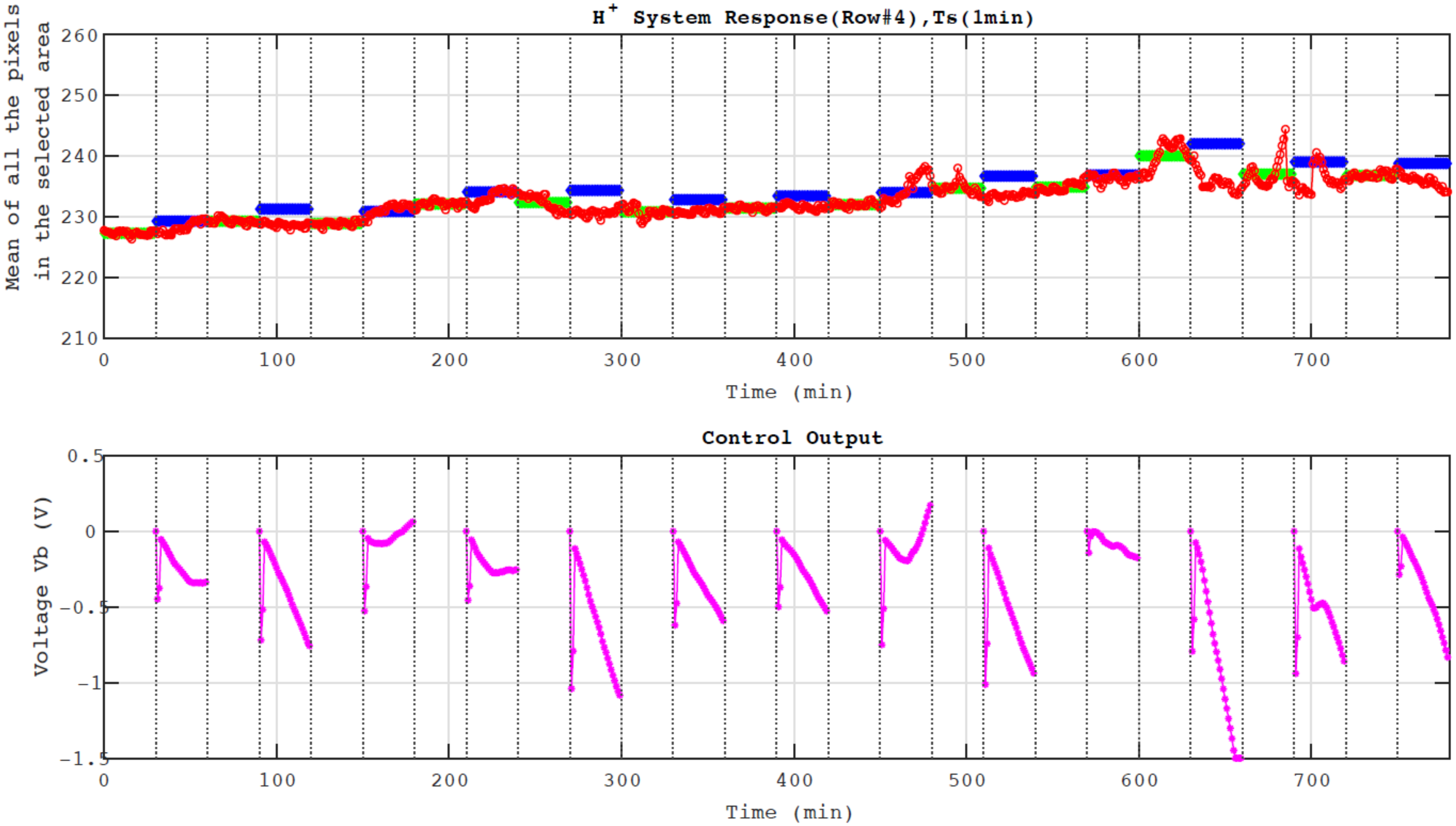

Figure 5.39: Long term V_{mem} control with H^+ ion pump (over 13 hours).

We are successful in demonstrating the ML-based feedback control on hIPSCs stem cells with Arclight and KRT14mCherry (keritinocytes) reporter in a microfluidic device with varying media flow using H+ pump with the new design (higher channel). Moreover, long term (over 19 hours) V_{mem} control with H+ pump has been achieved. To achieve differentiation through long term V_{mem} control, we proposed an updated version of the "Floating + Stimulation" method in which we alternate between stimulating cells and letting them rest by considering both GFP and RFP. Figure 5.40 shows the idea behind the proposed scheme that was tested towards achieving differentiation through long term V_{mem} control. The idea is to reach the target V_{mem} (i.e., at which the cells start to differentiate and the red reporter turns on) in a finite time ("Achieving the Target Time", Red turns on) by combining the floating and stimulating steps (shown in figure 5.38-left "Step 1"). We stimulated the cells during the "Stimulation Time" and gave them some time to rest during the "Floating Time". When the red reporter turns on, the proposed algorithm continues to the "Floating + Stimulation" however, this time the target is fixed to the V_{mem} detected in the previous step (i.e., Step 1).

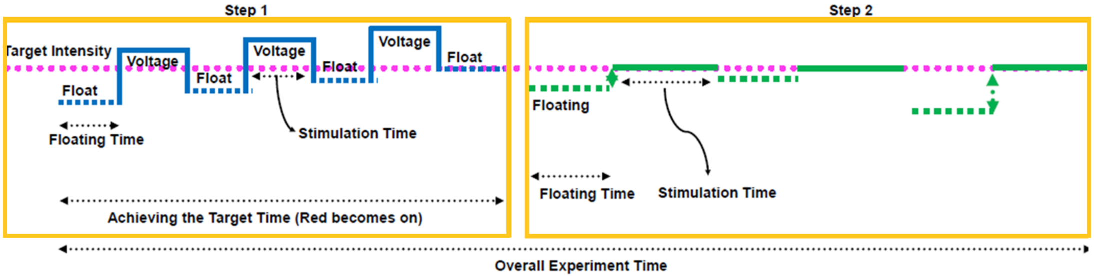

Figure 5.40: Proposed scheme for achieving differentiation through long term V_{mem} control with the updated "Floating + Stimulation" approach.

In Figure 5.41, the top plot shows the fluorescence intensity change of cell membrane potential at the selected areas controlled by ML-based controller for over 19 hours, where blue is reference signal, magenta is the mean value of the fluorescence intensity during floating time and green is the system output (i.e., fluorescence intensity). The middle plot shows the output of the controller applied to the ion pumps (no control during the floating time) and the red plot shows the RFP images at the selected areas.

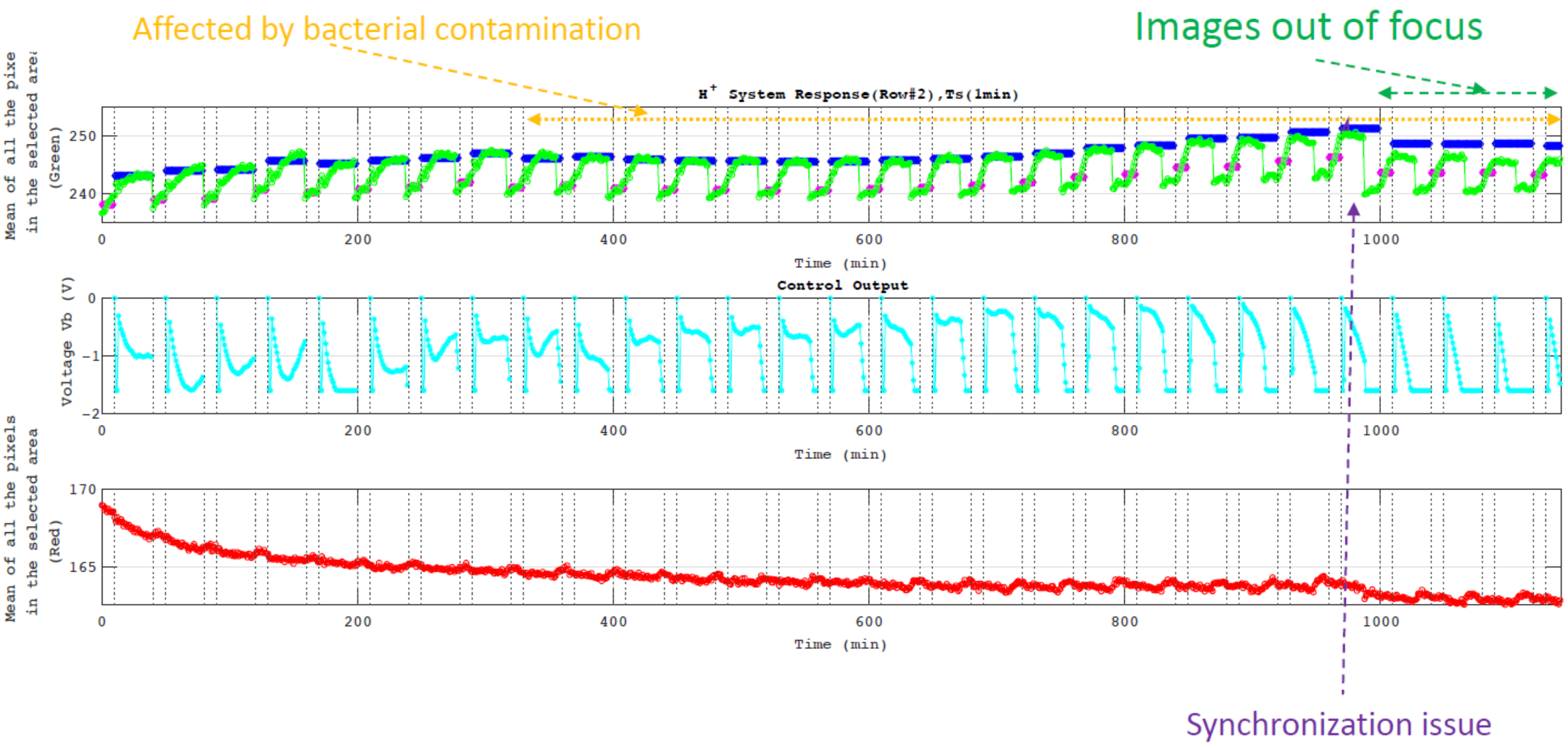

Figure 5.41: Long term V_{mem} control with H^+ ion pump (over 19 hours).

5.4 In-Vivo

The ultimate goal of the *in-vivo* experiment is to inject various ions and drugs into an wounded mouse and subsequently accelerate its healing process. However, mouse experiments impose many constraints on the system (i.e., weight, size, power consumption). Therefore, every component needs to be heavily miniaturized and optimized for the lowest power consumption.

For instance, a vertical ion pump was miniaturized into a 20 mm diameter circular PDMS piece with a PCB on top. In addition, we're working on designing a removable miniature fluorescence microscope to replace a tabletop fluorescence microscope. At the present time, all the works are still in-progress and the miniaturized H^+ ion pump only performs basic open-loop control.

Figure 5.42 shows a complete system where the integrated device is mounted on a mouse wound and consists of a removable imaging unit and a rigid or flexible PCB which attaches to miniaturize ion pump.

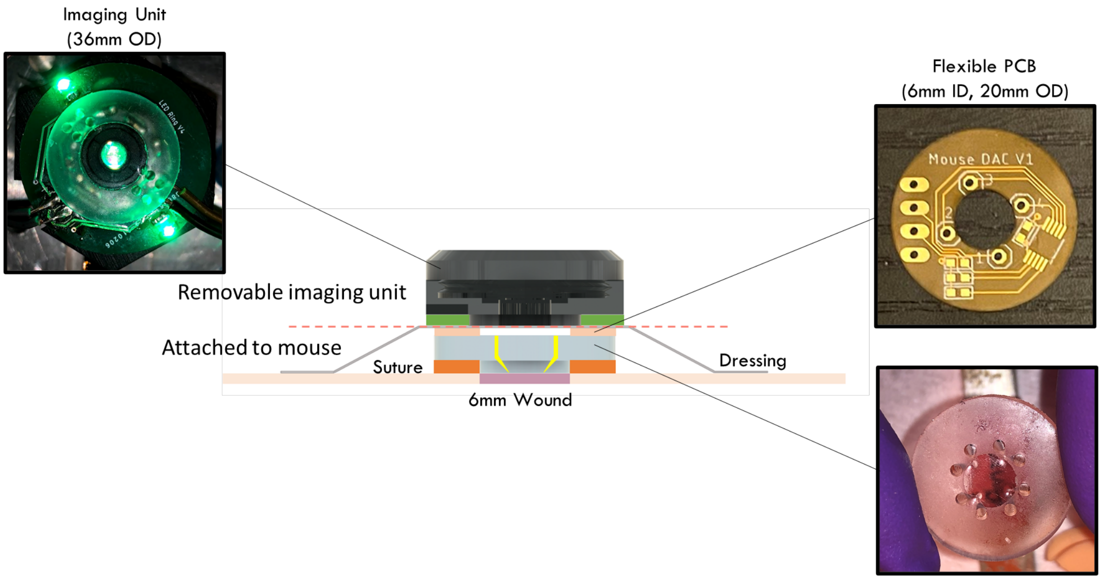

Figure 5.42: Overview of *in-vivo* device

Figure 5.43 shows a close-up of a PCB which sits on top of a PDMS, miniaturized ion pump. The PCB contains three Palladium electrodes, one Silver/Silver Chloride electrode and four jumper wires.

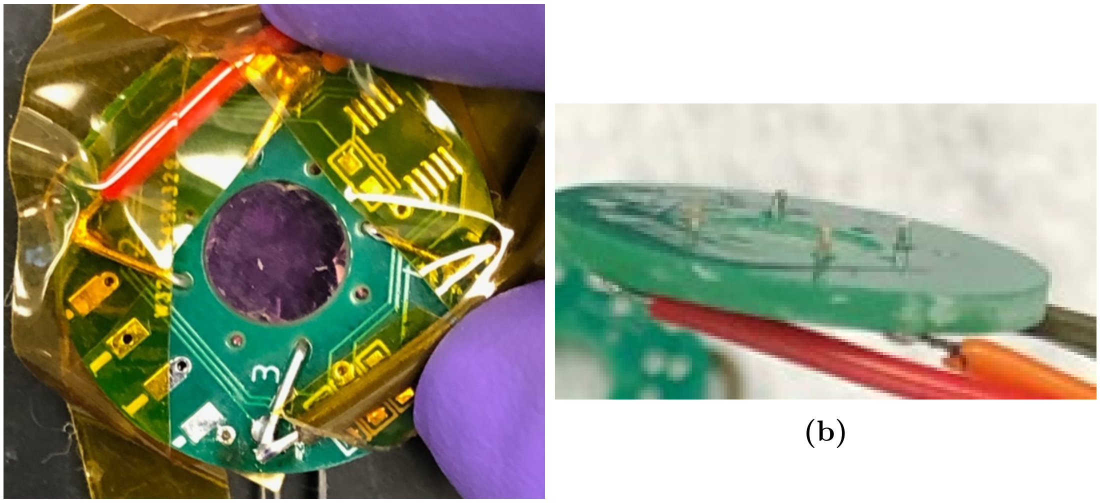
(a)

(b)

Figure 5.43: Close-up of the PCB which contains three Pd electrodes, one Ag/AgCl electrode and four jumper wires. a) Top-side b) Bottom-side

5.4.1 Open-Loop Control with Ion Pumps

Similar to other ion pumps, the system is first tested with a color-metric dye and later used in an animal experiment.

Color-metric dye

The unit is tested with Phenol red, water-soluble dye used as a pH indicator. The Phenol red changes from yellow to red over pH 6.6 to 8.0, and then turns a bright pink color above pH 8.1. In this experiment, a $3\,V_{pp}$ square wave is applied to electrode 1 and 4 as shown in Figure 5.44. The zoomed in picture shows yellow spots around electrode 1 and 4, indicating that the solution around electrode 1 and 4 are turning more acidic.

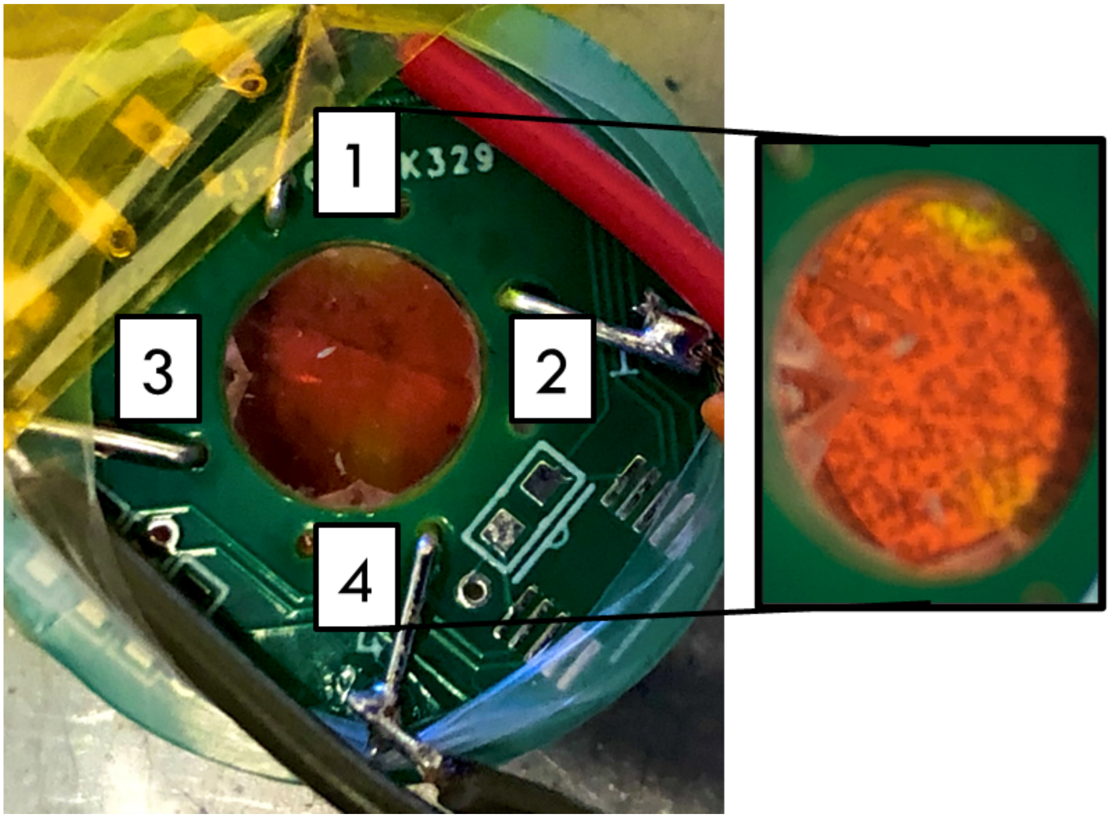

Figure 5.44: Phenol Red experiment. Applying $3V_{pp}$ square wave to the electrode 1 and 4. Zoomed in picture shows yellow spots around electrode 1 and 4 indicates the spots becoming more acidic.

Mouse Experiments

Once we successfully demonstrated the ability to inject H^+ or lower a pH with color-metric dye, we moved towards performing a mouse experiment. In this experiment, the system is mounted on a mouse directly on top of a 6 mm diameter wound. Later, a miniaturized H^+ ion pump is connected to the non-modular multi-channel potentiostat for actuation. We apply the same $3V_{pp}$ square wave to the unit, record a current via a potentiostat and image via a removable imaging unit.

Figure 5.45, 5.46 shows a surgeon attaching the system on top of a mouse. Figure 5.47 shows a removable imaging unit while imaging the wound site.

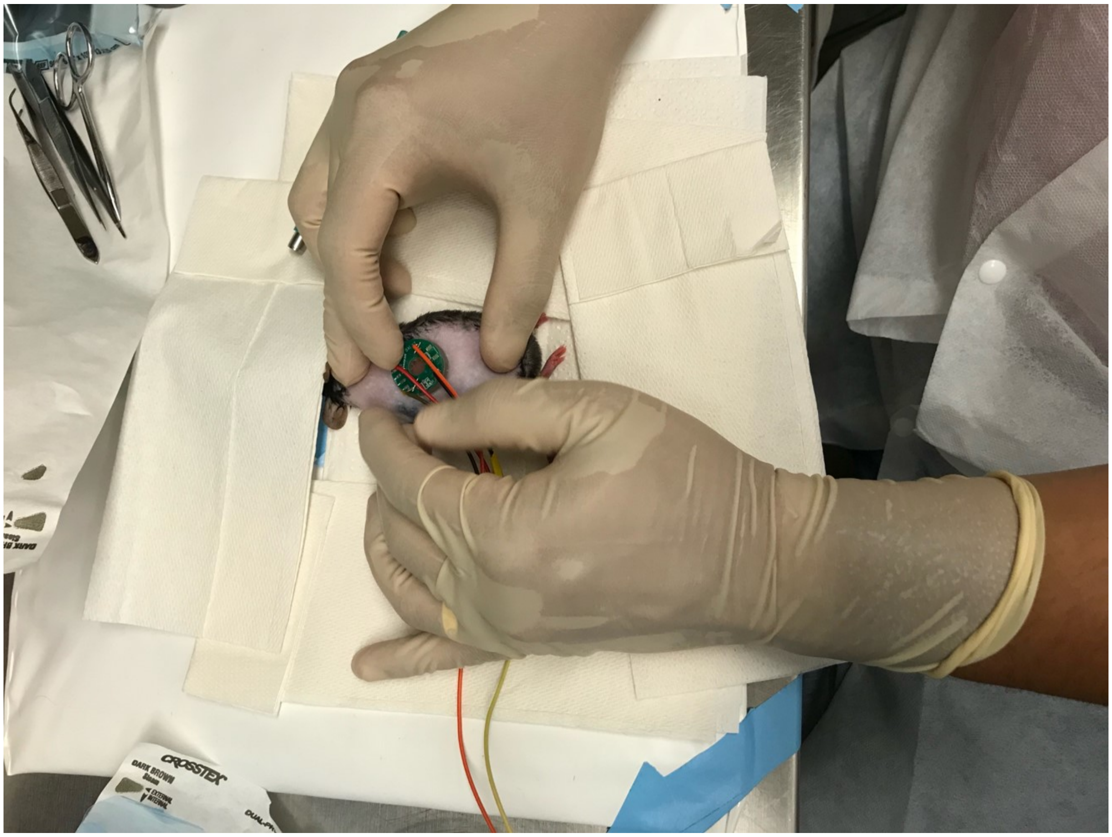

Figure 5.45: A surgeon attaching the system on top of a mouse.

Figure 5.48 and 5.49 show current profiles from device 4, 5, and 6 during experiments. The current maxes out at 2 μA due to an upper limit of a non-modular multi-channel potentiostat. From these preliminary results, we believe that the system is able to delivery H^+ to a wound site.

5.5 Conclusion

In this chapter, we explore the multi-potentiostat integration with various versions of ion pumps. I designed several versions of interface boards and acrylic holders for each variation of ion pumps. The work mainly focuses on *in-vitro* ion pump starting from open-loop control on fluorescent dyes and later closed-

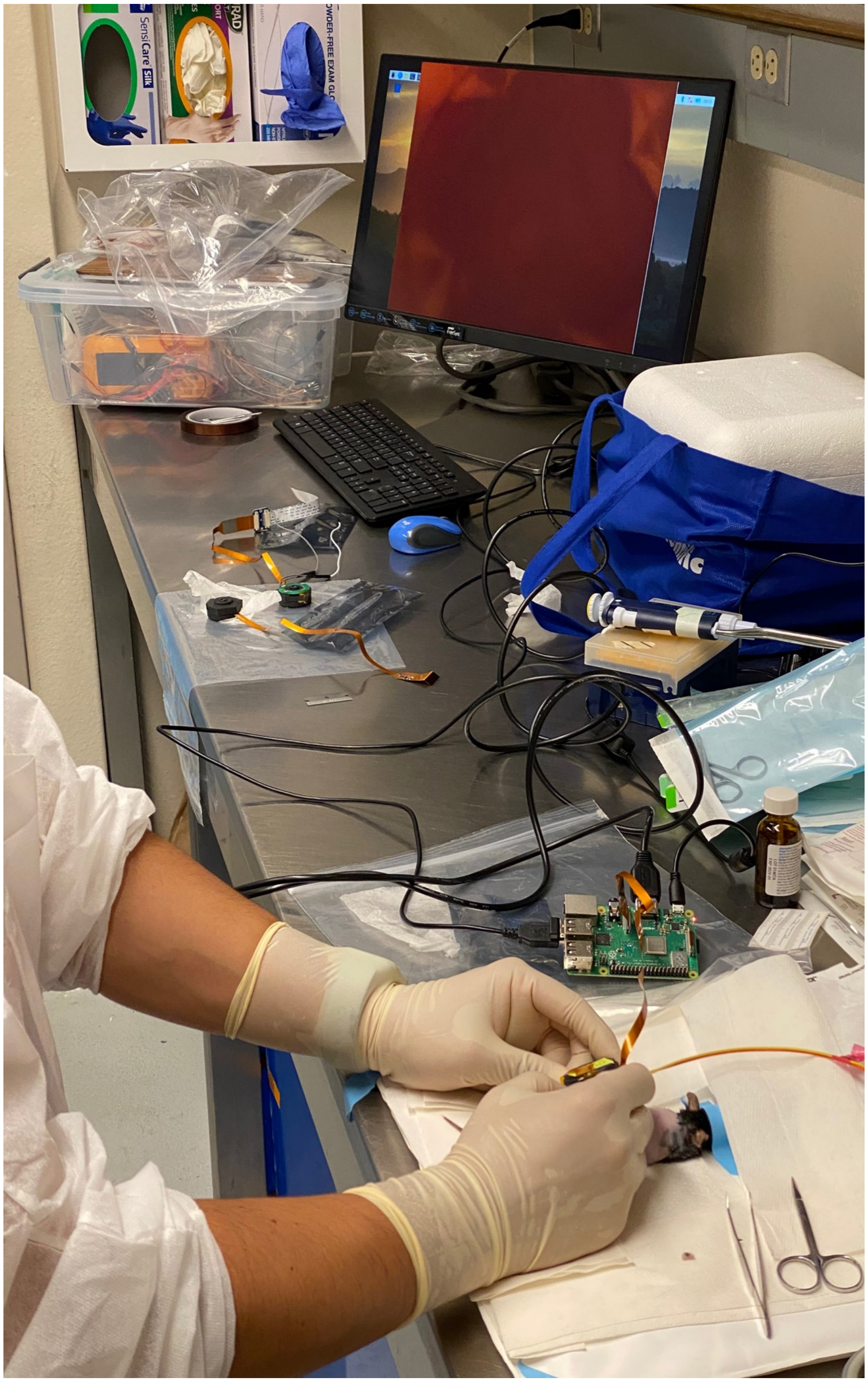

Figure 5.46: A surgeon attaching the system on top of a mouse.

loop control on fluorescent dyes and genetically modified stem cells. The system successfully demonstrates the ability to control different versions of ion pumps in

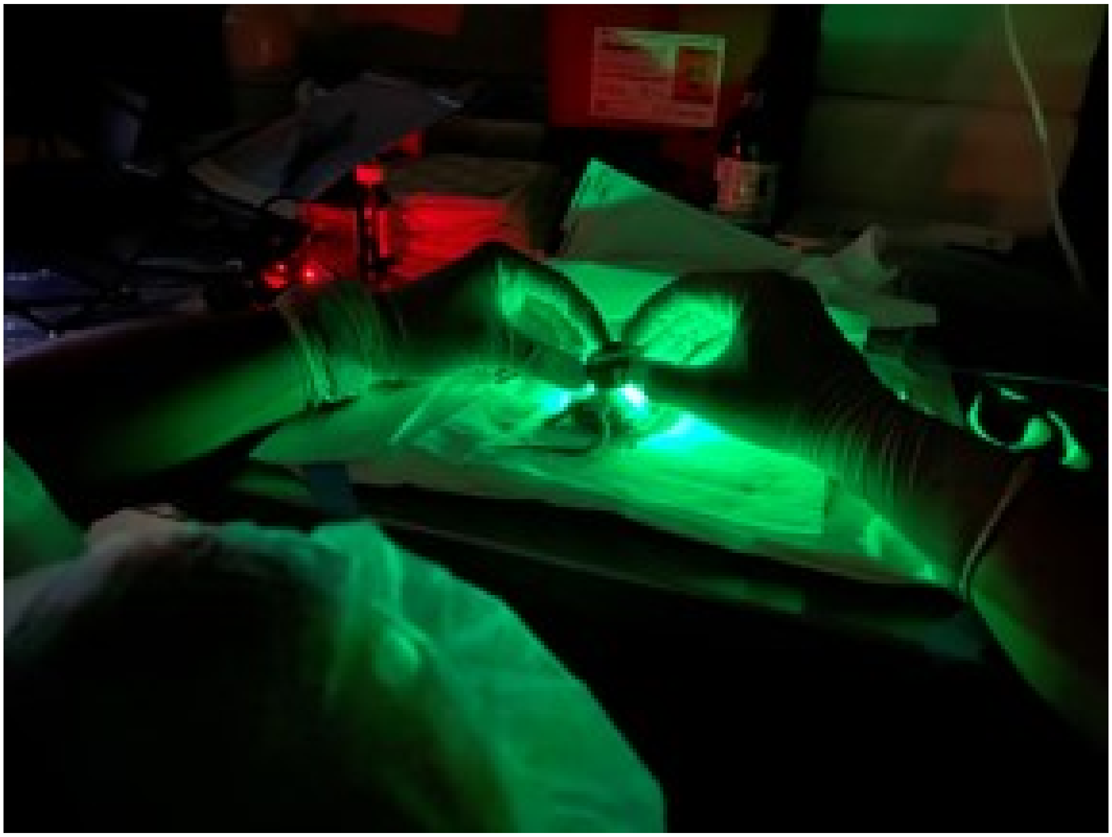

Figure 5.47: A removable imaging unit while imaging the wound site.

various environments in both standalone and externally controlled modes. As a result, combined with a fluorescence microscope, the system can perform closed-loop control in a biological sample. It is worth noting that this is the first time anyone has performed closed-loop control in a biological sample.

Finally, we conducted a preliminary study with an early prototype of an *in-vivo* ion pump and the non-modular multi-channel potentiostat on mice wounds. The experiments shows promising results suggesting that we are able to change pH on wounded mouses.

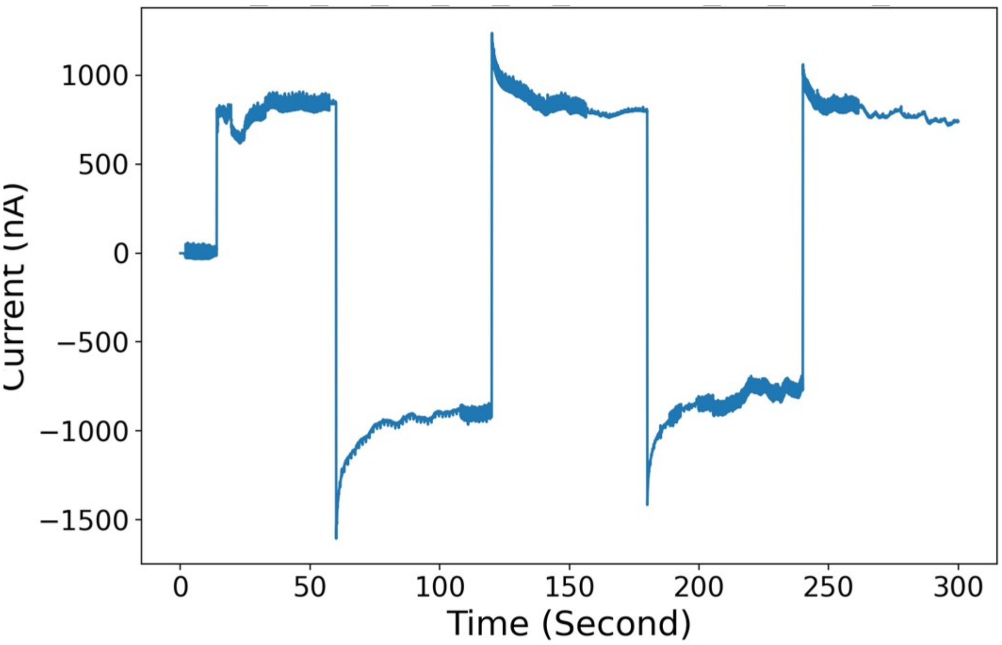

Figure 5.48: Current profile from device 4 while applying $3\,V_{pp}$ square wave.

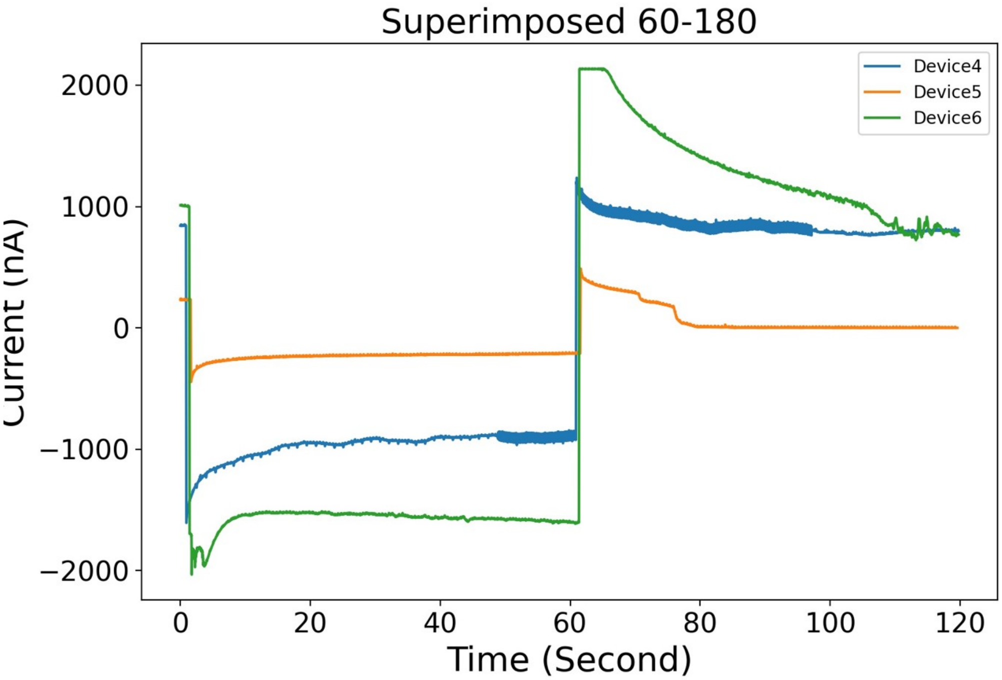

Figure 5.49: Current profile from device 4, 5, and 6 during experiments.

Appendix A

Appendix

A.1 Glucose sensor

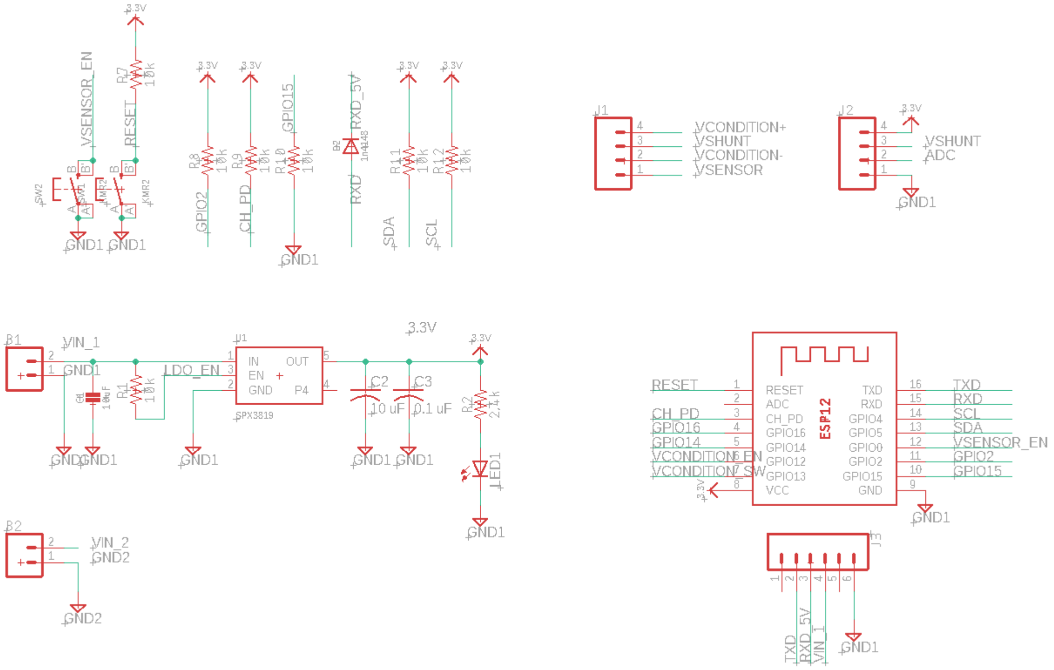

Figure A.1: Schematic of glucose data acquisition v4. 1/2

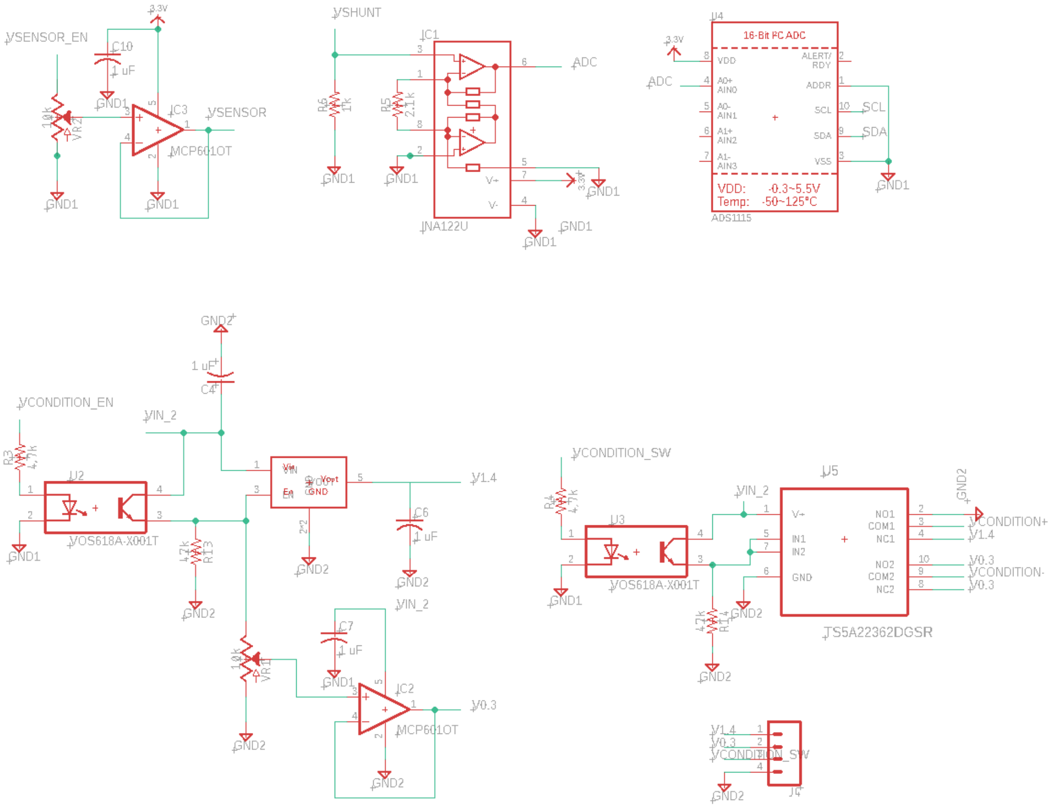

Figure A.2: Schematic of glucose data acquisition v4. 2/2

A.2 Ions sensor

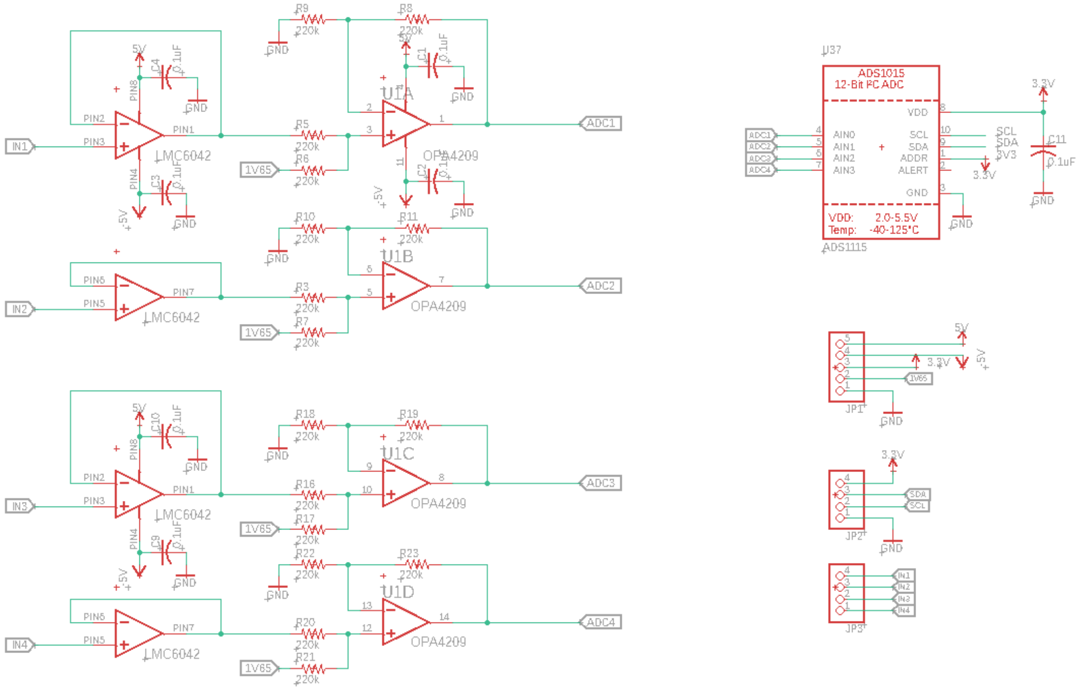

Figure A.3: Schematic of ion sensor data acquisition unit

A.3 Picroscope

A.3.1 Power distribution board

For left and right power distribution boards follow step#1-4 and 8. And for middle power distribution board follow step#1-8.

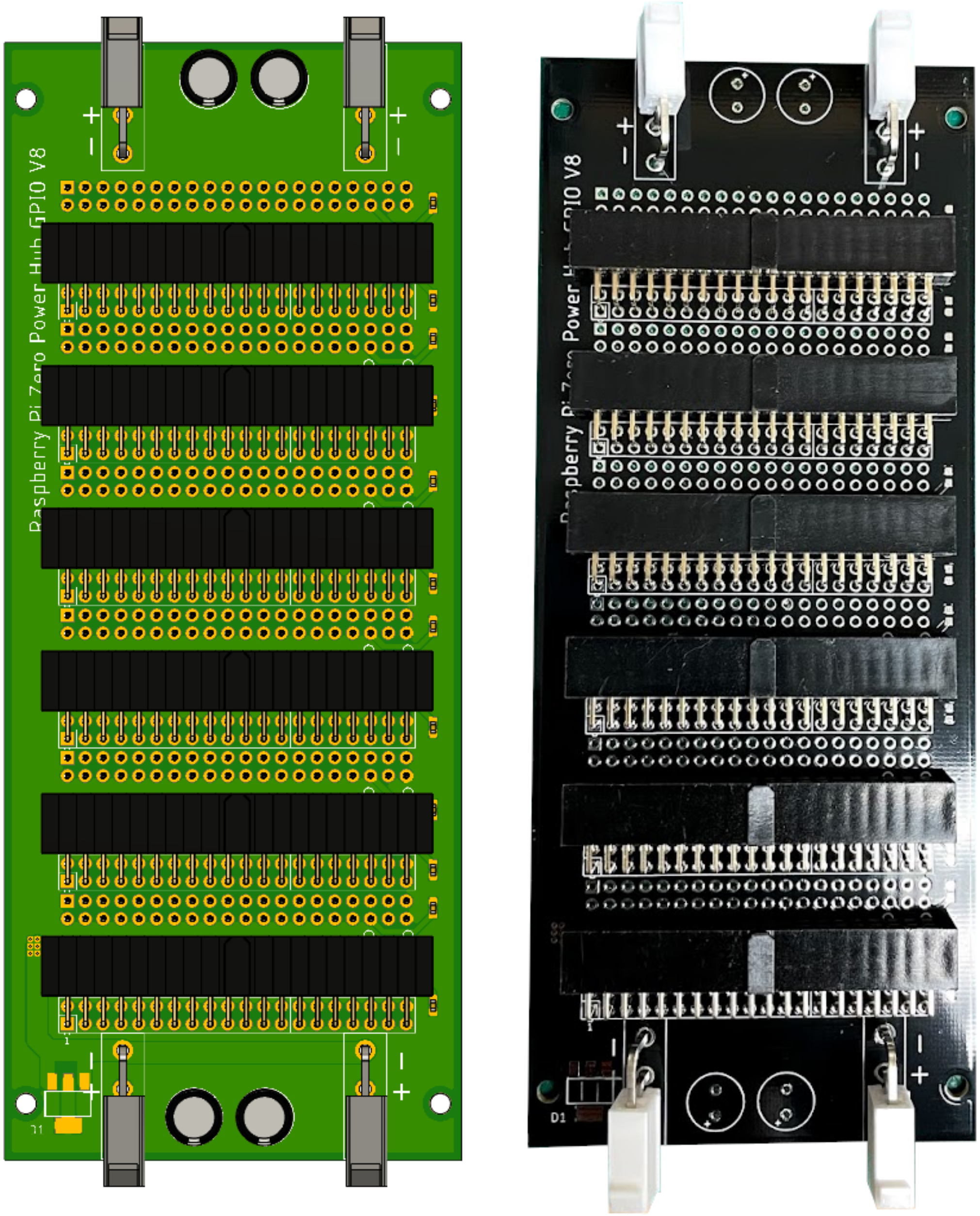

(a) Render of power distribution board

(b) Power distribution board

Figure A.4: Power distribution board

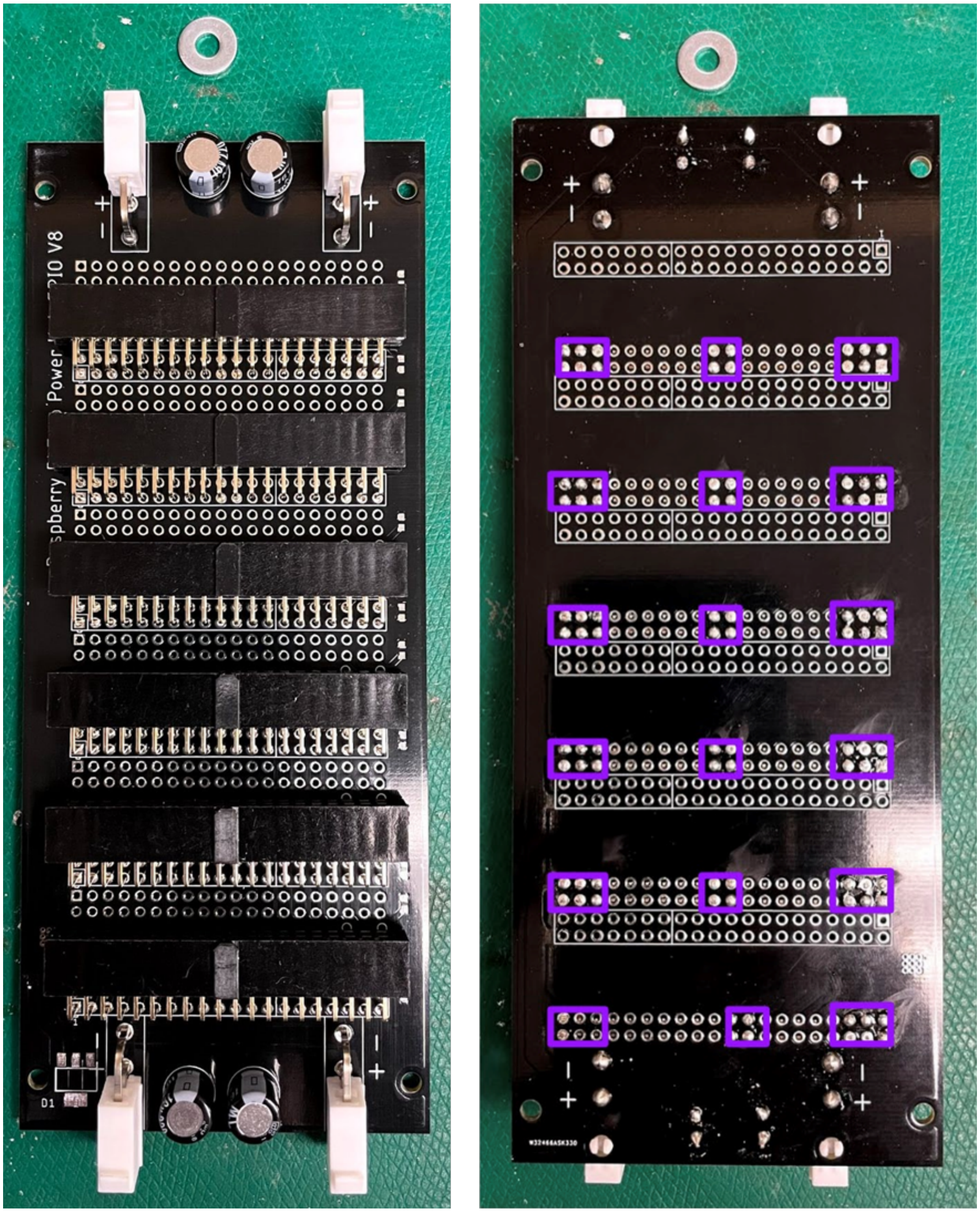

Figure A.5: Power distribution board - left: Top and Bottom (Purple: required soldering locations)

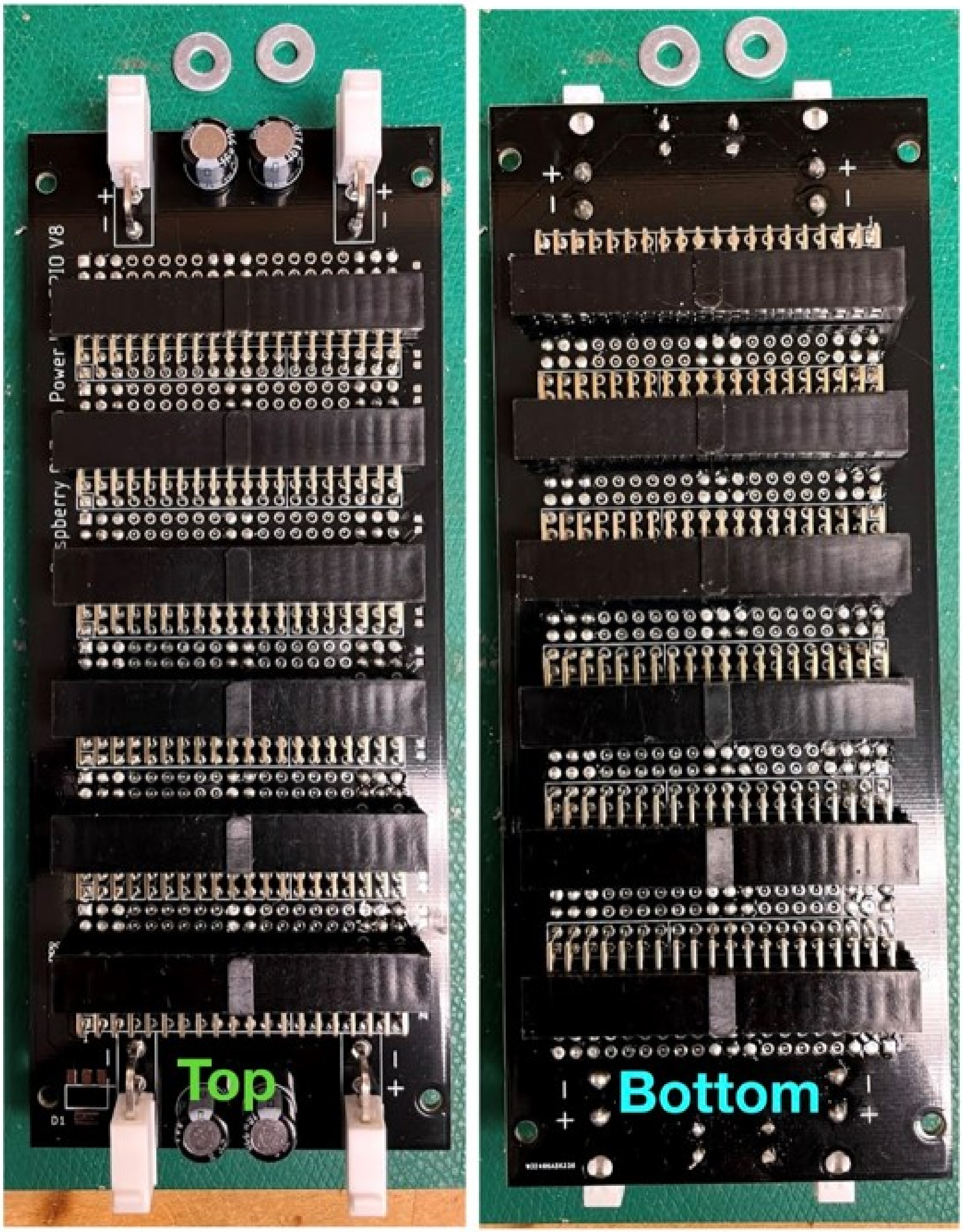

Figure A.6: Power distribution board - middle: Top and Bottom

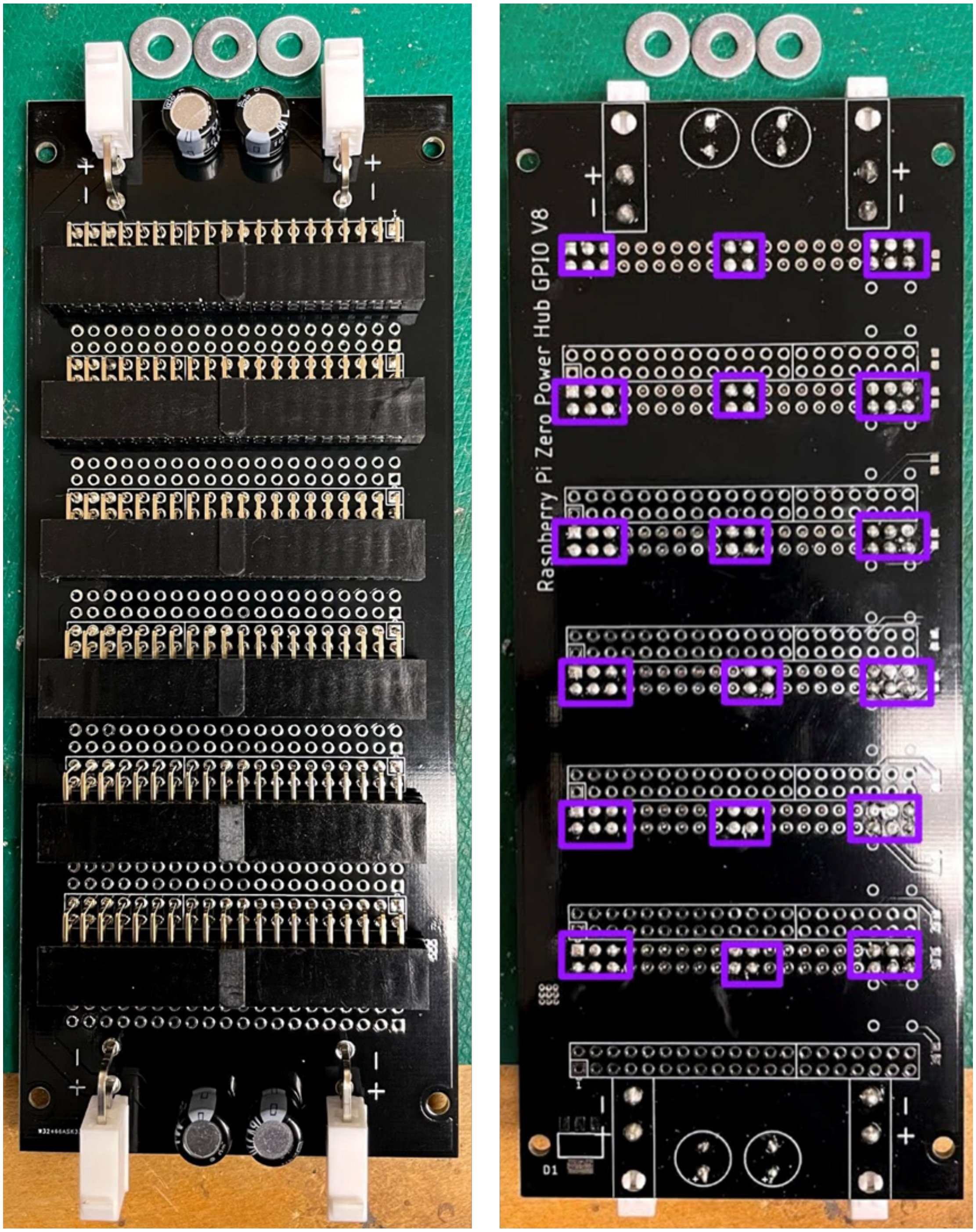

Figure A.7: Power distribution board - right : Top and Bottom (Purple: required soldering locations)

Figure A.8: Step#1: Place SFH11-PBPC-D20-RA-BK connector into a slot (left) and use a credit card to raise the connector before soldering (right).

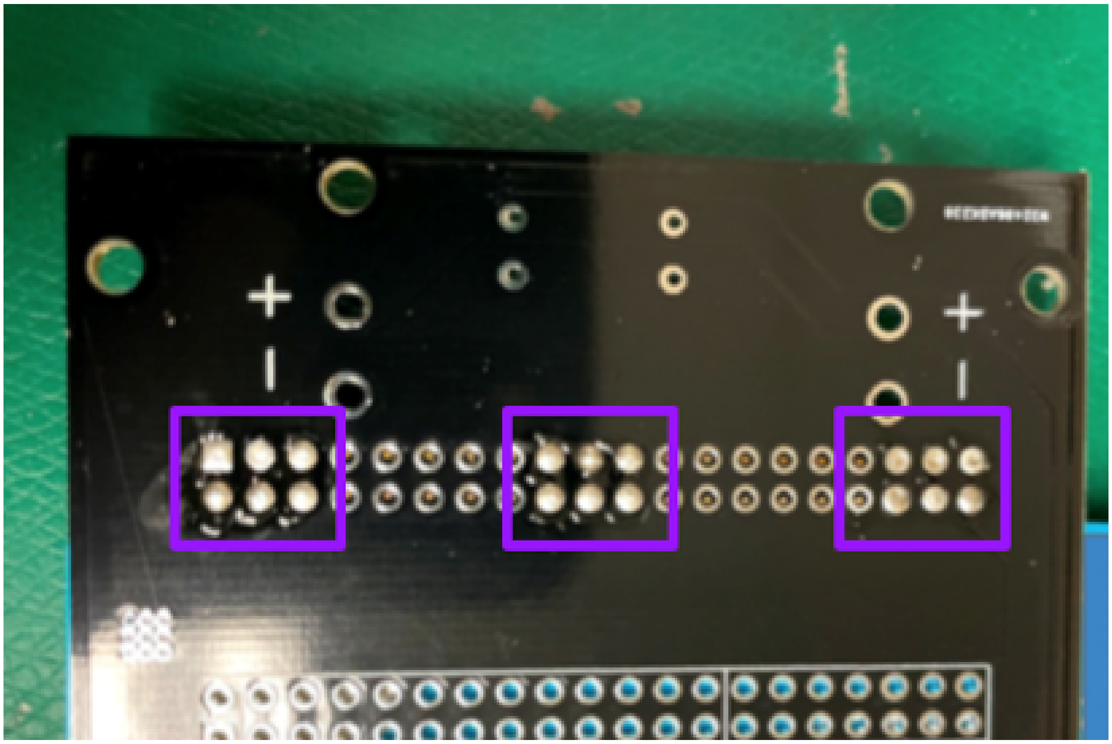

Figure A.9: Step#2: Soldering 6 pins (like the purple boxes) for the left, middle and right

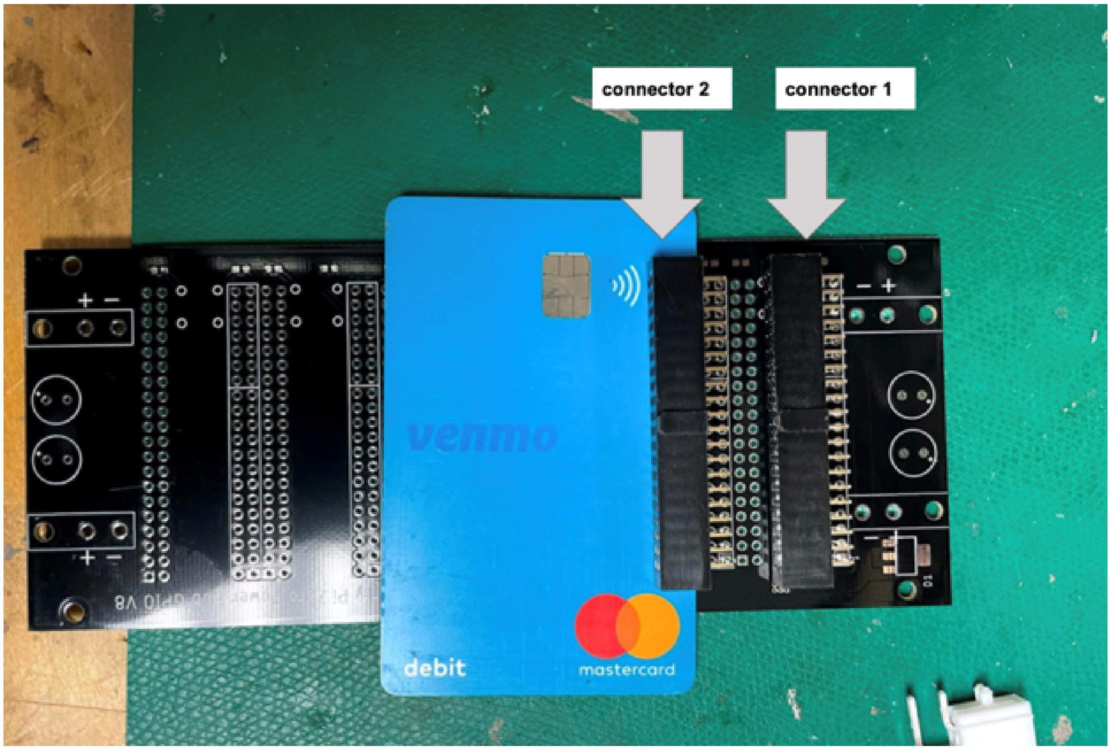

Figure A.10: Step#3: Soldering the rest of the connectors.

Figure A.11: Step#4: One side is complete

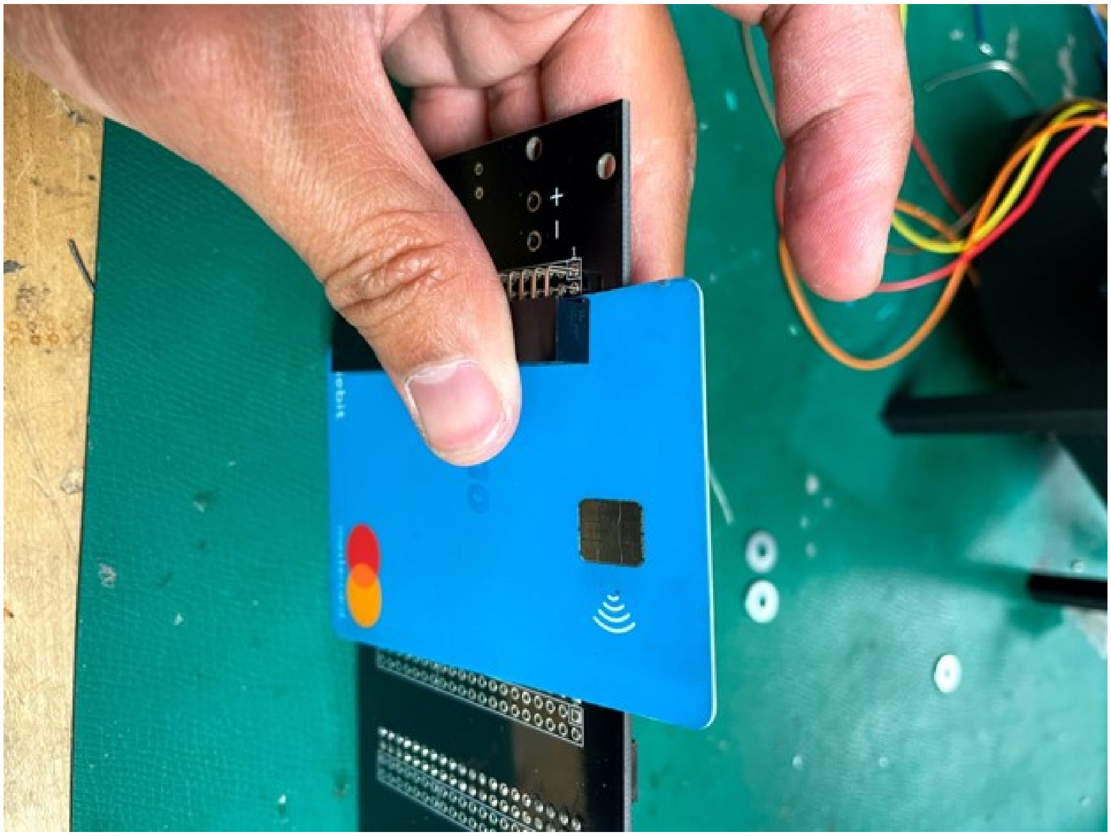

Figure A.12: Step#5: Insert the connector on the other side, and use a credit card to raise the connector gap.

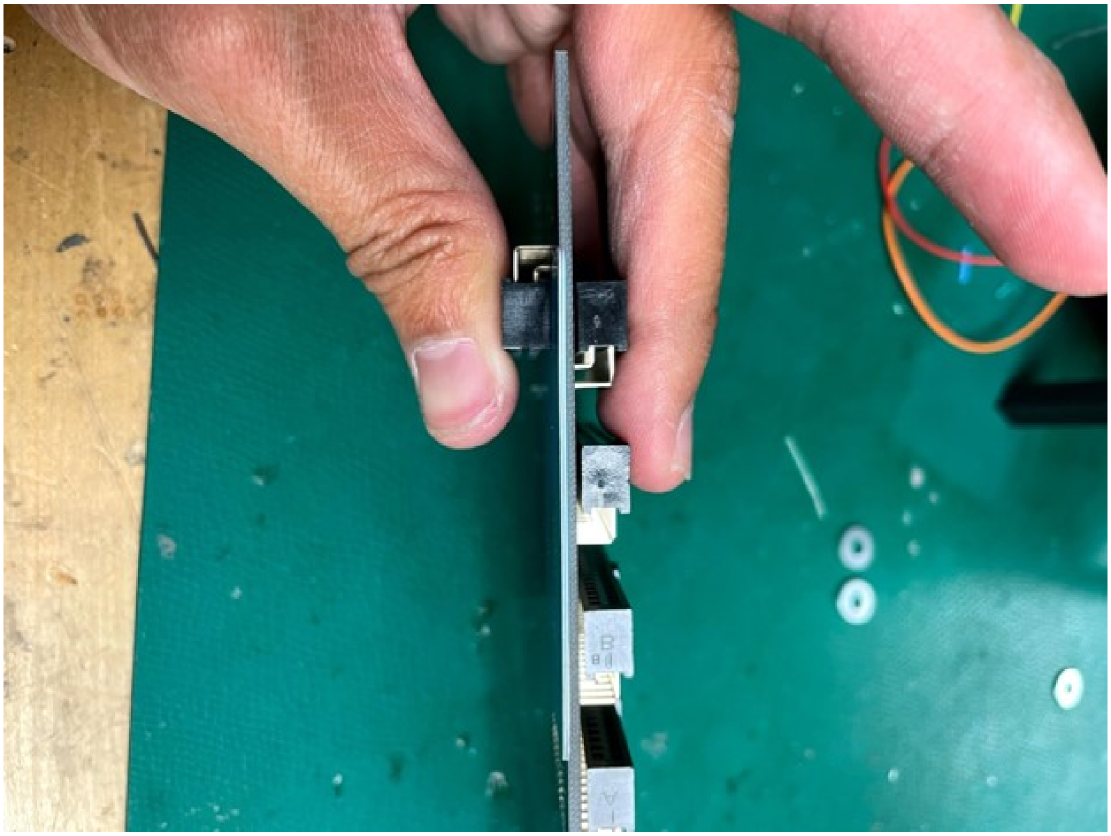

Figure A.13: Step#6: Avoid touching the soldering iron to the black plastic piece and make sure it is still lifted properly.

Figure A.14: Step#7: Continue until the PCB is fully populated.

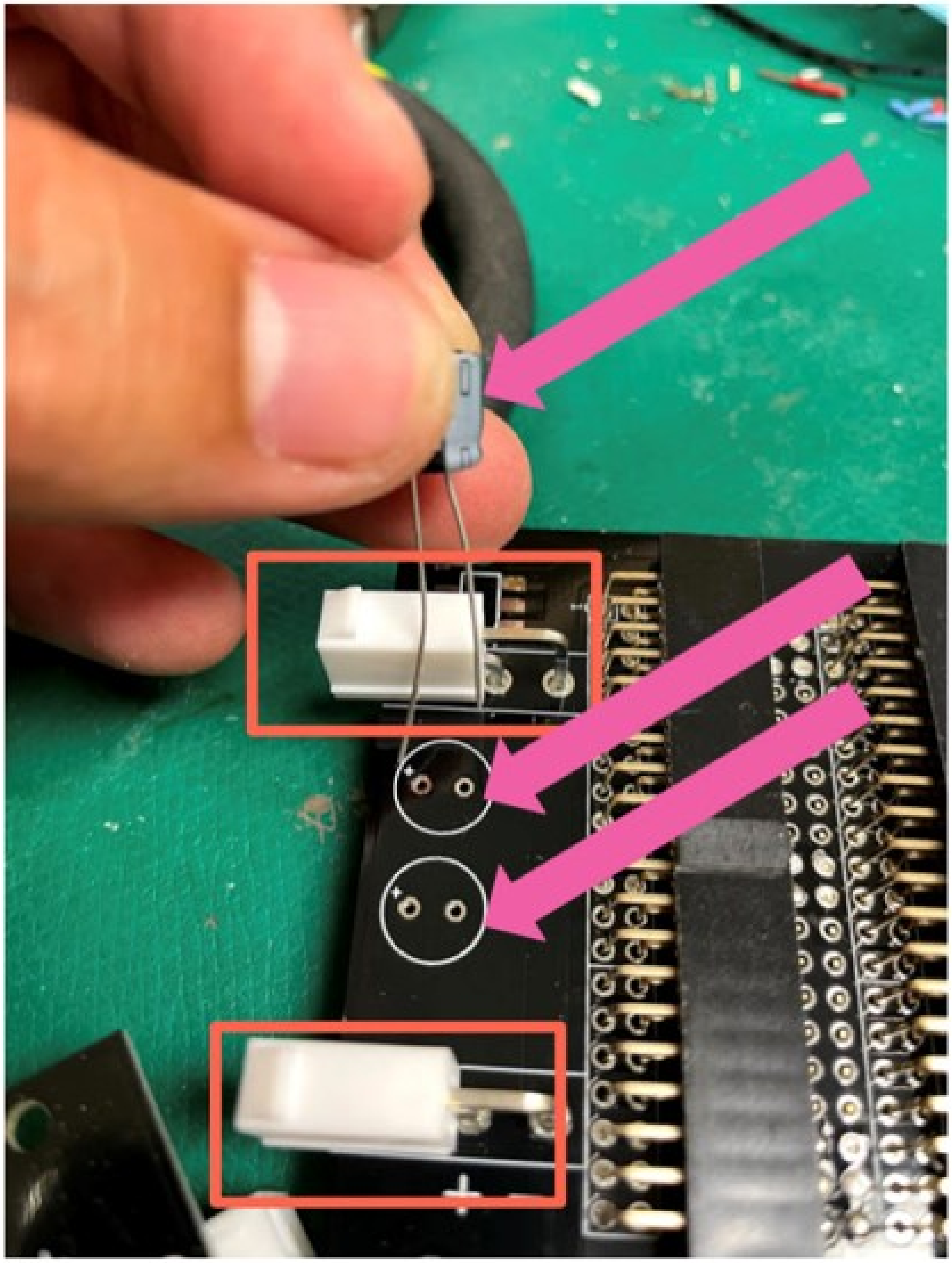

Figure A.15: Step#8: Solder the power connectors (Part number: WM21363-ND, 0039301022) [red rectangles] and capacitors (Part number: 16ML220MEFCT78X7.5) [pink arrows]

A.3.2 Relay board

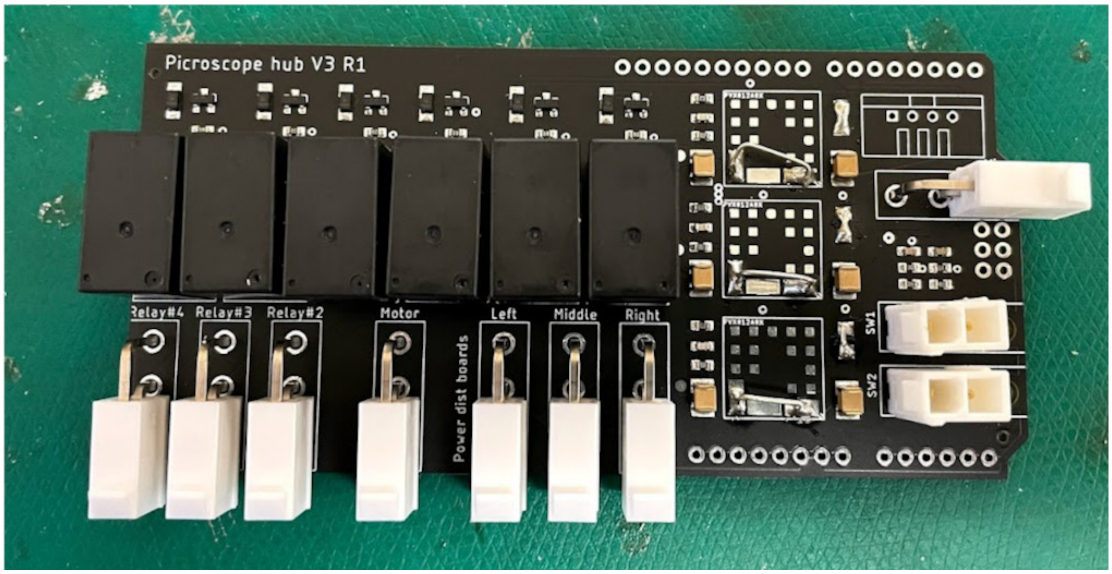

Figure A.16: Relay board

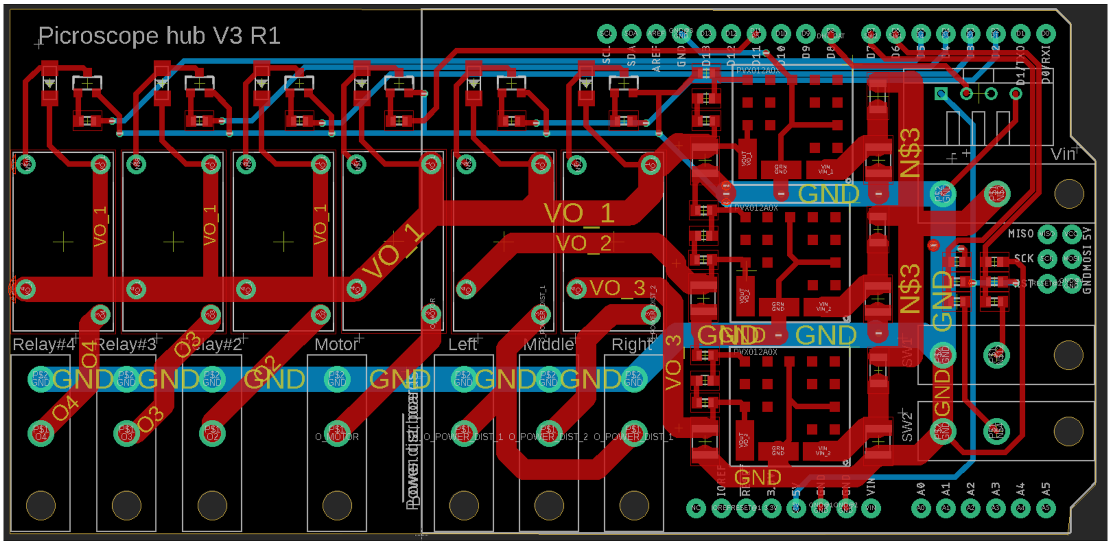

Figure A.17: Relay board design

Step#1: Order ”gen5/pi_relay_hub/v3r1/” from JLCPCB pre-populated using the following filing option: (a) Black PCB (b) Use the Bill of Materials (BOM) in the following file: jlc_bom.csv (c) Use the Part placement (PNP) in the following file: jlc_pnp.csv (d) SMT Assembly needs to be toggled and tools assembled by JLCPCB

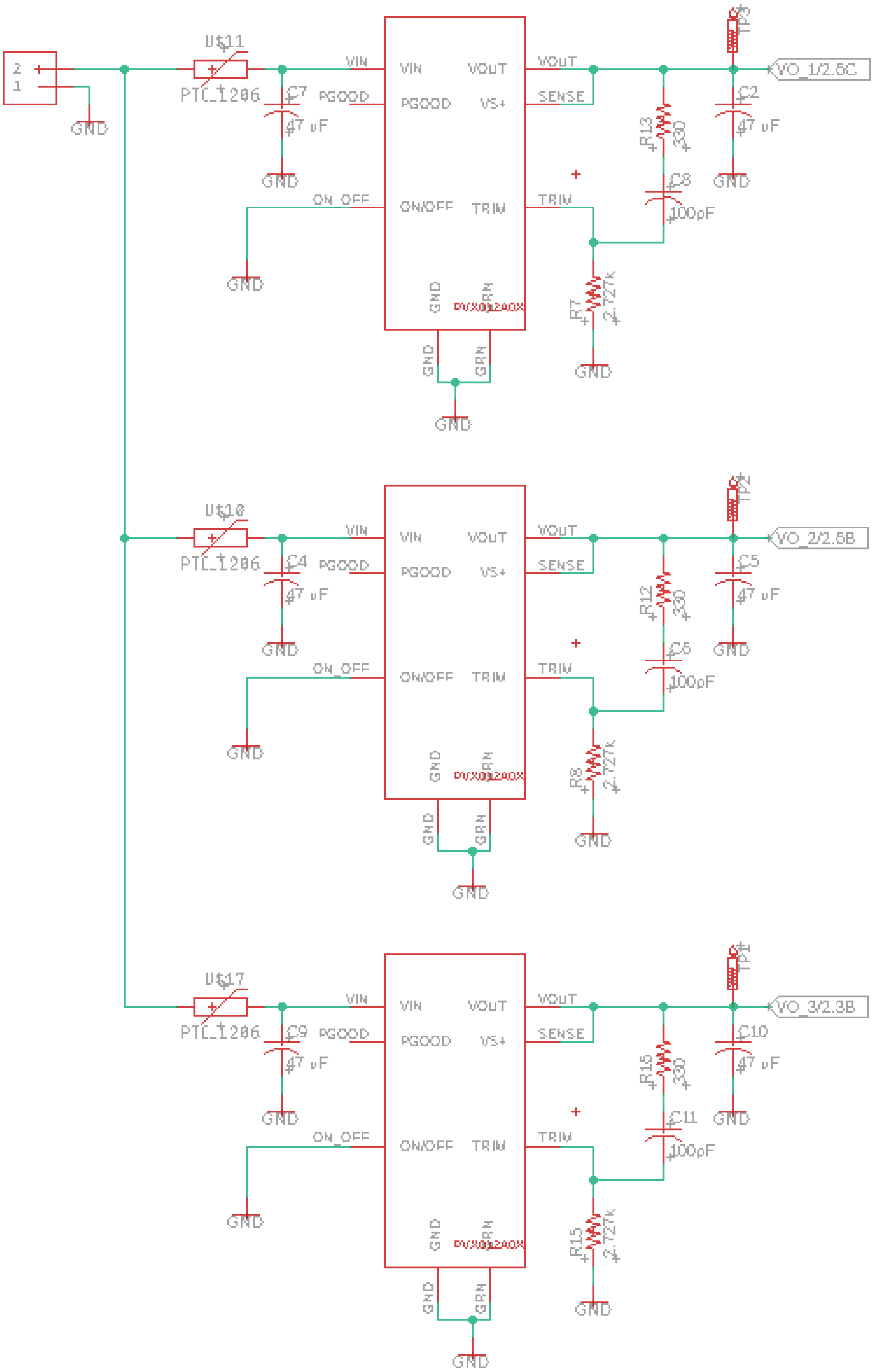

Figure A.18: Relay board schematic 1/3

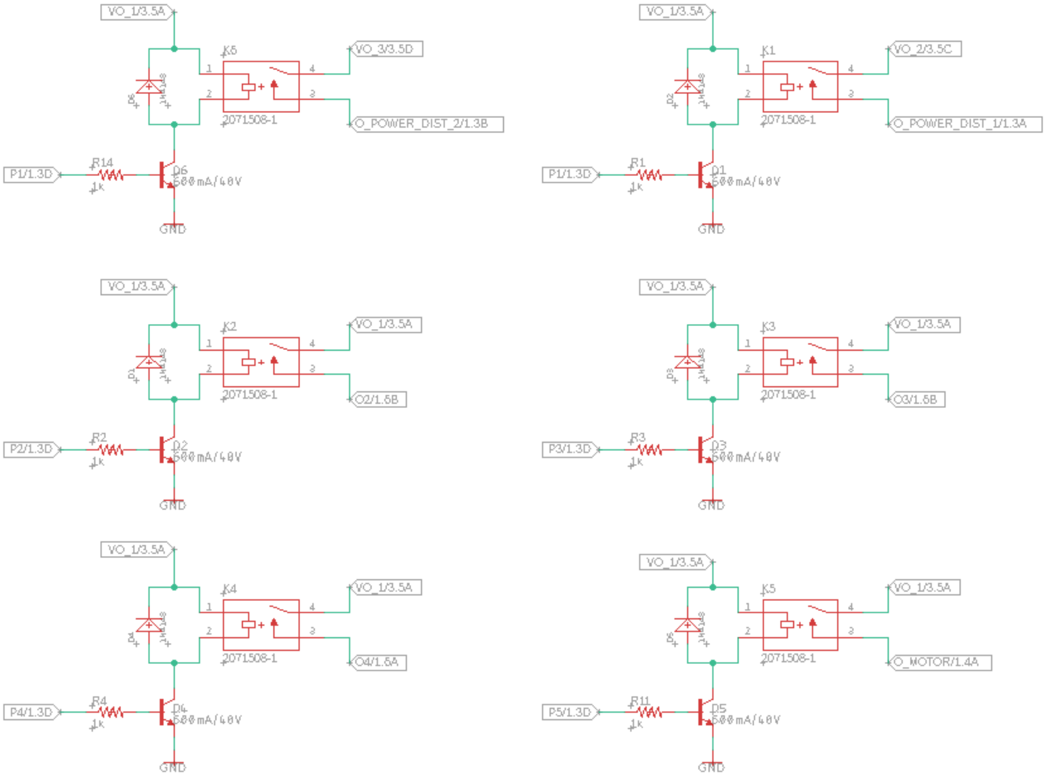

Figure A.19: Relay board schematic 2/3

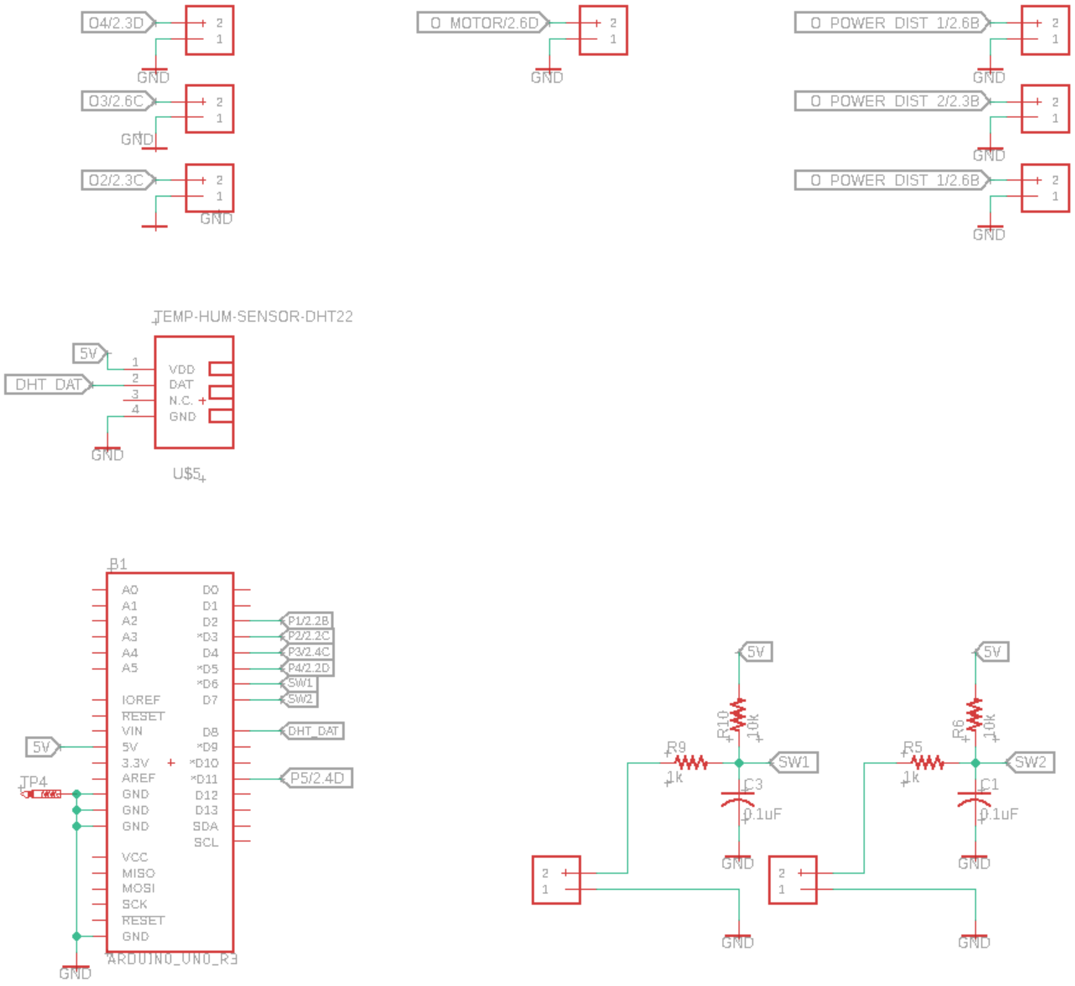

Figure A.20: Relay board schematic 3/3

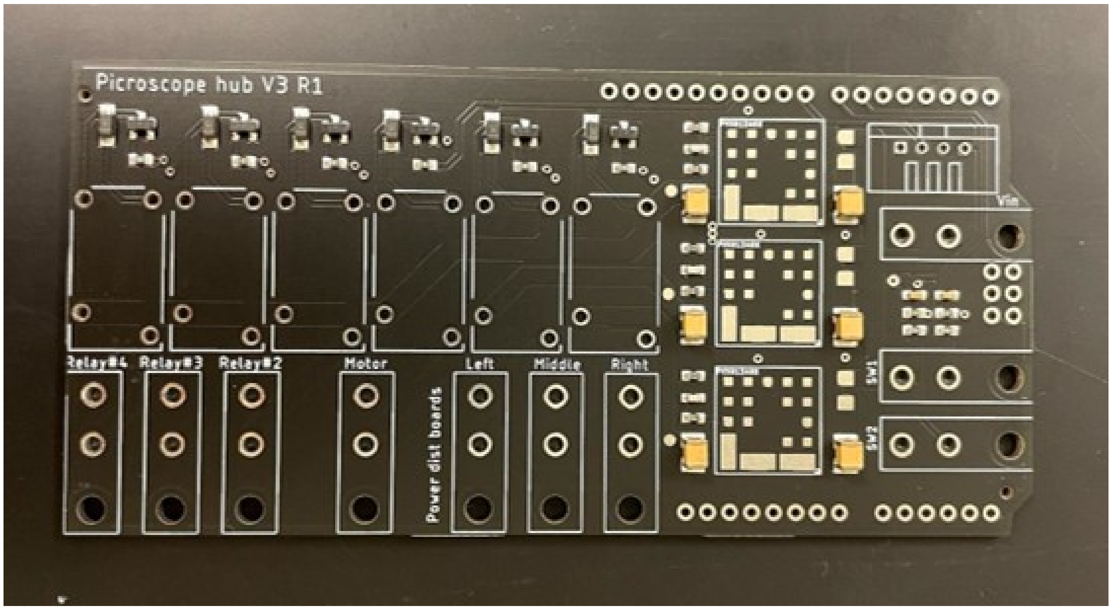

Figure A.21: This is a pre-populated PCB from JLCPCB.

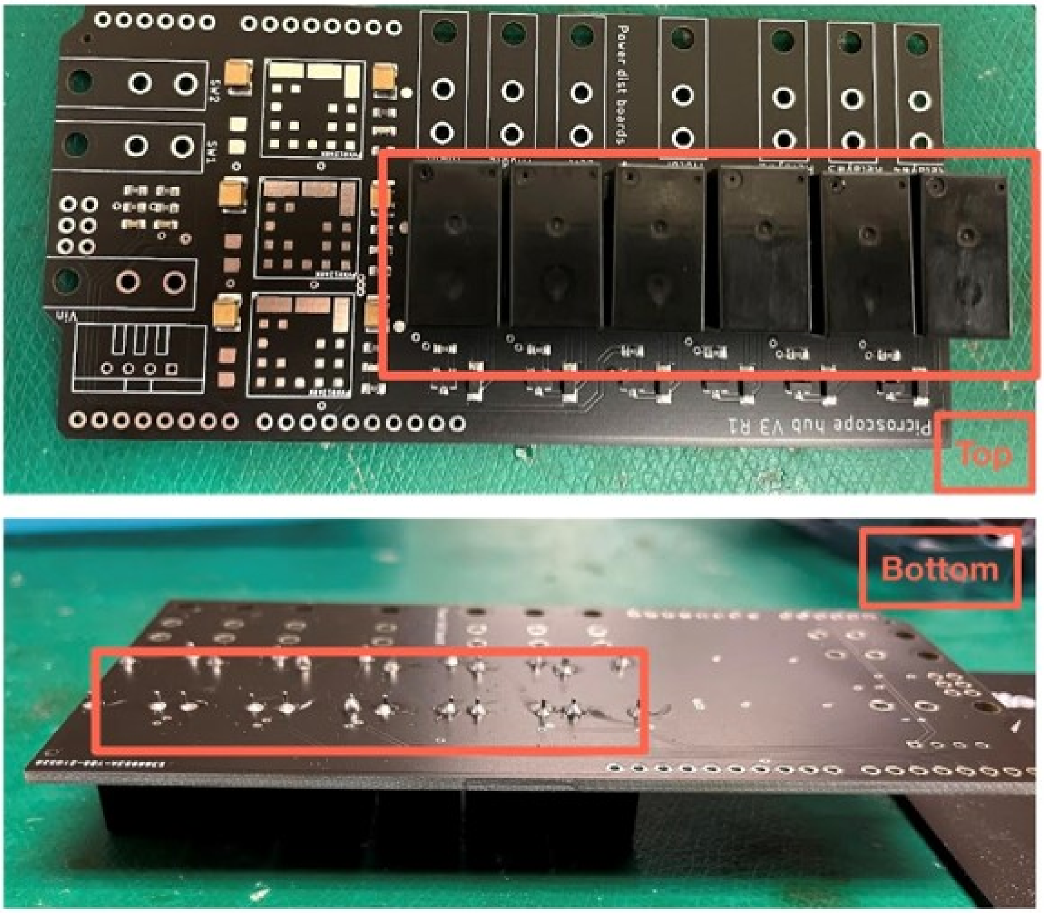

Figure A.22: Step#2: Solder 6 relays (Part number: OJT-SS-112HM, 0000)

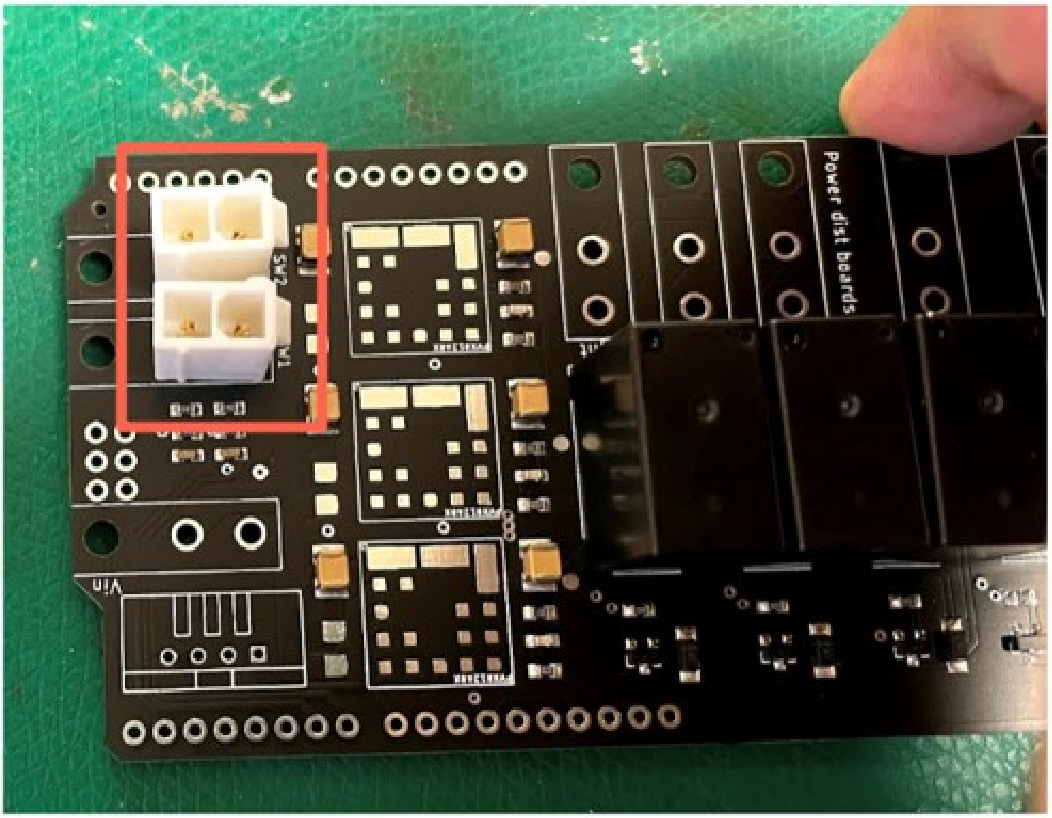

Figure A.23: Step#3: Solder 2 limit switch connectors (Part number: 0039296028) where the red box is located.

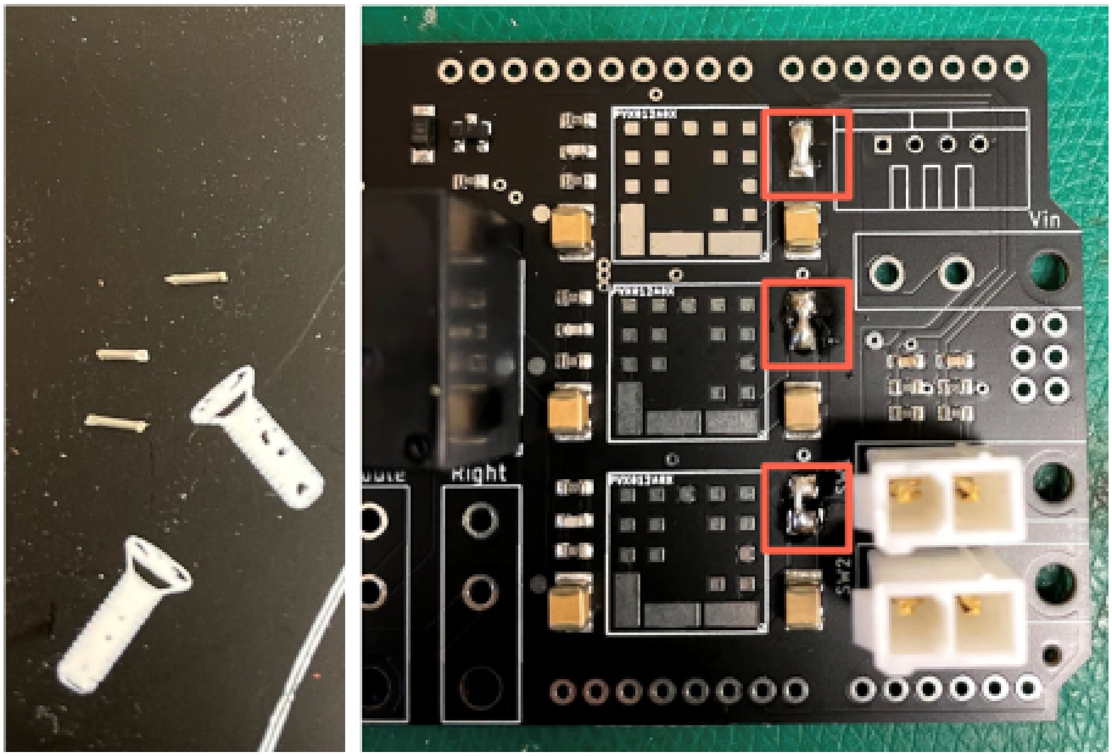

Figure A.24: Step#4: Cut three wires into 5 mm length each. We recommend using the legs of a resistor (left). Step#5: Solder three wires onto the pads above the capacitors (right).

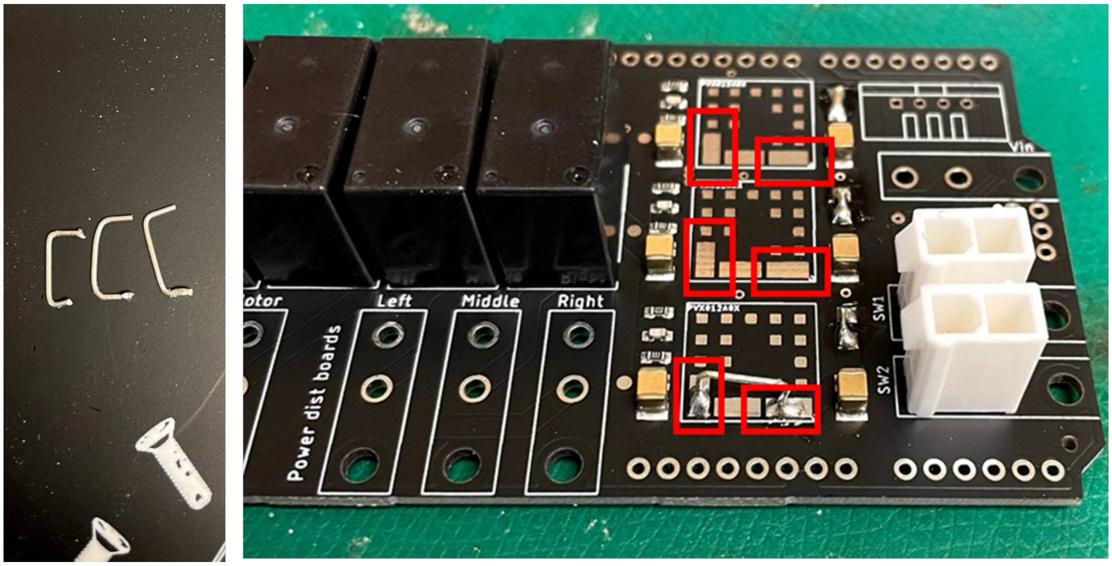

Figure A.25: Step#6: Cut another set of wire into 12 mm length, and bend them into a U-shape (left). Step#7: Solder a new set of wire between two big pads in the red boxes(right).

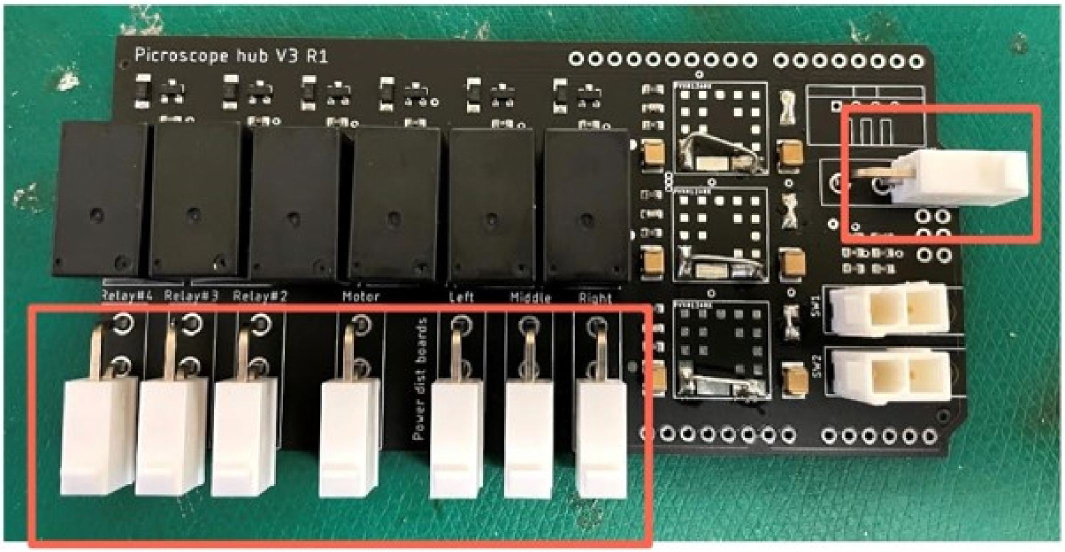

Figure A.26: Step#8: Solder the molex connector (Part number 0039301022) as seen in red.

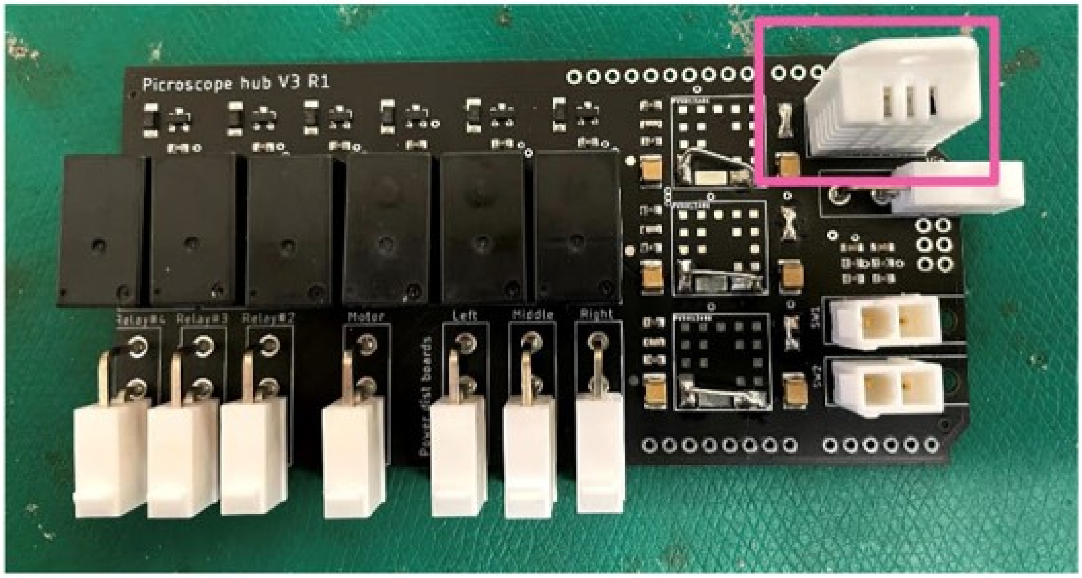

Figure A.27: Step#9: Solder the temperature sensor in pink (Part number 528-1504-ND)

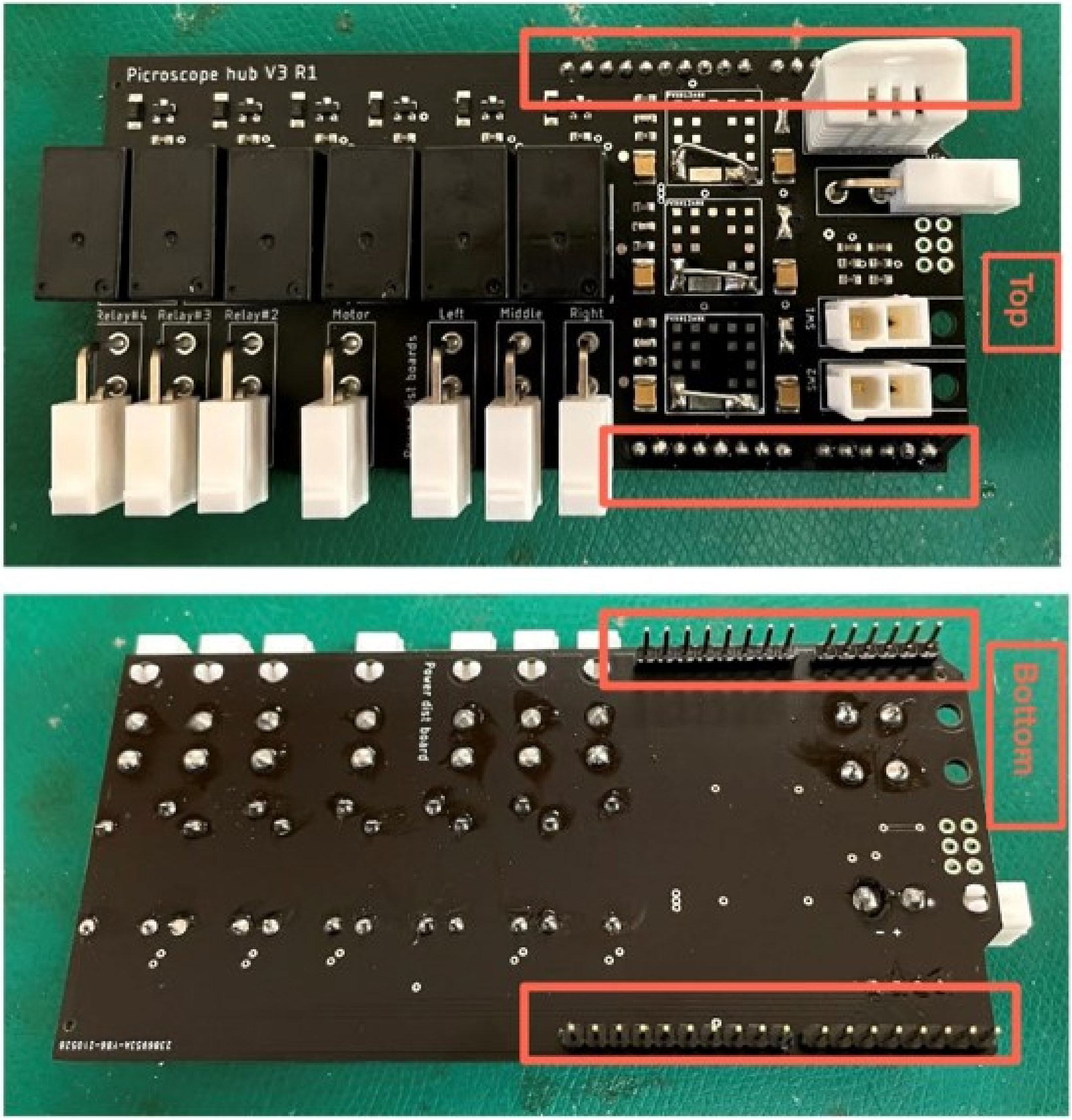

Figure A.28: Step#10: Solder the pin headers in red.

Illumination boards

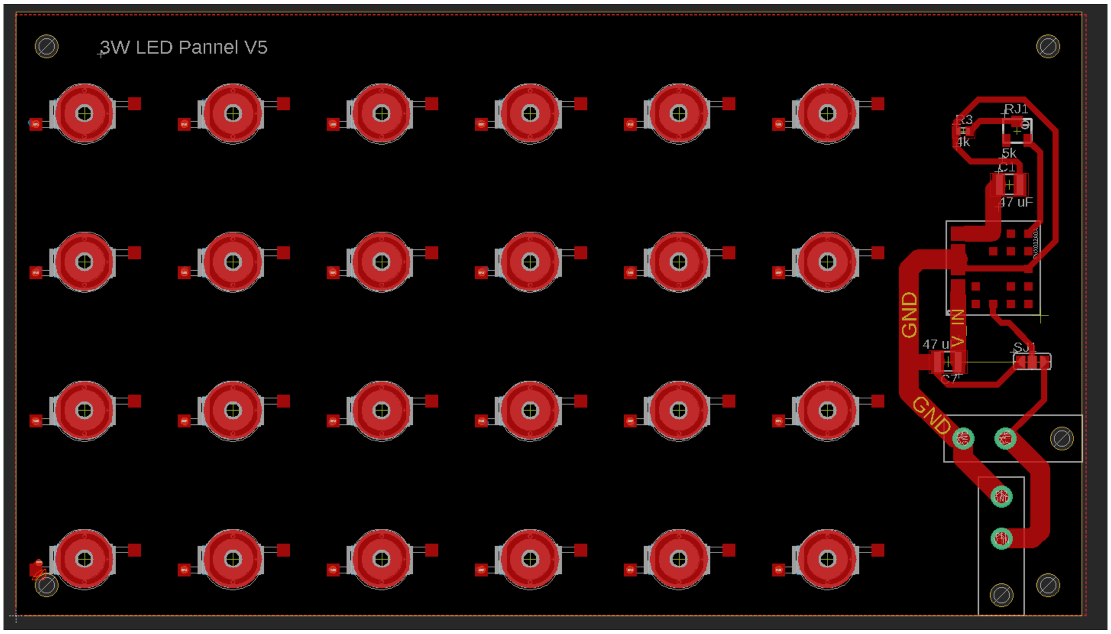

Figure A.29: Over-the-plate illumination board design

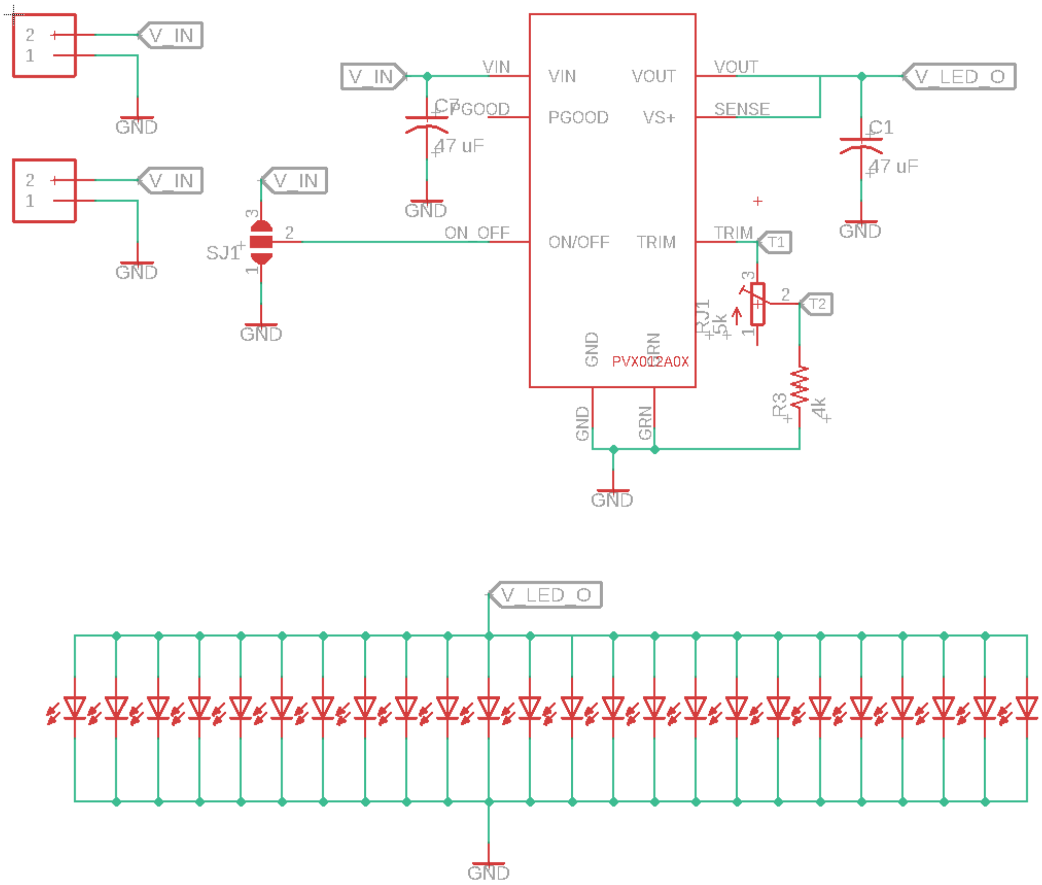

Figure A.30: Over-the-plate illumination board schematic

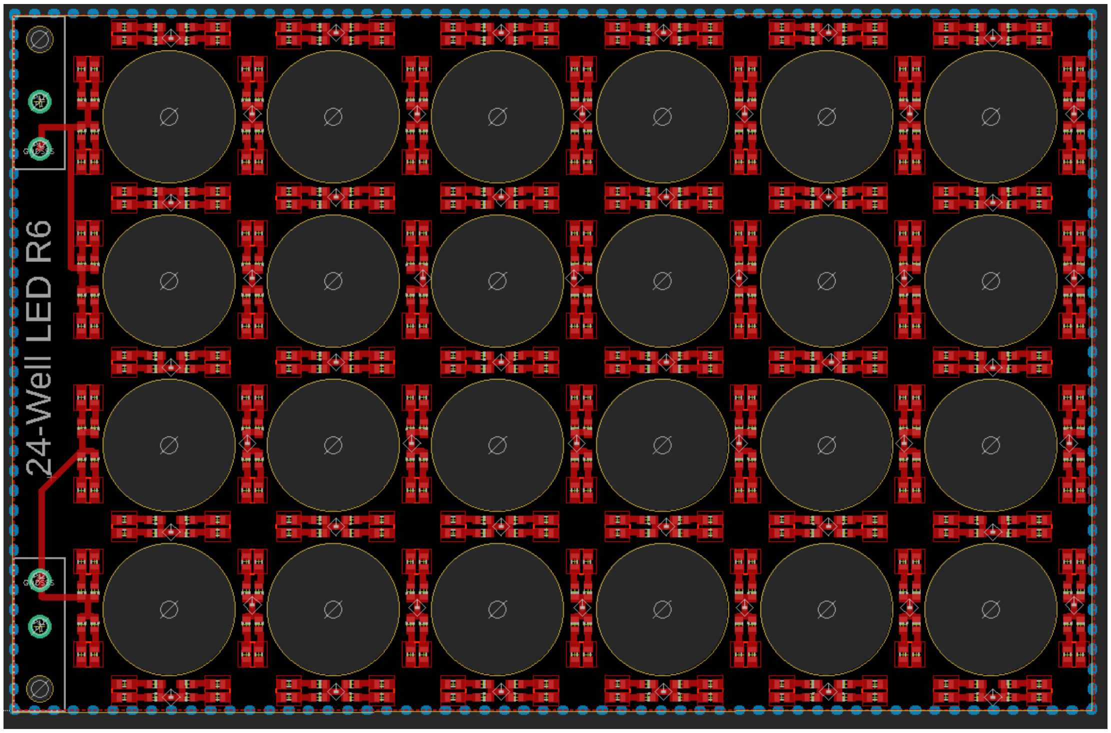

Figure A.31: Below-the-plate illumination board design

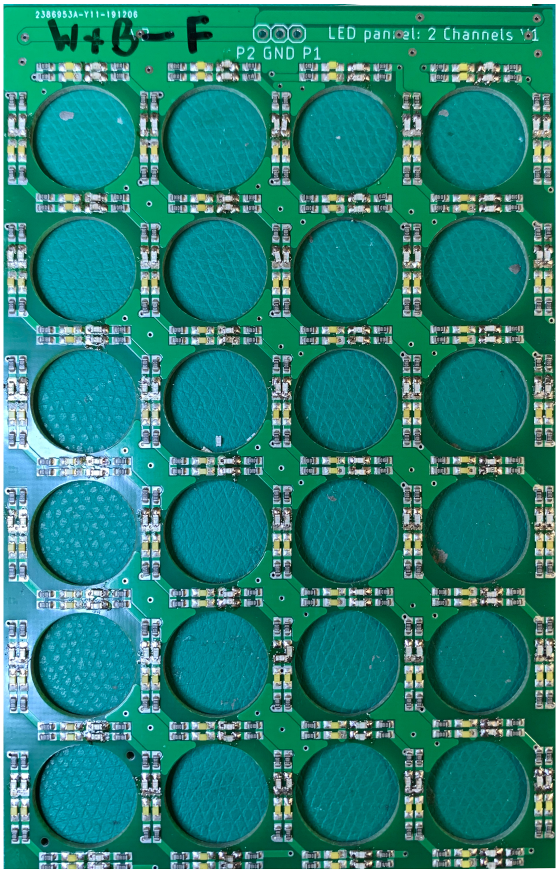

Figure A.32: Below-the-plate illumination board

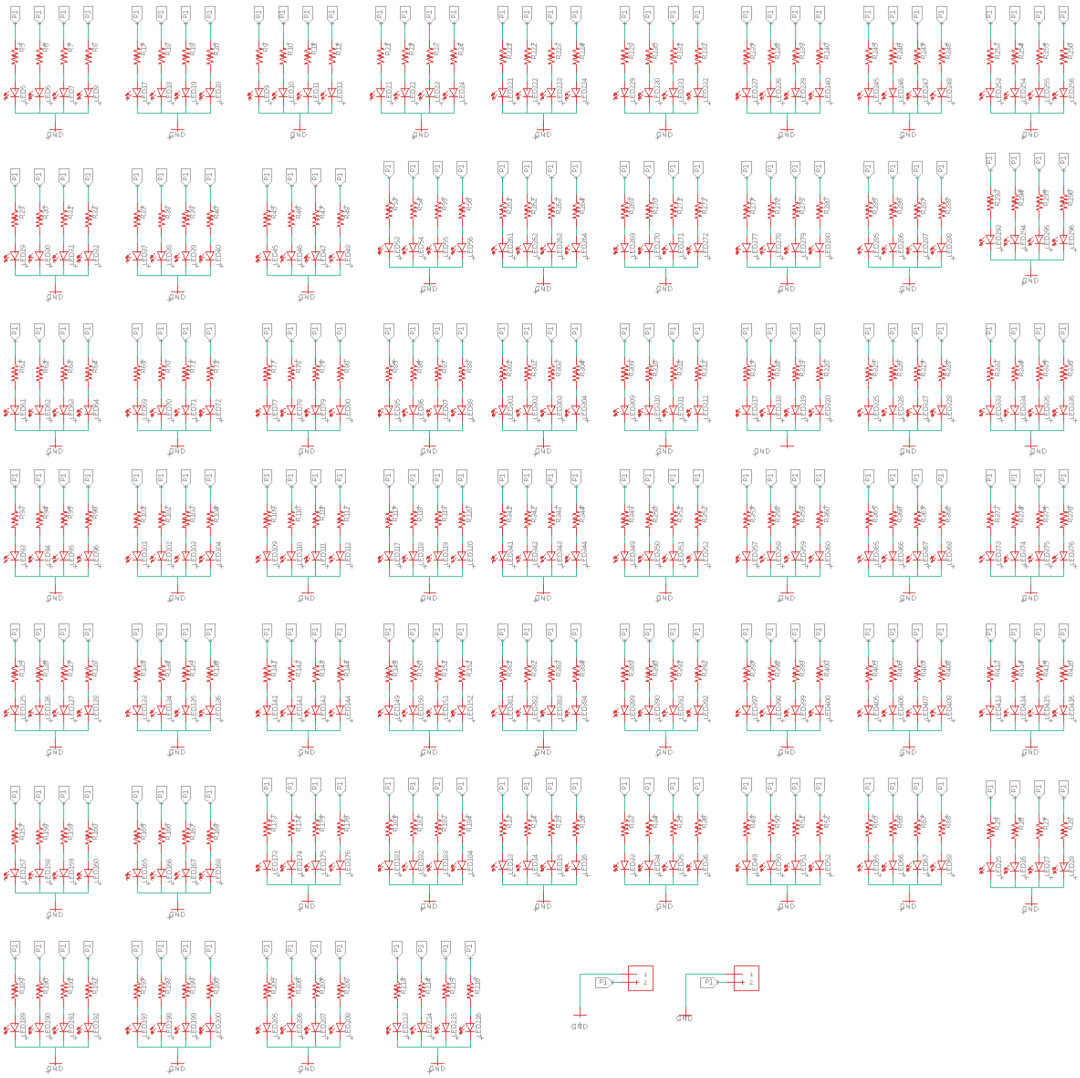

Figure A.33: Below-the-plate illumination board schematic

Wire Assembly

Black wire: Part number 2153401122 Red wire: Part number 2153402122 Connector: Part number 0039039022

Figure A.34: Power wire assembly

A.4 Potentiostat

Devices	Cyclic Volta-metry	Input Range (nA)	Output Range (V)	Number of Channel	Size (mm)	Interface	$ per channel
Modular multi-channel potentiostat	Yes	0.001 - 1.65	4	64	73 x 57	UDP	$
Non-modular multi-channel potentiostat	Yes	0.001 - 1.65	4	16	120 x 68	UDP	$
CheapStat [Rowe et al., 2011]	Yes	0.1 - 50,000	0.99	1*	140 x 66	USART	$$$
M-P [Cruz et al., 2014]	Yes	5 - 750	0.792	1*	-	-	$$
KickStat [Hoilett et al., 2020]	Yes	5 - 750	0.792	1*	21 x 20	-	$$
Friedman et al [Friedman et al., 2012]	Yes	200 - 2,000	-	1*	-	-	$$$$
DStat [Dryden and Wheeler, 2015]	Yes	-	1.46	1*	92 x 84	USART	$$$
Gabriel N. Meloni [Meloni, 2016]	Yes	200,000	1	1*	-	-	$
Dobbelaere et al [Dobbelaere et al., 2017]	Yes	2 - 20,000	8	1*	50 x 50	USBSTACK	$$$
Miniature Glucose measurement system [Adams et al., 2018]	No	50	1	1*	28 x 25	USART	$$
JUAMI [Li et al., 2018]	Yes	10,000,000	2.5	1*	87 x 75	USART	$
UWED [Ainla et al., 2018]	Yes	180,000	1.5	1*	80 x 40	Bluetooth	$$
MiniStat [Adams et al., 2019]	Yes	100	1.2	1*	27 x 20	USART	$$
ABE-Stat [Jenkins et al., 2019]	Yes	-	1.65	1*	74 x 89	Bluetooth	$$
SweepStat [Glasscott et al., 2019]	Yes	15 - 1,500	1.5	1*	-	Labview	$$
Emstat 3 [BV, 2020]	Yes	0.001 - 10,000	3	1*	67 x 50	PSTrace**	$$$
Li et al [Li et al., 2004]	Yes	-	2.048	4*	Benchtop	Labview	$$$
Pseudopotentiostat [Cumyn et al., 2003]	Yes	-	5	64*	Benchtop	-	$$
PGSTAT128N [Metrohm Autolab, 2020]	Yes	0.01 - 1,000,000	10	4	Benchtop	Autlab NOVA*	$$$$$
Arraystat-ULC [NuVant Systems, 2020]	Yes	0.003 - 10,000	15	25	Benchtop	EZware**	$$$$

Notes: 1 *: Number of working electrodes 2.**: Proprietary software

Table A.1: The multi-channel potentiostat in comparison with other potentiostat devices

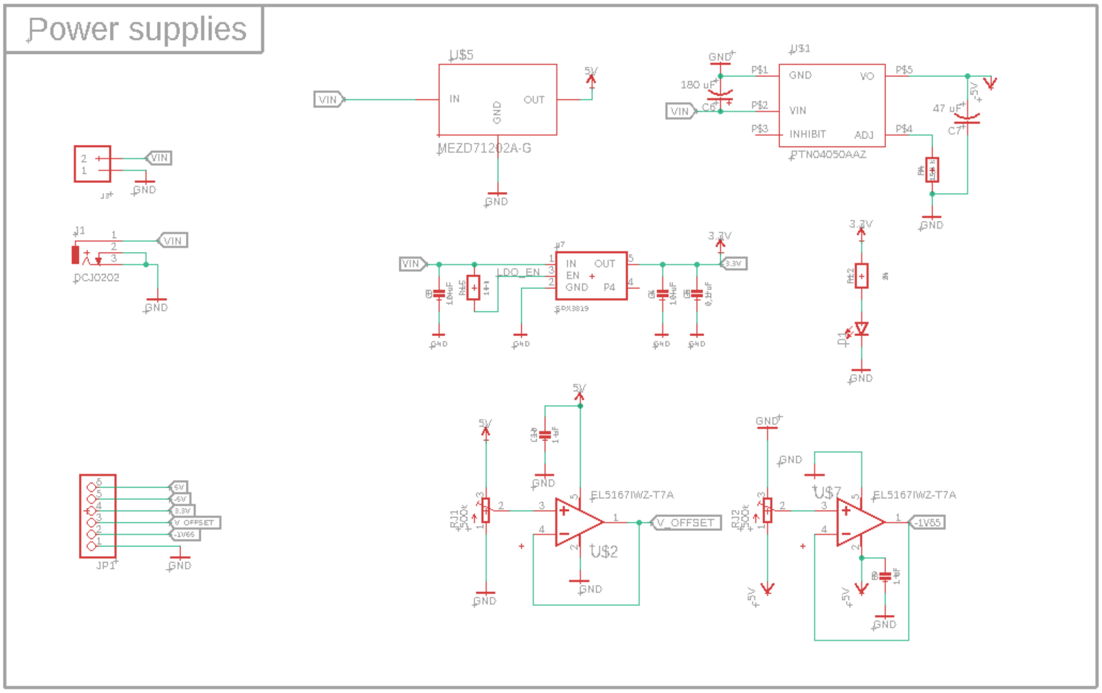

Figure A.35: Modular multi-channel potentiostat schematic base unit 1/3

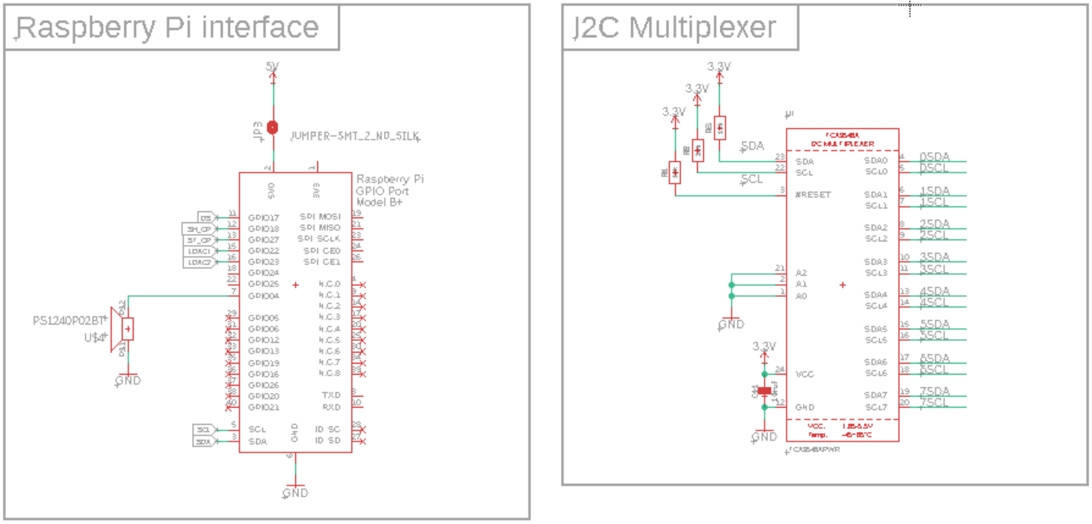

Figure A.36: Modular multi-channel potentiostat schematic base unit 2/3

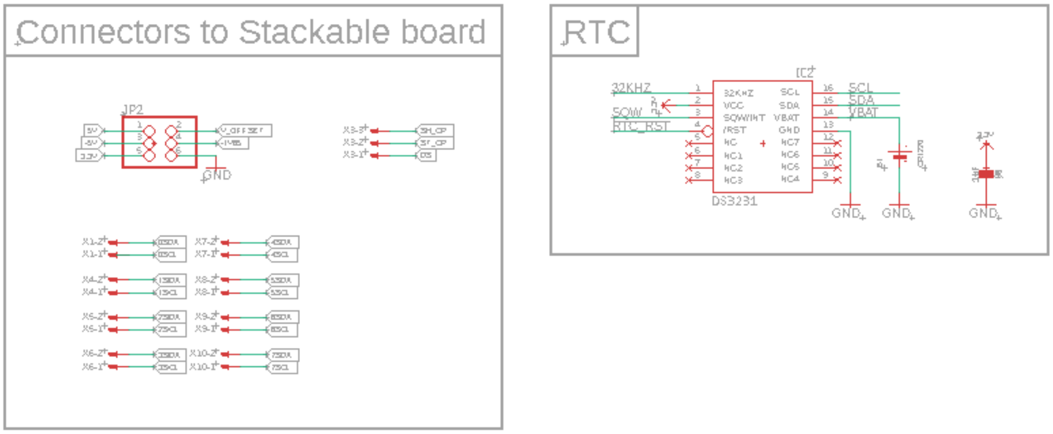

Figure A.37: Modular multi-channel potentiostat schematic base unit 3/3

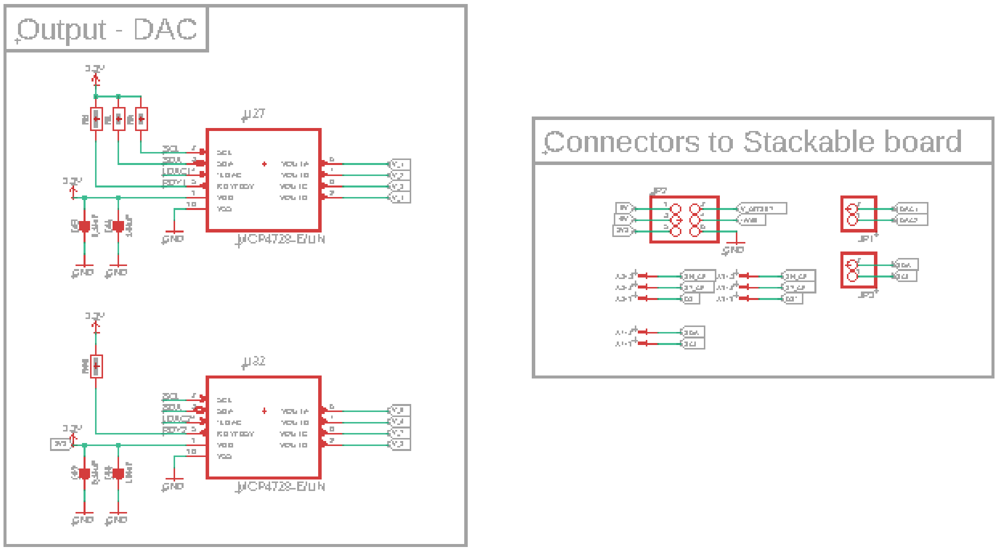

Figure A.38: Modular multi-channel potentiostat schematic stackable board 1/4

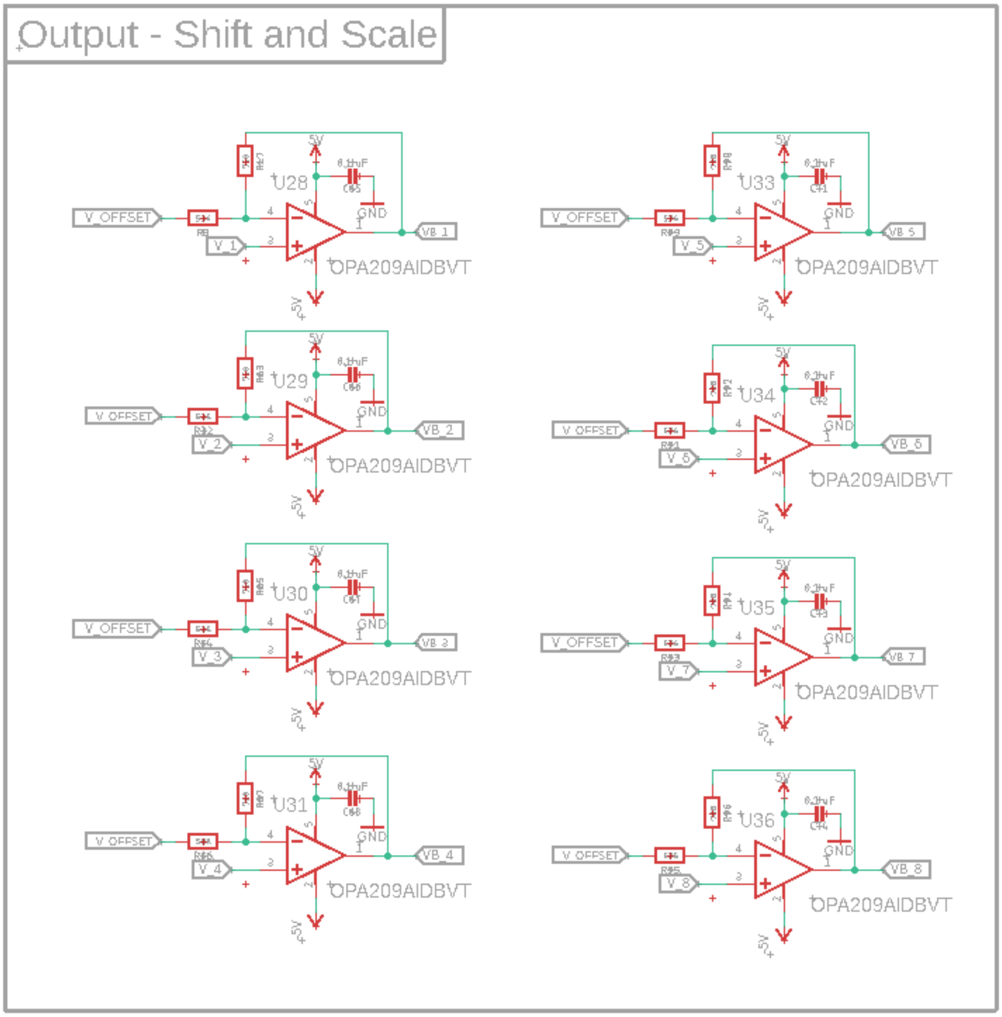

Figure A.39: Modular multi-channel potentiostat schematic stackable board 2/4

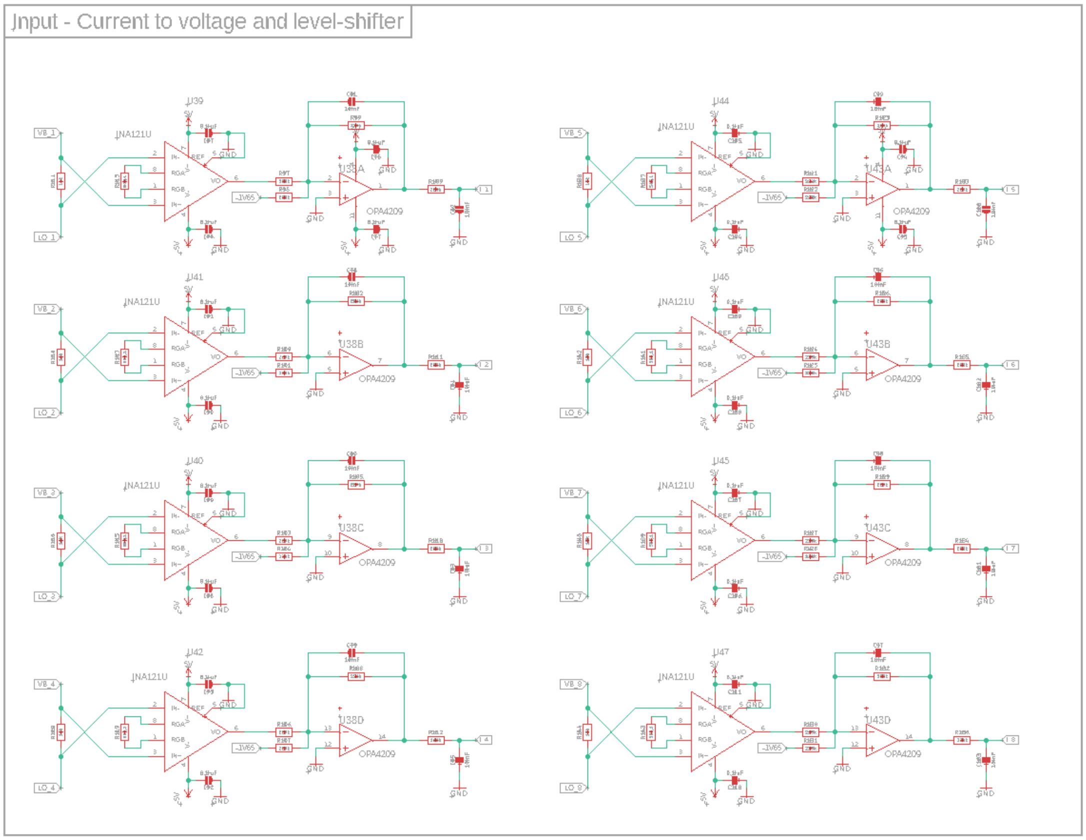

Figure A.40: Modular multi-channel potentiostat schematic stackable board 3/4

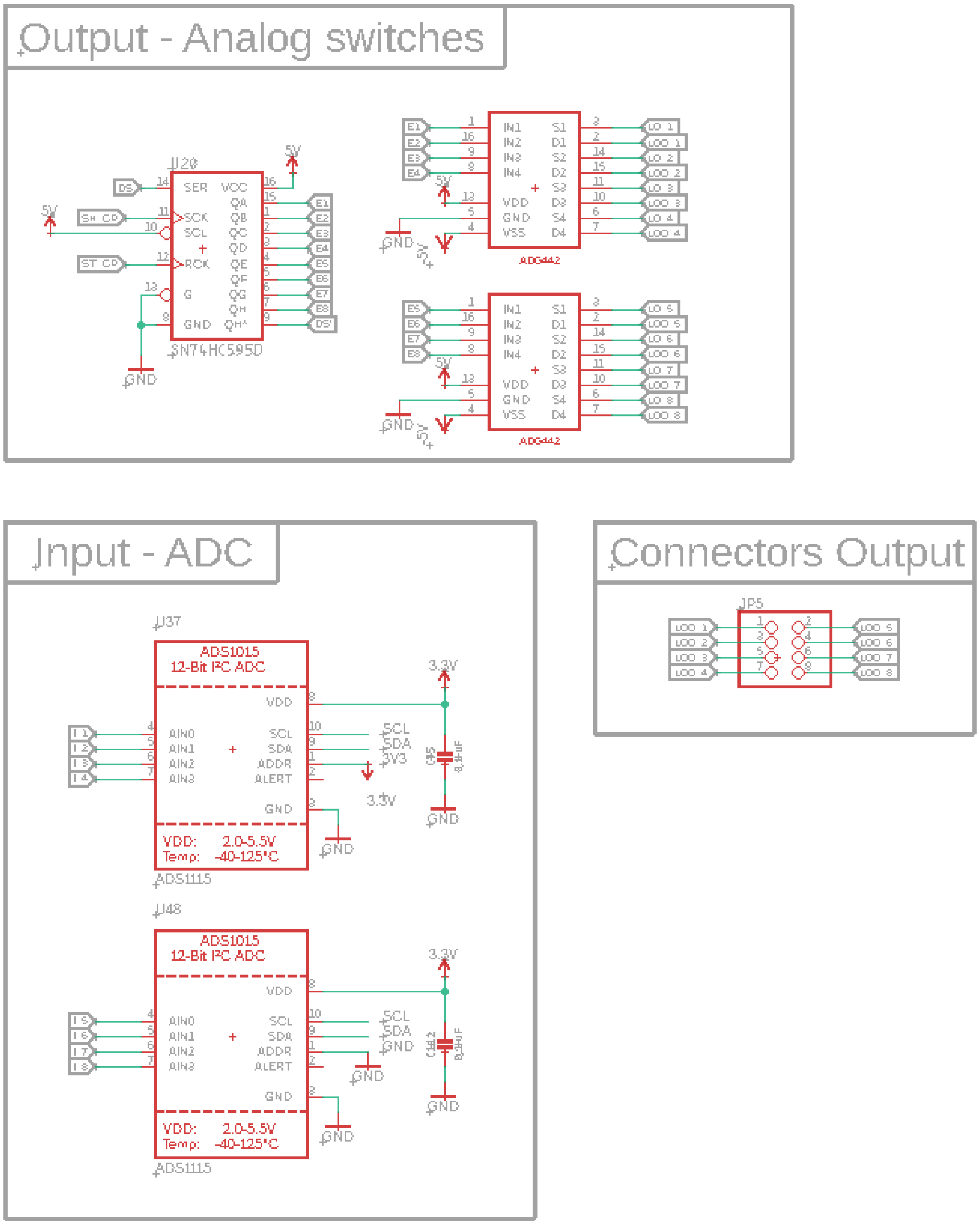

Figure A.41: Modular multi-channel potentiostat schematic stackable board 4/4

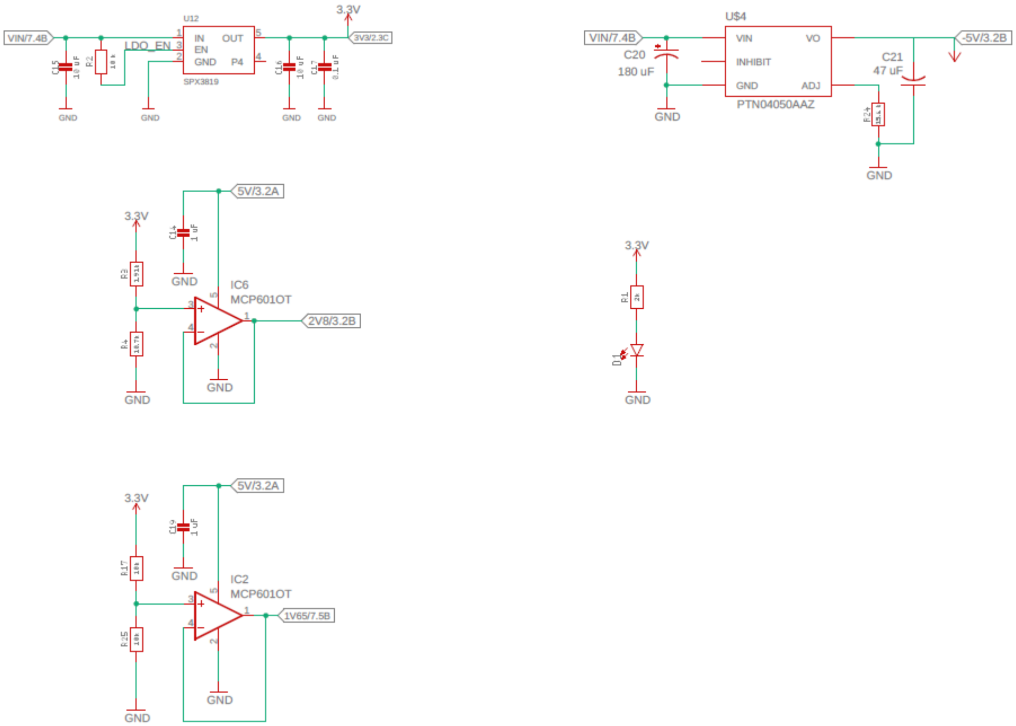

Figure A.42: Non-modular multi-channel potentiostat schematic 1/7

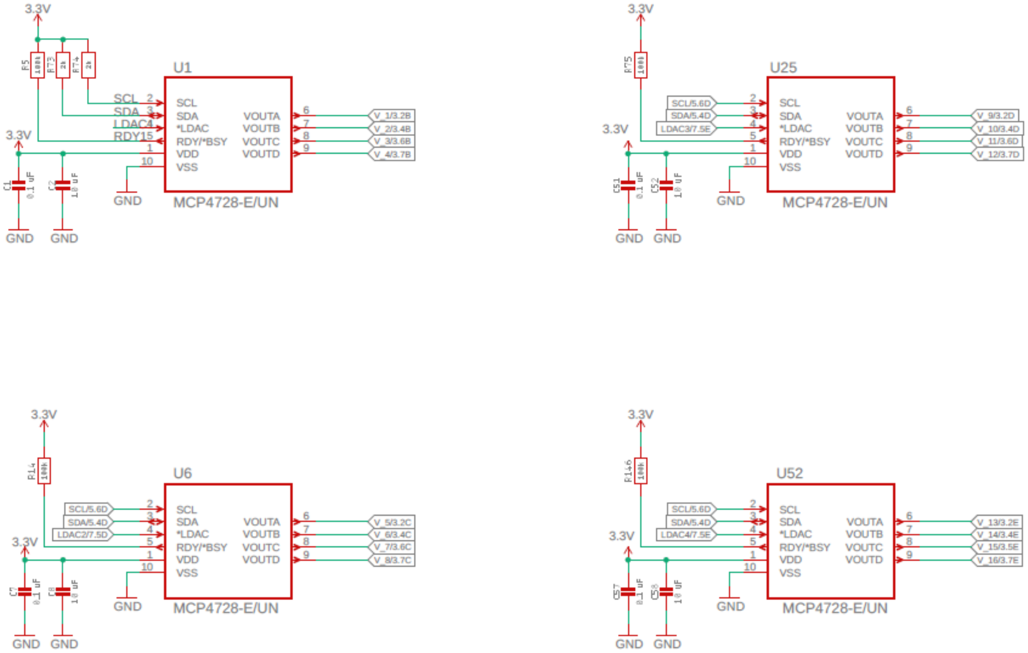

Figure A.43: Non-modular multi-channel potentiostat schematic 2/7

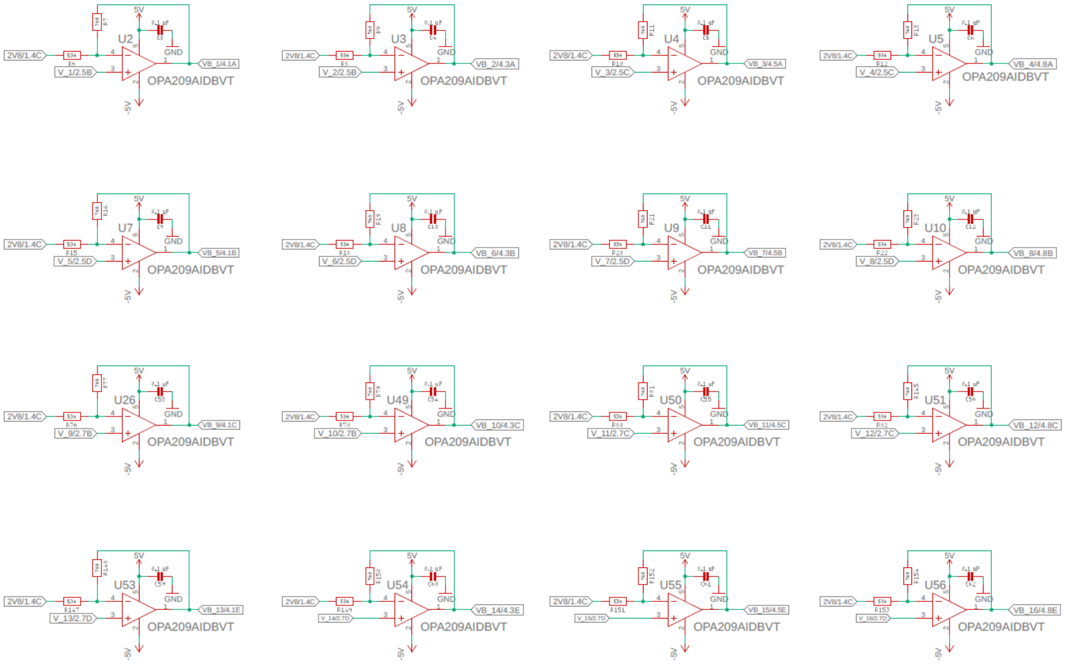

Figure A.44: Non-modular multi-channel potentiostat schematic 3/7

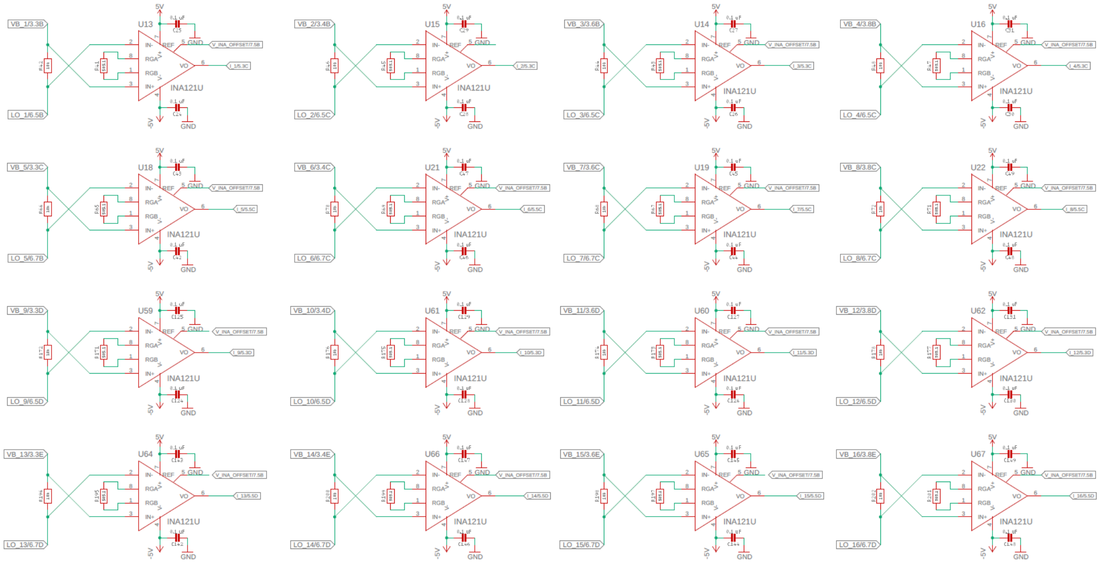

Figure A.45: Non-modular multi-channel potentiostat schematic 4/7

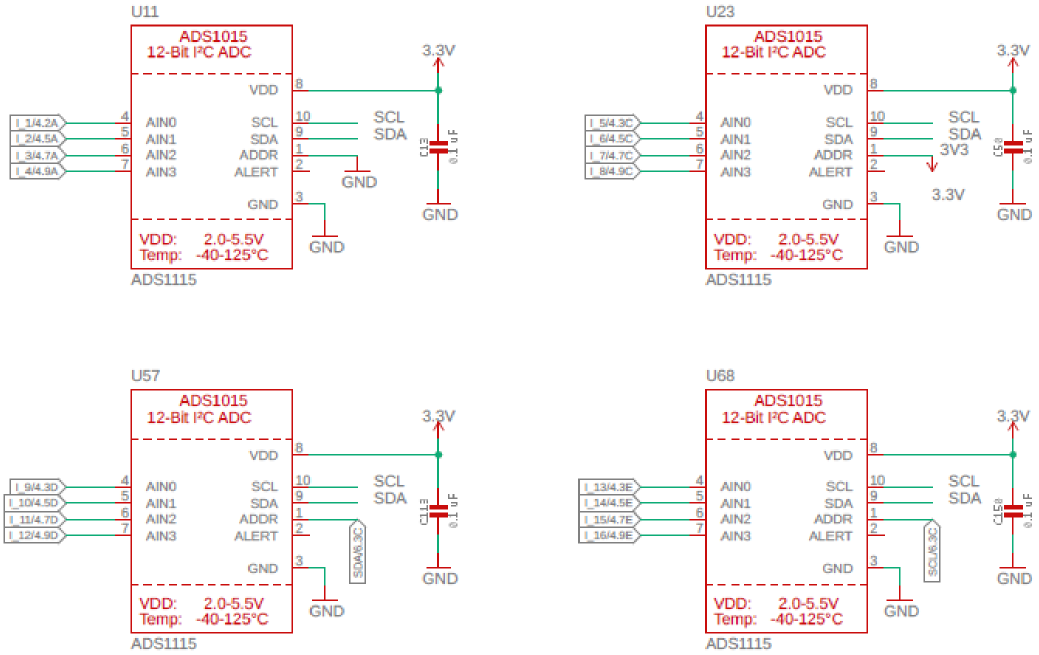

Figure A.46: Non-modular multi-channel potentiostat schematic 5/7

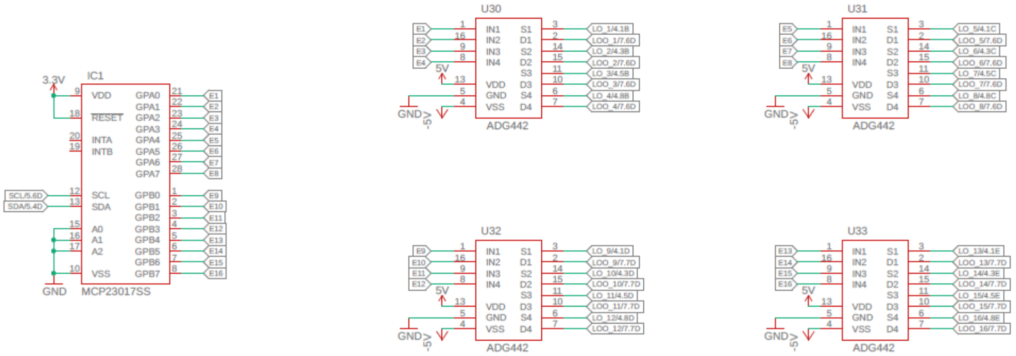

Figure A.47: Non-modular multi-channel potentiostat schematic 6/7

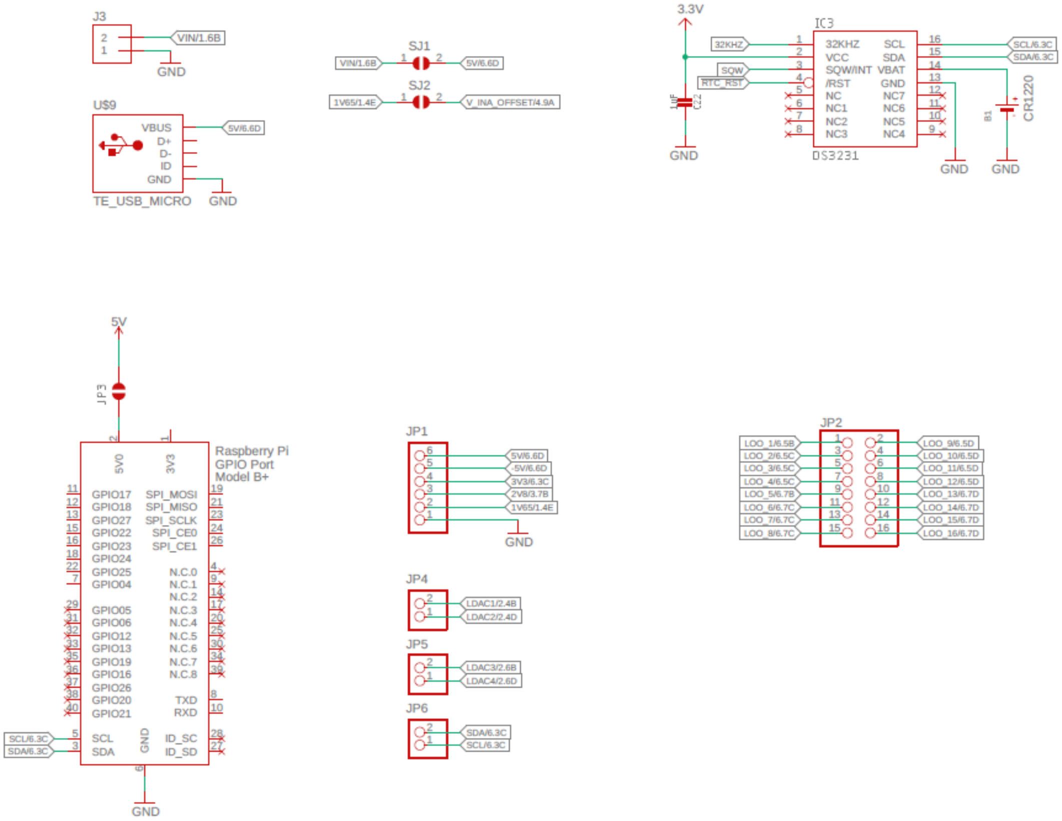

Figure A.48: Non-modular multi-channel potentiostat schematic 7/7

Bibliography

[Abdulbari and Basheer, 2017] Abdulbari, H. A. and Basheer, E. A. (2017). Electrochemical biosensors: electrode development, materials, design, and fabrication. ChemBioEng Reviews, 4(2):92–105.

[Abdullah et al., 2020] Abdullah, S., Serpelloni, M., and Sardini, E. (2020). Design of multichannel potentiostat for remote and longtime monitoring of glucose concentration during yeast fermentation. Review of Scientific Instruments, 91(5):054104.

[Adams et al., 2018] Adams, S., Buber, E., Bicak, T., Yagci, Y., Toppare, L., Kaynak, A., and Kouzani, A. (2018). A miniature and low-cost glucose measurement system. Biocybernetics and Biomedical Engineering, 38(4):841–849.

[Adams et al., 2019] Adams, S. D., Doeven, E. H., Quayle, K., and Kouzani, A. Z. (2019). Ministat: Development and evaluation of a mini-potentiostat for electrochemical measurements. IEEE Access, 7:31903–31912.

[Aidukas et al., 2019] Aidukas, T., Eckert, R., Harvey, A. R., Waller, L., and Konda, P. C. (2019). Low-cost, sub-micron resolution, wide-field computational microscopy using opensource hardware. Scientific reports, 9(1):7457.

[Ainla et al., 2018] Ainla, A., Mousavi, M. P., Tsaloglou, M.-N., Redston, J., Bell, J. G., Fernández-Abedul, M. T., and Whitesides, G. M. (2018). Open-source potentiostat for wireless electrochemical detection with smartphones. Analytical chemistry, 90(10):6240–6246.

[Alberts et al., 2002] Alberts, B., Johnson, A., Lewis, J., Raff, M., Roberts, K., and Walter, P. (2002). Ion channels and the electrical properties of membranes. In Molecular Biology of the Cell. 4th edition. Garland Science.

[Almeida, 2019] Almeida, M. D. (2019). Taking biotech to the next level with laboratory automation.

[Altuna et al., 2013] Altuna, A., Bellistri, E., Cid, E., Aivar, P., Gal, B., Berganzo, J., Gabriel, G., Guimerà, A., Villa, R., Fernández, L. J., et al. (2013).

Su-8 based microprobes for simultaneous neural depth recording and drug delivery in the brain. Lab on a Chip, 13(7):1422–1430.

[Ametek, 2021] Ametek, I. (2021). Parstat mc family - multichannel potentiostat and galvanostat.

[Arbring Sjöström et al., 2018] Arbring Sjöström, T., Berggren, M., Gabrielsson, E. O., Janson, P., Poxson, D. J., Seitanidou, M., and Simon, D. T. (2018). A decade of iontronic delivery devices. Advanced Materials Technologies, 3(5):1700360.

[Ayers et al., 2007] Ayers, S., Gillis, K. D., Lindau, M., and Minch, B. A. (2007). Design of a cmos potentiostat circuit for electrochemical detector arrays. IEEE Transactions on Circuits and Systems I: Regular Papers, 54(4):736–744.

[Baker, 2016] Baker, M. (2016). 1,500 scientists lift the lid on reproducibility. Nature News, 533(7604):452.

[Bakker et al., 1997] Bakker, E., Bühlmann, P., and Pretsch, E. (1997). Carrier-based ion-selective electrodes and bulk optodes. 1. general characteristics. Chemical Reviews, 97(8):3083–3132.

[Bard et al., 2001] Bard, A. J., Faulkner, L. R., et al. (2001). Fundamentals and applications. Electrochemical Methods, 2(482):580–632.

[Baudin et al., 2021] Baudin, P. V., Ly, V. T., Pansodtee, P., Jung, E. A., Currie, R., Hoffman, R., Willsey, H. R., Pollen, A. A., Nowakowski, T. J., Haussler, D., et al. (2021). Low cost cloud based remote microscopy for biological sciences. Internet of Things, page 100454.

[Bennett, 1993] Bennett, S. (1993). Development of the pid controller. IEEE Control Systems Magazine, 13(6):58–62.

[Berger, 1929] Berger, H. (1929). Über das elektrenkephalogramm des menschen. European archives of psychiatry and clinical neuroscience, 87(1):527–570.

[Bertrand and Jasper, 1965] Bertrand, G. and Jasper, H. (1965). Microelectrode recording of unit activity in the human thalamus. Stereotactic and Functional Neurosurgery, 26(3-5):205–208.

[Bihar et al., 2016] Bihar, E., Deng, Y., Miyake, T., Saadaoui, M., Malliaras, G. G., and Rolandi, M. (2016). A disposable paper breathalyzer with an alcohol sensing organic electrochemical transistor. Scientific reports, 6:27582.

[Blake et al., 2007] Blake, A., Pearce, T., Rao, N., Johnson, S., and Williams, J. (2007). Multilayer pdms microfluidic chamber for controlling brain slice microenvironment. Lab on a Chip, 7(7):842–849.

[Block et al., 2008] Block, C. D., Manuel-y Keenoy, B., and Van Gaal, L. (2008). A review of current evidence with continuous glucose monitoring in patients with diabetes. Journal of diabetes science and technology, 2(4):718–727.

[Bogue, 2012] Bogue, R. (2012). Robots in the laboratory: a review of applications. Industrial Robot: An International Journal, 39(2):113–119.

[Bongso et al., 1994] Bongso, A., Fong, C.-Y., Ng, S.-C., and Ratnam, S. (1994). Fertilization and early embryology: Isolation and culture of inner cell mass cells from human blastocysts. Human Reproduction, 9(11):2110–2117.

[Boyer et al., 2018] Boyer, C. J., Ballard, D. H., Barzegar, M., Yun, J. W., Woerner, J. E., Ghali, G. E., Boktor, M., Wang, Y., and Alexander, J. S. (2018). High-throughput scaffold-free microtissues through 3d printing. 3D printing in medicine, 4(1):1–6.

[Bridger et al., 1991] Bridger, N. J., Jones, C. P., and Neville, M. D. (1991). Electrochemical ion exchange. Journal of Chemical Technology & Biotechnology, 50(4):469–481.

[Buske et al., 2011] Buske, P., Galle, J., Barker, N., Aust, G., Clevers, H., and Loeffler, M. (2011). A comprehensive model of the spatio-temporal stem cell and tissue organisation in the intestinal crypt. PLoS computational biology, 7(1):e1001045.

[Buske et al., 2012] Buske, P., Przybilla, J., Loeffler, M., Sachs, N., Sato, T., Clevers, H., and Galle, J. (2012). On the biomechanics of stem cell niche formation in the gut–modelling growing organoids. The FEBS journal, 279(18):3475–3487.

[BV, 2020] BV, P. (2020 (accessed April 23, 2020)). Emstat 3 - hardware specification.

[Campbell et al., 1991] Campbell, P. K., Jones, K. E., Huber, R. J., Horch, K. W., and Normann, R. A. (1991). A silicon-based, three-dimensional neural interface: manufacturing processes for an intracortical electrode array. IEEE Transactions on Biomedical Engineering, 38(8):758–768.

[Carle et al., 1986] Carle, G. F., Frank, M., and Olson, M. V. (1986). Electrophoretic separations of large dna molecules by periodic inversion of the electric field. Science, 232(4746):65–68.

[Chang et al., 2021] Chang, Y., Wang, L., Li, R., Zhang, Z., Wang, Q., Yang, J., Guo, C. F., and Pan, T. (2021). First decade of interfacial iontronic sensing: from droplet sensors to artificial skins. Advanced Materials, 33(7):2003464.

[Chapp et al., 2018] Chapp, A. D., Schum, S., Behnke, J. E., Hahka, T., Huber, M. J., Jiang, E., Larson, R. A., Shan, Z., and Chen, Q.-H. (2018). Measurement of cations, anions, and acetate in serum, urine, cerebrospinal fluid, and tissue by ion chromatography. Physiological reports, 6(7):e13666.

[Cheon et al., 2015] Cheon, K., Kim, J., Hamadache, M., and Lee, D. (2015). On replacing pid controller with deep learning controller for dc motor system. Journal of Automation and Control Engineering Vol, 3(6).

[Cherian et al., 2019] Cherian, D., Armgarth, A., Beni, V., Linderhed, U., Tybrandt, K., Nilsson, D., Simon, D. T., and Berggren, M. (2019). Large-area printed organic electronic ion pumps. Flexible and Printed Electronics, 4(2):022001.

[Chin et al., 2009] Chin, M. H., Mason, M. J., Xie, W., Volinia, S., Singer, M., Peterson, C., Ambartsumyan, G., Aimiuwu, O., Richter, L., Zhang, J., et al. (2009). Induced pluripotent stem cells and embryonic stem cells are distinguished by gene expression signatures. Cell stem cell, 5(1):111–123.

[Clark Jr and Lyons, 1962] Clark Jr, L. C. and Lyons, C. (1962). Electrode systems for continuous monitoring in cardiovascular surgery. Annals of the New York Academy of sciences, 102(1):29–45.

[Convery and Gadegaard, 2019] Convery, N. and Gadegaard, N. (2019). 30 years of microfluidics. Micro and Nano Engineering.

[Cordero et al., 2019] Cordero, S., Selberg, J., Pansodtee, P., and Teodorescu, M. (2019). Electrophysiology characterization of cerebral organoids using non-invasive microelectrode array. Asilomar Bioelectronics.

[Corrie et al., 2015] Corrie, S. R., Coffey, J., Islam, J., Markey, K., and Kendall, M. (2015). Blood, sweat, and tears: developing clinically relevant protein biosensors for integrated body fluid analysis. Analyst, 140(13):4350–4364.

[Crawford, 1968] Crawford, W. (1968). The robot chemist: A new approach to the automation of wet-chemistry analysis. Annals of the New York Academy of Sciences, 153(1):655–659.

[Cruz et al., 2014] Cruz, A. F. D., Norena, N., Kaushik, A., and Bhansali, S. (2014). A low-cost miniaturized potentiostat for point-of-care diagnosis. Biosensors and Bioelectronics, 62:249–254.

[Cumyn et al., 2003] Cumyn, V. K., Fleischauer, M., Hatchard, T., and Dahn, J. R. (2003). Design and testing of a low-cost multichannel pseudopotentiostat for quantitative combinatorial electrochemical measurements on large electrode arrays. Electrochemical and Solid-State Letters, 6(6):E15–E18.

[Dahl-Jensen and Grapin-Botton, 2017] Dahl-Jensen, S. and Grapin-Botton, A. (2017). The physics of organoids: a biophysical approach to understanding organogenesis. Development, 144(6):946–951.

[de Souza, 2018] de Souza, N. (2018). Organoids. Nature Methods, 15(1):23.

[Deng et al., 2016] Deng, Y., Miyake, T., Keene, S., Josberger, E. E., and Rolandi, M. (2016). Proton mediated control of biochemical reactions with bioelectronic ph modulation. Scientific reports, 6:24080.

[Dhandayuthapani et al., 2011] Dhandayuthapani, B., Yoshida, Y., Maekawa, T., and Kumar, D. S. (2011). Polymeric scaffolds in tissue engineering application: a review. International journal of polymer science, 2011.

[Diederich et al., 2020] Diederich, B., Lachmann, R., Carlstedt, S., Marsikova, B., Wang, H., Uwurukundo, X., Mosig, A. S., and Heintzmann, R. (2020). A versatile and customizable low-cost 3d-printed open standard for microscopic imaging. Nature communications, 11(1):1–9.

[Dobbelaere et al., 2017] Dobbelaere, T., Vereecken, P. M., and Detavernier, C. (2017). A usb-controlled potentiostat/galvanostat for thin-film battery characterization. HardwareX, 2:34–49.

[Drake et al., 1988] Drake, K. L., Wise, K. D., Farraye, J., Anderson, D. J., and BeMent, S. L. (1988). Performance of planar multisite microprobes in recording extracellular single-unit intracortical activity. IEEE Transactions on Biomedical Engineering, 35(9):719–732.

[Dryden and Wheeler, 2015] Dryden, M. D. and Wheeler, A. R. (2015). Dstat: A versatile, open-source potentiostat for electroanalysis and integration. PloS one, 10(10):e0140349.

[Du et al., 2009] Du, J., Riedel-Kruse, I. H., Nawroth, J. C., Roukes, M. L., Laurent, G., and Masmanidis, S. C. (2009). High-resolution three-dimensional extracellular recording of neuronal activity with microfabricated electrode arrays. Journal of neurophysiology, 101(3):1671–1678.

[Durant et al., 2017] Durant, F., Morokuma, J., Fields, C., Williams, K., Adams, D. S., and Levin, M. (2017). Long-term, stochastic editing of regenerative anatomy via targeting endogenous bioelectric gradients. Biophysical journal, 112(10):2231–2243.

[Eiraku et al., 2008] Eiraku, M., Watanabe, K., Matsuo-Takasaki, M., Kawada, M., Yonemura, S., Matsumura, M., Wataya, T., Nishiyama, A., Muguruma, K., and Sasai, Y. (2008). Self-organized formation of polarized cortical tissues from escs and its active manipulation by extrinsic signals. Cell stem cell, 3(5):519–532.

[Ferguson et al., 2009] Ferguson, J. E., Boldt, C., and Redish, A. D. (2009). Creating low-impedance tetrodes by electroplating with additives. Sensors and Actuators A: Physical, 156(2):388–393.

[Finger, 2005] Finger, S. (2005). Minds behind the brain: A history of the pioneers and their discoveries. Oxford University Press.

[Freund et al., 1988] Freund, I., Rosenbluh, M., and Feng, S. (1988). Memory effects in propagation of optical waves through disordered media. Physical review letters, 61(20):2328.

[Friedman et al., 2012] Friedman, E. S., Rosenbaum, M. A., Lee, A. W., Lipson, D. A., Land, B. R., and Angenent, L. T. (2012). A cost-effective and field-ready potentiostat that poises subsurface electrodes to monitor bacterial respiration. Biosensors and Bioelectronics, 32(1):309–313.

[Gamry Instruments, 2021] Gamry Instruments, I. (2019 (accessed September 6, 2021)). Interface1010 - potentiostat/galvanostat/zero resistance ammeter.

[Gao et al., 2016] Gao, W., Emaminejad, S., Nyein, H. Y. Y., Challa, S., Chen, K., Peck, A., Fahad, H. M., Ota, H., Shiraki, H., Kiriya, D., et al. (2016). Fully integrated wearable sensor arrays for multiplexed in situ perspiration analysis. Nature, 529(7587):509–514.

[Ge et al., 2005] Ge, X., Kostov, Y., and Rao, G. (2005). Low-cost noninvasive optical co2 sensing system for fermentation and cell culture. Biotechnology and bioengineering, 89(3):329–334.

[Glasscott et al., 2019] Glasscott, M. W., Verber, M. D., Hall, J. R., Pendergast, A. D., McKinney, C. J., and Dick, J. E. (2019). Sweepstat: A build-it-yourself,y two-electrode potentiostat for macroelectrode and ultramicroelectrode studies.

[Gome et al., 2019] Gome, G., Waksberg, J., Grishko, A., Wald, I. Y., and Zuckerman, O. (2019). Openlh: Open liquid-handling system for creative experimentation with biology. In Proceedings of the Thirteenth International Conference on Tangible, Embedded, and Embodied Interaction, pages 55–64. ACM.

[Gopinath and Russell, 2005] Gopinath, A. V. and Russell, D. (2005). An inexpensive field-portable programmable potentiostat. Chem Educ, 10:1–6.

[Gray et al., 1995] Gray, C. M., Maldonado, P. E., Wilson, M., and McNaughton, B. (1995). Tetrodes markedly improve the reliability and yield of multiple single-unit isolation from multi-unit recordings in cat striate cortex. Journal of neuroscience methods, 63(1-2):43–54.

[Grdeń et al., 2008] Grdeń, M., Łukaszewski, M., Jerkiewicz, G., and Czerwiński, A. (2008). Electrochemical behaviour of palladium electrode: Oxidation, electrodissolution and ionic adsorption. Electrochimica Acta, 53(26):7583–7598.

[Guibert et al., 2005] Guibert, C., Savineau, J. P., Crevel, H., Marthan, R., and Rousseau, E. (2005). Effect of short-term organoid culture on the pharmacomechanical properties of rat extra-and intrapulmonary arteries. British journal of pharmacology, 146(5):692–701.

[Haisler et al., 2013] Haisler, W. L., Timm, D. M., Gage, J. A., Tseng, H., Killian, T., and Souza, G. R. (2013). Three-dimensional cell culturing by magnetic levitation. Nature protocols, 8(10):1940–1949.

[Harrison, 1910] Harrison, R. G. (1910). The outgrowth of the nerve fiber as a mode of protoplasmic movement. Journal of Experimental Zoology, 9(4):787–846.

[Haycock, 2011] Haycock, J. W. (2011). 3d cell culture: a review of current approaches and techniques. 3D cell culture, pages 1–15.

[Hellerstein et al., 2004] Hellerstein, J. L., Diao, Y., Parekh, S., and Tilbury, D. M. (2004). Feedback control of computing systems. John Wiley & Sons.

[Hoilett et al., 2020] Hoilett, O. S., Walker, J. F., Balash, B. M., Jaras, N. J., Boppana, S., and Linnes, J. C. (2020). Kickstat: A coin-sized potentiostat for high-resolution electrochemical analysis. Sensors, 20(8):2407.

[Hu et al., 2016] Hu, Y., Sharma, S., Weatherwax, J., Cass, A., and Georgiou, P. (2016). A portable multi-channel potentiostat for real-time amperometric measurement of multi-electrode sensor arrays. In 2016 IEEE International Symposium on Circuits and Systems (ISCAS), pages 1306–1309. IEEE.

[Hwang, 2007] Hwang, H. (2007). Electrochemical analysis.

[Isaksson et al., 2007] Isaksson, J., Kjäll, P., Nilsson, D., Robinson, N., Berggren, M., and Richter-Dahlfors, A. (2007). Electronic control of ca 2+ signalling in neuronal cells using an organic electronic ion pump. Nature materials, 6(9):673.

[Jafari et al., 2020] Jafari, M., Marquez, G., Selberg, J., Jia, M., Dechiraju, H., Pansodtee, P., Teodorescu, M., Rolandi, M., and Gomez, M. (2020). Feedback control of bioelectronic devices using machine learning. IEEE Control Systems Letters, 5(4):1133–1138.

[Jafri et al., 2019] Jafri, M., Mathews, J., Selberg, J., Jia, M., Pansodtee, P., Wu, C., Teodorescu, M., Rolandi, M., and Gomez, M. (2019). Machine learning control algorithm for control ionic concentration. In preparation.

[Jedrzejczak-Silicka, 2017] Jedrzejczak-Silicka, M. (2017). History of cell culture. InTech.

[Jenkins et al., 2019] Jenkins, D. M., Lee, B. E., Jun, S., Reyes-De-Corcuera, J., and McLamore, E. S. (2019). Abe-stat, a fully open-source and versatile wireless potentiostat project including electrochemical impedance spectroscopy. Journal of The Electrochemical Society, 166(9):B3056.

[Jensen and Teng, 2020] Jensen, C. and Teng, Y. (2020). Is it time to start transitioning from 2d to 3d cell culture? Frontiers in Molecular Biosciences, 7:33.

[Jia et al., 2020a] Jia, M., Dechiruji, H., Selberg, J., Pansodtee, P., Mathews, J., Wu, C., Levin, M., Teodorescu, M., and Rolandi, M. (2020a). Bioelectronic control of chloride ions and concentration with ag/agcl contacts. APL Materials, 8(9):091106.

[Jia et al., 2020b] Jia, M., Dechiruji, H., Selberg, J., Pansodtee, P., Mathews, J., Wu, C., Levin, M., Teodorescu, M., and Rolandi, M. (2020b). Bioelectronic control of chloride ions and concentration with ag/agcl contacts. APL Materials, 8(9):091106.

[Jonsson et al., 2016] Jonsson, A., Inal, S., Uguz, I., Williamson, A. J., Kergoat, L., Rivnay, J., Khodagholy, D., Berggren, M., Bernard, C., Malliaras, G. G., et al. (2016). Bioelectronic neural pixel: Chemical stimulation and electrical sensing at the same site. Proceedings of the National Academy of Sciences, 113(34):9440–9445.

[Kakerow et al., 1995] Kakerow, R. G., Kappert, H., Spiegel, E., and Manoli, Y. (1995). Low-power single-chip cmos potentiostat. In Proceedings of the International Solid-State Sensors and Actuators Conference-TRANSDUCERS'95, volume 1, pages 142–145. IEEE.

[Kalderon, 1983] Kalderon, A. E. (1983). The evolution of microscope design from its invention to the present days. The American journal of surgical pathology, 7(1):95.

[Kesavan et al., 2014] Kesavan, S. V., Momey, F., Cioni, O., David-Watine, B., Dubrulle, N., Shorte, S., Sulpice, E., Freida, D., Chalmond, B., Dinten, J., et al. (2014). High-throughput monitoring of major cell functions by means of lensfree video microscopy. Scientific reports, 4:5942.

[Khodagholy et al., 2011] Khodagholy, D., Doublet, T., Gurfinkel, M., Quilichini, P., Ismailova, E., Leleux, P., Herve, T., Sanaur, S., Bernard, C., and Malliaras, G. G. (2011). Highly conformable conducting polymer electrodes for in vivo recordings. Advanced Materials, 23(36):H268–H272.

[Khodagholy et al., 2013] Khodagholy, D., Doublet, T., Quilichini, P., Gurfinkel, M., Leleux, P., Ghestem, A., Ismailova, E., Hervé, T., Sanaur, S., Bernard, C., et al. (2013). In vivo recordings of brain activity using organic transistors. Nature communications, 4:1575.

[Khodagholy et al., 2015] Khodagholy, D., Gelinas, J. N., Thesen, T., Doyle, W., Devinsky, O., Malliaras, G. G., and Buzsáki, G. (2015). Neurogrid: recording action potentials from the surface of the brain. Nature neuroscience, 18(2):310.

[Kim et al., 2018a] Kim, G., Kim, K., Lee, E., An, T., Choi, W., Lim, G., and Shin, J. (2018a). Recent progress on microelectrodes in neural interfaces. Materials, 11(10):1995.

[Kim et al., 2018b] Kim, J., Campbell, A. S., and Wang, J. (2018b). Wearable non-invasive epidermal glucose sensors: A review. Talanta, 177:163–170.

[Kim et al., 2012] Kim, S. B., Koo, K.-i., Bae, H., Dokmeci, M. R., Hamilton, G. A., Bahinski, A., Kim, S. M., Ingber, D. E., and Khademhosseini, A. (2012). A mini-microscope for in situ monitoring of cells. Lab on a Chip, 12(20):3976–3982.

[Kindlundh et al., 2004] Kindlundh, M., Norlin, P., and Hofmann, U. G. (2004). A neural probe process enabling variable electrode configurations. Sensors and Actuators B: Chemical, 102(1):51–58.

[Kriss and Kriss, 1998] Kriss, T. C. and Kriss, V. M. (1998). History of the operating microscope: from magnifying glass to microneurosurgery. Neurosurgery, 42(4):899–907.

[Kuo et al., 2013] Kuo, J. T., Kim, B. J., Hara, S. A., Lee, C. D., Gutierrez, C. A., Hoang, T. Q., and Meng, E. (2013). Novel flexible parylene neural probe with 3d sheath structure for enhancing tissue integration. Lab on a Chip, 13(4):554–561.

[Lancaster and Knoblich, 2014] Lancaster, M. A. and Knoblich, J. A. (2014). Organogenesis in a dish: modeling development and disease using organoid technologies. Science, 345(6194):1247125.

[Lancaster et al., 2013] Lancaster, M. A., Renner, M., Martin, C.-A., Wenzel, D., Bicknell, L. S., Hurles, M. E., Homfray, T., Penninger, J. M., Jackson, A. P., and Knoblich, J. A. (2013). Cerebral organoids model human brain development and microcephaly. Nature, 501(7467):373.

[Lang et al., 2013] Lang, X.-Y., Fu, H.-Y., Hou, C., Han, G.-F., Yang, P., Liu, Y.-B., and Jiang, Q. (2013). Nanoporous gold supported cobalt oxide microelectrodes as high-performance electrochemical biosensors. Nature communications, 4(1):1–8.

[Langer and Jonsson, 2019] Langer, K. and Jonsson, H. (2019). Draft-robotic automation of production and the recovery of cell spheroids. BioRxiv, page 552687.

[Langhans, 2018] Langhans, S. A. (2018). Three-dimensional in vitro cell culture models in drug discovery and drug repositioning. Frontiers in pharmacology, 9:6.

[Lee et al., 2012] Lee, P. Y., Costumbrado, J., Hsu, C.-Y., and Kim, Y. H. (2012). Agarose gel electrophoresis for the separation of dna fragments. JoVE (Journal of Visualized Experiments), (62):e3923.

[Levin et al., 2017] Levin, M., Pezzulo, G., and Finkelstein, J. M. (2017). Endogenous bioelectric signaling networks: exploiting voltage gradients for control of growth and form. Annual review of biomedical engineering, 19:353–387.

[Li et al., 2004] Li, H., Luo, X., Liu, C., Jiang, L., Cui, D., Cai, X., and Yang, Q. (2004). Multi-channel electrochemical detection system based on labview. In International Conference on Information Acquisition, 2004. Proceedings., pages 224–227. IEEE.

[Li et al., 2018] Li, Y. C., Melenbrink, E. L., Cordonier, G. J., Boggs, C., Khan, A., Isaac, M. K., Nkhonjera, L. K., Bahati, D., Billinge, S. J., Haile, S. M., et al. (2018). An easily fabricated low-cost potentiostat coupled with user-friendly software for introducing students to electrochemical reactions and electroanalytical techniques.

[Lodish H, 2000] Lodish H, Berk A, Z. S. (2000). Intracellular ion environment and membrane electric potential. In Molecular Cell Biology. 4th edition, page 15.4. W. H. Freeman.

[Ly et al., 2021] Ly, V. T., Baudin, P. V., Pansodtee, P., Jung, E. A., Voitiuk, K., Rosen, Y., Willsey, H. R., Mantalas, G. L., Seiler, S. T., Selberg, J. A., et al. (2021). Development of a low-cost system for simultaneous longitudinal biological imaging. Communications Biology.

[Mansour et al., 2018] Mansour, A. A., Gonçalves, J. T., Bloyd, C. W., Li, H., Fernandes, S., Quang, D., Johnston, S., Parylak, S. L., Jin, X., and Gage, F. H. (2018). An in vivo model of functional and vascularized human brain organoids. Nature biotechnology, 36(5):432.

[Martin et al., 2009] Martin, S. M., Gebara, F. H., Strong, T. D., and Brown, R. B. (2009). A fully differential potentiostat. IEEE Sensors Journal, 9(2):135–142.

[Marvin, 1961] Marvin, M. (1961). Microscopy apparatus. US Patent 3,013,467.

[Masters, 2001] Masters, B. R. (2001). History of the optical microscope in cell biology and medicine. e LS.

[McMullan, 1995] McMullan, D. (1995). Scanning electron microscopy 1928–1965. Scanning, 17(3):175–185.

[McMurtrey, 2016] McMurtrey, R. J. (2016). Analytic models of oxygen and nutrient diffusion, metabolism dynamics, and architecture optimization in three-dimensional tissue constructs with applications and insights in cerebral organoids. Tissue Engineering Part C: Methods, 22(3):221–249.

[McNaughton et al., 1983] McNaughton, B. L., O'Keefe, J., and Barnes, C. A. (1983). The stereotrode: a new technique for simultaneous isolation of several single units in the central nervous system from multiple unit records. Journal of neuroscience methods, 8(4):391–397.

[Meloni, 2016] Meloni, G. N. (2016). Building a microcontroller based potentiostat: A inexpensive and versatile platform for teaching electrochemistry and instrumentation.

[Merces et al., 2021] Merces, G. O., Kennedy, C., Lenoci, B., Reynaud, E. G., Burke, N., and Pickering, M. (2021). The incubot: A 3d printer-based microscope for long-term live cell imaging within a tissue culture incubator. HardwareX, 9:e00189.

[Metrohm Autolab, 2020] Metrohm Autolab, I. (2020 (accessed April 23, 2020)). Metrohm Autolab - hardware specification.

[Molderez et al., 2020] Molderez, T. R., Rabaey, K., and Verhelst, M. (2020). An affordable multichannel potentiostat with 128 individual stimulation and sensing channels. In 2020 IEEE International Instrumentation and Measurement Technology Conference (I2MTC), pages 1–6. IEEE.

[Momey et al., 2016] Momey, F., Berdeu, A., Bordy, T., Dinten, J.-M., Marcel, F. K., Picollet-D'Hahan, N., Gidrol, X., and Allier, C. (2016). Lensfree diffractive tomography for the imaging of 3d cell cultures. Biomedical optics express, 7(3):949–962.

[Moreno et al., 2006] Moreno, L., Merlos, A., Abramova, N., Jimenez, C., and Bratov, A. (2006). Multi-sensor array used as an "electronic tongue" for mineral water analysis. Sensors and Actuators B: Chemical, 116(1-2):130–134.

[Nakano et al., 2012] Nakano, T., Ando, S., Takata, N., Kawada, M., Muguruma, K., Sekiguchi, K., Saito, K., Yonemura, S., Eiraku, M., and Sasai, Y. (2012). Self-formation of optic cups and storable stratified neural retina from human escs. Cell stem cell, 10(6):771–785.

[Napolitano et al., 2007] Napolitano, A. P., Dean, D. M., Man, A. J., Youssef, J., Ho, D. N., Rago, A. P., Lech, M. P., and Morgan, J. R. (2007). Scaffold-free three-dimensional cell culture utilizing micromolded nonadhesive hydrogels. Biotechniques, 43(4):494–500.

[Nguyen et al., 2013] Nguyen, N.-T., Shaegh, S. A. M., Kashaninejad, N., and Phan, D.-T. (2013). Design, fabrication and characterization of drug delivery systems based on lab-on-a-chip technology. Advanced drug delivery reviews, 65(11-12):1403–1419.

[Nicolelis et al., 2003] Nicolelis, M. A., Dimitrov, D., Carmena, J. M., Crist, R., Lehew, G., Kralik, J. D., and Wise, S. P. (2003). Chronic, multisite, multielectrode recordings in macaque monkeys. Proceedings of the National Academy of Sciences, 100(19):11041–11046.

[Nissa et al., 2021] Nissa, J., Janson, P., Berggren, M., and Simon, D. T. (2021). The role of relative capacitances in impedance sensing with organic electrochemical transistors. Advanced Electronic Materials, 7(4):2001173.

[Nitta et al., 2015] Nitta, N., Wu, F., Lee, J. T., and Yushin, G. (2015). Li-ion battery materials: present and future. Materials today, 18(5):252–264.

[Normann et al., 1999] Normann, R. A., Maynard, E. M., Rousche, P. J., and Warren, D. J. (1999). A neural interface for a cortical vision prosthesis. Vision research, 39(15):2577–2587.

[NuVant Systems, 2020] NuVant Systems, I. (2011 (accessed April 23, 2020)). Arraystat - The ultimate tool for high throughput electrochemistry.

[Pansodtee et al., 2021] Pansodtee, P., Selberg, J., Jia, M., Jafari, M., Dechiraju, H., Thomsen, T., Gomez, M., Rolandi, M., and Teodorescu, M. (2021). The multi-channel potentiostat: Development and evaluation of a scalable mini-potentiostat array for investigating electrochemical reaction mechanisms. PLOS ONE, 16(9):1–14.

[Pansodtee et al., 2019] Pansodtee, P., Selberg, J., Jia, M., Wu, C., Teodorescu, M., and Rolandi, M. (2019). Multi-purpose bioelectronic portable controller. To be submitted to PLOS One.

[Parrilla et al., 2019] Parrilla, M., Ortiz-Gomez, I., Canovas, R., Salinas-Castillo, A., Cuartero, M., and Crespo, G. A. (2019). Wearable potentiometric ion patch for on-body electrolyte monitoring in sweat: toward a validation strategy to ensure physiological relevance. Analytical chemistry, 91(13):8644–8651.

[Pessen, 1994] Pessen, D. W. (1994). A new look at pid-controller tuning.

[Phelan et al., 2018] Phelan, M. A., Lelkes, P. I., and Swaroop, A. (2018). Mini and customized low-cost bioreactors for optimized high-throughput generation of tissue organoids. Stem cell investigation, 5.

[Pin et al., 2014] Pin, C., Parker, A., Gunning, A. P., Ohta, Y., Johnson, I. T., Carding, S. R., and Sato, T. (2014). An individual based computational model of intestinal crypt fission and its application to predicting unrestrictive growth of the intestinal epithelium. Integrative Biology, 7(2):213–228.

[Poli et al., 2019] Poli, D., Magliaro, C., and Ahluwalia, A. (2019). Experimental and computational methods for the study of cerebral organoids: A review. Frontiers in neuroscience, 13.

[Poxson et al., 2019] Poxson, D. J., Gabrielsson, E. O., Bonisoli, A., Linderhed, U., Abrahamsson, T. F., Matthiesen, I., Tybrandt, K., Berggren, M., and Simon, D. T. (2019). Capillary fiber-based electrophoretic delivery device. ACS applied materials & interfaces.

[Poxson et al., 2017] Poxson, D. J., Karady, M., Gabrielsson, R., Alkattan, A. Y., Gustavsson, A., Doyle, S. M., Robert, S., Ljung, K., Grebe, M., Simon, D. T., et al. (2017). Regulating plant physiology with organic electronics. Proceedings of the National Academy of Sciences, 114(18):4597–4602.

[Prasher et al., 1992] Prasher, D. C., Eckenrode, V. K., Ward, W. W., Prendergast, F. G., and Cormier, M. J. (1992). Primary structure of the aequorea victoria green-fluorescent protein. Gene, 111(2):229–233.

[Quadrato et al., 2017] Quadrato, G., Nguyen, T., Macosko, E. Z., Sherwood, J. L., Yang, S. M., Berger, D. R., Maria, N., Scholvin, J., Goldman, M., Kinney, J. P., et al. (2017). Cell diversity and network dynamics in photosensitive human brain organoids. Nature, 545(7652):48.

[Renz, 2013] Renz, M. (2013). Fluorescence microscopy—a historical and technical perspective. Cytometry Part A, 83(9):767–779.

[Ringer, 1883] Ringer, S. (1883). A further contribution regarding the influence of the different constituents of the blood on the contraction of the heart. The Journal of physiology, 4(1):29–42.

[Rosen et al., 2019] Rosen, Y., Voitiuk, K., Baudin, P., Ly, V., Mantalas, G., Pansodtee, P., Jung, E., Salama, S., Haussler, D., and Teodorescu, M. (2019). A parallel microscope system for high throughput tissue imaging. Asilomar Bioelectronics.

[Rosenfeld, 2000] Rosenfeld, L. (2000). A golden age of clinical chemistry: 1948–1960. Clinical chemistry, 46(10):1705–1714.

[Rossi et al., 2018] Rossi, G., Manfrin, A., and Lutolf, M. P. (2018). Progress and potential in organoid research. Nature Reviews Genetics, page 1.

[Rowe et al., 2011] Rowe, A. A., Bonham, A. J., White, R. J., Zimmer, M. P., Yadgar, R. J., Hobza, T. M., Honea, J. W., Ben-Yaacov, I., and Plaxco, K. W. (2011). Cheapstat: an open-source,"do-it-yourself" potentiostat for analytical and educational applications. PloS one, 6(9).

[Ruska, 1987] Ruska, E. (1987). The development of the electron microscope and of electron microscopy. Reviews of modern physics, 59(3):627.

[Sakmann and Neher, 1984] Sakmann, B. and Neher, E. (1984). Patch clamp techniques for studying ionic channels in excitable membranes. Annual review of physiology, 46(1):455–472.

[Sanderson and Rayner, 2018] Sanderson, T. and Rayner, J. C. (2018). Plasmotron: an open-source platform for automated culture of malaria parasites. BioRxiv, page 241596.

[Sato et al., 2009] Sato, T., Vries, R. G., Snippert, H. J., Van De Wetering, M., Barker, N., Stange, D. E., Van Es, J. H., Abo, A., Kujala, P., Peters, P. J., et al. (2009). Single lgr5 stem cells build crypt–villus structures in vitro without a mesenchymal niche. Nature, 459(7244):262.

[Scott et al., 2013] Scott, A., Weir, K., Easton, C., Huynh, W., Moody, W. J., and Folch, A. (2013). A microfluidic microelectrode array for simultaneous electrophysiology, chemical stimulation, and imaging of brain slices. Lab on a Chip, 13(4):527–535.

[Selberg et al., 2020a] Selberg, J., Jafari, M., Bradley, C., Gomez, M., and Rolandi, M. (2020a). Expanding biological control to bioelectronics with machine learning. APL Materials, 8(12):120904.

[Selberg et al., 2020b] Selberg, J., Jafari, M., Mathews, J., Jia, M., Pansodtee, P., Dechiraju, H., Wu, C., Cordero, S., Flora, A., Yonas, N., et al. (2020b). Machine learning-driven bioelectronics for closed-loop control of cells. Advanced Intelligent Systems, 2(12):2000140.

[Selberg et al.,] Selberg, J., Jafari, M., Mathews, J., Jia, M., Pansodtee, P., Dechiraju, H., Wu, C., Cordero, S., Flora, A., Yonas, N., Jannetty, S., Diberardinis, M., Teodorescu, M., Levin, M., Gomez, M., and Rolandi, M. Machine learning-driven bioelectronics for closed-loop control of cells. Advanced Intelligent Systems, n/a(n/a):2000140.

[Shanelec, 1992] Shanelec, D. (1992). Optical principles of loupes. Journal of the California Dental Association, 20(11):25–32.

[Shen et al., 2018] Shen, T., Zhou, T., Wan, Y., and Su, Y. (2018). High-precision and low-cost wireless 16-channel measurement system for malachite green detection. Micromachines, 9(12):646.

[Shobe et al., 2015] Shobe, J. L., Claar, L. D., Parhami, S., Bakhurin, K. I., and Masmanidis, S. C. (2015). Brain activity mapping at multiple scales with silicon microprobes containing 1,024 electrodes. Journal of neurophysiology, 114(3):2043–2052.

[Simon et al., 2009] Simon, D. T., Kurup, S., Larsson, K. C., Hori, R., Tybrandt, K., Goiny, M., Jager, E. W., Berggren, M., Canlon, B., and Richter-Dahlfors, A. (2009). Organic electronics for precise delivery of neurotransmitters to modulate mammalian sensory function. Nature materials, 8(9):742.

[Spence et al., 2011] Spence, J. R., Mayhew, C. N., Rankin, S. A., Kuhar, M. F., Vallance, J. E., Tolle, K., Hoskins, E. E., Kalinichenko, V. V., Wells, S. I., Zorn, A. M., et al. (2011). Directed differentiation of human pluripotent stem cells into intestinal tissue in vitro. Nature, 470(7332):105.

[Stanacevic et al., 2007] Stanacevic, M., Murari, K., Rege, A., Cauwenberghs, G., and Thakor, N. V. (2007). Vlsi potentiostat array with oversampling gain modulation for wide-range neurotransmitter sensing. IEEE Transactions on Biomedical Circuits and Systems, 1(1):63–72.

[Stett et al., 2003] Stett, A., Egert, U., Guenther, E., Hofmann, F., Meyer, T., Nisch, W., and Haemmerle, H. (2003). Biological application of microelectrode arrays in drug discovery and basic research. Analytical and bioanalytical chemistry, 377(3):486–495.

[Strakosas et al., 2019a] Strakosas, X., Selberg, J., Pansodtee, P., Yonas, N., Manapongpun, P., Teodorescu, M., and Rolandi, M. (2019a). A non-enzymatic glucose sensor enabled by bioelectronic ph control. Scientific Reports, 9(1):10844.

[Strakosas et al., 2019b] Strakosas, X., Selberg, J., Zhang, X., Christie, N., Hsu, P.-H., Almutairi, A., and Rolandi, M. (2019b). A bioelectronic platform modulates ph in biologically relevant conditions. Advanced Science, 6(7):1800935.

[Stratmann et al.,] Stratmann, L., Heery, B., and Coffey, B. Emstat pico: Embedded electrochemistry with a miniaturized, software-enabled, potentiostat system on module.

[Strumwasser, 1958] Strumwasser, F. (1958). Long-term recording from single neurons in brain of unrestrained mammals. Science, 127(3296):469–470.

[Tapsak et al., 2007] Tapsak, M. A., Houseknecht, J. G., and Goode, P. V. (2007). A low cost-computer-controlled and powered multichannel potentiostat for general use in development of inexpensive electrochemical sensors. Instrumentation Science and Technology, 35(6):589–598.

[Theodosiou et al., 2017] Theodosiou, P., Faina, A., Nejatimoharrami, F., Stoy, K., Greenman, J., Melhuish, C., and Ieropoulos, I. (2017). Evobot: towards a robot-chemostat for culturing and maintaining microbial fuel cells (mfcs). In Conference on Biomimetic and Biohybrid Systems, pages 453–464. Springer.

[Toghill and Compton, 2010] Toghill, K. E. and Compton, R. G. (2010). Electrochemical non-enzymatic glucose sensors: a perspective and an evaluation. Int. J. Electrochem. Sci, 5(9):1246–1301.

[Türker et al., 2018] Türker, E., Demirçak, N., and Arslan-Yildiz, A. (2018). Scaffold-free three-dimensional cell culturing using magnetic levitation. Biomaterials science, 6(7):1745–1753.

[Turner, 2013] Turner, A. P. (2013). Biosensors: sense and sensibility. Chemical Society Reviews, 42(8):3184–3196.

[Turner et al., 1987] Turner, R. F., Harrison, D. J., and Baltes, H. P. (1987). A cmos potentiostat for amperometric chemical sensors. IEEE Journal of Solid-State Circuits, 22(3):473–478.

[Uguz et al., 2017] Uguz, I., Proctor, C. M., Curto, V. F., Pappa, A.-M., Donahue, M. J., Ferro, M., Owens, R. M., Khodagholy, D., Inal, S., and Malliaras, G. G. (2017). A microfluidic ion pump for in vivo drug delivery. Advanced Materials, 29(27):1701217.

[van de Wetering et al., 2015] van de Wetering, M., Francies, H. E., Francis, J. M., Bounova, G., Iorio, F., Pronk, A., van Houdt, W., van Gorp, J., Taylor-Weiner, A., Kester, L., et al. (2015). Prospective derivation of a living organoid biobank of colorectal cancer patients. Cell, 161(4):933–945.

[Van Enter and Von Hauff, 2018] Van Enter, B. J. and Von Hauff, E. (2018). Challenges and perspectives in continuous glucose monitoring. Chemical Communications, 54(40):5032–5045.

[Walsh et al., 2014] Walsh, A. J., Cook, R. S., Sanders, M. E., Aurisicchio, L., Ciliberto, G., Arteaga, C. L., and Skala, M. C. (2014). Quantitative optical imaging of primary tumor organoid metabolism predicts drug response in breast cancer. Cancer research, 74(18):5184–5194.

[Wang et al., 1998] Wang, F., Weaver, V. M., Petersen, O. W., Larabell, C. A., Dedhar, S., Briand, P., Lupu, R., and Bissell, M. J. (1998). Reciprocal interactions between β1-integrin and epidermal growth factor receptor in three-dimensional basement membrane breast cultures: a different perspective in epithelial biology. Proceedings of the National Academy of Sciences, 95(25):14821–14826.

[Wang et al., 2017] Wang, Z., Boddeda, A., Parker, B., Samanipour, R., Ghosh, S., Menard, F., and Kim, K. (2017). A high-resolution minimicroscope system for wireless real-time monitoring. IEEE Transactions on Biomedical Engineering, 65(7):1524–1531.

[Weltin et al., 2014] Weltin, A., Slotwinski, K., Kieninger, J., Moser, I., Jobst, G., Wego, M., Ehret, R., and Urban, G. A. (2014). Cell culture monitoring for drug screening and cancer research: a transparent, microfluidic, multi-sensor microsystem. Lab on a Chip, 14(1):138–146.

[Williams and Carter, 1996] Williams, D. B. and Carter, C. B. (1996). The transmission electron microscope. In Transmission electron microscopy, pages 3–17. Springer.

[Williamson et al., 2015] Williamson, A., Rivnay, J., Kergoat, L., Jonsson, A., Inal, S., Uguz, I., Ferro, M., Ivanov, A., Sjöström, T. A., Simon, D. T., et al. (2015). Controlling epileptiform activity with organic electronic ion pumps. Advanced Materials, 27(20):3138–3144.

[Wilson, 1907] Wilson, H. (1907). A new method by which sponges may be artificially reared. Journal of the Elisha Mitchell Scientific Society, 23(3):91–97.

[Wong et al., 2018] Wong, B. G., Mancuso, C. P., Kiriakov, S., Bashor, C. J., and Khalil, A. S. (2018). Precise, automated control of conditions for high-throughput growth of yeast and bacteria with evolver. Nature biotechnology, 36(7):614.

[Wu et al., 1967] Wu, A., Till, J., Siminovitch, L., and McCulloch, E. (1967). A cytological study of the capacity for differentiation of normal hemopoietic colony-forming cells. Journal of cellular physiology, 69(2):177–184.

[Wu et al., 2019] Wu, C., Selberg, J., Nguyen, B., Pansodtee, P., Chen, M., Jia, M., Dechiraju, H., and Rolandi, M. (2019). Ion sensor array for cell metabolism detection. To be submitted to Advanced Healthcare Materials.

[Wu et al., 2020] Wu, C., Selberg, J., Nguyen, B., Pansodtee, P., Jia, M., Dechiraju, H., Teodorescu, M., and Rolandi, M. (2020). A microfluidic ion sensor array. Small, 16(6):1906436.

[Wu and Ozcan, 2018] Wu, Y. and Ozcan, A. (2018). Lensless digital holographic microscopy and its applications in biomedicine and environmental monitoring. Methods, 136:4–16.

[Xu et al., 2019] Xu, G., Cheng, C., Liu, Z., Yuan, W., Wu, X., Lu, Y., Low, S. S., Liu, J., Zhu, L., Ji, D., et al. (2019). Battery-free and wireless epidermal electrochemical system with all-printed stretchable electrode array for multiplexed in situ sweat analysis. Advanced Materials Technologies, 4(7):1800658.

[Yao et al., 2012] Yao, H., Liao, Y., Lingley, A., Afanasiev, A., Lähdesmäki, I., Otis, B., and Parviz, B. (2012). A contact lens with integrated telecommunication circuit and sensors for wireless and continuous tear glucose monitoring. Journal of Micromechanics and Microengineering, 22(7):075007.

[Yin et al., 2016] Yin, X., Mead, B. E., Safaee, H., Langer, R., Karp, J. M., and Levy, O. (2016). Engineering stem cell organoids. Cell stem cell, 18(1):25–38.

[Zernike, 1942] Zernike, F. (1942). Phase contrast, a new method for the microscopic observation of transparent objects. Physica, 9(7):686–698.

[Zhang et al., 2005] Zhang, J., Huang, Y., Trombly, N., Yang, C., and Mason, A. (2005). Electrochemical array microsystem with integrated potentiostat. In SENSORS, 2005 IEEE, pages 4–pp. IEEE.

[Zhang et al., 1991] Zhang, Y., Bindra, D. S., Barrau, M.-B., and Wilson, G. S. (1991). Application of cell culture toxicity tests to the development of implantable biosensors. Biosensors and Bioelectronics, 6(8):653–661.

[Zhang et al., 2015] Zhang, Y. S., Ribas, J., Nadhman, A., Aleman, J., Selimović, Š., Lesher-Perez, S. C., Wang, T., Manoharan, V., Shin, S.-R., Damilano, A., et al. (2015). A cost-effective fluorescence mini-microscope for biomedical applications. Lab on a Chip, 15(18):3661–3669.

[Zhang et al., 2018] Zhang, Z., Kashiwagi, H., Kimura, S., Kong, S., Ohta, Y., and Miyake, T. (2018). A protonic biotransducer controlling mitochondrial atp synthesis. Scientific reports, 8(1):10423.

[Zhao et al., 2020] Zhao, Y., Wang, B., Hojaiji, H., Wang, Z., Lin, S., Yeung, C., Lin, H., Nguyen, P., Chiu, K., Salahi, K., Cheng, X., Tan, J., Cerrillos, B. A., and Emaminejad, S. (2020). A wearable freestanding electrochemical sensing system. Science Advances, 6(12).

[Zhu et al., 2017] Zhu, Y., Wang, L., Yin, F., Yu, Y., Wang, Y., Liu, H., Wang, H., Sun, N., Liu, H., and Qin, J. (2017). A hollow fiber system for simple generation of human brain organoids. Integrative Biology, 9(9):774–781.